

**Small Body Orbital Dynamics in the Solar System:  
Celestial Mechanics and Impacts**

by

Sarah Greenstreet

B.S., Western Washington University, 2007

M.S., The University of British Columbia, 2011

A THESIS SUBMITTED IN PARTIAL FULFILLMENT  
OF THE REQUIREMENTS FOR THE DEGREE OF

**Doctor of Philosophy**

in

THE FACULTY OF GRADUATE AND POSTDOCTORAL  
STUDIES  
(Astronomy)

The University Of British Columbia  
(Vancouver)

July 2015

© Sarah Greenstreet, 2015

# Abstract

Studying the orbital dynamics of small body populations in the Solar System allows us to understand both their current population and past orbital structure. Planet-crossing populations can also provide impact speeds and probabilities, and when coupled to cratering histories of solid bodies can provide planetary surface ages.

The *Wide-field Infrared Survey Explorer* Near-Earth Object (NEOWISE) detections of the near-Earth object (NEO) orbital distributions (Mainzer et al., 2012) are used to illustrate that a pure-gravity NEO orbital model (Greenstreet et al., 2012a) is not rejectable (at  $> 99\%$  confidence). Thus, no non-gravitational physics is required to model the NEO orbital distribution.

We discovered in the NEO model numerical integrations the unexpected production of retrograde orbits from main asteroid belt sources, estimating that  $\sim 0.1\%$  of the steady-state NEO population is on retrograde orbits. These retrograde near-Earth asteroids (NEAs) may answer two outstanding questions in the literature: the origin of two known MPC NEOs with asteroidal designations on retrograde orbits and the origin of high-strength, high-velocity meteoroids on retrograde orbits.

Moving to the outer Solar System, we constructed a Centaur ( $a_{Jupiter} < a < a_{Neptune}$ ) model, supplied from the transneptunian region, to estimate temporary co-orbital capture frequency and duration with the giant planets, finding that at any time 0.4% and 2.8% of the population will be Uranian and Neptunian co-orbitals, respectively. This is in agreement with the known fraction of temporary Ura-

nian and Neptunian co-orbitals, respectively. Thus, the scattering transneptunian population provides a self-consistent external source for the unstable giant-planet co-orbitals.

In addition to studying the orbital dynamics of small body populations in the Solar System, impact and cratering rates onto planetary surfaces can be determined. The upcoming New Horizons spacecraft fly-through of the Pluto system in July 2015 will provide humanity's first data for the crater populations on Pluto and its moons. In principle, absolute ages for these surfaces could be determined using the observed surface crater density. However, due to the uncertainty in how the Kuiper belt size distribution extends to small ( $d < 100$  km) projectiles, absolute ages are entirely model-dependent and thus fraught with uncertainty.

# Preface

The text of this dissertation includes modified reprints of previously published material as listed below.

## **Chapter 3** (published):

- S. Greenstreet and B. Gladman *High-inclination Atens are Indeed Rare*, *ApJ* **767**, L18 (2013).

This paper compares the detected orbital element distributions detected by the NEOWISE space telescope and the Bottke et al. (2002) NEO orbital distribution model as published by Mainzer et al. (2012) to the newer NEO model from Greenstreet et al. (2012a). I contributed to this project by taking the published biases for the orbital element distributions from Mainzer et al. (2012) for the NEOWISE detections and applying them to the one-dimensional orbital element distributions from the NEO model from Greenstreet et al. (2012a) to compare to the biased distributions from the Bottke et al. (2002) model as published by Mainzer et al. (2012). I also executed the Kolmogorov-Smirnov tests to determine the probability of getting the NEOWISE detected distributions from each model. I wrote the majority of the manuscript, with editing by Brett Gladman, and produced all the figures and tables.

## **Chapter 4** (published):

- S. Greenstreet, B. Gladman, H. Ngo, M. Granvik, and S. Larson, *Production of Near-Earth Asteroids on Retrograde Orbits*, *ApJ* **749**, L39 (2012).

This paper discusses the unexpected production of near-Earth asteroids (NEAs) onto retrograde (backwards around the Sun) orbits from accepted main belt asteroidal sources in the numerical integrations used to produce the Greenstreet et al. (2012a) NEO orbital distribution model. I discovered these NEAs on retrograde orbits when searching through the numerical integrations. The surprising nature of these objects was pointed out to me by Brett Gladman, which prompted the closer look into their production mechanism and typical orbital evolutions. I wrote the code used to sift through the integration outputs to find retrograde behavior as well as extract examples of typical retrograde orbital evolutions. I also ran one of the two sets of numerical integrations for the best-fit orbits for the two known retrograde NEAs, while Mikael Granvik ran the other set, and ran the additional integrations for both objects. I produced all the figures and wrote the majority of the manuscript, with edits done by Brett Gladman, Henry Ngo, Mikael Granvik, and Steve Larson.

**Chapter 6** (published):

- M. Alexandersen, B. Gladman, S. Greenstreet, J. J. Kavelaars, J. M. Petit, S. Gwyn, *A Uranian Trojan and the Frequency of Temporary Giant-Planet Co-Orbitals*, *Science* **341**, 994 (2013).

This paper examined the frequency of co-orbitals temporarily trapped in the 1:1 mean-motion resonance with the giant planets in order to explain the discovery of the first known Uranian Trojan. This was a joint project with PhD student Mike Alexandersen who brought me into the project. Mike's observational survey detected the object, tracked it to determine a high-precision orbit, and then recognized the Trojan character. I set-up and performed the numerical integrations of the four giant planets and scattering objects as they entered the Centaur region. I then wrote the code to search through the numerical output for co-orbital behavior and computed the fraction of the steady-state population in co-orbital resonance with Uranus and Neptune as well as the mean, median, and maximum durations of the temporary captures. I wrote the following

sections of the published supplementary material for the manuscript: details on dynamical integrations, co-orbital detection, resonant island classification, and quasi-satellites, since I performed all of the analysis presented in these sections. I also provided editing for the manuscript.

**Chapter 7** (published):

- S. Greenstreet, B. Gladman, and W. B. McKinnon, *Impact and Cratering Rates onto Pluto*, *Icarus* **258**, 267 (2015).

This paper discusses the impact and cratering rates onto Pluto and its binary companion Charon from the various Kuiper belt sub-populations as well as the catastrophic disruption rate of the four smaller satellites: Styx, Nix, Kerberos, and Hydra. The idea for this project came from Brett Gladman and he helped provide me with the background knowledge I needed. Understanding and interpreting the outcome was a joint effort by the two of us with help from co-author Bill McKinnon. I modified and wrote all the code used in this project. I modified an existing piece of collision probability code to produce the impact velocity distributions and impact probabilities for each Kuiper belt sub-population. I set-up and ran the numerical integrations used to correct for Pluto's dynamical effects that were not accounted for in the collision probability code. I also wrote the code to convert the impact rates for each sub-population to cratering rates as well as the integrated number of craters over the past 4 Gyr. In addition, I wrote the code to compute the crater density plots and R plots as well as the code to compute the catastrophic disruption rates for Pluto's four smaller satellites. The writing of the manuscript was divided up as follows: Bill McKinnon wrote the sections on Triton and Secondary craters, Brett Gladman wrote the first three sub-sections of the Discussion section, and I wrote the rest of the manuscript with editing by both Brett and Bill. I also produced all the tables and figures, except figure 2, which was made by Brett.

## **Appendix A:**

This appendix discusses a set of integrations that were performed to determine whether the numerical integrations used to create the Greenstreet et al. (2012a) NEO orbital distribution model had reached convergence at the 4 hour base integration time step used by running the same set of initial conditions with five different time steps: 2 hours, 4 hours, 8 hours, 16 hours, and 84 hours (3.5 days, used in the Bottke et al. (2002) model integrations). The initial conditions and time steps chosen for these integrations were decided upon by both myself and Brett Gladman. I performed the integrations and analyzed the orbital distribution of the particles at the end of the 1 Myr integrations to determine if convergence had reached for the 4 hour time step. I wrote the appendix with the exception of Section A.4, which was written by Brett. I also produced all the figures.

# Table of Contents

<b>Abstract</b> . . . . .	<b>ii</b>
<b>Preface</b> . . . . .	<b>iv</b>
<b>Table of Contents</b> . . . . .	<b>viii</b>
<b>List of Tables</b> . . . . .	<b>xii</b>
<b>List of Figures</b> . . . . .	<b>xiii</b>
<b>List of Symbols and Abbreviations</b> . . . . .	<b>xv</b>
<b>Acknowledgements</b> . . . . .	<b>xxii</b>
<b>Dedication</b> . . . . .	<b>xxiv</b>
<b>1 Introduction</b> . . . . .	<b>1</b>
1.1 Motivation . . . . .	1
1.1.1 Small Body Populations . . . . .	2
1.1.2 Impact Rates & Cratering in the Solar System . . . . .	2
1.2 Thesis Outline . . . . .	3
<b>2 An Introduction to Near-Earth Objects and the Main Asteroid Belt</b>	<b>5</b>
2.1 Near-Earth Objects . . . . .	5
2.1.1 NEO Dynamical Classification . . . . .	6

2.1.2	NEO Orbital Distribution . . . . .	7
2.2	Main Belt Dynamics and Near-Earth Object Source Regions . . . .	11
2.2.1	Resonances in the Main Belt . . . . .	11
2.2.2	Jupiter Family Comets . . . . .	19
2.2.3	Past Work with Numerical Integrations . . . . .	19
2.2.4	Non-Gravitational Forces . . . . .	23
2.3	Size Distributions of the Main Asteroid Belt and Near-Earth Objects	24
2.3.1	Surveys of the Main Asteroid Belt . . . . .	26
2.3.2	Surveys of Near-Earth Objects . . . . .	29
2.3.3	Origin of a Wavy Size Distribution . . . . .	29
2.4	Conclusions . . . . .	31
<b>3</b>	<b>High-Inclination Atens are Indeed Rare . . . . .</b>	<b>32</b>
3.1	Introduction . . . . .	32
3.2	Integration Methods . . . . .	33
3.2.1	Comparison of $a$ , $e$ , $i$ Distributions for the Two Models . . . .	34
3.3	Two Models Compared to NEOWISE Aten Detections . . . . .	35
3.3.1	Semimajor Axis Distributions . . . . .	37
3.3.2	Eccentricity and Inclination Distributions . . . . .	40
3.4	Discussion . . . . .	41
<b>4</b>	<b>Production of Near-Earth Asteroids on Retrograde Orbits . . . . .</b>	<b>44</b>
4.1	Introduction . . . . .	44
4.2	Integration Methods . . . . .	45
4.3	Typical Retrograde NEAs . . . . .	46
4.3.1	Sample Retrograde Production . . . . .	50
4.3.2	Short-Lived Retrograde Production . . . . .	53
4.3.3	Long-Lived Retrograde Production . . . . .	54
4.3.4	Completeness of Retrograde Population . . . . .	56
4.4	Two Known Retrograde NEAs . . . . .	57
4.5	Estimated Extinct Comet Population . . . . .	60

4.6	High-Strength, High-Velocity Meteoroids on Retrograde Orbits . . .	61
<b>5</b>	<b>A Brief Introduction to the Kuiper Belt and Cratering in the Outer Solar System . . . . .</b>	<b>62</b>
5.1	Current Structure of the Kuiper Belt . . . . .	62
5.1.1	Orbital Classification . . . . .	63
5.1.2	Mean-Motion Resonances in the Kuiper Belt . . . . .	67
5.2	Giant Planet Migration in our Solar System . . . . .	73
5.2.1	Population Decay . . . . .	75
5.3	Size Distributions of Kuiper Belt Sub-Populations . . . . .	76
5.3.1	Population Estimates of Kuiper Belt Objects . . . . .	78
5.4	Cratering in the Outer Solar System . . . . .	80
<b>6</b>	<b>A Uranian Trojan and the Frequency of Temporary Giant-Planet Co-Orbitals . . . . .</b>	<b>86</b>
6.1	Discovery of the First Uranian Trojan . . . . .	86
6.2	Numerical Integrations . . . . .	88
6.2.1	Co-Orbital Detection in Numerical Integrations . . . . .	90
6.2.2	Resonant Island Classification . . . . .	92
6.3	Frequency and Duration of Temporary Giant-Planet Co-Orbitals . . . . .	92
6.3.1	Quasi-Satellites . . . . .	94
6.4	Conclusions . . . . .	96
<b>7</b>	<b>Impact and Cratering Rates onto Pluto . . . . .</b>	<b>99</b>
7.1	Introduction . . . . .	99
7.1.1	Motivation . . . . .	100
7.2	Methods . . . . .	109
7.2.1	Kuiper Belt Population Models . . . . .	109
7.2.2	Öpik Collision Probability Code . . . . .	110
7.2.3	Impact Rates onto Pluto . . . . .	112
7.2.4	Cratering Rates onto Pluto . . . . .	118

7.2.5	Number of Craters on Pluto’s Surface . . . . .	121
7.3	Discussion . . . . .	125
7.3.1	Interpretation of Young Surfaces . . . . .	125
7.3.2	The Issue of the Size Distribution Below the Break . . . . .	127
7.3.3	Returning to Crater Retention Ages for Young Surfaces . . . . .	135
7.3.4	The Effect of Varying $\alpha_{faint}$ . . . . .	136
7.3.5	Secondary Craters . . . . .	140
7.3.6	Implications of a “Wavy” Size Distribution . . . . .	140
7.3.7	Charon . . . . .	149
7.3.8	The Four Smaller Moons . . . . .	153
7.4	Summary and Conclusions . . . . .	157
7.5	Some Predictions for the 2015 New Horizons Observations of the Cratering Record in the Pluto System . . . . .	161
<b>8</b>	<b>Future Work . . . . .</b>	<b>163</b>
	<b>Bibliography . . . . .</b>	<b>165</b>
<b>A</b>	<b>Appendix . . . . .</b>	<b>180</b>
A.1	Close Encounter Scheme of SWIFT-RMVS . . . . .	180
A.2	Convergence Tests for SWIFT-RMVS4 . . . . .	181
A.3	Discussion . . . . .	182
A.4	Recommendations . . . . .	187

# List of Tables

Table 2.1	NEO class percentages . . . . .	8
Table 3.1	K-S test results . . . . .	40
Table 5.1	KBO sub-population estimates for $d \geq 100$ km from CFEPS . . . . .	79
Table 5.2	Pluto system characteristics . . . . .	81
Table 7.1	Öpik collision probability calculations onto Pluto . . . . .	113
Table 7.2	<i>Current</i> primary cratering rates onto Pluto . . . . .	120
Table 7.3	Cumulative number of craters on Pluto in past $\approx 4$ Gyr . . . . .	123
Table 7.4	<i>Current</i> primary cratering rates onto Pluto for varying $\alpha$ . . . . .	136
Table 7.5	<i>Current</i> primary cratering rates onto Charon . . . . .	150
Table 7.6	Cumulative number of craters on Charon in past $\approx 4$ Gyr . . . . .	152

# List of Figures

Figure 2.1	Sample orbits of objects in the four asteroidal NEO classes . . .	6
Figure 2.2	NEO class distinctions and source regions in $a, e$ space . . . .	9
Figure 2.3	$\mathcal{R}_{NEO}(a, e, i)$ for NEOSSat-1.0 orbital model . . . . .	10
Figure 2.4	Main asteroid belt orbital distribution . . . . .	12
Figure 2.5	Approximate $(a, i)$ locations of 3:1, $\nu_5$ , $\nu_6$ , and $\nu_{16}$ resonances for $e = 0$ orbits . . . . .	15
Figure 2.6	Kirkwood gaps in the main asteroid belt . . . . .	17
Figure 2.7	Size distribution of known main belt asteroids and NEOs . . .	28
Figure 3.1	$\mathcal{R}_{NEO}(a, e, i)$ from B02 and G12 . . . . .	36
Figure 3.2	Fractional NEO $a, e$ , and $\sin(i)$ distributions . . . . .	38
Figure 3.3	Cumulative NEO $a, e$ , and $\sin(i)$ distributions . . . . .	39
Figure 4.1	$\mathcal{R}_{NEO}(a, e, i)$ for $i < 180^\circ$ from G12 . . . . .	48
Figure 4.2	Retrograde asteroid lifetime vs semimajor axis . . . . .	49
Figure 4.3	Sample retrograde asteroid $a, e, i$ history . . . . .	51
Figure 4.4	Zoomed in sample retrograde asteroid $a, e, i$ history . . . . .	52
Figure 4.5	Short-lived retrograde asteroid $a, e, i$ history . . . . .	53
Figure 4.6	Zoomed in short-lived retrograde asteroid $a, e, i$ history . . . .	55
Figure 4.7	Longest-lived retrograde asteroid $a, e, i$ history . . . . .	56
Figure 4.8	Observational completeness of $18 < H < 23$ NEOs . . . . .	58
Figure 5.1	CFEPS discovered Kuiper belt main classical orbital distribution	64

Figure 5.2	CFEPS debiased Kuiper belt orbital distribution . . . . .	66
Figure 5.3	CFEPS debiased classical Kuiper belt orbital distribution . . . . .	68
Figure 5.4	Lagrange points of a planet-Sun system . . . . .	72
Figure 5.5	Schematic of the Pluto system . . . . .	80
Figure 6.1	Orbital evolution of temporary Uranian co-orbitals . . . . .	87
Figure 6.2	$\mathcal{R}_{KRQ11}(a, e, i)$ for $a < 34$ AU . . . . .	91
Figure 6.3	Orbital evolution of temporary Neptunian co-orbitals . . . . .	95
Figure 6.4	Orbital evolution of temporary quasi-satellites . . . . .	97
Figure 7.1	Numerical integration of Pluto's ecliptic nodal distances . . . . .	103
Figure 7.2	Schematic of three $H_g$ -magnitude differential size distribution scenarios . . . . .	106
Figure 7.3	Impact velocity spectrum onto Pluto . . . . .	111
Figure 7.4	Primary crater density on Pluto's surface versus age (Gyr) . . . . .	126
Figure 7.5	Cumulative crater density on Pluto's surface . . . . .	128
Figure 7.6	Relative crater frequency plot for Pluto . . . . .	132
Figure 7.7	Relative crater frequency for Iapetus . . . . .	133
Figure 7.8	Cumulative crater density on Pluto's surface for varying $\alpha$ . . . . .	138
Figure 7.9	Relative crater frequency plot for Pluto for varying $\alpha$ . . . . .	139
Figure 7.10	Cumulative crater density on Pluto's surface for M12 and S13 . . . . .	143
Figure 7.11	Relative crater frequency plot for Pluto for M12 and S13 . . . . .	145
Figure 7.12	Largest crater in 1 Gyr cumulative crater density on Pluto for M12 and S13 . . . . .	147
Figure 7.13	Charon 4 panel cumulative crater density and R plots . . . . .	151
Figure 7.14	Catastrophic disruption timescale for Pluto system satellites . . . . .	156
Figure A.1	Convergence test $a, q$ distributions for high- $i$ . . . . .	183
Figure A.2	Convergence test $a, q$ distributions for low- $i$ . . . . .	184
Figure A.3	Convergence test $a$ histograms . . . . .	185
Figure A.4	Convergence test $a, i$ distributions for high- $i$ . . . . .	188
Figure A.5	Convergence test $a, i$ distributions for low- $i$ . . . . .	189

# List of Symbols and Abbreviations

**B02** (Bottke et al., 2002)

**CFEPS** Canada-France Ecliptic Plane Survey

**CSA** Canadian Space Agency

**DES** Deep Ecliptic Survey

**DRDC** Defense Research and Development Canada

**EBF** Enhanced Bombardment Factor

**ESA** European Space Agency

**G12** (Greenstreet et al., 2012a)

**HTC** Halley-Type Comet

**IAU** International Astronomical Union

**IEO** Inner Earth Object

**IMC** Intermediate Mars Crosser

**JAXA** Japan Aerospace Exploration Agency

**JFC** Jupiter Family Comet

**KBO** Kuiper Belt Object

**KRQ11** (Kaib et al., 2011)

**KS** Kolmogorov-Smirnov

**LHB** Late-Heavy Bombardment

**LPS** Palomar-Leiden Survey

**LSST** Large Synoptic Survey Telescope

**MOST** Microvariability and Oscillations of Stars space telescope

**MPC** Minor Planet Center

**MPCORB** Minor Planet Center Orbit database

**NASA** National Aeronautics and Space Administration

**NEA** Near-Earth Asteroid

**NEAR** Near-Earth Asteroid Rendezvous

**NEAT** Near-Earth Asteroid Tracking program

**NEO** Near-Earth Object

**NEOSSat** Near-Earth Object Surveillance Satellite

**NEOWISE** Wide-field Infrared Survey Explorer Near-Earth Object extended mission

**OMB** Outer Main Belt

**Pan-STARRS** Panoramic Survey Telescope & Rapid Response System

**PHA** Potentially Hazardous Asteroid

**SFD** Size Frequency Distribution

**SKADS** Sub-Kilometer Asteroid Diameter Survey

**SO** Scattering Object

**SPL** Single Power-Law

**TNO** Trans-Neptunian Object

**WISE** Wide-field Infrared Survey Explorer

**YMS** Yerkes-McDonald survey

**Amor** - Near-Earth object with  $1.017 < q < 1.3$  AU.

**Apollo** - Near-Earth object with  $a > 1.0$  AU,  $q < 1.017$  AU.

**Aten** - Near-Earth object with  $a < 1.0$  AU,  $Q > 0.983$  AU.

**Atira** - Near-Earth object with  $0.718 < Q < 0.983$  AU.

**Vatira** - Near-Earth object with  $0.307 < Q < 0.718$  AU.

**Vulcanoid** - Near-Earth object with  $Q < 0.307$  AU.

**Centaur** - Object located in the giant planet region ( $5 < a < 30$  AU).

**AU** - Astronomical Unit. Roughly the mean Earth-Sun distance. Defined as 149,597,870,700 metres, exactly.

**$a$**  - Semimajor axis of an orbit. Defined as half of the major axis of the ellipse of the orbit.

**$e$**  - Eccentricity. Describes an orbit's ellipticity. A perfect circle has  $e = 0$ , an ellipse has  $0 < e < 1$ , a parabolic orbit has  $e = 1$ , and a hyperbolic orbit has  $e > 1$ .

**$q$**  - Pericenter distance. Pericenter (also called perihelion for orbits around the Sun) is the point of the elliptical orbit where the object is closest to the central body.  $q$  can be calculated using  $a(1 - e)$ .

$Q$  - Apocenter distance. Apocenter (also called aphelion for orbits around the Sun) is the point of the elliptical orbit where the object is farthest from the central body.  $Q$  can be calculated using  $a(1 + e)$ .

$i$  - The inclination of the plane of an orbit to a reference plane. For objects in our Solar System, the reference plane is the ecliptic plane, which is the plane through Earth's orbit around the Sun.

$\Omega$  - The longitude of the ascending node in the reference plane is the angle between the reference direction (this is the vernal equinox direction) and where the orbit passes upward through the reference plane.

$\omega$  - The argument of pericenter is the angle in the orbital plane between where the orbit passes upward through the reference plane and the location of pericenter, the object's closest approach to the central body.

$\varpi$  - The longitude of pericenter is the sum of  $\Omega$  and  $\omega$ .

$\mathcal{M}$  - The mean anomaly is a fictitious angle that describes the average position of an object along its orbit and is defined by  $n(t - T_o)$ , where  $n$  is the mean-motion,  $t$  is time, and  $T_o$  is the time since the object was last at pericenter.

$n$  - The mean-motion is the rate of change of the mean anomaly  $\mathcal{M}$  and describes the average angular velocity of an object along its orbit around the Sun, defined by  $n = \sqrt{\frac{\mu}{a^3}}$ .

$\theta$  - The true anomaly describes the angle in the orbital plane from the pericenter to the location of the body along its orbit.

$\lambda$  - The mean longitude is the sum of  $\Omega$ ,  $\omega$ , and  $\mathcal{M}$ .

$P$  - The orbital period.  $P = \sqrt{\frac{4\pi^2 a^3}{GM_\odot}}$ .

$M_\oplus$  - The mass of the Earth.  $5.97219 \times 10^{24}$  kg.

$M_\odot$  - The mass of the Sun.  $1.9886 \times 10^{30}$  kg.

**G** - Gravitational constant.  $6.67384 \times 10^{-11} \text{ m}^3 \text{ kg}^{-1} \text{ s}^{-2}$ .

**$\mu$**  - Gravitational parameter. For objects with  $\frac{m_{object}}{M_{\odot}} < 10^{-11}$ ,  $\mu = GM_{\odot} = 1.32712440018 \times 10^{20} \text{ m}^3 \text{ s}^{-2}$ . Above this threshold,  $\mu$  should be calculated as  $\mu = G(M_{\odot} + m_{object})$  to maintain the given precision.

**$R_H$**  - Hill sphere. For  $M_{planet}/M_{\odot} \ll 1$ , the sphere around a planet where the gravitational dominance of the planet exceeds that of the sun.  $R_H = a \left( \frac{M_{planet}}{3M_{\odot}} \right)^{1/3} \text{ AU}$ .

**$T_J$**  - Tisserand parameter. This quantity is conserved during planetary close encounters (in this case with Jupiter) in the circular restricted three-body problem.  $T_J = \frac{a_J}{a} + 2\sqrt{(1 - e^2)\frac{a}{a_J}\cos(i)}$ .

**$\phi_{11}$**  - The 1:1 mean-motion resonant argument is the difference between the  $\lambda$  of a small body of negligible mass and  $\lambda$  of a planet. Libration around  $0^\circ$  indicates quasi-satellite behaviour, libration around  $180^\circ$  indicates horseshoe behaviour, and libration around  $60^\circ$  or  $300^\circ$  indicates leading and trailing Trojan behaviour, respectively.

**$\phi_{31}$**  - The 3:1 mean-motion resonant argument indicates whether an object is in the 3:1 resonance when the resonant argument librates around  $180^\circ$ .  $\phi_{31} = 3\lambda_J - \lambda - 2\varpi$

**$\phi_{41}$**  - The 4:1 mean-motion resonant argument indicates whether an object is in the 4:1 resonance when the resonant argument librates around  $180^\circ$ .  $\phi_{41} = 4\lambda_J - \lambda - 3\varpi$

**L1** - First Lagrange point. Located directly between the Sun and a planet marking a stable gravitational location for a third body of negligible mass.

**L2** - Second Lagrange point. Located directly opposite the Sun from a planet marking a stable gravitational location for a third body of negligible mass.

**L3** - Third Lagrange point. Located directly opposite a planet from the Sun marking a stable gravitational location for a third body of negligible mass.

**L4** - Leading triangular Lagrange point. Located  $60^\circ$  ahead of a planet along its orbit around the Sun marking a stable gravitational location for a third body of negligible mass.

**L5** - Trailing triangular Lagrange point. Located  $60^\circ$  behind a planet along its orbit around the Sun marking a stable gravitational location for a third body of negligible mass.

$\mathcal{R}(a, e, i)$  - Residence time probability distribution. Represents the percentage of the steady-state population contained in each bin of a grid of  $a, e, i$  cells placed throughout the Solar System.

**H**-magnitude - Absolute magnitude. The apparent magnitude an object would have if it were located in an equilateral triangle 1 AU from the Sun and the Earth and at zero phase angle  $\phi$ .  $m = H + 2.5 \log_{10} \frac{r_{helio}^2 r_{geo}^2}{P(\phi)}$ .

$\phi$  - Phase angle. Measured between the incident and reflected light directions of an observed object with values ranging from  $0^\circ$  to  $180^\circ$ , where a  $0^\circ$  phase angle refers to a fully illuminated object.

**p** - Albedo. An object's reflectivity. Defined as the fraction of incident light reflected from the surface, where a value of 0 means an object reflects no light and a value of 1 means an object reflects all light incident upon it.

$\alpha$  - Logarithmic "slope" of the power-law differential distribution in number.

$q_{slope}$  - Logarithmic "slope" of the power-law differential distribution in diameter.

$$q_{slope} = 5\alpha + 1.$$

**d** - Impactor or small body diameter in km.

**D** - Crater diameter in km.

$U$  - Impact velocity in km/s.

$\delta$  - Volume mass density of an impactor.

$\rho$  - Volume mass density of a target at the surface.

$Q^*_{RD}$  - Specific energy required for dispersal of a catastrophically disrupted body, where  $\mu$  is the reduced mass,  $M_{projectile}M_{target}/M_{total}$ .  $Q^*_{RD} = 0.5\mu U^2/M_{total}$ .

# Acknowledgements

Thank you to my supervisor, Brett Gladman, for providing me with fantastic research opportunities and for being a patient teacher over the past six years we have worked together. You saw potential in me as a new graduate student despite my inexperience and helped me to grow into the scientist I have become.

Thank you to the Canadian Space Agency for providing the Science Support Contract that has made the work presented in this thesis and other projects possible.

Thank you to my supervisory committee members, Jeremy Heyl, Paul Hickson, and Catherine Johnson for providing support and guidance along the way.

Thank you to Mike Alexandersen, Mikael Granvik, Steve Larson, Bill McKinnon, and Henry Ngo for the expertise they brought to these projects as co-authors and to Bill Bottke, Clark Chapman, Luke Dones, and Amy Mainzer for their valuable insights, discussions, and reviews for portions of this thesis.

Thank you to every one of my family members (immediate and extended, through blood or marriage) and friends who have provided support through numerous conversations about my work and research (especially Jim) that have continued to remind me how lucky I am to be doing something so exciting.

Thank you to my good friends Maggie, Steve, Patrick, Belinda, Amanda, Ben, and Nick for providing me with support through fun game nights, delicious home-cooked meals, and a constant fascination with my research that has kept me motivated to keep reaching for the stars.

Thank you to my husband, Matt, who has been with me every step of this journey, providing love and support at every turn, and for always believing in me.

Thank you to the wonderful women in my family that have set both an example and the foundation upon which I have chased after my dreams, to Grandma Schotzie for her encouragement and expectations of great things from me starting at a young age, to “Ant” Sandy for her constant support and fascination with my work in astronomy, and to my sister, Amy, for countless hours of conversations and activities filled with laughter and silliness that have reminded me to never take myself too seriously.

And thank you to my parents for their constant love and support as I have worked to fulfill my dream of becoming an astronomer.

# Dedication

For my family, with love.

# Chapter 1

## Introduction

### 1.1 Motivation

The Solar System has three large reservoirs of small bodies: the main asteroid belt, the Kuiper belt, and the Oort cloud. The Oort cloud is only indirectly related to this thesis via its relation to the scattering object population in the Kuiper belt. Each of the populations in the main asteroid belt and the Kuiper belt are divided into several sub-populations according to their orbital parameters and dynamical properties. The main asteroid belt sits between the orbits of Mars and Jupiter from roughly 1.8 AU to 4.5 AU and the Kuiper belt is located beyond to the orbit of Neptune, extending from 30 AU to several hundred AU with the majority of the classical and resonant populations lying between roughly 30 AU and 85 AU. Objects from these two belts can leave these reservoirs via slow diffusive dynamical processes that can put them onto planet-crossing orbits. The near-Earth object (NEO) population, which have perihelia  $q < 1.3$  AU is an example of one such population which has its sources in the main asteroid belt. The processes by which the orbits of small bodies in the Solar System are perturbed can help us understand the current orbital parameters of today's small body populations. Impact probabilities and speeds can be computed for planet-crossing populations and cratering

histories can tell us something about the age of planetary surfaces under today's population of potential impactors.

### **1.1.1 Small Body Populations**

Small body populations in the Solar System are scientifically interesting, because they were formed during the formation of the Solar System roughly 4.5 Gyr ago and thus can provide valuable information about the formation process. Dynamically speaking, their current orbital structure can provide clues about the orbital structure in the early stages of the Solar System. Because these populations are not static, but can move around the Solar System via gravitational and non-gravitational forces, studying the dynamics of these processes helps us understand the current orbital distribution of today's populations. The interest in future manned and unmanned space probe missions to study these small bodies has fuelled the desire to complete a census of the current population of near-Earth objects, especially those on Earth-like orbits (Abell et al., 2009; Binzel et al., 2004; Hildebrand et al., 2004). Recent missions to have landed on NEOs include NASA's Near-Earth Asteroid Rendezvous (NEAR) to 433 Eros (Veeverka et al., 2001) and JAXA's Hayabusa to 25143 Itokawa (Yano et al., 2006). ESA's Rosetta mission recently achieved the first comet-landing with its Philae probe touching down on comet 67P/Churyumov-Gerasimenko. A census of the current small body populations can also provide an understanding of the impact and cratering history of planetary surfaces and, in particular, can provide the impact threat of potentially hazardous asteroids (PHAs) that could impact the Earth (Morrison et al., 1994).

### **1.1.2 Impact Rates & Cratering in the Solar System**

In addition to understanding the impact threat to Earth, studying impact and cratering rates onto planetary surfaces can allow us to date such surfaces either absolutely, as in the case of the Moon for which we have samples from the surface, or in a relative sense. The absolute dating of cratered surfaces on the Moon has al-

lowed us to assign a specific time ( $\approx 3.9$  Gyr ago) to the period known as the lunar cataclysm (Tera et al., 1974) when the Moon experienced a spike in its impacting history during a violent time in the early stages of the Solar System. Studying cratered surfaces can also tell us about past resurfacing events and processes such as geological activity on planetary surfaces. Very few craters on a surface implies, as in the case of Neptune’s moon Triton, that the “planetary” body has had recent geologic activity that has erased or eroded many of its craters. In addition, the size distribution of craters on planetary surfaces can be used to infer the size distribution of the impacting populations. For example, Strom et al. (2005) show that the crater size frequency distribution on the lunar mare and the size distribution of the near-Earth asteroid population confirms that NEOs are the source of lunar craters. In the outer Solar System, cratered surfaces can provide insights into the size distribution of small body populations for which we have less knowledge than the main asteroid belt due to their farther distances from the Earth. Particularly in the case of Pluto, which is the target of the upcoming New Horizons fly-by in July 2015, the crater size frequency distribution on its (and its binary companion Charon’s) surface can provide insights into the size distribution of the Kuiper belt sub-populations. Unfortunately, without knowing the size distribution of the Kuiper belt sub-populations down to the smallest sizes (sub-km diameters), little can be said about the inferred age of Pluto’s (or Charon’s) surface other than to make model-dependent predictions (Greenstreet et al., 2015). However, perhaps the New Horizons fly-through of the Pluto system will provide some clues to the inferred shape of the Kuiper belt size distribution at small diameters.

## 1.2 Thesis Outline

Chapter 2 is an introduction to the near-Earth object and main asteroid belt populations, including their orbital structure, dynamics, and size distributions. Previous work related to the production of a near-Earth asteroid (NEA) orbital model (Greenstreet et al., 2012a) was the subject of my Master’s thesis and is not part of

this PhD thesis. The details of the NEA orbital distribution produced in the model is discussed, but the production of the model is not.

Chapter 3 is based on Greenstreet and Gladman (2013) and compares NEO orbital distribution models to the detected orbital element distributions of Aten-class NEOs detected by the NEOWISE spacecraft (Mainzer et al., 2012).

Chapter 4 discusses (based on Greenstreet et al. (2012b)) the production of retrograde NEAs from main belt asteroidal sources and their connection to high-strength, high-velocity meteoroids on retrograde orbits.

At this point, the focus shifts from small body orbital dynamics in the inner Solar System to small body dynamics and cratering in the outer Solar System.

Chapter 5 is an introduction to the current and past orbital structure of the Kuiper belt as well as its sub-population size distributions and cratering in the outer Solar System.

Chapter 6 discusses the capture of scattering Kuiper belt objects into co-orbital resonance with the icy giant planets, motivated by the discovery of the first Uranian Trojan by Alexandersen et al. (2013).

Chapter 7 (based on Greenstreet et al. (2015)) focuses on the current impact rate from the Kuiper belt sub-populations onto Pluto and its binary companion Charon as well as their cratering rates over the past 4 Gyr. Model-dependent ages are computed based on assumed extrapolations of the impactor size distribution at small sizes (diameter  $d < 100$  km).

# Chapter 2

## An Introduction to Near-Earth Objects and the Main Asteroid Belt

### 2.1 Near-Earth Objects

The orbital elements that describe the motions of bodies around the Sun in the Solar System include the semimajor axis  $a$  (half the distance of the longest diameter of the orbit), the eccentricity  $e$  (deviation of the orbit from a perfect circle), and the inclination  $i$  (tilt of the body's orbital plane with respect to the Earth-Sun orbital plane). The pericenter  $q$  measures an object's closest distance to the Sun and is calculated via  $q = a(1 - e)$ . Similarly, the apocenter  $Q = a(1 + e)$  measures an object's farthest distance from the Sun. Near-Earth objects have perihelia  $q < 1.3 \text{ AU}^a$  and are divided into dynamical sub-groups according to their orbital elements.

---

<sup>a</sup>There is no standard upper limit on semimajor axis for the NEO population, although we use  $a < 4.20 \text{ AU}$  from Bottke et al. (2002).

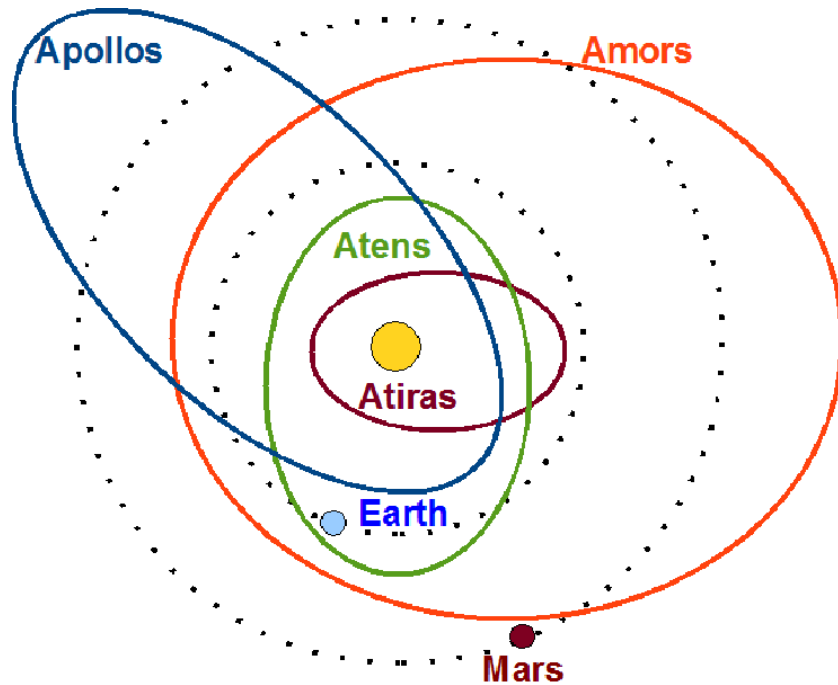


**Figure 2.1:** Sample schematic orbits of objects in the four traditional NEO classes. Apollos and Atens cross the orbit of the Earth while Amors lie entirely exterior to the Earth's orbit and Atiras lie completely interior to the Earth's orbit.

### 2.1.1 NEO Dynamical Classification

Near-Earth objects are traditionally divided into dynamical classes as follows: Amors ( $1.017 < q < 1.3$  AU), Apollos ( $a > 1.0$  AU,  $q < 1.017$  AU), Atens ( $a < 1.0$  AU,  $Q > 0.983$  AU), and Atiras ( $0.718 < Q < 0.983$  AU). In recent literature, Atira-class asteroids form part of what has been called interior-Earth objects (IEOs) (Michel et al., 2000), because their orbits lie completely interior to Earth's orbit ( $Q < 0.983$  AU). Following historical precedent, we adopt the name Atira for this class of NEO, after its first named member, 163693 Atira.

Apollos and Atens are on Earth-crossing orbits, and thus make up the potential Earth impacting populations. Apollos have orbits larger than the Earth's orbit and thus spend more time at farther distances from the Sun than the Earth, while Atens

are on orbits smaller than that of the Earth, spending much of their time interior to Earth's orbit. Amors have orbits which lie entirely exterior to the orbit of the Earth with perihelia greater than the aphelion of Earth ( $q > 1.017$  AU). Atiras, on the other hand, lie on orbits completely interior to the Earth's orbit with aphelia less than the perihelion of Earth ( $Q < 0.983$  AU). Figure 2.1 shows a schematic of objects in the four traditional NEO classes. We further expand these into six NEO classes. As mentioned above, Atira-class NEOs have been referred to as interior-Earth objects (IEOs), which include all objects with orbits interior to that of the Earth ( $Q < 0.983$  AU). We subdivide this region into three orbital classes: Atiras ( $0.718 < Q < 0.983$  AU) are objects decoupled from (interior to the orbit of) Earth but can cross the orbits of Venus and Mercury, Vatiras ( $0.307 < Q < 0.718$  AU) are objects decoupled from Venus but can be on Mercury-crossing orbits, and Vulcanoids have orbits with  $Q < 0.307$  AU and are decoupled from Mercury. No Vulcanoid or Vatira NEOs are currently known, which is unsurprising due to their tiny solar elongations (angle from the Sun as viewed from Earth).

### 2.1.2 NEO Orbital Distribution

Table 2.1 lists the best estimates for the fractions of NEOs in each orbital class from the Greenstreet et al. (2012a) NEO orbital distribution model. Apollos make up the majority ( $\approx 63\%$ ) of NEOs, however, as is shown in Figure 2.2 of the NEO boundaries in semimajor axis/eccentricity space, the Apollos cover the largest area of the NEO region. The population of NEOs drops off with decreasing semimajor axis from the Aten to the Vulcanoid populations, with no objects predicted to exist on orbits scattered down to the innermost portions of the Solar System interior to the orbit of Mercury (see Table 2.1). Objects are gravitationally scattered by a planet when they pass within a few Hill radii from a planet. The Hill sphere indicates the region around a planet where the planet has gravitational dominance

NEO Class	Best Estimate (%)
Amor	$30.1 \pm 0.8$
Apollo	$63.3 \pm 0.4$
Aten	$5.0 \pm 0.3$
Atira	$1.38 \pm 0.04$
Vatira	$0.22 \pm 0.03$
Vulcanoid	0.0

**Table 2.1:** NEO class percentages from the Greenstreet et al. (2012a) NEO orbital distribution model. An Atira has  $0.718 < Q < 0.983$  AU while a Vatira is a Venus-decoupled object with  $0.307 < Q < 0.718$  AU. We define Vulcanoids as objects with  $Q < 0.307$  AU. The dynamical model does not produce any NEOs that get scattered down to the innermost portions of the Solar System onto orbits that are completely interior to the orbit of Mercury (the population we call Vulcanoids).

over the Sun, and for  $M_{planet}/M_{\odot} \ll 1$ , can be computed for a given planet via:

$$R_H = a \left( \frac{M_{planet}}{3M_{\odot}} \right)^{1/3} \quad (2.1)$$

In order for a main belt asteroid to reach an orbit in the innermost portion of the Solar System (especially near Mercury), an object must experience a sequence of fortuitous close encounters that “hand it down” to planets closer to the Sun, which becomes increasingly unlikely as an object gets to smaller heliocentric distances. The NEO population estimates, including the dropping trend at smaller semimajor axes can also be seen in Figure 2.3. This figure shows the residence time probability distribution (i.e. the fraction of time NEOs are predicted to spend at any given semimajor axis, eccentricity, and inclination) from the Greenstreet et al. (2012a) NEO orbital distribution model, where the population at low- $a$  drops off as expected.

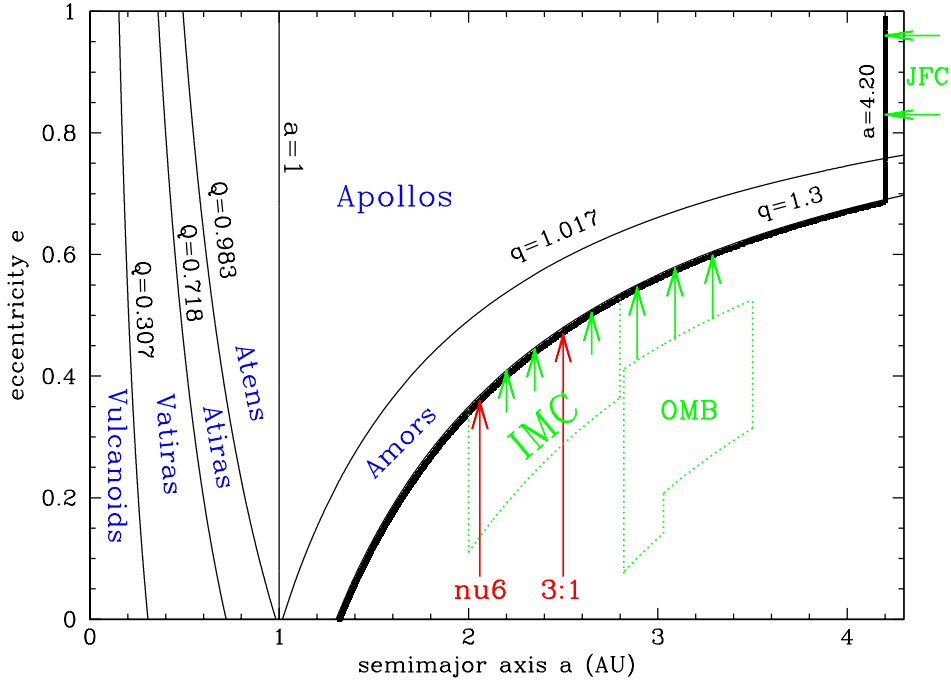


**Figure 2.2:** NEO class distinctions and source regions in  $a, e$  space. The NEO population is restricted to orbits with  $q < 1.3$  AU and  $a < 4.2$  AU. Amors ( $1.017 < q < 1.3$  AU), Apollos ( $a > 1.0$  AU,  $q < 1.017$  AU), Atens ( $a < 1.0$  AU,  $Q > 0.983$  AU), Atiras ( $0.718 < Q < 0.983$  AU), Vatriras ( $0.307 < Q < 0.718$  AU), and Vulcanoids ( $Q < 0.307$  AU) are the six NEO classes (blue) we adopt. The  $\nu_6$  secular resonance (red), 3:1 mean-motion resonance (red), intermediate Mars crossers (IMC) (green), and the outer main belt (OMB) (green) population constitute the asteroidal source regions and the Jupiter family comets (JFCs) (green) are the cometary source region for the NEO population.

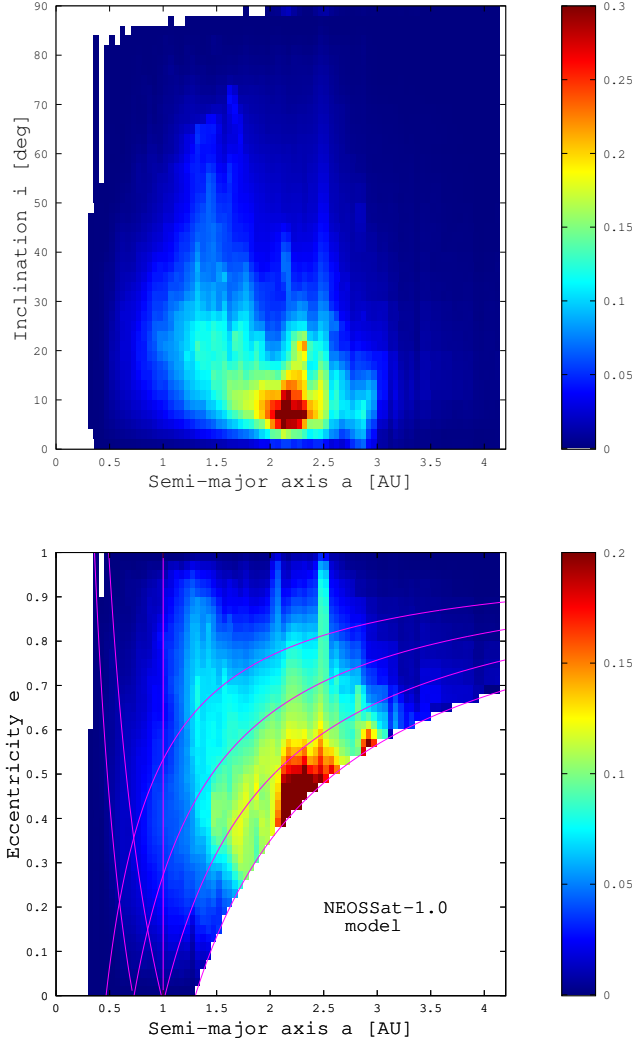


**Figure 2.3:** Residence time probability distribution,  $\mathcal{R}_{NEO}(a, e, i)$ , for the Greenstreet et al. (2012a) NEO orbital model. The space is divided into a grid of  $a, e, i$  cells from  $a < 4.2$  AU,  $e < 1.0$ , and  $i < 90^\circ$  with volume  $0.05$  AU  $\times$   $0.02$   $\times$   $2.00^\circ$ . To create the  $a, e$  plot the  $i$  bins are summed and the  $e$  bins are summed to create the  $a, i$  plot. The color scheme represents the percentage of the steady-state NEO population contained in each bin. Red colors represent cells where there is a high probability of particles spending their time. The curved lines divide the NEO region into Amor, Apollo, Aten, and Atira populations as well as indicating Venus- and Mercury-crossing orbits.

Figure 2.3 shows a high concentration of NEOs between roughly 2 AU and 3 AU. This reflects the entry point of most objects into the NEO region from sources in the main asteroid belt. As shown in Figure 2.2, the asteroidal source regions for the NEO population are located just outside the  $q < 1.3$  AU NEO boundary. These NEO source regions are discussed in the next section.

## 2.2 Main Belt Dynamics and Near-Earth Object Source Regions

The main asteroid belt spans semimajor axes between Mars and Jupiter from roughly 2 AU to 3.5 AU. As can be seen in Figure 2.4 of the main belt ( $a, e$ ) and ( $a, i$ ) projections, the majority of the asteroids in the main belt have orbits of moderate eccentricity ( $e < 0.35$ ) and inclination ( $i < 20^\circ$ ), with a few high-inclination groups. The structure visible in Figure 2.4 is important for the near-Earth object population, because it marks the source regions that feed the NEO population.

### 2.2.1 Resonances in the Main Belt

Resonances located in the main asteroid belt also have the ability to modify asteroidal orbits and are often much more powerful than planetary gravitational scattering. Historically, people began looking at resonances in the main belt as a means to transport meteorites from the asteroid belt to the Earth (Greenberg and Chapman, 1983; Wetherill, 1979). The steady flux of meteorites arriving at Earth prompted researchers to look at the nearby large reservoir of small bodies, the main asteroid belt, as their source. Because planetary close encounters are unable to remove objects from the main belt, resonances located in the main belt began to be explored as the transportation mechanism for getting meteorites to the Earth. Further discussion of past work with numerical integrations of NEO source regions can be found in Section 2.2.3.

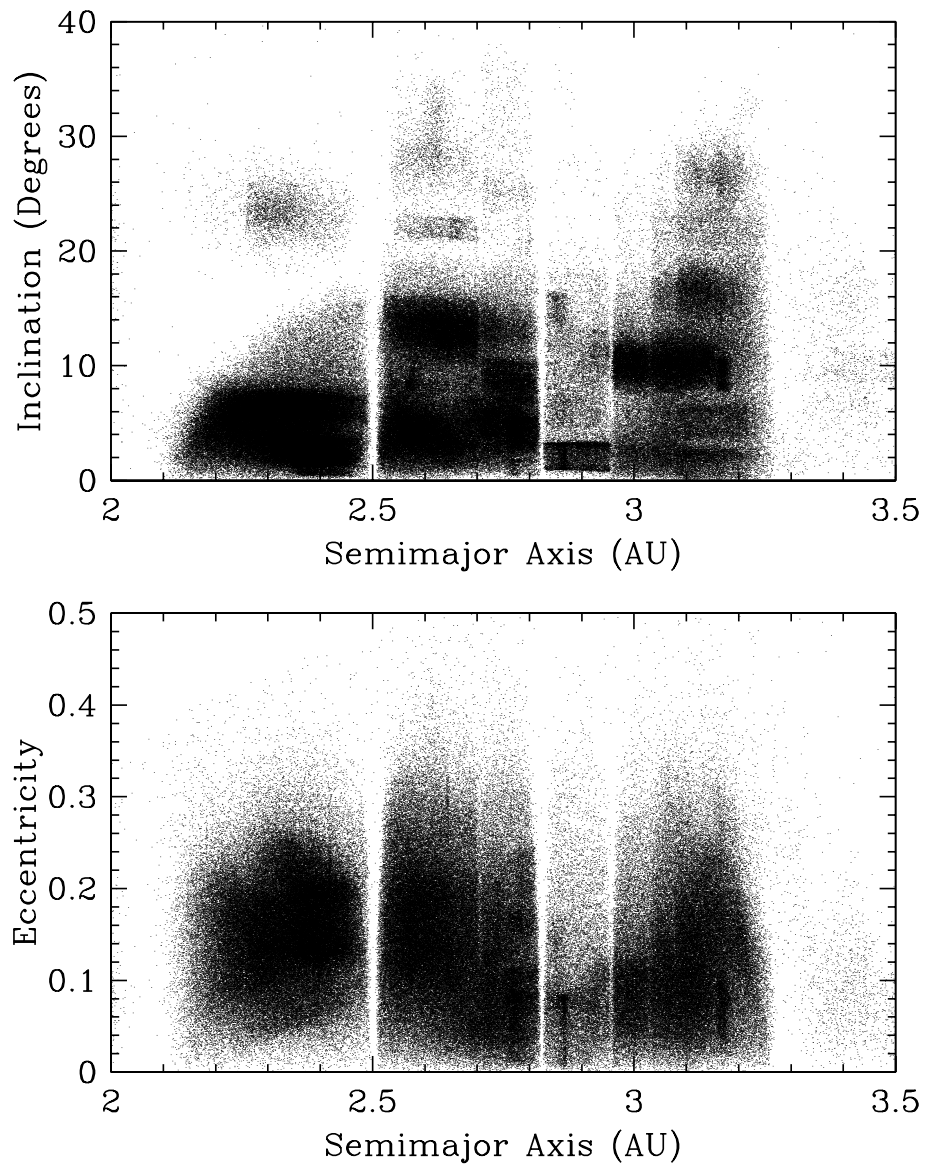


**Figure 2.4:** Main asteroid belt orbital distribution in  $a, e$  and  $a, i$  projections for the 422,910 numbered asteroids in the Minor Planet Center Orbit (MPCORB) database on February 5, 2015.

## Secular Resonances

In addition to the orbital semimajor axis, eccentricity, and inclination, the longitude of the ascending node  $\Omega$  (angle projected onto the Earth-Sun orbital plane from the reference direction of the vernal equinox to the location of the ascending node where the orbit plane intersects the Earth-Sun plane), the argument of pericenter  $\omega$  (angle in the orbital plane from the ascending node to the pericenter), and the true anomaly  $\theta$  (angle in the orbital plane from the pericenter to the location of the body along its orbit) are also used to describe an object's orbit.

The existence of more than two bodies in the Solar System causes the angular orientation of the orbits of all bodies to change over time at a secular precession rate. This secular precession rate of the longitude of pericenter  $\varpi$  (sum of the longitude of the ascending node and the argument of pericenter  $\varpi = \Omega + \omega$ ) for each planet is made up of a linear combination of the secular precession frequencies, or eigenfrequencies  $g_j$  ( $j = 1 - 8$ ), of all the planets. Likewise, the secular precession rate of the longitude of the ascending node  $\dot{\Omega}$  for each planet is made up of a linear combination of the eigenfrequencies  $s_j$  ( $j = 1 - 8$ ). An equally common naming convention is  $\nu_1 - \nu_8$  for  $g_1 - g_8$  and  $\nu_{11} - \nu_{18}$  for  $s_1 - s_8$ .

In addition to exciting secular precession in each other's orbits, the planets induce secular precession in the orbits of small bodies in the Solar System. Eccentricity-type (or inclination-type) secular resonances occur when the precession rate of a body's longitude of pericenter (or longitude of ascending node) is commensurable with an eigenfrequency, or combination of eigenfrequencies, of the Solar System, i.e.  $\dot{\varpi} = g_j$  (or  $\dot{\Omega} = s_j$ ). (Michel and Froeschlé, 1997; Wetherill and Faulkner, 1981). Eccentricity-type secular resonances excite the eccentricities of objects located in the resonance, increasing the object's chances of having planetary close encounters due to intersecting more planetary orbits as  $e$  increases. On the other hand, inclination-type secular resonances that excite the inclination of objects in the resonance can protect objects from planetary close encounters as objects are tilted farther out of the ecliptic plane. The  $\nu_6$  secular resonance, which occurs when  $\dot{\varpi} \simeq g_6$ , is among the strongest of the eccentricity-

exciting secular resonances in the Solar System. It is located at the inner edge of the main belt near  $a \approx 2$  AU and  $i < 20^\circ$  (see Figure 2.5). It's presence can be seen in the top panel of Figure 2.4 where it has sculpted the curved edge of the inner main belt population in  $a, i$  space.

Objects enter the  $\nu_6$  resonance from the adjacent main belt as objects random walk in  $a$  at roughly constant inclination. This random walk is due to the chaotic nature of many overlapping resonances (see Section 2.2.1) located within the main asteroid belt. Once objects enter the resonance their eccentricities can quickly be increased to values large enough to put them on Mars-crossing orbits where subsequent Martian close encounters can remove them from the resonance and put them onto a near-Earth orbit (Greenberg and Chapman, 1983; Wetherill, 1979). If planetary close encounters do not kick an object out of the secular resonance, the body can have its eccentricity increased to unity  $e = 1$ , pushing it into the Sun, in only a few hundred thousand years (Farinella et al., 1994; Gladman et al., 1997). However, if an object leaves the resonance, it can live for tens to hundreds of millions of years random walking in  $a$  as it experiences a sequence of planetary close encounters.

### **Kozai Resonance & Kozai Effect**

The Kozai secular resonance (Kozai, 1962) offers an additional protection mechanism from planetary close encounters. This secular resonance does not relate to the precession rate of the planets, but that of the asteroid alone. It occurs for a small body when the precession rate of its longitude of pericenter  $\dot{\varpi}$  matches that of its nodal longitude  $\dot{\Omega}$ . When these two precession rates are equal, the argument of pericenter stops precessing, i.e.  $\dot{\omega} \simeq 0$ , and begins librating around  $90^\circ$  or  $270^\circ$  (Kozai, 1962). For orbits with  $a < 2$  AU, Michel and Thomas (1996) showed the argument of pericenter can also librate around  $180^\circ$ . For near-resonant objects, the related Kozai *effect* results in the argument of pericenter continuing to precess (explore all values between  $0^\circ - 360^\circ$ ), but at a highly-variable rate, coupled to large  $e$  variations.

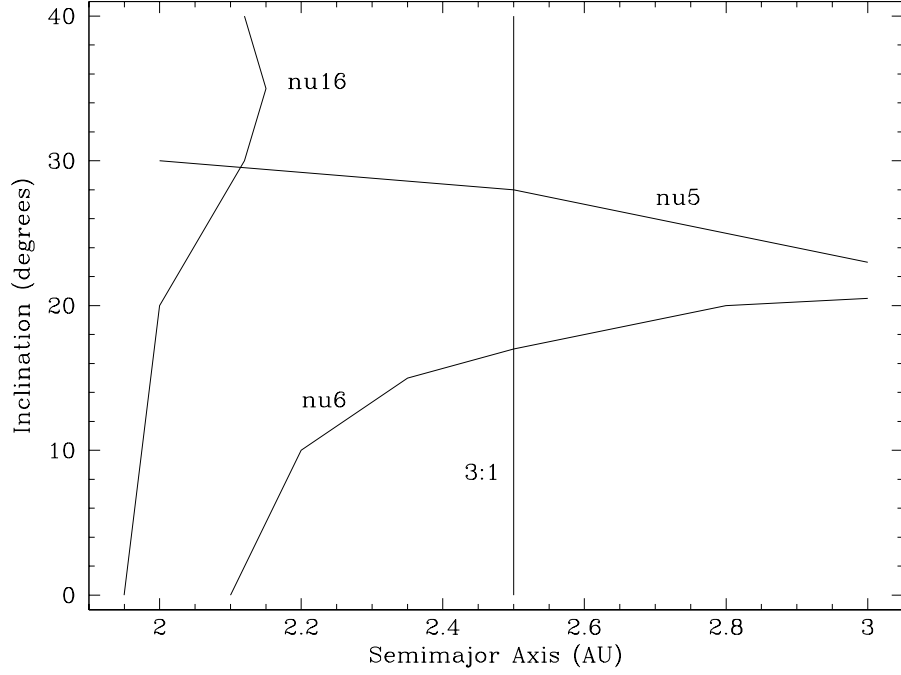


**Figure 2.5:** Approximate  $(a, i)$  locations of the 3:1 mean-motion resonance and  $\nu_5$ ,  $\nu_6$ , and  $\nu_{16}$  secular resonances for  $e = 0$  orbits. As an example, to the right of the  $\nu_6$  curve an object has a longitude of pericenter precession rate  $\dot{\varpi} > g_6$ , while to the left of the curve  $\dot{\varpi} < g_6$ . A resonant response occurs when an object is located on a point along the  $\nu_6$  curve where  $\dot{\varpi} \simeq g_6$ . This resonant response can quickly increase the eccentricity of an object to a Sun-grazing orbit within 1 Myr (Farinella et al., 1994) unless a planetary close encounter removes the object from the resonance. A similar resonant response occurs for objects located along the  $\nu_5$  secular resonance curve as well as the 3:1 mean-motion line, which is discussed in Section 2.2.1. The  $\nu_{16}$  secular resonance induces a resonant response in an object’s inclination when the longitude of the ascending node  $\dot{\Omega} \simeq s_{16}$ .

As the argument of pericenter librates due to Kozai dynamics, the z-component of angular momentum is conserved, and thus the quantity  $\sqrt{(1 - e^2)}\cos(i)$  remains constant. This causes the small body's eccentricity and inclination to oscillate against each other (i.e., high- $e$  corresponds to low- $i$  and vice versa). This mechanism offers protection against planetary close encounters due to the orbital orientations it forces for the asteroid. For objects in the asteroid belt with orbits well inside Jupiter's orbit and outside Mars' orbit, close encounters can only happen at the asteroid's aphelion or perihelion, respectively. However, because the asteroid's argument of pericenter  $\omega$  librates around  $90^\circ$  or  $270^\circ$  and the inclination remains large, the asteroid's perihelion and aphelion most often lie well outside the ecliptic plane, keeping the asteroid from planetary close encounters (Michel and Thomas, 1996). Thus, objects in Kozai resonance can be stable for tens to hundreds of Myr (Gladman et al., 2000). However, the stability of such orbits comes from their high orbital inclinations. Oscillations in  $e$  and  $i$  can allow orbital configurations when  $e$  is very high and  $i$  is very low, putting the asteroid in a position where fortuitous planetary close encounters could potentially dislodge it from the Kozai resonance or other simultaneous resonances such as mean-motion resonances (see below), before  $e$  gets large enough to push the object into the Sun (Gladman et al., 2000). Planetary close encounters removing objects from mean-motion resonances while also in the Kozai resonance is important for NEAs on long-lived retrograde ( $i > 90^\circ$ ) orbits and is discussed in Chapter 4.

### **Mean-Motion Resonances**

Mean-motion resonances divide the main asteroid belt into the inner, middle, and outer belt. The inner belt is located between  $\approx 2.1$  AU and  $\approx 2.5$  AU, the middle belt lies between  $\approx 2.5$  AU and  $\approx 2.8$  AU, and the outer belt covers  $\approx 2.8$  AU to  $\approx 3.5$  AU. Figure 2.6 depicts the main asteroid belt semimajor axis distribution where it can clearly be seen that there are severe gaps in the number of asteroids located at specific values of  $a$ . These gaps are called the Kirkwood gaps

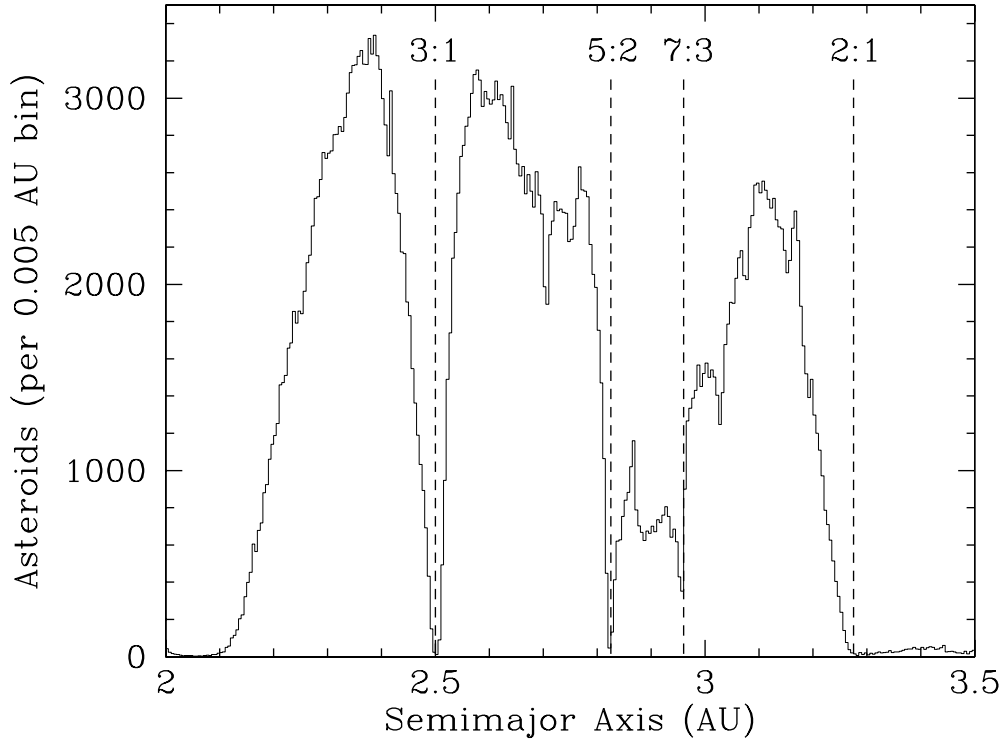


**Figure 2.6:** Main asteroid belt semimajor axis histogram for the 422,910 numbered asteroids in the Minor Planet Center Orbit (MPCORB) database on February 5, 2015. The gaps at roughly 2.5 AU, 2.8 AU, 2.95 AU, and 3.3 AU are the Kirkwood gaps corresponding to the 3:1, 5:2, 7:3, and 2:1 mean-motion resonances with Jupiter, respectively.

(Kirkwood, 1867) and the most obvious ones correspond to the 3:1, 5:2, 7:3, and 2:1 mean-motion resonances with Jupiter.

The mean-motion,  $n$ , of an object describes the average angular velocity of an object's orbit around the Sun, and is calculated by:

$$n = \sqrt{\frac{\mu}{a^3}} \quad (2.2)$$

where  $\mu$  is the gravitational parameter and  $a$  is the semimajor axis. For objects with  $\frac{m_{object}}{M_{\odot}} < 10^{-11}$ ,  $\mu = GM_{\odot} = 1.32712440018 \times 10^{20} \text{ m}^3 \text{ s}^{-2}$ . Above this threshold,  $\mu$  should be calculated as  $\mu = G(M_{\odot} + m_{object})$  to maintain the given precision. Mean-motion resonances occur when an asteroid's orbital period is commensurable with the orbital period of a planet. For example, the 2:1 mean-motion resonance with Jupiter occurs when the asteroid orbits the Sun twice for every single orbit of Jupiter, i.e.  $2n_J = n_{ast}$ . The repetitious positioning of the asteroid and planet in a mean-motion resonance causes their gravitational interactions to be periodic.

In principle, this could protect the asteroid from Jupiter's gravitational perturbations, which can otherwise kick the asteroid out of the inner Solar System, creating a stable niche in  $(a, e, i)$  space. However, when resonances (mean-motion or secular or a combination of the two) overlap, that  $a, e, i$  region no longer remains stable. The main asteroid belt is quite crowded with numerous overlapping mean-motion resonances with Mars, Jupiter, and Saturn (Nesvorný et al., 2002). In the inner main belt, the 3:1 mean-motion resonance located near  $a \approx 2.5$  AU is one such unstable resonance. The  $\nu_6$  secular resonance (see Figure 2.5) and several mean-motion resonances intersect the 3:1, resulting in its unstable nature. The strong  $e$ -pumping mechanism within the unstable 3:1 resonance causes objects located in the resonance to evolve quickly onto at least Mars-crossing orbits (Wisdom, 1985), as depicted in Figure 2.2. Martian close encounters can then cause changes in  $a$  and kick the object out of the resonance, leaving it in near-Earth space. If the object stays in the resonance, it can get to Earth-crossing without the help of Martian close encounters.

### Other Resonances

Asteroids can also escape the main belt through mean-motion resonances with Mars or three-body mean-motion resonances with the giant planets (Nesvorný and Morbidelli, 1998) and reach Mars-crossing orbits (Bottke et al., 2002). Martian close encounters can then scatter these objects onto near-Earth

orbits (Gladman et al., 2000). The outer main belt region ( $\approx 2.8$  AU to  $\approx 3.5$  AU) also has strong mean-motion resonances, such as the 7:3, 5:2, and 2:1 resonances with Jupiter, and three-body mean-motion resonances with Jupiter and Saturn (Nesvorný and Morbidelli, 1998) which can supply NEOs (Bottke et al., 2002). These resonances can push asteroids to high- $e$  orbits and into the NEO region.

## 2.2.2 Jupiter Family Comets

The last important NEO source region comes from the Jupiter family comets (JFCs). The JFC population is bounded by the Tisserand parameter. In the circular restricted three-body problem, the following quantity is conserved during planetary close encounters (in this case with Jupiter):

$$T_J = \frac{a_J}{a} + 2\sqrt{(1 - e^2)\frac{a}{a_J}}\cos(i) \quad (2.3)$$

where  $a_J$  is Jupiter’s semimajor axis. Jupiter family comets are defined to be those with  $2 < T_J < 3$ , all of whom are on Jupiter-crossing orbits. Jupiter is then excellent at kicking these objects out of the Solar System, however some JFCs can be kicked into the inner Solar System and into the NEO region (Bottke et al., 2002; Levison and Duncan, 1997).

## 2.2.3 Past Work with Numerical Integrations

The ability to compute n-body numerical integrations has provided enormous advantages to understanding orbital dynamics and chaotic behavior in the Solar System. Numerical integrations showing the chaotic nature of the main asteroid belt as a source for near-Earth objects and meteorites began in the 1970s when Wetherill developed Monte-Carlo models of injecting collisionally-fragmented objects into the  $\nu_6$  and 3:1 resonances, which slowly raised their eccentricities until they became Mars-crossing and Mars could gravitationally remove them from the resonance (Wetherill, 1979). Martian close encounters could then remove the object from the resonance and cause its orbit to evolve along the perihelion curve at

Mars' aphelion and eventually the aphelion curve at Mars' perihelion (similar to the Earth-crossing curves shown in Figure 2.3), until reaching an Earth-crossing orbit (Greenberg and Nolan, 1993; Wetherill, 1985). Eventually, it was realized that resonances alone could move objects from the main asteroid belt to Earth-crossing orbits. Similar models by Greenberg and Chapman (1983) of material being injected into main belt resonances from large-body impacts produced objects being transported onto near-Earth orbits. Both models found  $\approx 1$  Myr to be the typical timescale to transport objects from the main asteroid belt to near-Earth space via resonances, with typical lifetimes of tens of Myr (Greenberg and Nolan, 1993). Computational improvements by the 1990s allowed statistically significant numbers of objects to be numerically integrated with starting positions in main belt resonances. The turning point in our modern understanding of the efficiency of main belt resonances at supplying NEOs came when Farinella et al. (1994) showed that eccentricities of objects injected into main belt resonances could not only reach Earth-crossing orbits, but Sun-grazing orbits ( $e = 1$ ) on timescales of only  $\approx 1$  Myr. After this, numerical integrations showed typical dynamical lifetimes of particles placed within many main belt resonances to be only a few million years, most particles being terminated by becoming Sun grazers or being ejected from the Solar System by Jupiter (Gladman et al., 1997).

Morbidelli and Nesvorný (1999) showed that in addition to the  $\nu_6$  and 3:1 resonances, both Mars-crossing asteroids and the outer main belt also efficiently populate the NEO region. Many of the Mars-crossing objects are located near several mean-motion resonances with Mars and three-body mean-motion resonances, while outer main belt (OMB) objects sit near several mean-motion resonances with Jupiter as well as many three-body mean-motion resonances. Chaotic diffusion of objects migrating in  $e$  can both produce and transport Mars-crossing and outer main belt objects into the near-Earth region on timescales of  $\approx 25$  Myr (Morbidelli and Nesvorný, 1999).

The higher-than-previously-thought number of Sun grazing comets found in numerical integrations by Levison and Duncan (1994) pointed to the short-period

( $P < 200$  yr) comet population as a non-negligible NEO source. These numerical integrations found a median lifetime (from the current time) of  $\approx 500,000$  years until most objects were either ejected from the Solar System or became Sun grazers. Levison and Duncan (1997) found that  $\approx 30\%$  of particles evolving out of the Kuiper belt reached orbits with  $q < 2.5$  AU at some time during their lives; some having  $a < 4.2$  AU and thus could become NEOs. The short amount of time spent in the JFC region by the known JFCs ( $\approx 0.1$  Myr; (Levison and Duncan, 1994)), requires a significant population of objects in the Kuiper belt to supply the known JFC population (Bottke et al., 2002). This allows the JFC population to supply some NEOs.

The first numerical model of the NEO orbital distribution using these five main NEO source regions (the  $\nu_6$  and 3:1 resonances, Mars-crossers, OMBs, and JFCs) was produced by Bottke et al. (2002). Bottke et al. (2002) fit their integrated steady-state orbital distribution for each NEO source to the Spacewatch observations to determine the contribution of each source region to the overall  $a < 4.2$  AU NEO orbital distribution. Their best-fit parameters for the source contributions were  $37 \pm 8\%$  from the  $\nu_6$  resonance,  $27 \pm 3\%$  from an initially Mars-crossing population,  $20 \pm 8\%$  from the 3:1 resonance,  $10 \pm 1\%$  from the outer-portion of the main belt, and  $6 \pm 4\%$  from the JFCs. Their model also broke down the resulting predicted population into each NEO class<sup>b</sup>, with Amors constituting  $31 \pm 1\%$ , Apollos  $61 \pm 1\%$ , Atens  $6 \pm 1\%$ , and IEOs  $2 \pm 0.5\%$  of the NEO population.

### **Greenstreet et al. 2012 NEO Model**

The most recent numerical model of the NEO orbital distribution was produced by Greenstreet et al. (2012a). The numerical integrations used in the Greenstreet et al. (2012a) model were similar to those of Bottke et al. (2002) with several improvements due to recent increases in computational power (see Chap-

---

<sup>b</sup>Bottke et al. (2002) normalized their population fractions only to the  $Q > 0.983$  AU region. Greenstreet et al. (2012a) have included the near-Sun populations and renormalized these fractions.

ter 3 for a discussion of these improvements). The updated model was motivated by the needs of Canada’s microsatellite NEOSSat (Near-Earth Object Surveillance Satellite).

Canada’s NEOSSat is a joint project between the Canadian Space Agency (CSA) and Defense Research and Development Canada (DRDC) (Hildebrand et al., 2004). The science mission via CSA is to search for and track NEOs, specifically those on orbits with  $a < 1.0$  AU. NEOSSat is designed similarly to the Microvariability and Oscillations of Stars (MOST) space telescope (Walker et al., 2003). NEOSSat features an attached baffle allowing the satellite to look as close as  $45^\circ$  to the Sun, and was launched in February 2013. In order to optimize an efficient pointing strategy for NEOSSat to maximize the number of detections as well as reach orbits for discoveries that are good enough to no longer need follow-up observations (fractional uncertainty,  $\delta a/a$ , is small), a model of the NEO orbital distribution with good statistics in the  $a < 1.0$  AU region was needed.

Though the dominant population regions (Amors and Apollos) of the NEO orbital distribution are well represented in the Bottke et al. (2002) model, it was obvious that the uncertainty in the  $a < 1.0$  AU region was too large to plan an optimal pointing strategy for NEOSSat to discover and track Atens and Atiras. There was also concern that the exclusion of Mercury from the Bottke et al. (2002) integrations could have caused the  $a < 1.0$  AU populations to inaccurately represent the intrinsic orbital distribution. These reasons motivated the computation of the new steady-state NEO orbital distribution model, which have better statistics and greater integrator accuracy than the previous model. Figure 2.3 depicts the resulting orbital distribution of the NEO population from the Greenstreet et al. (2012a) model. Table 2.1 lists the best estimates for the fractions of NEOs in each orbital class from the Greenstreet et al. (2012a) NEO orbital distribution model, which are in agreement with the previous model’s estimates to within their estimated uncertainties. The better accuracy of this NEO orbital distribution model for the  $a < 1.0$  AU orbital element distribution and agreement with the NE-

OWISE detections (Mainzer et al., 2012) is the subject of Chapter 3. In addition, the surprising discovery of main belt sources producing near-Earth objects on retrograde orbits within the Greenstreet et al. (2012a) numerical integrations (Greenstreet et al., 2012b) is discussed in Chapter 4.

#### **2.2.4 Non-Gravitational Forces**

The dynamical lifetime of objects inside many main belt resonances is much shorter than the age of the Solar System, requiring a stable source to resupply these asteroidal source regions within the main asteroid belt. Possible supply mechanisms include collisions (Farinella et al., 1993), semimajor axis drift driven via the Yarkovsky effect (Bottke et al., 2001; Farinella and Vokrouhlický, 1999), and chaotic dissipation (Carruba et al., 2003; Morbidelli and Nesvorný, 1999).

It has long been thought that collisional fragments or the break-up of asteroids in the main asteroid belt can push debris into the strong  $e$ -pumping  $\nu_6$  and 3:1 resonances and supply asteroids to near-Earth orbits as well as meteorites to the Earth (Farinella et al., 1993; Greenberg and Chapman, 1983; Wetherill, 1985). Collisions at closer distances to the Sun where the volume is smaller could also change the orbital distribution of NEAs at low semimajor axes (Grun et al., 1985). Tidal disruptions due to planetary close encounters could also break apart weak rubble-pile (non-monolithic structure consisting of coalesced pieces of rock from gravitational forces) asteroids (Richardson et al., 1998) that could also migrate into resonances.

The Yarkovsky effect affects small, rotating asteroids, causing them to drift in semimajor axis due to the anisotropic emission of radiation absorbed by the asteroid. For a rotating body, the absorbed solar energy it re-radiates will not be in a direction opposite to incoming solar radiation due to thermal properties of the body that produce a lag between the absorption of sunlight and the re-radiation of heat. This causes a net force on the body along the direction of motion. This effect is known as the diurnal Yarkovsky effect. Prograde rotators (those that rotate in the counter-clockwise direction from a top-down view of the Solar System)

have a net force in the direction of motion along their orbit, and so have their semimajor axis slightly increased, causing the object to drift outward from the Sun. Retrograde rotators drift inward. The effect of semimajor axis drift due to Yarkovsky as well as direct radiation pressure effects is very slow compared to the gravitational forces discussed above. Thus, non-gravitational forces have not traditionally not been included in models of NEO orbital dynamics.

### 2.3 Size Distributions of the Main Asteroid Belt and Near-Earth Objects

Another well-studied aspect of the main asteroid belt and NEO populations is their size frequency distributions (SFDs) (cumulative number of objects as a function of size). The SFD of asteroids can tell us about their collisional evolution over the age of the Solar System, the impact strength of asteroids, the “original” mass in the main asteroid belt, and the cratering rate onto the terrestrial planets, among other things (Jedicke and Metcalfe, 1998). SFD determination is done through telescopic surveys of apparent brightness distributions, which are then translated to absolute magnitudes (directly related to an object’s size).

The  $H$ -magnitude (absolute magnitude) of a Solar System object is defined to be the apparent magnitude an object would have if it were located in an equilateral triangle 1 AU from the Sun and the Earth and at zero phase angle  $\phi$ . The phase angle is measured between the incident and reflected light directions of an observed object. Phase angles range from  $0^\circ$  to  $180^\circ$ , where a  $0^\circ$  phase angle refers to a fully illuminated object. The  $H$ -magnitude of a Solar System body can be computed from its observed (from Earth) apparent magnitude by:

$$m = H + 2.5 \log_{10} \frac{r_{helio}^2 r_{geo}^2}{P(\phi)} \quad (2.4)$$

where  $r_{helio}$  is the heliocentric distance of the body,  $r_{geo}$  is the body’s geocentric distance, and  $P(\phi)$  is the phase function with  $P(0) = 1$ . The  $H$ -magnitude relates

to an object's diameter  $D$ , in km, via:

$$D_{\text{km}} = \frac{1329}{\sqrt{p}} 10^{-0.2H} \quad (2.5)$$

where the object's visual albedo  $p$ , or reflectivity, is defined as the fraction of incident light reflected from the surface. An albedo of 0 means an object reflects no light and a value of 1 means an object reflects all light incident upon it. Typical NEO albedos range from 0.05-0.25. Using equation 2.5, a NEO with  $H = 18$  has a diameter range of roughly 0.7 km to 1.5 km for the usual albedo range.

The differential number of objects  $N$  as a function of  $H$ -magnitude can be modeled as a power-law (equation 2.6), where  $\alpha$  is the logarithmic slope (hereafter referred to simply as the slope) and allows mapping to the differential distribution in diameter  $d$  given in equation 2.7 by  $q_{\text{slope}} = 5\alpha + 1$ .

$$\frac{dN}{dH} \propto 10^{(\alpha * H)} \quad (2.6)$$

$$\frac{dN}{dD} \propto D^{(-q_{\text{slope}})} \quad (2.7)$$

The size distribution of the main asteroid belt has collisionally evolved over the past  $\approx 4.5$  Gyr. Dohnanyi (1969) theoretically examined the size frequency distribution of objects undergoing collisions, assuming the strength of an asteroid per unit mass is independent of size. He found the SFD of such a collisionally evolved population should follow a single power-law with slope  $\alpha = 0.5$  ( $q_{\text{slope}} = 3.5$ ) at all sizes. O'Brien and Greenberg (2003) examined the collisional evolution of the main belt size distribution analytically and found the same result only for objects of constant strength independent of their size. As O'Brien and Greenberg (2003) discuss, this does not hold, however, when an object's strength depends on its size (see Section 2.3.3).

Observationally, the main asteroid belt SFD is difficult to determine due to observational biases of magnitude limited surveys. At opposition, a main belt asteroid can be at a large variety of distances from the Earth (0.3 to 4.9 AU) and

express apparent brightness fluctuations up to  $\sim 6.5$  magnitudes depending on its location along its orbit (Jedicke and Metcalfe, 1998). Thus, debiasing asteroid surveys is key to understanding the intrinsic population. This observational difficulty is also present for the near-Earth asteroid population.

### 2.3.1 Surveys of the Main Asteroid Belt

The earliest systematic magnitude survey of main belt asteroids performed on photographic plates was the Yerkes-McDonald survey (YMS) by Kuiper et al. (1958), photographing the ecliptic plane to latitudes of  $20^\circ$  and to a limiting photographic magnitude of  $\sim 16.5$  (Jedicke and Metcalfe, 1998). They discovered 1,550 asteroids, determining magnitudes for roughly two-thirds.

The Palomar-Leiden Survey (LPS) (van Houten et al., 1970) extended the magnitude frequency distribution to a photographic magnitude of roughly 20, discovering  $> 2,000$  main belt asteroids, of which they used  $\sim 1,800$  to determine the magnitude frequency distribution (Jedicke and Metcalfe, 1998). van Houten et al. (1970) were the first to measure a change in slope from the  $\alpha = 0.5$  slope predicted and observationally confirmed for the largest asteroids to a shallower slope now measured to be  $\alpha = 0.3$  for  $d < 30$  km (Gladman et al., 2009).

The advances in both CCD technology and computers in the 1990s greatly aided the ability to perform automated scanning and searching algorithms for main belt asteroids at sizes smaller than tens of km. The University of Arizona's Spacewatch system located on Kitt Peak was the first to successfully use CCD technology to systematically find main belt asteroids and near-Earth objects. Jedicke and Metcalfe (1998) used the Spacewatch observational data of 59,226 asteroids found between 23 September 1992 and 8 June 1995 to investigate the orbital and absolute magnitude distribution of main belt asteroids. They found that a single power-law slope in the range  $8 < H < 16$  (roughly 2.5 km to 105 km for an assumed albedo of 10%) did not fit the observed distribution well, finding a distinctive break in the power-law at roughly  $H = 13$  (corresponding to a diameter of

roughly 6.5 to 15 km, depending on the assumed albedo) (Jedicke and Metcalfe, 1998). They found  $\alpha \approx 0.3 \pm 0.2$  best fit the  $8 < H < 13$  (roughly 10.5 km to 105 km for  $p = 10\%$ ) range,  $\alpha \approx 0.5 \pm 0.2$  for  $13 < H < 15$  (roughly 4 km to 10.5 km for  $p = 10\%$ ), and a slightly less steep slope ( $\alpha \approx 0.22 - 0.26 \pm 0.04$ ) for  $15 < H < 17$  (roughly 1.5 km to 4 km for  $p = 10\%$ ). Thus, a “wavy” size distribution with multiple slope changes was beginning to emerge from the observational data. Figure 2.7 shows the size distribution in  $H$ -magnitude of the known (biased) main belt asteroids and NEOs for objects with diameter  $d \gtrsim 1$  km assuming  $p = 10\%$ , where the gradual change in slope at smaller diameters can be seen.

The (S)ub-(K)ilometer (A)steroid (D)iameter (S)urvey, or SKADS, conducted by Gladman et al. (2009) used observations from the Kitt Peak National Observatory, confirming the power-law slopes found by previous surveys (Ivezić et al., 2001; Jedicke and Metcalfe, 1998; Wiegert et al., 2007; Yoshida and Nakamura, 2007; Yoshida et al., 2003) for  $H < 15$  (corresponding to  $d \gtrsim 4$  km for  $p = 10\%$ ) and found a shallower slope for  $15 < H < 18$  (corresponding to roughly  $d = 1$  km to  $d = 4$  km for  $p = 10\%$ ) of  $\alpha = 0.30 \pm 0.02$ , also roughly consistent with previous surveys. By this point, it became fairly clear that the main asteroid belt size distribution was “wavy”, however not all surveys agreed on the slope for sub-km-sized asteroids ( $H > 18$ ) (Gladman et al., 2009).

The most recent large-scale space-based observational platform for detecting main belt asteroids and near-Earth objects is NASA’s Wide Field Infrared Explorer (WISE)/NEOWISE thermal infrared space telescope. Launched in 2009, it performed an all-sky survey from 15 January 2010 to 5 August 2011, when its coolant depleted (Mainzer et al., 2011). During that time it identified almost 130,000 main belt asteroids. Masiero et al. (2011) used these main belt asteroid observations to measure its SFD, confirming the  $13 \lesssim H \lesssim 18$  slope of  $\alpha \approx 0.5$  from Gladman et al. (2009) as well as the kink at  $H = 13$  from Jedicke and Metcalfe (1998) and the shallower than 0.5 Dohnanyi (1969) slope for  $10 < H < 13$  from van Houten et al. (1970).

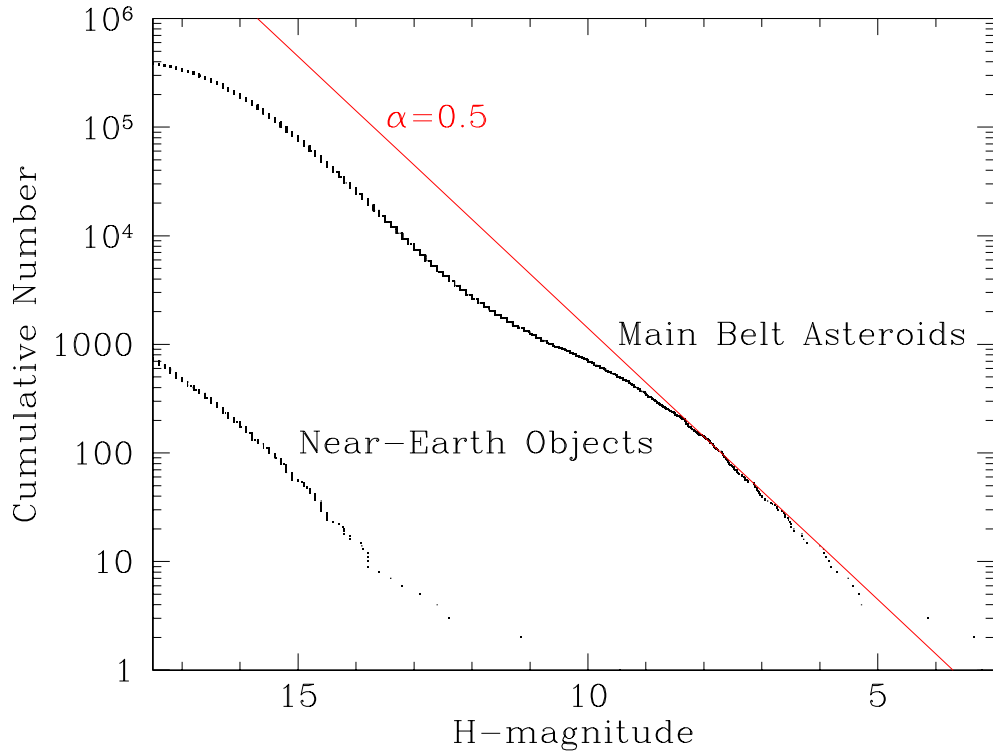


**Figure 2.7:** Main asteroid belt size distribution in  $H$ -magnitude for the 422,910 numbered asteroids and the 12,132 NEOs in the Minor Planet Center Orbit (MPCORB) database on February 5, 2015. Observational biases have not been removed from these size distributions. Note the gradual change in slope for both distributions at smaller diameters. To convert  $H$ -magnitudes to diameters,  $\Delta H = 5$  corresponds to a factor of ten change in diameter. For example,  $H = 13$  corresponds to  $d = 10$  km and  $H = 8$  corresponds to  $d = 100$  km.

### 2.3.2 Surveys of Near-Earth Objects

Surveys of main belt asteroids can also naturally produce observations of near-Earth asteroids (NEAs). Some of the above asteroid surveys, in addition to several NEA focused surveys, were also used to measure the SFD of NEOs. Because NEAs originate in the main asteroid belt, one may assume the NEA SFD should follow the main belt SFD, but shifted by some normalization due to the smaller number of NEOs than are present in the main belt. However, if some size-dependent mechanism is important to the supply of NEOs from the main belt, this shift may be more complicated.

Rabinowitz (1993) used the Spacewatch observations of roughly 25 NEOs to determine that for NEOs with  $d > 100$  m,  $\alpha \approx 0.2$ , similar to the main asteroid belt's SFD. They also found that for  $10 < d < 100$  m, the main belt SFD has a shallower slope than  $\alpha \approx 0.2$  (a slope change agreed upon by Harris (2008)). Using NEOWISE data of NEOs, Mainzer et al. (2011) found  $\alpha = 0.26$  for  $d < 1.5$  km,  $\alpha = 0.42$  for  $1.5 < d < 5$  km, and  $\alpha = 1.0$  for  $d > 5$  km, in rough agreement with previous surveys depicting a “wavy” size distribution for the NEA population as well.

### 2.3.3 Origin of a Wavy Size Distribution

As discussed above, objects smaller than  $\sim 100$  km in diameter in the main asteroid belt have been measured to have a shallower slope ( $\alpha \sim 0.3$ ) (Gladman et al., 2009; Ivezić et al., 2001; Jedicke and Metcalfe, 1998; Yoshida and Nakamura, 2007; Yoshida et al., 2003) than that predicted by Dohnanyi (1969) ( $\alpha = 0.5$ ) using a scale-independent theory. The observed “wavy” size distribution of main belt asteroids and near-Earth objects thus has implications for size-strength scaling laws and the behavior of  $Q_D^*$ , the energy per unit target mass delivered by the projectile required for catastrophic disruption of the target (requiring one-half the mass of the target body to escape).

Benz and Asphaug (1999) simulated impacts into targets of basalt and ice and found that the energy needed per unit mass of a target to cause fragmentation does

not follow a constant relationship with a target’s size. They found that  $Q_D^*$  has two regimes: the “strength-scaled” regime at small sizes, where the tensile strength of a target governs its fragmentation, and the “gravity-scaled” regime at large sizes, where the target’s self-gravity controls fragmentation. In other words, on the small target end, a lower value of  $Q_D^*$  is required for fragmentation as targets get larger until a critical size is reached when the self-gravity of the target becomes more important and an increasingly higher value of  $Q_D^*$  is required for fragmentation. Benz and Asphaug (1999)’s simulations found the transition from the “strength-scaled” regime to the “gravity-scaled” regime to occur at  $100 < d < 200$  m.

The “bump” in the main belt size distribution at  $d \approx 3$  km ( $H \approx 16$  for  $p = 10\%$ ) is attributed the transition from the “strength-scaled” regime at small sizes to the “gravity-scaled” regime at large sizes (Bottke et al., 2015). O’Brien and Greenberg (2003) explored this analytically. Considering the number of objects present in the population in the two regimes, the two segments will have differing slopes (the “strength-scaled” regime being the steeper of the two). The change in slope at the transition diameter ( $100 < d < 200$  m) will cause a wave to develop in the “gravity-scaled” regime as a discontinuity is created between the number of targets and impactors (that can catastrophically disrupt the targets) at the transition diameter and then fluctuates under the collisional evolution of the population. At the beginning of the collisional evolution, the overabundance of impactors present at sizes just smaller than the transition diameter compared to the number of targets at sizes just larger than the transition diameter creates a system that is not in steady-state. The system will compensate by decreasing the number of impactors through collisional grinding due to the relative underabundance of targets until a deficit of impactors compared to targets requires another compensation. The targets would then collisionally grind themselves down until the relative number of targets just larger than the transition to impactors just smaller than the transition (that can catastrophically disrupt the targets) creates an underabundance of targets. This fluctuation continues as the system tries to reach equilibrium.

The determination that the transition occurs at  $100 < d < 200$  m by Benz and Asphaug (1999) was used by O’Brien and Greenberg (2003) to estimate the positions of the “peaks” and “troughs” in the main belt SFD. They found that the strength-to-gravity scale transition at  $100 < d < 200$  m created a “bump” in the asteroid SFD at  $d \approx 3$  km, as is observed. The “waviness” in the main belt and consequently near-Earth asteroid SFDs is thus credited to the transition from the “strength-scaled” regime to the “gravity-scaled” regime that has propagated from small sizes to larger sizes.

The “bump” at  $d \approx 100$  km is believed to be primordial, however, which would indicate a favored size during formation of objects with  $d \approx 100$  km (Bottke et al., 2015). Bottke et al. (2005) attempted to recreate the main belt SFD from assumptions of the primordial main belt and included the transition between the “strength-scaled” regime and “gravity-scaled” regime and found evidence to support the primordial nature of the “peak” at  $d \approx 100$  km.

The “wavy” nature of the Kuiper belt SFD in the outer Solar System and its comparison to the main asteroid belt SFD will be discussed in Chapter 5.

## 2.4 Conclusions

The NEO population is fed by chaotic resonant and planetary-scattering mechanisms present in the main asteroid belt. Dynamical modeling of these processes help us understand the current orbital distribution of today’s near-Earth objects. The size distribution of the small body populations in the inner Solar System coupled with the dynamical nature of their orbits can help us estimate the abundance of objects in each sub-population as well as those on dynamically interesting orbits, as will be discussed in the following two chapters.

# Chapter 3

## High-Inclination Atens are Indeed Rare

### 3.1 Introduction

The motivation for this study came from Mainzer et al. (2012), in which the detected *Wide-field Infrared Survey Explorer* Near-Earth Object (NEOWISE) orbital element distributions for the NEA sub-populations were compared to the expected distribution given the Bottke et al. (2002) NEO orbital model. The largest discrepancy reported for the detected orbital element distributions for the Amor, Apollo, and Aten NEA sub-populations was a factor of 6.5 times more low-inclination Atens than is predicted by the Bottke et al. (2002) model, with correspondingly fewer high-inclination Atens detected (Mainzer et al., 2012). The Bottke et al. (2002) model is a pure-gravity point-mass model of dynamical transfer of NEAs from main belt sources to smaller semimajor axes. The observed rarity of high- $i$  Atens prompts the question of whether there is some physical effect which confines or enhances the production of low semimajor axis NEAs to the ecliptic plane (other than purely gravitational effects).

---

This chapter is based on the following published work: S. Greenstreet and B. Gladman, *High-inclination Atens are Indeed Rare*, *ApJ* **767**, L18 (2013).

Coincidentally, Greenstreet et al. (2012a) computed a new NEO orbital distribution model explicitly designed to have higher resolution and lower uncertainty in the  $a < 1.0$  AU region.<sup>a</sup>

## 3.2 Integration Methods

The Greenstreet et al. (2012a) model was constructed using the integration algorithm SWIFT-RMVS4, which is an improvement of the algorithm described in Levison and Duncan (1994) that prevents test particle encounters from influencing the planetary orbits. The improvements of the Greenstreet et al. (2012a) model over the previous model (Bottke et al., 2002) involve the inclusion of the planet Mercury in the integrations,  $\sim 7$  times as many particles integrated to provide better statistics, and (most importantly to this work) a much smaller integration time step which provided finer resolution. Due to the computational limitations 10 years ago, Bottke et al. (2002) were forced to use a base time step between 3.5 and 7 days, whereas Greenstreet et al. (2012a) used a base time step of 4 hours for 200 Myr integrations; the integrator adaptively reduces this time step by up to a factor of 30 upon detecting a planetary close encounter to ensure accurate resolution of the encounter. Tests with different time steps (B. Gladman, private communication), when the model integrations were being defined in 2008, showed that the fraction of NEAs was stable under changes of factor of two in the integration time step. This provides evidence that the time step is small enough that results are not being affected by convergence issues (for further convergence tests, see Appendix A). Because the RMVS integrator is second-order accurate in the perturbations, the Greenstreet et al. (2012a) integration is roughly  $(3.5/0.17)^2 = 425$  times as accurate in terms of truncation error than the previous integrations, and thus is the most accurate long-duration NEA integration yet performed.

---

<sup>a</sup>The construction of this model was the subject my Master's thesis, and is not part of this PhD thesis. The publication by Mainzer et al. (2012) was not available to perform a comparison between the Bottke et al. (2002) and Greenstreet et al. (2012a) NEO orbital models until after completion of the Master's degree.

To anticipate a planetary close encounter, at each time step the integrator performs a linear extrapolation of an object’s position forward by a single base time step. If the linear extrapolation shows the object will be within 3.5 Hill radii of a planet, the integrator will reduce the time step by a factor of 10 to continue to accurately integrate the particle’s position. Further to this time step reduction, if a linear extrapolation of the object’s position shows it will be within a single Hill radii of a planet, the integrator will reduce the time step by another factor of three, using a patched-conic hyperbolic orbit in the planetocentric reference frame to continue the integration.

The importance of such a small base time step as is used in the Greenstreet et al. (2012a) integrations comes from the existence (especially in the perihelion  $q < 1.0$  AU regime) of NEAs on highly eccentric, highly inclined orbits. Such NEAs can encounter Venus and Mercury (in particular) at speeds of up to 50 or 60 km/s. At this speed, an NEA can travel  $> 15$  Venusian Hill spheres in a single 3.5 day time step (reduced to  $< 1$  Venusian Hill sphere in a 4 hour time step). This can result in the linear extrapolation performed by the integrator failing to predict an upcoming planetary close encounter (Dones et al., 1999) and thus drop the NEA into the planetary Hill sphere without correctly time-resolving the approach phase of the encounter. This can cause the NEA to be incorrectly scattered to higher post-encounter eccentricity and inclination than it should have. For further discussion of this effect, see Appendix A.

### 3.2.1 Comparison of $a$ , $e$ , $i$ Distributions for the Two Models

The consequences of this time step difference between the two orbital models in the  $a < 1.0$  AU region can be seen in the residence time probability distributions. The residence time (Bottke et al., 2002) is the fraction of the steady-state NEO population distributed throughout a grid of  $a$ ,  $e$ ,  $i$  cells encompassing the inner Solar System covering  $a < 4.2$  AU,  $e < 1.0$ , and  $i < 90^\circ$  with cell volume  $0.1$  AU x  $0.05$  x  $5.00^\circ$  for the Bottke et al. (2002) model and  $0.05$  AU x  $0.02$  x  $2.00^\circ$  for the Greenstreet et al. (2012a) model. The Greenstreet et al. (2012a) cells are

smaller due to the finer resolution for this model enabled by the larger number of particles.

Figure 3.1 shows two different projections of the  $a < 1.0$  AU residence time probability distributions for the Bottke et al. (2002) (right) and Greenstreet et al. (2012a) (left) models. The Bottke et al. (2002) residence time portrays a broad maximum in inclination from  $20^\circ$  to  $60^\circ$  and a very broad eccentricity distribution extending up to 0.9. This is in contrast to the Greenstreet et al. (2012a) model which shows the inclination distribution more strongly confined to below  $40^\circ$  and the eccentricities mostly below 0.6. We believe the typically higher  $e$  and  $i$  values shown in the older model are incorrect and were caused by the large time step issue. However, there was no data set with sufficient  $a < 1.0$  AU detections to verify if there was indeed a problem.

### 3.3 Two Models Compared to NEOWISE Aten Detections

To quantify the difference between the two model NEO orbital distributions, we have used the NEOWISE space telescope’s detection biases published in Mainzer et al. (2012) to compare the orbital element distributions expected for the Aten population from the Greenstreet et al. (2012a) model as well as the Bottke et al. (2002) model with the detected NEOWISE Aten distributions. Fig. 7 of Mainzer et al. (2012), provides the NEOWISE detection biases for the  $a$ ,  $e$ , and  $\sin(i)$  Aten distributions. We applied the one-dimensional biases to the  $a$ ,  $e$ , and  $\sin(i)$  Aten distributions from the Greenstreet et al. (2012a) model. We note that although the NEOWISE biases are provided as one-dimensional quantities, there must be hidden correlations between the biases. For example, the NEOWISE survey pattern makes it good at finding Atens with aphelia near 1 AU, so the NEOWISE  $a$  and  $e$  biases for the Aten population will be strongly correlated. Figure 3.2 shows the fractional distribution of the NEOWISE detections (blue), biased Bottke et al. (2002) model (black), and biased Greenstreet et al. (2012a) model (green) for the Aten  $a$ ,  $e$ , and  $\sin(i)$  distributions as histograms, and Fig-

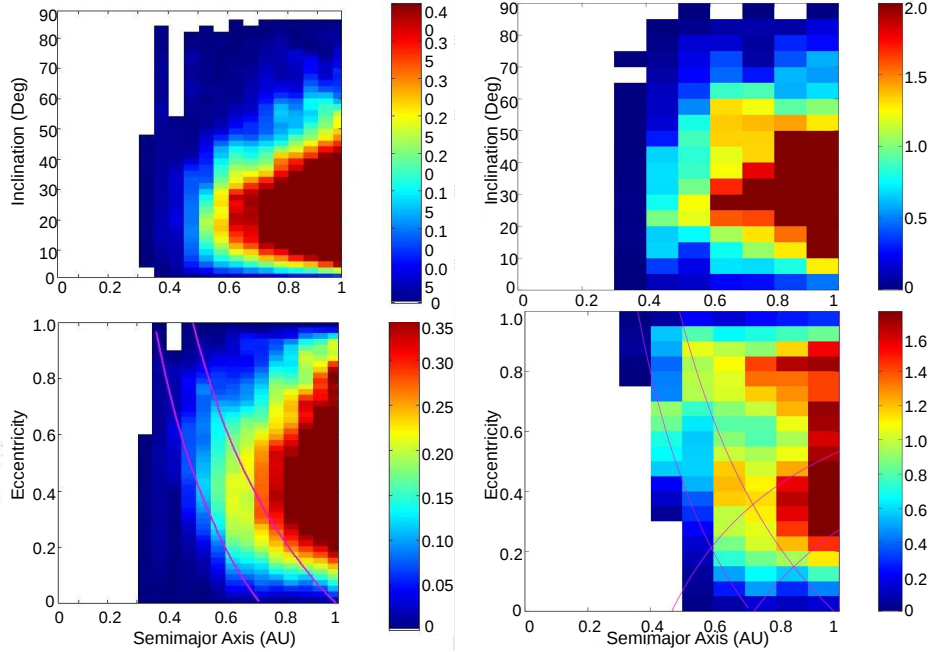


**Figure 3.1:** Residence time probability distributions from the Bottke et al. (2002) model (right) and Greenstreet et al. (2012a) model (left). To monitor the orbital evolution of each particle, a grid of  $a$ ,  $e$ ,  $i$  cells was placed throughout the inner Solar System from  $a < 4.2$  AU,  $e < 1.0$ , and  $i < 90^\circ$  with volume  $0.1$  AU  $\times$   $0.05$   $\times$   $5.00^\circ$  for the Bottke et al. (2002) model and  $0.05$  AU  $\times$   $0.02$   $\times$   $2.00^\circ$  for the Greenstreet et al. (2012a) model. These plots show only the  $a < 1.0$  AU region. To create the  $a$ ,  $e$  plot the  $i$  bins are summed and the  $e$  bins are summed to create the  $a$ ,  $i$  plot. The color scheme represents the percentage of the steady-state NEO population contained in each bin. Red colors represent cells where there is a high probability of particles spending their time. The different stretch in color scales between the left and right panels is to compensate for the 5x larger cells in the Bottke et al. (2002) model. The curved lines indicate Earth-, Venus-, and Mercury-crossing orbits.

Figure 3.3 shows cumulative versions of the distribution. Although the Aten  $a$ ,  $e$ , and  $\sin(i)$  NEO distributions for both the biased Greenstreet et al. (2012a) and biased Bottke et al. (2002) models extend beyond the range shown in Figure 3.2, the NEOWISE Aten detections and thus the detection biases shown in fig. 7 of Mainzer et al. (2012) do not. Thus, to compare the Greenstreet et al. (2012a) model (biased by the NEOWISE Aten detection biases) to the NEOWISE detections, we restrict the comparison to the same  $a$ ,  $e$ , and  $\sin(i)$  range and binning boundaries as used by Mainzer et al. (2012).

### 3.3.1 Semimajor Axis Distributions

Examining first the semimajor axis distributions (top left of Figure 3.2), one can see only small variations between the expected distributions of the two models, with the main difference being that the Greenstreet et al. (2012a) model is shifted to a slightly larger fraction of Atens at high- $a$  than the Bottke et al. (2002) model. These distributions are converted to the cumulative fraction less than a given  $a$ ,  $e$ , or  $\sin(i)$  value in Figure 3.3. The top left panel of Figure 3.3 shows the cumulative fraction less than a given semimajor axis for the NEOWISE detections (blue), the biased Bottke et al. (2002) model expectations (black), and the biased Greenstreet et al. (2012a) model expectations (green). One can see the Greenstreet et al. (2012a) model more closely matches the NEOWISE detections than the previous model, but the significance of this difference needs to be established. A Kolmogorov-Smirnov (KS) test was used to measure the probability of drawing the detected NEOWISE Aten semimajor axis distribution from the biased Bottke et al. (2002) model. The test gave a probability of 30% (Table 3.1), clearly not rejectable at  $> 99\%$  confidence, the level we have chosen for strong rejection. The KS test gives the probability of drawing the NEOWISE detections from the biased Greenstreet et al. (2012a) model as 80%, also not rejectable at a high-level of confidence. Although plausibly a better match, this result alone would not lead one to prefer the newer model.

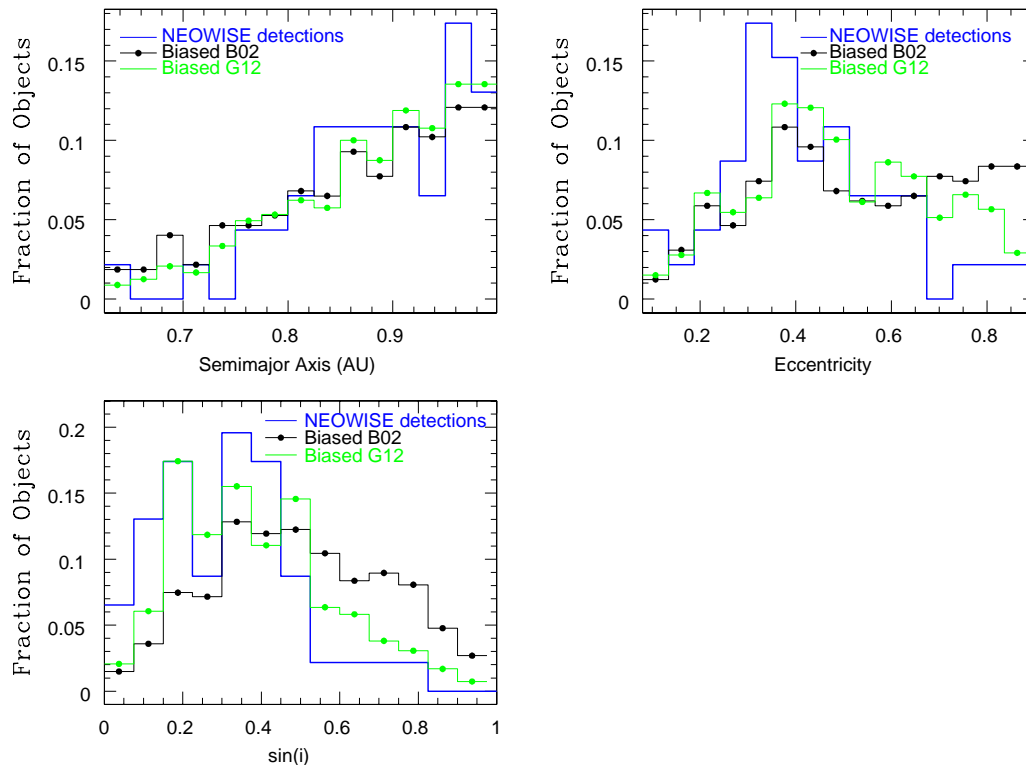


**Figure 3.2:** The fractional distribution of the  $a$  (top left),  $e$  (top right), and  $\sin(i)$  (bottom left) NEOWISE detections (blue), biased Bottke et al. (2002) model (black), and biased Greenstreet et al. (2012a) model (green). There is little difference in  $a$  between the three distributions. In contrast, the  $e$  and  $\sin(i)$  distributions expected from the Greenstreet et al. (2012a) model more closely matches the NEOWISE detections than do the Bottke et al. (2002) expectations.

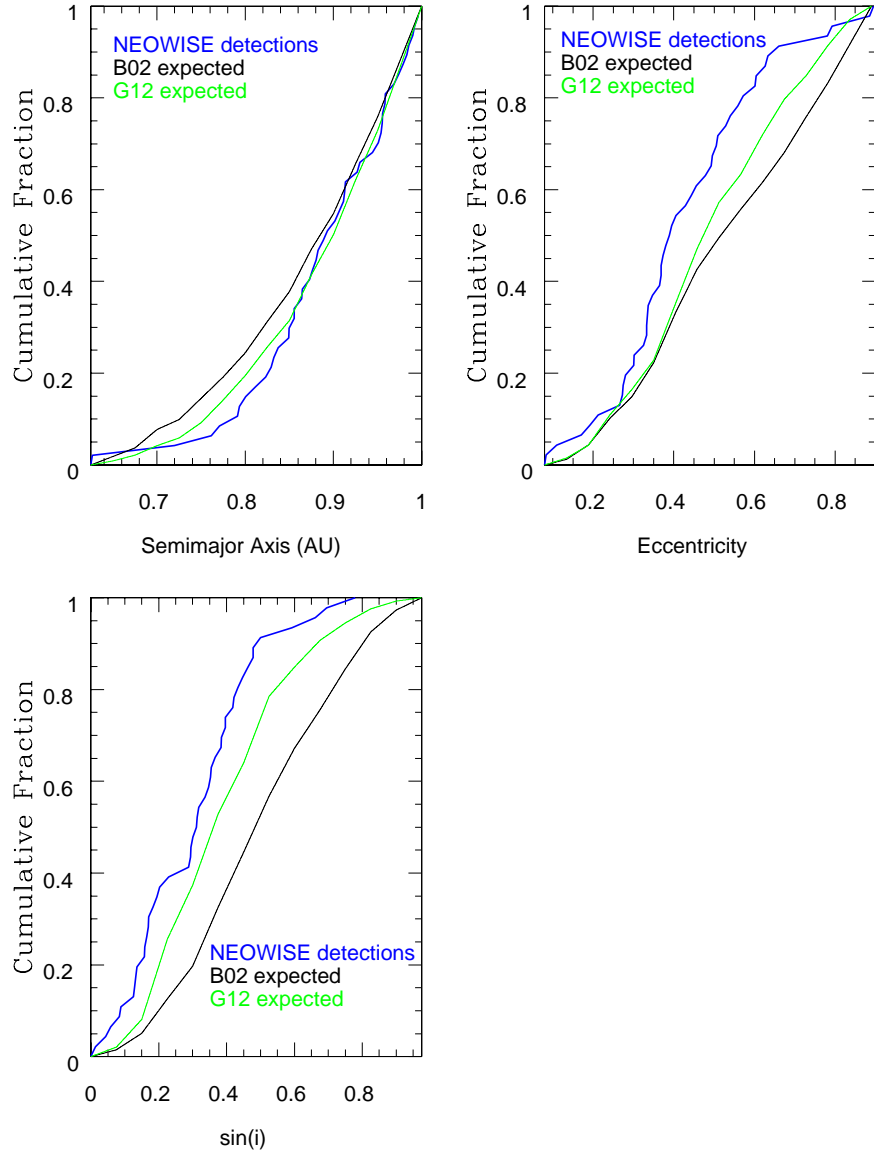


**Figure 3.3:** The cumulative distributions of the  $a$  (top left),  $e$  (top right), and  $\sin(i)$  (bottom left) NEOWISE detections (blue), biased Bottke et al. (2002) model (black), and biased Greenstreet et al. (2012a) model (green). In all distributions, the Greenstreet et al. (2012a) model more closely matches the NEOWISE detections than do the expectations from the Bottke et al. (2002) model.

$a < 1.0$ AU Orbital Model	$a$ (%)	$e$ (%)	$\sin i$ (%)
Bottke et al. (2002)	30	$< 0.5$	$< 0.01$
Greenstreet et al. (2012a)	80	6	5

**Table 3.1:** Results of Kolmogorov-Smirnov tests for the probability of drawing each detected NEOWISE Aten distribution from the orbital element distributions of the Bottke et al. (2002) model and the Greenstreet et al. (2012a) model. Neither model is rejectable at  $> 99\%$  confidence given the detected semimajor axis distribution. The Bottke et al. (2002) model *is* rejectable at  $> 99\%$  confidence given the detected eccentricity and inclination distributions, whereas the Greenstreet et al. (2012a) model is *not* rejectable at this high level of confidence given the NEOWISE  $e$  and  $i$  detections.

### 3.3.2 Eccentricity and Inclination Distributions

The eccentricity distributions, using the Mainzer et al. (2012) published bin boundaries, shown in the top right panel of Figure 3.2 show an overabundance of detected NEAs with moderate eccentricities at  $\sim 0.3$  to  $\sim 0.4$  and a relative deficit of high eccentricities ( $e > 0.674$ ), compared to the predictions of the Bottke et al. (2002) model. A difference in the Aten eccentricity distributions for the two models is evident, with the Greenstreet et al. (2012a) model more closely following the detected distribution. The top right panel of Figure 3.3 gives a clearer picture of this difference, showing that the new model has a smaller fraction with  $e > 0.674$ . The KS probability of drawing the NEOWISE Aten eccentricity detections from the Bottke et al. (2002) model is  $< 0.5\%$  (rejectable at  $> 99\%$  confidence), whereas the probability of drawing the  $e$  distribution of the NEOWISE detections from the Greenstreet et al. (2012a) model is 6% (non-rejectable).

More importantly, the inclination distributions shown in the final panel of Figure 3.2 clearly show the relative deficit of detected high- $i$  Atens that Mainzer et al. (2012) observed compared to the Bottke et al. (2002) model's expectations. This plot already makes it apparent that the Greenstreet et al. (2012a) model shares

the lack of large orbital inclinations present in the NEOWISE detections. The KS probability of drawing the NEOWISE Aten inclination distribution from the biased Bottke et al. (2002) model is rejectable at the  $\gg 99\%$  confidence level, whereas the biased Greenstreet et al. (2012a) model is not rejectable with a probability of 5%.

### 3.4 Discussion

It is important to point out that for the heavily populated  $a > 1.0$  AU region, both the Greenstreet et al. (2012a) and Bottke et al. (2002) models agree with the NEOWISE detections. Fig. 8 and 9 from Mainzer et al. (2012) show a comparison between the detected NEOWISE orbital element distributions and the Bottke et al. (2002) predictions for the Apollo and Amor populations. This is perhaps unsurprising since the Amors and Apollos are the dominant NEA populations and are well characterized by the Spacewatch observations which were used to compile the Bottke et al. (2002) model. Although there are  $q \ll 1.0$  AU Apollos, the close encounter problems mentioned above, which must be present for the small fraction of objects, are fractionally less and do not cause a detectable problem. The main difference between the two models is thus in the low- $a$  region as has just been shown.

For this preliminary study we chose a 99% confidence level before choosing to reject a model expectation. However, our  $e$  and  $\sin(i)$  distributions themselves are approaching being rejectable at a 95% confidence level. It is very likely that some significant part of the remaining discrepancy is that we have used one-dimensional biases computed for the wrong orbital distribution. That is, Mainzer et al. (2012) computed the inclination bias (for example) for the  $a/e$  distribution of the Bottke et al. (2002) model, and thus our use of the published  $\sin(i)$  bias is not rigorously correct. However, although differences in the two orbital distributions are apparent, their gross features are generally similar. As was seen in Figure 3.1, the general trend in both  $a/e$  distributions for the  $a < 1$  AU region is a monotonic decrease in the  $a$  population from  $a$  near 1 AU to smaller

semimajor axes and a peak in the  $e$  distribution near  $\sim 0.4$  with a smaller fraction of the population at lower and higher eccentricities. The  $a/i$  distributions for both models have a peak between  $i \sim 20^\circ$  and  $i \sim 30^\circ$  with less of the population at lower and higher inclinations. We believe the recomputed biases using the Greenstreet et al. (2012a) model would not be hugely different from the current biases which use the Bottke et al. (2002) model due to these general similarities between the two orbital models. Because of the correlations expected in the biases, it would be better to compute the 4D  $B[a, e, i, H]$  bias (the fraction of objects in that cell the survey could detect) for the NEOWISE survey; additional parameters related to the thermal model will likely also be necessary. Recomputing the biases is a major computational effort (Mainzer 2012, private communication). It is unclear how the complex pointing history of the NEOWISE spacecraft transforms the 3D orbital element distribution into the three 1D biases, making it difficult to estimate how different the “corrected” biases would be. Nevertheless, to improve the analysis presented in this chapter, the NEOWISE detection biases should be recomputed using the Greenstreet et al. (2012a) model and will be the subject of future work (see Chapter 8). It is plausible this will further improve the match of the Greenstreet et al. (2012a) model to the NEOWISE detections.

If both NEO orbital distribution models *had* been rejectable given the NEOWISE detections, one may have been inclined to invoke non-gravitational physics into the model. The effects that can cause NEAs to migrate in semimajor axis could include radiation pressure (Vokrouhlický and Milani, 2000) and the Yarkovsky effect (Bottke et al., 2000b; Farinella and Vokrouhlický, 1999); once km-scale NEAs are strongly coupled to the planets these slow effects may become negligible in the long-term orbital evolution. Nevertheless, one could imagine that tidal disruption by planetary encounters (Richardson et al., 1998) or perhaps more frequent collisions in the reduced volume closer to the Sun (Grun et al., 1985) could change the relative orbital distribution of low- $a$  objects. Given the non-rejectable match between the Greenstreet et al. (2012a) NEO orbital model and the detected NEOWISE Aten orbital element distributions, in particular the rarity

of large-inclination Atens, a purely gravitational model is non-rejectable, and thus no additional physics is required.

# Chapter 4

## Production of Near-Earth Asteroids on Retrograde Orbits

### 4.1 Introduction

Large-scale numerical integrations of particle histories for asteroids leaving the main asteroid belt were used to calculate the steady-state orbital distribution of NEOs (Greenstreet et al., 2012a). Upon analyzing the numerical integrations, I discovered the surprising production of retrograde orbits from main belt asteroidal sources, that is, asteroids which orbit “backwards” around the Sun. The transfer of asteroids to such orbits has not been previously discussed in the literature. In this chapter I will first discuss the integration methods used to compute the new NEO orbital distribution model (Greenstreet et al., 2012a) before investigating the typical dynamical evolution of these retrograde NEAs along with the completeness of the retrograde population. The origin of two known retrograde NEAs as well as the origin of high-strength, high-velocity meteoroids on retrograde orbits will

---

This chapter is based on the following published work: S. Greenstreet, B. Gladman, H. Ngo, M. Granvik, and S. Larson, *Production of Near-Earth Asteroids on Retrograde Orbits*, *ApJ* **749**, L39 (2012).

then be connected to the production of retrograde NEAs from main belt asteroidal sources.

## 4.2 Integration Methods

The unexpected appearance of these retrograde orbits led us to ensure this was not a numerical artifact and to attempt to understand why this behavior had not been reported before.

The improvements of the new model (Greenstreet et al., 2012a) over the previous model (Bottke et al., 2002) were discussed in the previous chapter, most important of which is our use of a smaller integration time step. Although we are unable to easily determine its importance, we remark that the small time step ensures that close encounters are correctly detected by the integration and that a particle’s integration is “slowed down” to correctly resolve the encounter. It is difficult to ascertain what effect a too large time step would have, but it is plausible that incorrectly-resolved close encounters would kick high- $e$  and high- $i$  particles to Jupiter-crossing orbits and remove them from the integration prematurely (as discussed in Chapter 3).

In any case, it is not clear that our greater short-term accuracy is particularly important to the retrograde transition, because on the observed time scales (below illustrated) it takes for particles to transition to retrograde orbits planetary close encounters seem not to be significant. Nearly all of the transitions to retrograde occur in a smooth fashion, over thousands to tens of thousands of years, rendering the higher accuracy of our integration irrelevant as even a 3.5-day time step should correctly incorporate distant planetary perturbations (with close encounters with Earth and Venus being demonstrably unimportant due to the observed lack of sudden orbital element changes). We tested the independence of our results by re-integrating a subsample of our simulations with a different planet set (Venus through Neptune rather than Mercury through Saturn) and the previous generation integrator RMVS3 (more heavily tested) and found no statistically-significant differences in the retrograde production mechanism or lifetimes.

The appearance of these retrograde particles in our integrations but not in the previous Bottke et al. (2002) integrations leads one to the question of why the previous simulations didn't report finding any retrograde objects. The reason may be due to a variety of factors. The previous, larger time step study (Bottke et al., 2002) may potentially have been removing test particles prematurely via incorrectly resolving close encounters as mentioned above, incorrectly moving particles to Jupiter-crossing orbits and thus cutting off the evolution before the retrograde state could be reached. Secondly, we have integrated roughly seven times as many particles as previous groups, and this is a rare endstate; this is compounded by the fact that the majority of the retrograde residence time is in a minority of long-lived retrograde particles. Thirdly, there is a chance Bottke et al. (2002) produced NEAs on retrograde orbits in their integrations and simply binned them away by forcing these few, rare objects into their  $85^\circ < i < 90^\circ$  bin. Lastly, upon further analysis of our recomputation of the Bottke et al. (2002) integrations (Greenstreet et al., 2012a), we observed two example test particles which each flip to retrograde orbits roughly 2 Myr into their lifetimes and live for only  $\sim 300$  and  $\sim 900$  years post flip. These two extremely short-lived, rare test particles may not have been detected without the higher frequency (300 year) orbital output used in the Greenstreet et al. (2012a) model. Bill Bottke later confirmed (private communication 2013) the production of a couple retrograde NEAs in their model, providing further support that these retrograde particles are not an artifact of our integrations.

### 4.3 Typical Retrograde NEAs

The production of retrograde orbits coming from any one of the initial asteroidal sources has not been discussed in the literature and was thus surprising. Analysis showed that the retrograde population accounts for  $\simeq 0.10\%$  (within a factor of two) of the steady-state NEO population ( $q < 1.3$  AU); this fraction is estimated by computing the normalized fraction of time particles in the Greenstreet et al. (2012a) model spend on orbits with inclinations  $i > 90^\circ$ , similar to determining

the fraction of NEOs in each NEO-class (shown in Table 2.1). This residence time probability distribution for the retrograde NEA population (similar to the top panel of Figure 2.3, but for  $0^\circ < i < 180^\circ$ ) is shown in Figure 4.1 of the logarithm of the normalized fraction of time spent by particles in each cell ( $\mathcal{R}_{180}(a, e, i)$ ) for the region  $a < 4.2$  AU,  $e < 1.0$ ,  $i < 180^\circ$  (with cell volume  $0.05$  AU x  $0.02$  x  $2.00^\circ$ ).

The typical orbital path, after leaving their asteroidal source regions, for objects which become retrograde is a random walk in semimajor axis  $a$  due to planetary close encounters. Some evolve to  $a < 2$  AU and spend many Myr in this state before returning to larger semimajor axis (Gladman et al., 1997). Often the orbital inclination  $i$  rises above  $30^\circ$  during the random walk before the particle returns to  $a > 2$  AU.

The majority of the asteroids which become retrograde eventually find their way into the 3:1 mean-motion resonance with Jupiter, after migrating out of any one of the initial asteroidal source regions. Figure 4.2 shows the logarithm of the amount of time (in Myr) particles live after they become retrograde versus their semimajor axis at the instant their orbits tilt past  $i = 90^\circ$ . As can be seen in Figure 4.2, the great majority of the asteroids that become retrograde do so while in the 3:1 resonance (near  $a = 2.5$  AU), although other mean-motion resonances are evident, such as the 4:1 at  $a \approx 2.06$  AU, the 2:1 at  $a \approx 3.3$  AU, the 5:2 at  $a \approx 2.8$  AU, and the 7:3 at  $a \approx 3.0$  AU. Because the vast majority of retrograde particles appear to flip while in mean-motion resonances, it is plausible the mechanism that causes the flip is linked to these resonances. However, it is not clear that *every* flip occurs inside a mean-motion resonance (i.e., we have not checked this for every retrograde particle), but because this appears to be the case for the vast majority of retrograde particles it is likely mean-motion resonances play some role in the flipping mechanism.

If the retrograde particle stays in the resonance it can terminate almost immediately (as little as hundreds of years later) when the resonance pushes the high- $e$  particle into the Sun. Roughly 98% of the retrograde NEAs are eliminated

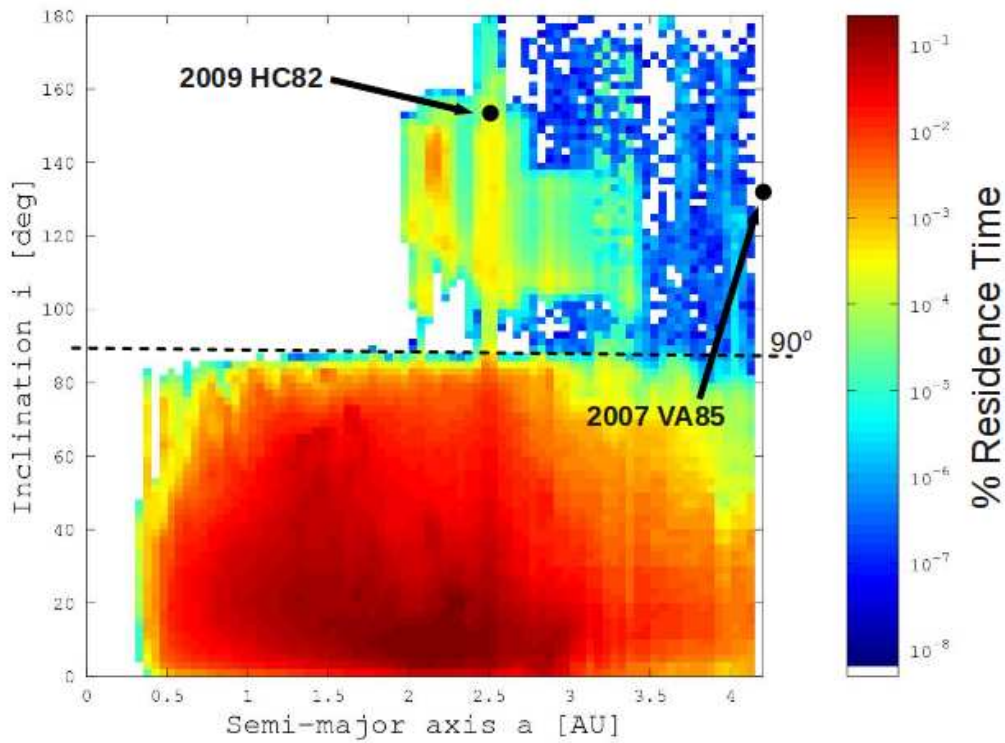


**Figure 4.1:** Residence time probability distribution,  $\mathcal{R}_{NEO}(a, e, i)$ , for inclinations up to  $180^\circ$  for the Greenstreet et al. (2012a) NEO orbital model. The color scheme represents the logarithm of relative density of residence time spent in any given cell in relation to the amount of residence time spent in all cells. The dashed line divides retrograde from direct orbits. The retrograde NEA population makes up  $\simeq 0.10\%$  of the steady-state NEO population. Two known retrograde NEOs are shown.

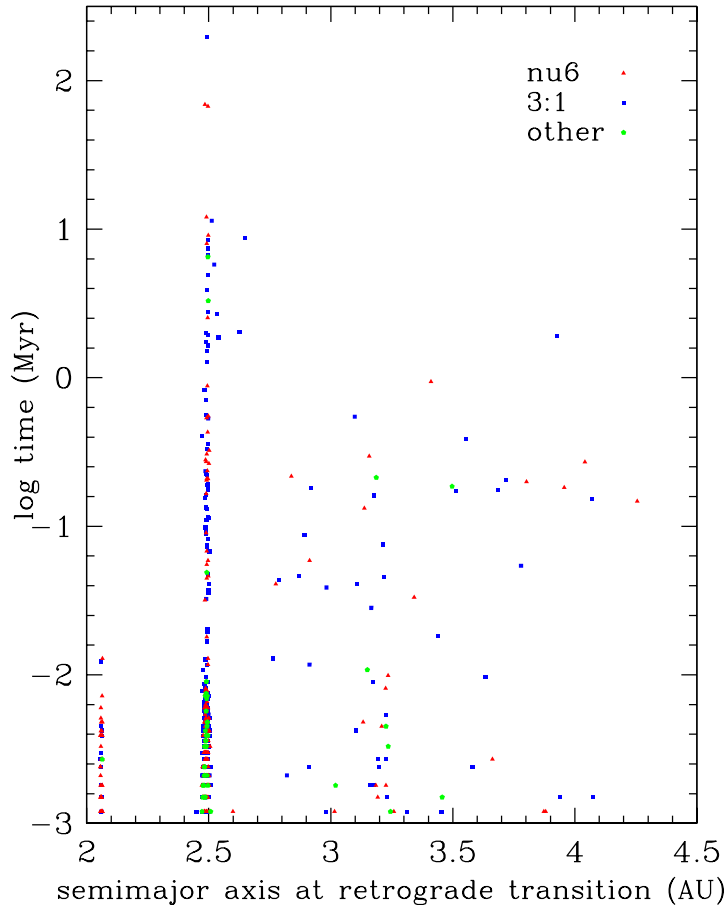


**Figure 4.2:** The logarithm of the amount of time (in Myr) particles live after they become retrograde versus their semimajor axis at the instant they flip to a retrograde state. Colored symbols indicate the source region in which the particle originated at the start of the integration. ‘Other’ refers to particles originating in the outer main belt and Mars-crossing regions, where resonances can put particles into near-Earth space. The retrograde particles shown here make up 3% of the particles integrated in the Greenstreet et al. (2012a) NEO model. Particles starting in any of the asteroidal source regions can flip to retrograde orbits. The vast majority of particles become retrograde while in the 3:1 resonance (near  $a = 2.5$  AU) although other resonant semimajor axes are obvious, such as the 4:1 near  $a \approx 2.06$  AU, the 2:1 at  $a \approx 3.3$  AU, the 5:2 at  $a \approx 2.8$  AU, and the 7:3 at  $a \approx 3.0$  AU.

from the integrations because they reach perihelia distances lying inside the Sun, a common fate for resonant asteroids (Farinella et al., 1994). The remaining are either thrown out of the Solar System, most often by Jupiter, or suffer planetary collisions. The median lifetime once NEAs become retrograde is only  $\sim 3,000$  years, but if kicked out of the resonance due to a planetary close encounter, the integrations show examples of retrograde asteroids living tens or even hundreds of millions of years.

Although most of the retrograde objects flip while in the 3:1 resonance, Figure 4.1 of  $\mathcal{R}_{180}(a, e, i)$  shows most of the power for the retrograde objects near  $a \approx 2$  AU. This is due to a single particle which flips in the 3:1 resonance early in its lifetime and then spends  $\approx 200$  Myr near 2 AU (see Section 4.3.3 and Figure 4.7).

### 4.3.1 Sample Retrograde Production

Figure 4.3 shows an example of the orbital history of a NEA from our numerical integrations which emerges from the main belt via the  $\nu_6$  secular resonance, which is a common mechanism by which asteroids reach planet-crossing space (Bottke et al., 2002; Gladman et al., 1997). This particle gets kicked out of the resonance and random walks in  $a$  due to planetary close encounters for most of its lifetime as an Apollo-class NEA. It begins to experience Kozai oscillations (Kozai, 1962) in  $e$  and  $i$  starting at  $t \sim 10$  Myr, reaching inclinations up to  $75^\circ$ . Near 70 Myr, the particle has an Earth close encounter which puts it on an orbit near the 3:1 resonance and upon being perturbed into the 3:1 it flips to a retrograde state at  $t \sim 72$  Myr. It then survives in the retrograde state another 3 Myr before colliding with the Sun. A more detailed analysis of the epoch around the flip (Figure 4.4) proves the particle enters the 3:1 resonance. The libration of the 3:1 resonant argument ( $\phi_{31} = 3\lambda_J - \lambda - 2\varpi$ ) around  $180^\circ$  indicates the importance of the 3:1 resonance at the time of the flip.

It is clear that Kozai alone does not result in the inclination passing through  $90^\circ$ , because only a tiny fraction of particles (if any) become retrograde outside

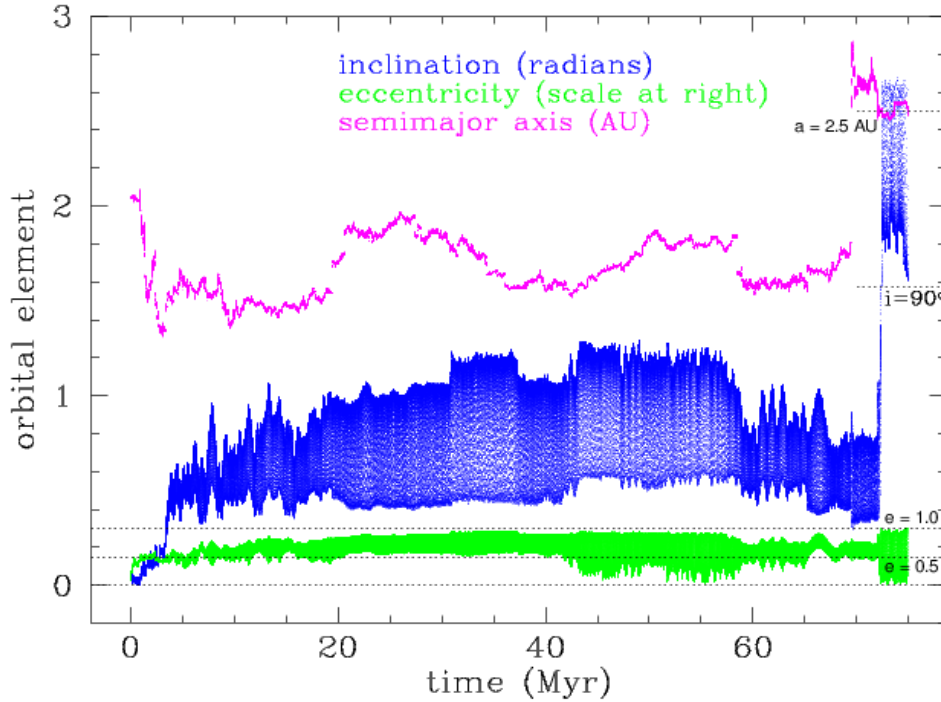


**Figure 4.3:** The  $a$ ,  $e$ ,  $i$  history from our NEO model integrations of an asteroid which becomes a retrograde NEA. This particle originates in the  $\nu_6$  secular resonance with low  $e$  and  $i$ . After a  $\sim 70$  Myr sojourn as a high- $i$  Apollo, it flips to a retrograde state crossing  $i = 90^\circ = 1.57$  rad (detail in Figure 4.4) and lives for another  $\sim 3$  Myr before colliding with the Sun.

a mean-motion resonance even if very high- $i$ 's are reached. A dynamical phenomenon in the resonance then causes the particle's inclination to make a smooth transition through  $90^\circ$  (see Figure 4.4); the detailed nature of this mechanism is still unclear. However, the smooth evolution of all particle orbital elements during the transition to a retrograde orbit rules out planetary close encounters as the mechanism causing the flip.

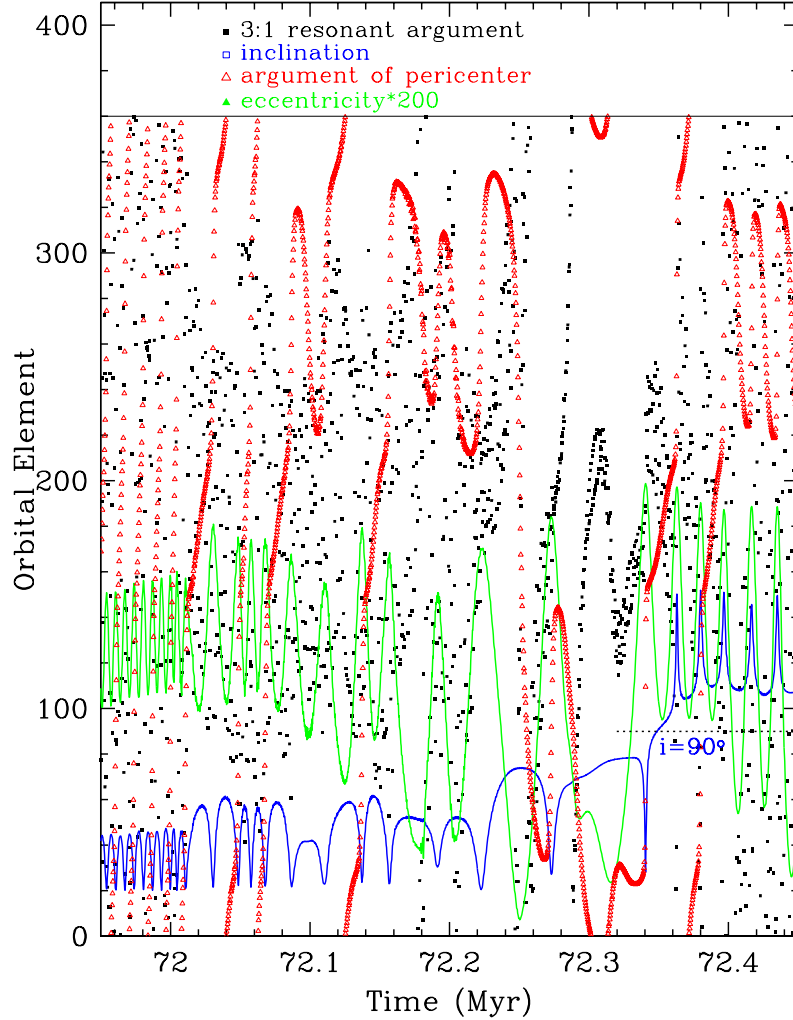


**Figure 4.4:** The orbital history of the particle shown in Figure 4.3 around the time of its flip to a retrograde orbit. Kozai oscillations in  $e$  and  $i$  are evident from their anti-coupled oscillations and the argument of pericenter librating around  $270^\circ$  from  $\sim 72.1$  Myr to  $\sim 72.2$  Myr. The 3:1 resonant argument (black points) switches from circulating to librating around  $180^\circ$ , indicating the particle has entered the 3:1 resonance, at  $\sim 72.3$  Myr just before the particle flips to a retrograde state.

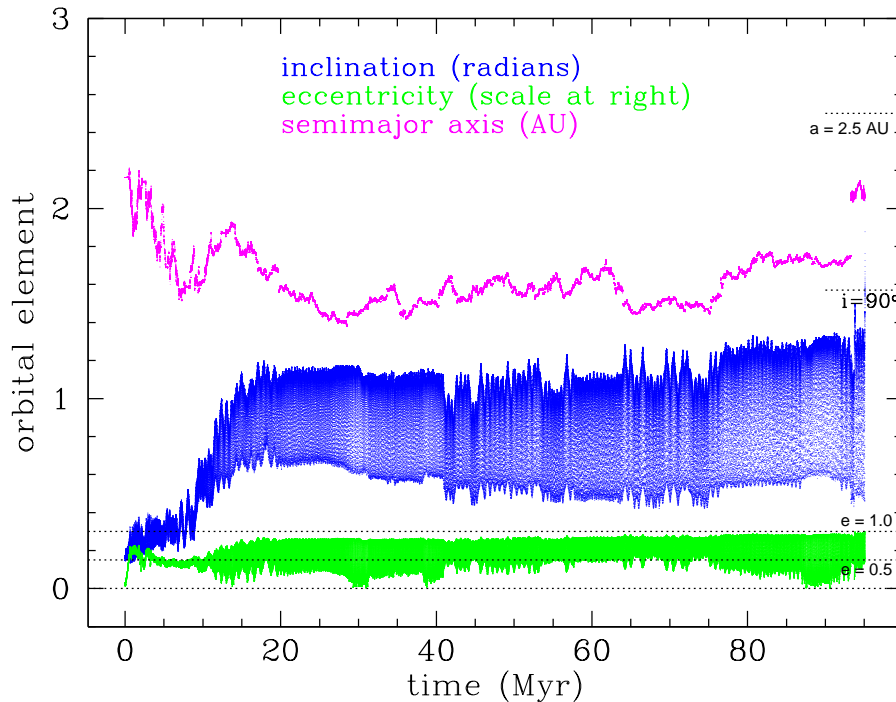


**Figure 4.5:** The  $a$ ,  $e$ ,  $i$  history from the integrations of a short-lived retrograde asteroid. This particle originates in the  $\nu_6$  secular resonance with low  $e$  and  $i$ , similar to the particle shown in Figure 4.3. It spends  $\sim 95$  Myr as a high- $i$  Apollo, before flipping to a retrograde state (detail in Figure 4.6) while near the 4:1 mean-motion resonance with Jupiter. This particle dies immediately ( $\sim 6000$  years) after flipping when it is pushed into the Sun ( $e = 1$ ).

### 4.3.2 Short-Lived Retrograde Production

Most retrograde objects are eliminated from the integrations immediately (hundreds to thousands of years) after becoming retrograde when their eccentricities increase to unity ( $e = 1$ ) due to Kozai oscillations. A typical short-lived retrograde particle orbital evolution is shown in Figure 4.5. This retrograde particle originates in the  $\nu_6$  resonance before a planetary close encounter removes it from the resonance and it lives as a high- $i$  Apollo for  $\sim 95$  Myr.

Contrary to the particle shown in Figure 4.3, the retrograde particle shown in Figure 4.5 experiences a very short-lived ( $\sim 6,000$  year) life as a retrograde NEA and flips while near the 4:1 mean-motion resonance instead of in the 3:1 resonance. As depicted in Figure 4.6, this particle also experiences Kozai oscillations in  $e$  and  $i$ . Unlike the particle shown in Figure 4.3, which is in the Kozai resonance (argument of pericenter librating around  $270^\circ$ ) before becoming retrograde, the particle shown in Figure 4.5 experiences the Kozai *effect*, where the argument of pericenter continues to circulate, but at a highly-variable rate. Shortly before the object flips to a retrograde orbit, it has a planetary close encounter that puts it near the 4:1 mean-motion resonance. The 4:1 resonant argument ( $\phi_{41} = 4\lambda_J - \lambda - 3\varpi$ ) ceases to circulate just before the flip occurs, indicating the importance of the resonance as the particle makes a smooth transition through  $i = 90^\circ$  to a retrograde orbit.

### 4.3.3 Long-Lived Retrograde Production

The longest-lived retrograde particle found in the integrations spends  $\sim 98\%$  of its lifetime in a retrograde state. Figure 4.7 shows its  $a$ ,  $e$ ,  $i$  history. Starting in the 3:1 resonance, the particle's orbit flips  $\sim 5$  Myr into its  $\sim 210$  Myr lifetime having remained in the 3:1 resonance up to that time. About 5 Myr after becoming retrograde, it gets kicked out of the resonance by a planetary close encounter. Roughly 10 Myr later, it has another close encounter that moves it even farther from the 3:1 resonance, beginning a  $\sim 195$  Myr random walk in  $a$  near 2 AU. It collides with the Sun after a total of  $\sim 210$  Myr.

Although the majority of the NEAs that become retrograde do so while in the 3:1 resonance, as is shown in Figure 4.2, the longest-lived retrograde NEAs do not remain in the resonance. The particle depicted in Figure 4.7 is responsible for the majority of the power in the residence time distribution for retrograde objects near  $a \approx 2$  AU shown in Figure 4.1.

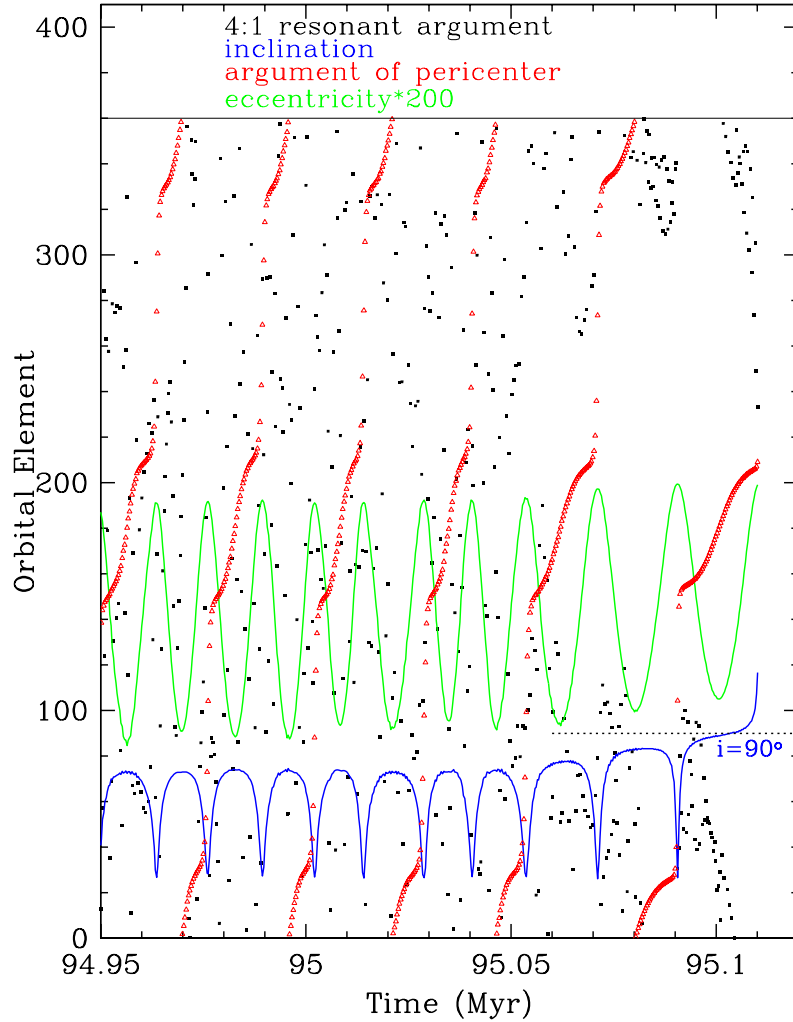


**Figure 4.6:** The orbital history of the particle shown in Figure 4.5 around the time of its flip to a retrograde orbit. Similar to Figure 4.4, Kozai oscillations in  $e$  and  $i$  are evident from their anti-coupled oscillations, however the argument of pericenter continues to circulate indicating the particle is not in the Kozai resonance, but experiencing the Kozai effect. The 4:1 resonant argument (black points) stops circulating at  $\sim 95.1$  Myr just before the particle flips to a retrograde state, indicating the importance of the 4:1 resonance to the flip.

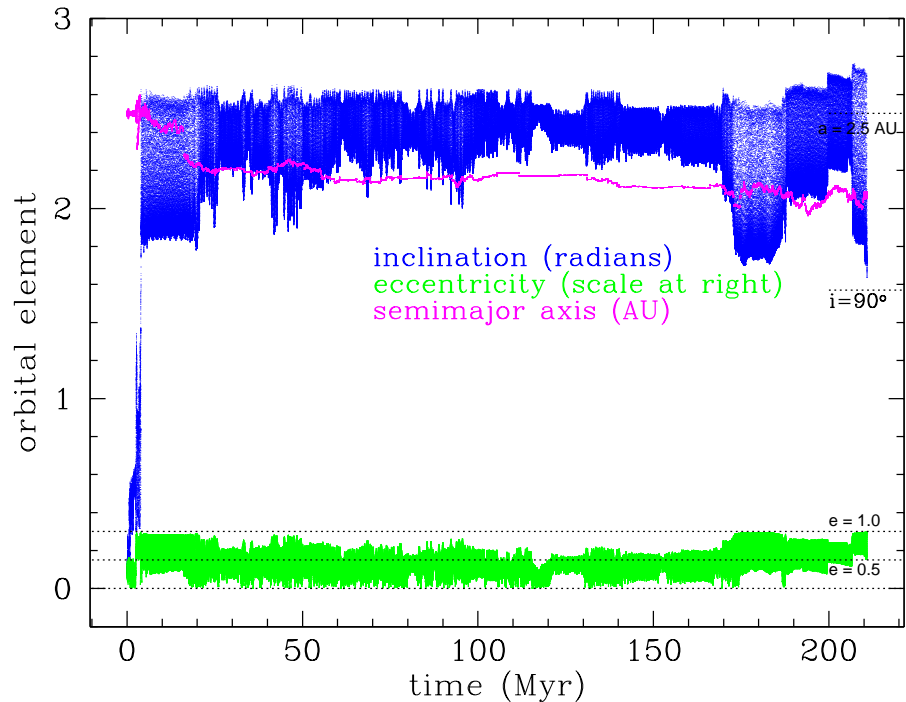


**Figure 4.7:** The  $a$ ,  $e$ ,  $i$  history of the longest-lived retrograde asteroid from the integrations. This particle originates in the 3:1 mean-motion resonance with low  $e$  and  $i$ . It flips to a retrograde orbit only  $\sim 5$  Myr into its lifetime while still in the 3:1 resonance. This particle then lives for  $\approx 195$  Myr on a retrograde orbit before getting pushed into the Sun ( $e = 1$ ).

#### 4.3.4 Completeness of Retrograde Population

Given our estimate that  $\sim 0.1\%$  (within a factor of two) of the steady-state NEA population is on retrograde orbits, because there are  $\sim 1,000$  NEOs with  $H < 18$  (Bottke et al., 2002; Mainzer et al., 2011; Stuart, 2001), of order one retrograde NEA of this size ( $d > 1$  km) should exist at any time. Because NEAs reaching retrograde orbits often visit low perihelion orbits during their evolution then, perhaps like comets (Reach et al., 2009), thermal driven breakup could decrease (if catastrophic) or increase (if many new smaller fragments are produced) this num-

ber estimate. In contrast, given that there are  $\sim 7,000$  known NEAs with  $H < 23$ , one might expect more retrograde NEOs to be known, but this neglects detection biases. The high- $e$ , high- $i$  NEOs are the most incomplete portion of the overall NEO population. The fact that the two known retrograde  $H < 18$  NEAs were only discovered in the last 5 years (near the end of completing the  $H < 18$  population) proves that these hard-to-find NEOs constitute the most incomplete portion of the NEO population. The incompleteness increases even more for smaller objects.

The Greenstreet et al. (2012a) NEO orbital distribution model can be represented as three one-dimensional histograms normalized to the NEOWISE estimate of  $\sim 19,500$  NEOs with  $18 < H < 23$  (Mainzer et al., 2011) and compared to the distributions of already detected NEOs with  $18 < H < 23$  as seen in Figure 4.8.

Figure 4.8 expresses the observational completeness of the  $18 < H < 23$  NEO population as a fraction. Our  $\sim 0.1\%$  estimate for the retrograde NEO population indicates there should be  $\approx$  twenty  $18 < H < 23$  NEAs on retrograde orbits. However, the retrograde population at this size are on orbits which are observationally difficult to find; Figure 4.8 illustrates that as  $e$  and  $i$  rise observational completeness plummets rapidly to zero. We thus expect more retrograde NEAs will be discovered in the near future as the completeness increases for this part of the NEO population.

## 4.4 Two Known Retrograde NEAs

There are currently two known retrograde NEAs: 2007 VA85 ( $a = 4.23$  AU,  $e = 0.74$ ,  $i = 131.8^\circ$ ) and 2009 HC82 ( $a = 2.53$  AU,  $e = 0.81$ ,  $i = 154.5^\circ$ ), which were found by the LINEAR (Stokes et al., 2000) and the Catalina Sky Survey (Larson et al., 2003), respectively. These are plotted in Figure 4.1. The Catalina team has recently carefully examined their available imaging of both objects for any evidence of a coma and have found none. It is thus possible these objects are asteroids that have become NEAs and found their way to  $i > 90^\circ$  orbits rather than retrograde devolatilized comets. We do find examples of particles which exit a resonance after flipping with  $a > 3$  AU (Figure 4.2) and then migrate to larger

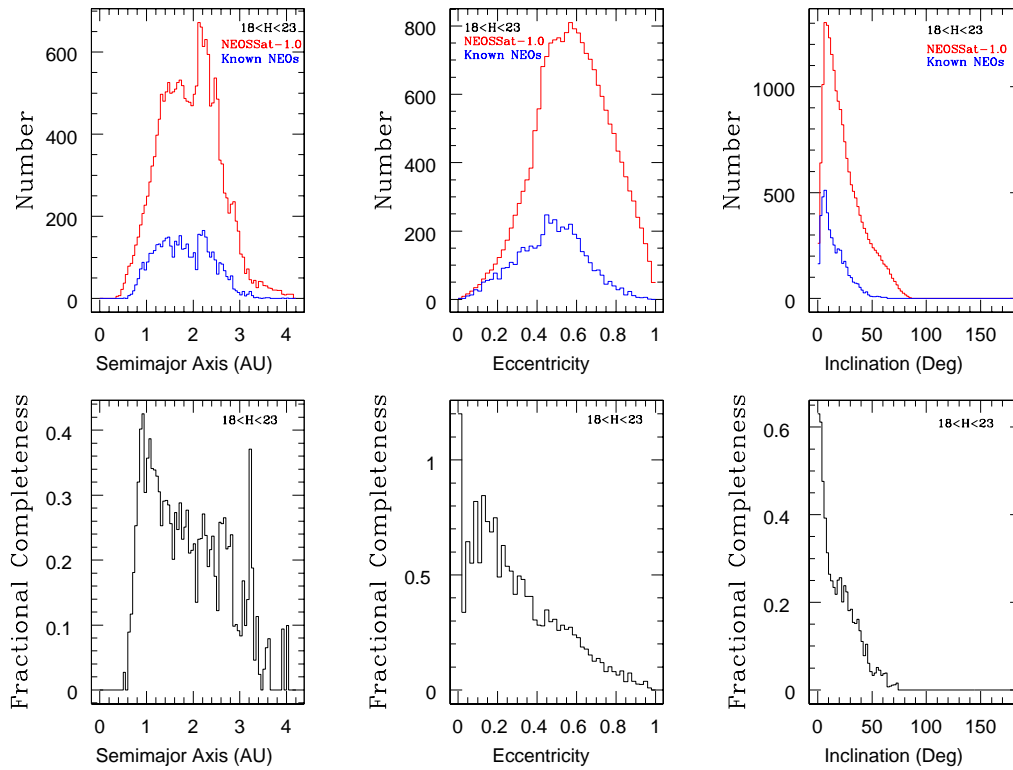


**Figure 4.8:** The NEO orbital distribution (NEOSSat-1.0 or Greenstreet et al. (2012a) model) for NEOs with  $18 < H < 23$  normalized to  $\sim 19,500$  NEOs and compared to the 3,486 known NEOs with  $18 < H < 23$  along with the observational completeness for NEOs with  $18 < H < 23$ .

$a$ ; 2007 VA85 has  $a = 4.23$  AU and could possibly be explained by this process. However, 2007 VA85's current orbital nodes are outside of Jupiter's orbit, so a past close encounter with Jupiter to put it on its current orbit is also possible and it may be of cometary origin.

We performed two independent sets of integrations (with the two different integrators SWIFT-RVMS4 and MERCURY) of the best-fit orbit for each of 2007 VA85 and 2009 HC82 for 1 Myr. 2007 VA85 was terminated by being pushed into the Sun at 0.74 Myr in one integration and was thrown out of the Solar System at 0.53 Myr in the other. In both cases, 2007 VA85 quickly migrates to larger  $a$  outside Jupiter's orbit. In addition to the best-fit orbit for 2007 VA85, 2,000 initial conditions which map the volume in phase space containing 99.9% of the total probability mass (Granvik et al., 2009) for 2007 VA85 were integrated for 1 Myr. About 51% of the clones were pushed into the Sun,  $\sim 37\%$  were thrown out of the Solar System,  $\sim 0.5\%$  collided with Jupiter, and  $\sim 11\%$  were still alive after 1 Myr. About 61% of the remaining clones were no longer NEAs ( $q > 1.3$  AU) and had migrated out past Jupiter ( $a > a_{Jupiter}$ ).

2009 HC82 on the other hand, is on an orbit very near the 3:1 resonance (where it most likely flipped) for the entirety of both independent 1 Myr integrations of the best-fit orbit. This behavior is exactly like the typical steady-state retrograde NEA evolution we discovered. Integrations of 2009 HC82's nominal orbit show it not to be currently in the 3:1 resonance. Our model shows that the long-lived (and thus most likely to be observed) NEAs are those which no longer reside in the resonance and thus this makes sense in this context. In addition to the best-fit orbit integrations for 2009 HC82, a set of 1,458 clones were integrated for 3 Myr. At the end of the 3 Myr integration,  $\sim 51\%$  became Sun grazers,  $\sim 0.5\%$  were terminated due to planetary collisions, and  $\sim 48\%$  were still alive. Of the 2009 HC82 clones still alive,  $\sim 92\%$  were still near their initial conditions ( $a \simeq 2.5$  AU,  $q < 1.3$  AU), again similar to our expectation.

We therefore believe 2009 HC82 is a NEA that has evolved onto a retrograde orbit and 2007 VA85 is a devolatilized comet nucleus (the plausibility of which will be examined in the next section).

## 4.5 Estimated Extinct Comet Population

A possible production mechanism for an activity-free retrograde NEO is to have a retrograde Halley-type comet (HTC) (defined to have a period of  $20 < P < 200$  yr) reach a  $q < 1.3$  AU orbit and have its surface volatiles depleted during numerous perihelion passages. This is expected to be a rare occurrence. To estimate the number of devolatilized HTCs which would exist in a steady-state on orbits with  $a < 5.2$  AU and  $q < 1.3$  AU, we scaled the HTC population model of Levison et al. (2006). Levison et al. (2006) peg the number of active HTCs with  $d > 10$  km and  $q < 1$  AU to be 4 since this population is believed to be observationally complete. Their figure 5 shows that  $\simeq 60\%$  of the  $q < 1.3$  AU population has  $q < 1$  AU, which leads to  $4/0.6 \approx 7$  HTCs with  $d > 10$  km and  $q < 1.3$  AU. Also from figure 5 of Levison et al. (2006), only  $\sim 3\%$  of the  $q < 1.3$  AU HTCs have  $a < 5.2$  AU. This means the number of HTCs  $N_{HTC}$  ( $d > 10$  km,  $q < 1.3$  AU,  $a < 5.2$  AU)  $\approx 0.03 \times 7 \sim 0.2$ . In order to obtain the number of even smaller  $d > 1$  km HTCs on such orbits, the slope  $\alpha$  of the logarithmic absolute  $H$ -magnitude distribution is needed. Kuiper-belt objects of comparable sizes have  $\alpha \sim 0.35$  (Fraser et al., 2010) (see Chapter 5). For  $\alpha = 0.35$ , because  $\Delta H = 5$ ,  $N_{HTC}(d > 1 \text{ km}) = N_{HTC}(d > 10 \text{ km}) \times 10^{1.75} \sim 10$ , which is for *active* HTCs. Figure 11 from Levison and Duncan (1997) shows that for Jupiter-family comets the favored fade time is  $\sim 10^4$  years and the ratio of extinct to active comets is  $\sim$  four. This results in an estimate of  $\sim 10 * 4 \sim 40$  devolatilized HTC nuclei with  $a < a_{Jupiter}$  at any time. Cometary splitting (Reach et al., 2009) could alter this estimate, but the existence of one or more  $d > 1$  km HTCs, like 2007 VA85, interior to Jupiter is likely. As a final note, the Levison et al. (2006) simulations show that HTCs do not reach  $a \approx 2.5$  AU, so such an origin for 2009 HC82 seems implausible.

## 4.6 High-Strength, High-Velocity Meteoroids on Retrograde Orbits

The production of retrograde orbits from main belt asteroidal sources also resolves an outstanding question on the origin of high-strength, high-velocity meteoroids on retrograde orbits. The existence of strongly-differentiated material on very high entry-speed orbits (which must be retrograde) has been known since the 1970s (Harvey, 1974), and more recent meteor surveys have succeeded in precisely measuring the pre-atmospheric orbits of high-strength meteoroids from retrograde heliocentric orbits (Borovička et al., 2005). The uncomfortable explanation to date for the origin of these high-strength, high-velocity retrograde meteoroids has been cometary (Borovička et al., 2005), but the puzzle existed as to how macroscopic solid rocky components could be on “cometary” orbits. It had been suggested that comets may have internal inhomogeneity which would account for this population of high-strength retrograde meteoroids (Borovička et al., 2005), but little discussion of this appears in the literature. We propose the simpler explanation that these meteoroids are derived from main belt asteroidal sources. In this scenario, larger (0.01 – 1 km) NEAs are transferred to long-lived retrograde orbits near (but not in) main belt resonances and then serve as targets. The collisional production of fragments off these retrograde NEAs would produce smaller retrograde debris on orbits similar to these parent bodies and this debris would then produce the observed high-strength retrograde meteoroids. This explains both the high-velocity, retrograde orbits as well as the high-strength of these meteoroids better than the ad-hoc cometary source hypothesis.

## **Chapter 5**

# **A Brief Introduction to the Kuiper Belt and Cratering in the Outer Solar System**

### **5.1 Current Structure of the Kuiper Belt**

Similarly to the main asteroid belt, which sits between the orbits of Mars and Jupiter from roughly 2 AU to 3.5 AU, the Kuiper belt provides a reservoir of small bodies that can potentially interact with the giant planets. The Kuiper belt is located beyond to the orbit of Neptune, extending from 30 AU to  $\sim 1,000$  AU with the majority of the classical and resonant populations lying between roughly 30 AU and 85 AU. Pluto is the second-largest (136199 Eris is slightly larger) known Kuiper belt object (KBO), and is located in the 3:2 mean-motion resonance with Neptune at 39.4 AU.

The Kuiper belt is less well understood than the main asteroid belt, largely because of its greater distance from the Earth. After the discovery of Pluto in 1930 by Clyde Tombaugh, it was hypothesized by Edgeworth (1943) that a belt of small bodies should exist beyond the orbit of Neptune. Later, Kuiper (1951) speculated that a similar disk may have existed in the early Solar System. For this

reason, the Kuiper belt is sometimes referred to as the Edgeworth-Kuiper belt. The next discovery (after Pluto) of a Kuiper belt object, 1992 QB<sub>1</sub>, came in 1992 by Jewitt and Luu (1993). Since then,  $\sim 4,500$  KBOs have been discovered, but much of the population remains unseen by telescopic surveys. More historical background on the theoretical understanding of the Kuiper belt can be found in Davies et al. (2008).

Figure 5.1 shows the  $a$ ,  $e$  and  $a$ ,  $i$  distributions of the main classical objects (see definition in Section 5.1.1 below) discovered in the Canada France Ecliptic Plane Survey (CFEPS) (Gladman et al., 2012; Petit et al., 2011). Kuiper belt surveys are biased toward discovering objects with low- $i$  and high- $e$  that are confined to the ecliptic plane and come to small heliocentric distances at perihelion. Currently, debiased surveys are the only method available to determine the intrinsic population of objects in the Kuiper belt. As the number of known KBOs has continued to increase it became clear that the Kuiper belt is divided into dynamical sub-groups; these dynamical sub-populations are described in the next section.

### 5.1.1 Orbital Classification

Gladman et al. (2008) provide a detailed classification scheme for the Kuiper belt sub-populations; their division is as follows. *Resonant* objects are those currently in a mean-motion resonance with Neptune. *Scattering* objects (SOs) are those which over 10 Myr numerical integrations experience encounters with Neptune resulting in a semimajor axis  $a$  deviation of more than 1.5 AU. Scattering objects are thus currently actively scattering off Neptune. The remaining *classical* and *detached* bodies are further sub-divided into the *inner classical objects* ( $a$  interior to the 3:2 mean-motion resonance), *main classical objects* ( $a$  between the 3:2 and 2:1 mean-motion resonances), *outer classical objects* ( $a$  exterior to the 2:1 mean-motion resonance and eccentricity  $e < 0.24$ ), and the *detached* objects ( $a$  beyond the 2:1 mean-motion resonance with  $e > 0.24$ ). Detached objects are probably (but not certainly) those that scattered off Neptune in the past, and thus are on high-eccentricity orbits but no longer actively scatter off Neptune, hence they are

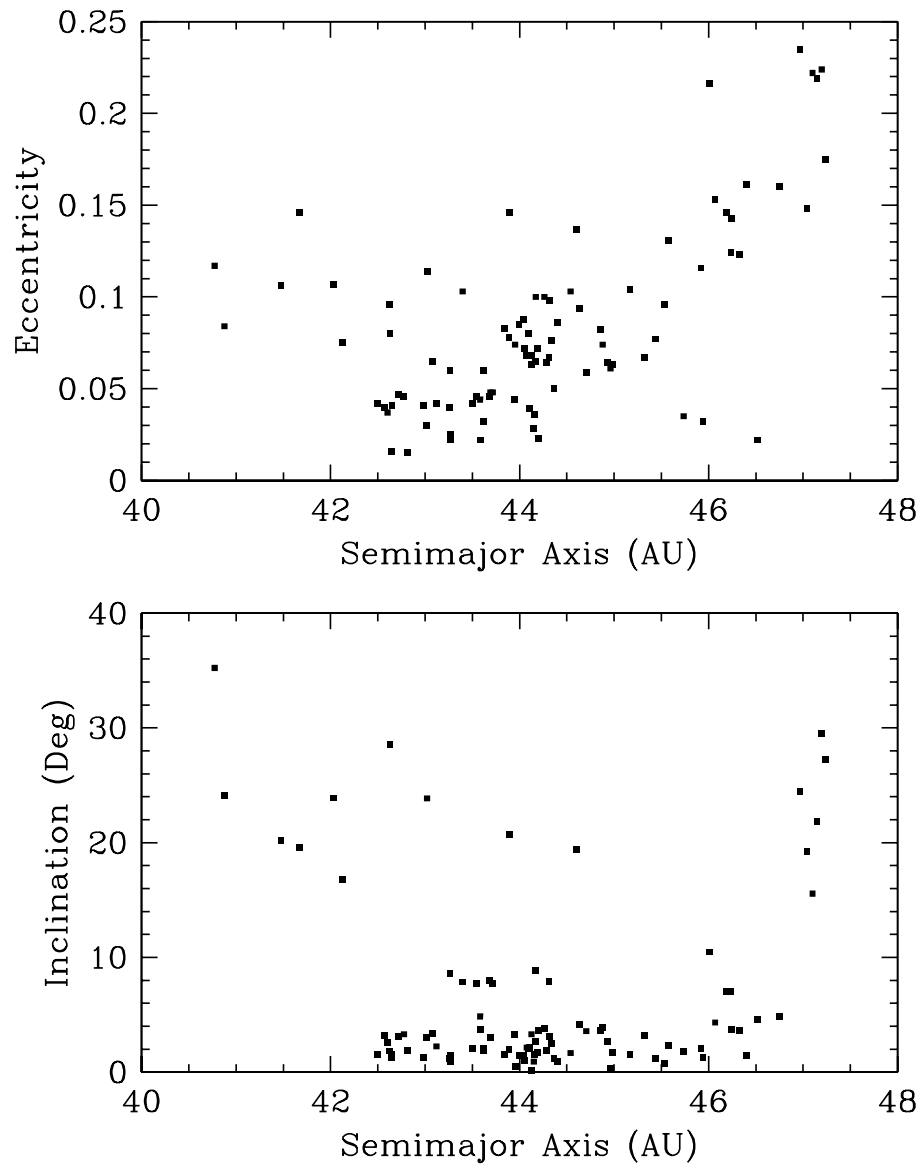


**Figure 5.1:** Orbital distribution for the 93 discovered Kuiper belt main classical objects in the Canada France Ecliptic Plane Survey (CFEPS) (Petit et al., 2011).

detached from Neptune. In Chapter 7, the detached objects are combined with the outer classical objects, since both sub-populations mostly have semimajor axes greater than Pluto’s aphelion ( $a > Q_{Pluto}$ ). The reader is cautioned that in the literature, the term “scattered disk” often refers to objects which have either scattered off Neptune in the past and are now decoupled from Neptune (but have perihelia near Neptune’s aphelion at  $q \approx 30$  AU) or are actively scattering off Neptune currently (i.e., what we define to be the scattering objects (Gladman et al., 2008)). The detached objects are also sometimes referred to as the “extended scattered disk” in the literature (Gladman et al., 2008). Figure 5.2 shows a model of the  $a, e, i$  distribution of the debiased Kuiper belt sub-populations from the Canada France Ecliptic Plane Survey (CFEPS) (Gladman et al., 2012; Kavelaars et al., 2009; Petit et al., 2011) L7-v09 synthetic model. The CFEPS will be further discussed in Section 5.3.1. It is best to think of the Kuiper belt sub-populations as superposed components, similar to the various disk and halo components of our galaxy, where the relationship of the Kuiper belt components to each other is less clear.

The classical main belt (depicted in Figure 5.3) is further subdivided in the CFEPS population definitions (Petit et al., 2011) into hot (wide inclination distribution) and cold (narrow inclination) components, where the cold population contains stirred and kernel sub-components. The hot classical main objects have  $a = 40 - 47$  AU, perihelia  $q = 35 - 40$  AU, and an inclination distribution proportional to  $\sin(i)$  times a Gaussian with a width of  $16^\circ$ . The stirred cold classical objects have  $a = 42.4 - 47$  AU, a  $q$  distribution that is a function of semimajor axis (Petit et al., 2011), and an inclination distribution proportional to  $\sin(i)$  times a Gaussian with a width of  $2.6^\circ$ . Lastly, the kernel sub-component of the cold classical objects have  $a = 43.8 - 44.4$  AU,  $e = 0.03 - 0.08$ , and the same inclination distribution as the stirred cold classical objects. The sub-structure defined by Petit et al. (2011) and shown in Figure 5.2 can be seen in Figure 5.1, with a concentration of objects at  $a \simeq 43.5 - 44$ . AU  $e = 0.03 - 0.08$ , and very low  $i$  that

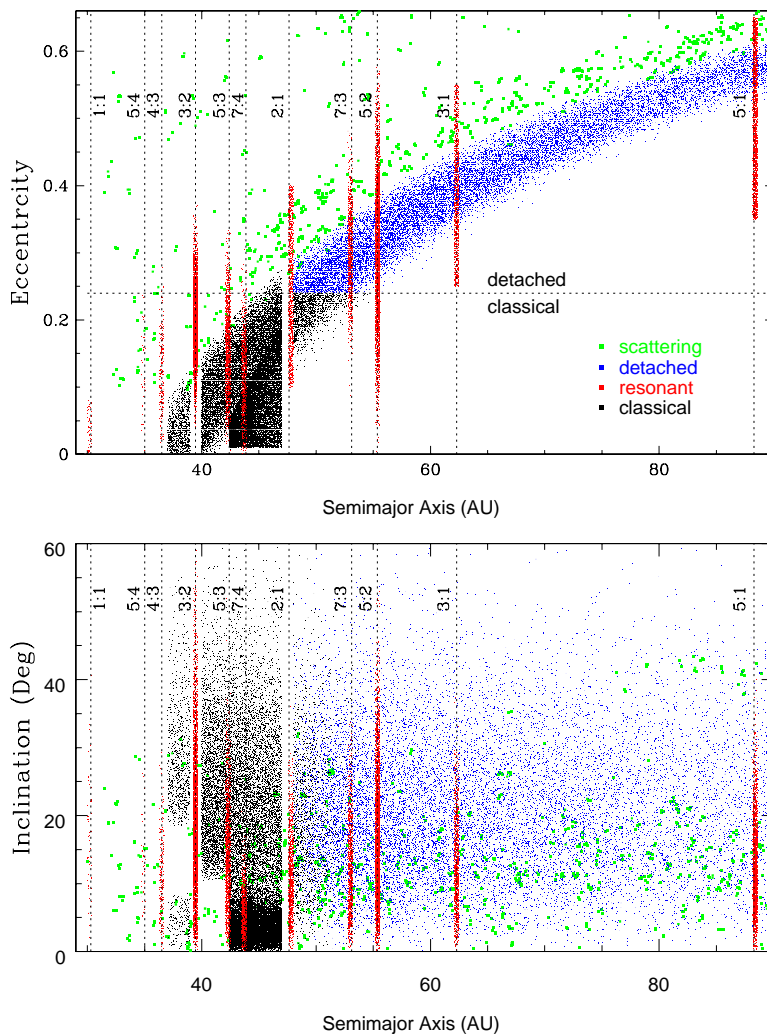


**Figure 5.2:** Debiased Kuiper belt orbital distribution from the Canada France Ecliptic Plane Survey (CFEPS) L7 synthetic model v09 data release (Gladman et al., 2012; Kavelaars et al., 2009; Petit et al., 2011). The dot color denotes the dynamical class of the object. Although the sub-classes of the classical belt are not shown here, the concentration of low- $i$  and low- $e$  points between  $a \simeq 42$  and 47 AU that is the cold classical belt can be seen. The classical belt components are shown in Figure 5.3.

makes up the kernel sub-component of the cold classicals as well as the stirred cold classical and hot main classical sub-populations.

The dynamical boundaries of the Kuiper belt sub-populations are important to determining the impact and cratering rates onto Pluto (and its large moon Charon and four smaller moons – Styx, Nix, Kerberos, and Hydra) because the Pluto system’s heliocentric orbit intersects the Kuiper belt, thus all sub-populations can in principle contribute to the impact flux onto Pluto. The impact and cratering rates onto Pluto and Charon from each of the various Kuiper belt sub-populations are discussed in Chapter 7. Pluto is unique in its impacting populations, because all other cratered bodies studied to date in the outer Solar System, (i.e., the satellites of the four giant planets) are dominantly cratered by the scattering objects that get transferred by Neptune into the giant planet region as Centaurs ( $5 < a < 30$  AU). Cratering of bodies in the outer Solar System will be discussed in Section 5.4.

Centaurs are accepted to have leaked out of the Kuiper belt and scattering region into the giant planet region and can get temporarily captured into resonances with the giant planets as they migrate in semimajor axis  $a$ . The efficiency of transferring escaped main belt asteroids to low- $e$  orbits near Uranus and Neptune is so low that the asteroid belt cannot possibly be the source of these objects. Those objects which get captured into the 1:1 mean-motion resonance with a planet are called co-orbital objects, because they share the same orbital period as a planet. Objects in the 1:1 mean-motion resonance with Neptune can be seen in Figure 5.2 at roughly 30 AU. The frequency and duration of temporary captures into 1:1 resonance with Uranus and Neptune are discussed in Chapter 6.

### **5.1.2 Mean-Motion Resonances in the Kuiper Belt**

It is evident from Figure 5.2 that many objects in the Kuiper belt are located in mean-motion resonances with Neptune. In addition to performing numerical integrations of large numbers of test particles located in the main asteroid belt acting under the gravitational influence of the planets, numerical studies of the Kuiper belt were also being performed in the 1990s (Davies et al., 2008). Contrary to

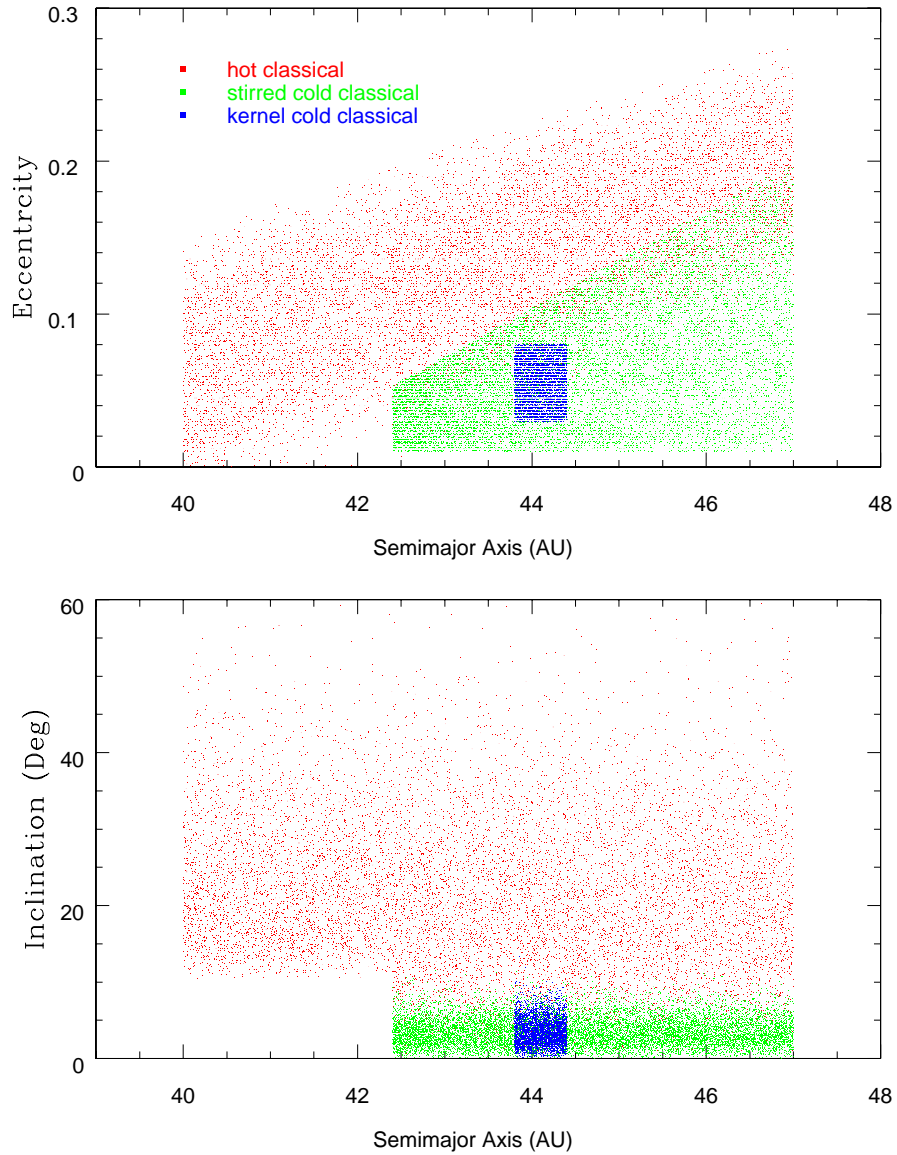


**Figure 5.3:** Debiased Kuiper belt orbital distribution for the classical sub-populations from the Canada France Ecliptic Plane Survey (CFEPS) L7 synthetic model v09 data release (Gladman et al., 2012; Kavelaars et al., 2009; Petit et al., 2011).

the main asteroid belt, the Kuiper belt is less chaotic because the planetary perturbations in this part of the Solar System are weak, causing the longitude of perihelion  $\varpi$  and longitude of the ascending node  $\Omega$  to precess much more slowly than the eigenfrequencies of the Solar System (Morbidelli et al., 1995). Thus, the lack of secular resonances overlapping mean-motion resonances (like in the main asteroid belt) prevents KBOs from leaking out of the Kuiper belt as efficiently as objects in the main asteroid belt. To study the stability of the Kuiper belt, Levison and Duncan (1993) ran numerical integrations of test particles in the theoretical (at the time) Kuiper belt on billion-year timescales and found a great deal of complex structure between 35 and 45 AU at the end of their simulation. At the same time, Holman and Wisdom (1993) ran large-scale numerical integrations of test particles placed between 5 and 50 AU. In addition to finding that the giant planets are efficient at removing particles from their vicinities due to close encounters, they also discovered that objects on initially low- $e$ , low- $i$  orbits out to 42 AU can develop eccentricities large enough to encounter Neptune while remaining at roughly a constant semimajor axis. Morbidelli et al. (1995) began exploring the resonant structure of the Kuiper belt as well as the orbits of the first five known KBOs. Based on preliminary orbits, they found that four of these five objects are currently in mean-motion resonances, three of which are in the 3:2. Today, it is believed that the most populous Neptunian mean-motion resonance is the 3:2 (population estimates can be found in Section 5.3). The relatively high fraction of plutinos among the first discovered KBOs is due to the fact that surveys are biased toward finding the closest objects, thus plutinos at perihelion are more easily visible than classical KBOs and spend more time at perihelion than the large- $a$  scattering objects.

### 3:2 Resonance

The longest known KBO, Pluto, currently sits in the 3:2 mean-motion resonance with Neptune. Pluto is currently on an orbit with  $a \approx 39.3$  AU,  $e \approx 0.24$ , and  $i \approx 17^\circ$ . This orbit puts Pluto's perihelion at  $q \approx 29.7$  AU (its aphelion is  $Q \approx$

48.9 AU) closer to the Sun than the semimajor axis of Neptune. In order for Pluto to be stable on its current orbit, some mechanism is needed to protect it from planetary close encounters with Neptune that could scatter Pluto away. When Pluto was discovered to be on a Neptune-crossing orbit in 1930, it was known that this protection mechanism must exist, but it wasn't until the 1960s when numerical integrations of Pluto and the four giant planets allowed the first look at this protection mechanism (Cohen and Hubbard, 1965).

As discussed in Section 2.2.1, the existence of more than two bodies in the Solar System causes the angular orientation of the orbits of all bodies in the Solar System to change over time at a uniform secular precession rate. If Pluto's orbit did uniformly precess, it would very likely have been kicked onto a scattering orbit by Neptune long ago. However, Pluto is in the 3:2 mean-motion resonance with Neptune, which protects Pluto from planetary close encounters with Neptune, allowing its current orbit to be stable on Gyr timescales. Pluto is also in the Kozai resonance, which causes its argument of pericenter  $\omega$  to librate around  $90^\circ$ . This libration causes Pluto's orbital nodes (where it intersects the plane of the Solar System) to stay within a heliocentric distance of  $\approx 33 - 42$  AU rather than exploring all values between its perihelion at  $q \approx 30$  AU and its aphelion at  $Q \approx 49$  AU. This mechanism further protects Pluto from close encounters with Neptune. As was mentioned above, the 3:2 mean-motion resonance has many objects located within it. These objects are called plutinos after the largest member of the dynamical class. Some of the plutinos also undergo Kozai oscillations (Gladman et al., 2012). In the context of impacts onto Pluto, the affect of Pluto's orbital libration on its collisional probability with the various Kuiper belt sub-populations is discussed in Chapter 7.

### **1:1 Resonance**

As scattering objects interact with Neptune, some can get kicked onto smaller orbits and into the giant planet region ( $5 < a < 30$  AU). Objects can then get captured into resonances located in this region as they migrate in  $a$  due to planetary

close encounters. That is, after a gravitational encounter, the object may find itself at an  $a$  that is resonant with a planet, and the angular variables like  $\omega$  and  $\Omega$  may be such that one or more resonant oscillations may occur.

Objects in the 1:1 mean-motion resonance with a planet are called co-orbitals, having the same orbital period and a librating resonant angle  $\phi_{11} = \lambda - \lambda_{Planet}$ . Here  $\lambda$  is the mean longitude (the sum of the longitude of ascending node  $\Omega$ , the argument of pericenter  $\omega$ , and the mean anomaly  $\mathcal{M}$ ). The resonant angle  $\phi_{11}$  measures roughly<sup>a</sup> how far ahead in its orbit the object is relative to the planet, librating around one of four values (Mikkola et al., 2006) when objects are in co-orbital motion.

Figure 5.4 shows the Lagrange points for a system with a planet orbiting the Sun. In the restricted three-body problem, the Lagrange points mark positions at which a third body of negligible mass can be placed and maintain its position relative to the two massive bodies. An object located at L1, directly between the planet and the Sun would normally have a smaller orbital period than the planet, but is slowed down due to the gravitational pull of the planet to the same orbital period as the planet. An object located at L2 (outside the planet's orbit), conversely, would typically have a higher orbital period than the planet, but is sped up due to the gravitational influence of the planet. L1 and L2 are located at a planet's Hill radius (discussed in Section 2.1.2). Quasi-satellites have  $\phi_{11}$  librate around  $0^\circ$  and appear, in the corotational reference frame, to move around the planet as retrograde satellites even though they are located at several Hill radii away from the planet. L3 is located  $180^\circ$  away from the Earth, and L4 and L5 are located  $60^\circ$  ahead of and behind a planet, respectively, forming an equilateral triangle with the Sun and the planet. A horseshoe co-orbital has a resonant angle  $\phi_{11}$  that librates around L3 with high amplitudes that encompass the L3, L4, and L5 Lagrange points. When a horseshoe co-orbital is on the inner edge of its path in

---

<sup>a</sup>Because  $\phi_{11}$  measures the difference in the *mean* longitudes of the object and planet, only if the object's orbit is a perfect circle would the resonant angle measure exactly how far an object is on its orbit relative to the planet. However, since most small body orbits are ellipses, this is an approximation.

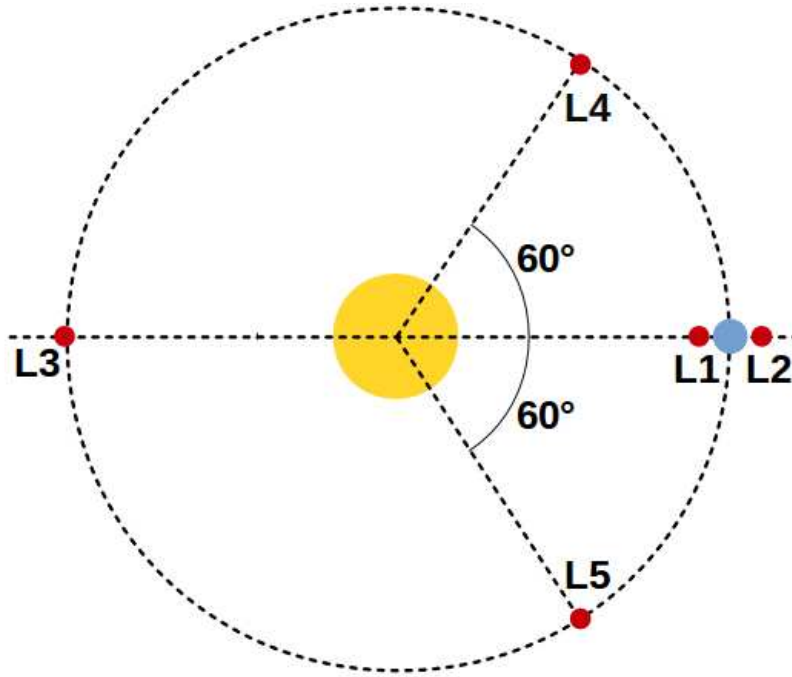


**Figure 5.4:** Schematic of the Lagrange points of a planet-sun system. Quasi-satellites have their resonant angle  $\phi_{11}$  librate around  $0^\circ$ , leading and trailing Trojans librate around L4 and L5, and horseshoe orbits librate around L3 with high amplitudes that encompass the L3, L4, and L5 Lagrange points.

the corotating frame, it is located at a point along its orbit that is closer to the Sun than the Earth. As the object moves to a greater distance from the Sun than the Earth, the horseshoe co-orbital appears to turn around in the corotating reference frame and then moves along the outer edge of its horseshoe path. Trojan objects have  $\phi_{11}$  librate around either L4 or L5, remaining roughly  $60^\circ$  or  $300^\circ$  ahead of the planet, respectively, in the corotating frame.

There are objects known to be in co-orbital motion (of all libration varieties) with several of the planets in the Solar System (Alexandersen et al., 2013), both as long-term stable, presumably primordial (on  $\sim 4$  Gyr timescales) populations and also as temporarily captured co-orbitals. The largest population of co-orbitals

are the roughly 6,000 known Jupiter Trojans, of which the vast majority exhibit long-term stability. Neptune is also known to have a large stable Trojan population. However, the roughly comparable number of stable and unstable Neptunian co-orbitals requires an external source (Alexandersen et al., 2014) for the unstable co-orbitals (i.e., other than stable co-orbitals that are currently becoming dislodged from the co-orbital state) with the scattering TNO population being consistent. Secular and mean-motion resonances located in the giant-planet region inhibit stable co-orbital motion with Saturn and Uranus (Nesvorný and Dones, 2002), although Dvorak et al. (2010) show a stable niche near Uranus where long-term co-orbital motion can be sustained. The frequency and duration of objects temporarily trapped into 1:1 resonance with Uranus and Neptune are discussed in Chapter 6.

## 5.2 Giant Planet Migration in our Solar System

The complex nature of the Kuiper belt, which includes many objects located in mean-motion resonances with Neptune, the excited (moderate- $e$  and moderate- $i$ ) hot component of the main classical belt, and the scattering and detached populations on high- $e$ , high- $i$  orbits, has cosmogonic implications for the early stages of the Solar System. A massive ( $10\text{--}100 M_{\oplus}$ ) disk of planetesimals located from the giant planet region to the outer edge of the primordial Kuiper belt would cause the giant planets to migrate (Saturn, Uranus, and Neptune moving outward and Jupiter moving inward) as they exchange angular momentum with the planetesimal disk, which gets scattered onto high- $e$ , high- $i$  orbits (Fernandez and Ip, 1984; Hahn and Malhotra, 1999). This would imply that the giant planets were originally on more tightly packed, smaller- $a$  orbits than their current orbits. Studies include initial heliocentric distances that range from between roughly 5.2 AU and 27 AU at varying separations (in some works, Neptune is even located inside 15 AU) (Gomes, 2003; Hahn and Malhotra, 1999; Tsiganis et al., 2005).

The migration of the giant planets is instigated by a very large number of close encounters with smaller bodies in the massive planetesimal disk, and is only

halted when Neptune reaches the outer edge of the disk (Gomes et al., 2004). The scattering disk that remains today is believed to be a remnant of a much larger population of scattering objects kicked onto high- $e$ , high- $i$  orbits during the migration of Neptune (Duncan and Levison, 1997). Continued scattering off Neptune has depleted this population by 99% during the past 4 Gyr, after the migrational period ended (Duncan and Levison, 1997). Under this scenario, the detached population are objects that were once scattered off Neptune and then had their perihelia raised due to secular effects (including Kozai) located in mean-motion resonances (Gomes et al., 2008), galactic tides, or gravitational interactions with passing stars, decoupling them from Neptune. It is also possible that Neptune simply had a larger  $e$  which damped (Levison and Morbidelli, 2003) and left formerly coupled particles well past the reduced aphelion distance of Neptune; this is constrained by the current orbital distribution (Batygin et al., 2011; Dawson and Murray-Clay, 2012).

During Neptune’s outward migration, its mean-motion resonances would have also migrated outward through the massive disk of planetesimals. Malhotra (1993) considered Pluto’s capture in the 3:2 mean-motion resonance during this process, and later Malhotra (1995) showed that many pre-existing objects would have been swept up into Neptune’s mean-motion resonances during its outward migration.

Currently, a heavily explored model of giant planet migration in the early Solar System, which aims to reproduce the orbital architecture of the giant planet system (Tsiganis et al., 2005), the capture of the Jupiter (Morbidelli et al., 2005) and Neptune (Tsiganis et al., 2005) Trojan populations, and the triggering of the late heavy bombardment of the terrestrial planets (Gomes et al., 2005), is the Nice model. The Nice model assumes the giant planets were initially located between 5.5 AU and 14 AU with a massive ( $\sim 35 M_{\oplus}$ ) planetesimal disk located from the giant planet region out to  $\sim 34$  AU. Migration of the giant planets is initially slow as they gravitationally interact with the distant, mostly-decoupled massive planetesimal disk. Only a small trickle of planetesimals leave the disk and scatter through the giant planets. Then, Jupiter and Saturn cross their mutual 1:2 mean-

motion resonance, exciting their eccentricities and subsequently the eccentricities of Uranus and Neptune. This triggers chaotic behavior in the ice giants as they rapidly migrate outward into the disk, where eventually their eccentricities are damped back down due to interactions with the abundant planetesimals. When most of the disk has been eliminated and Neptune reaches the outer edge of the disk, the migration stops. The timescale for the initially slow migration of the giant planets lasts for 350 Myr to 1.1 Gyr before Jupiter and Saturn cross their mutual 1:2 resonance. The chaotic period then lasts for only  $\sim 5$  Myr before the planets reach their current orbits, according to the Nice model (Gomes et al., 2008).

The largest difficulty of the Nice model is getting the massive planetesimal disk to last for several hundred Myr without accreting into planets or collisionally grinding itself down into dust before the planets are able to disperse it into the structure we see today. Other issues include keeping both the hot and cold classical populations at low eccentricities (Batygin et al., 2011; Dawson and Murray-Clay, 2012), explaining the color differences between the hot and cold classical populations (Peixinho et al., 2008), and accounting for the large number of binaries found to exist in the cold Kuiper belt (Noll et al., 2008). Thus, a complete picture of the dynamical evolution of the early Solar System has yet to be developed. How the Kuiper belt arrived at its current state is not very important for the rest of this thesis, which is more confined to processes in the current belt. We do, however, assume that the major structures have been in place since  $\simeq 4$  Gyr ago and only slow decay of the existing populations is occurring.

### **5.2.1 Population Decay**

Since the time of giant planet migration, the sub-populations of the Kuiper belt have dynamically depleted over the past  $\approx 4$  Gyr at differing rates due to their differing orbital parameters. The scattering objects have dynamically eroded due to continued gravitational interactions with Neptune. As Neptune scatters them to larger eccentricities, they can eventually scatter off the other giant planets. As

Dones et al. (2004) show, the giant planets can deplete the scattering disk, ejecting them or depositing some into the Oort cloud at  $a = 10,000 - 100,000$  AU. (Scattering objects that get kicked onto very high- $e$  orbits by the giant planets can then have their perihelia increased due to galactic tides and gravitational interactions with passing stars.)

The classical Kuiper belt is slowly depleted due to the presence of the  $\nu_8$  secular resonance and the overlapping  $\nu_{17}$  and  $\nu_{18}$  resonances located in the classical belt (Hahn and Malhotra, 2005; Kuchner et al., 2002; Lykawka and Mukai, 2005). Objects which enter these resonances can have their eccentricities and inclinations raised, eventually pulling them out of the classical belt. Objects located in or on the borders of the mean-motion resonances within the Kuiper belt can also chaotically diffuse (Morbidelli, 1997) out of the resonances over time (Hahn and Malhotra, 2005; Tiscareno and Malhotra, 2009).

These effects are small compared to similar processes in the highly-chaotic main asteroid belt, but are not negligible over Gyr timescales. Quantitative measurements from the literature of the decay rates for each of the Kuiper belt sub-populations can be found in Section 7.2.5.

### 5.3 Size Distributions of Kuiper Belt Sub-Populations

In order to quantify the number of objects in the Kuiper belt sub-populations today, the size distribution must be measured. Unfortunately, the size distribution is not well measured for objects with absolute g-band magnitude  $H_g > 9.16$  (corresponding to a diameter  $d < 100$  km for an assumed g-band albedo  $p$  of 5%), which obeys the relation:

$$d \simeq 100 \text{ km} \sqrt{\frac{0.05}{p}} 10^{0.2(9.16-H_g)} \quad (5.1)$$

Section 2.3, equation (2.6) defines the differential number of objects  $N$  as a function of  $H$ -magnitude as well as the differential distribution in diameter  $d$  given

in equation (2.7). The Kuiper belt size distribution was recently absolutely calibrated down to  $H_g \approx 8-9$  by the CFEPS survey (Gladman et al., 2012; Petit et al., 2011). The  $H_g = 4 - 9$  range seems well modeled by a single slope  $\alpha$  in a given population. The only caveat to this would be the hot and cold components of the main classical Kuiper belt sub-populations appear to have different values of  $\alpha$ . The bright end of the Kuiper belt size distribution has values in the literature ranging from 0.66–0.90 for the hot classical sub-population and 1.2–1.36 for the cold component of the classical objects (Adams et al., 2014; Bernstein et al., 2004; Fraser et al., 2014; Petit et al., 2011).

It is clear in the literature that a single power law extended past  $H_g = 9$  does not fit the observations and that a break in the differential size distribution at this  $H_g$ -magnitude is required (Bernstein et al., 2004; Fraser et al., 2014; Fraser and Kavelaars, 2008; Fuentes and Holman, 2008; Shankman et al., 2013). In any case, a slope with  $\alpha > 0.6$  cannot continue as its mass would diverge; a transition to a shallower slope is required (Gladman et al., 2001). The break is discussed in the literature as either having the form of a knee, which has a sudden change in the differential number of objects from a steep slope at the bright end to a shallower slope at the faint end (Fraser and Kavelaars, 2008; Fuentes and Holman, 2008), or in the form of a divot, which has a sudden drop in the differential number of objects that recovers to a shallower slope (Shankman et al., 2013). Values for  $\alpha_{faint}$  vary between 0.2 to 0.6 across various outer Solar System small body populations (Larsen et al., 2001; Schlichting et al., 2013; Solonoi et al., 2012; Szabó et al., 2007; Trujillo et al., 2001) as well as the Kuiper belt size distribution literature (Bernstein et al., 2004; Fraser et al., 2014; Fraser and Kavelaars, 2008, 2009; Fuentes and Holman, 2008; Shankman et al., 2013) down to the observational limit of  $H_g \approx 8 - 10$  for the various sub-populations.

As in the main asteroid belt (O’Brien and Sykes, 2011), the analysis of saturnian craters used to infer the size distribution of the impacting scattering object population by Minton et al. (2012) and the model for the collision-generated pop-

ulation of KBOs today from Schlichting et al. (2013) both indicate that several sequential slope transitions in the size distribution occur as one drops below roughly  $H_g \approx 8 - 10$  and continues to the sub-km regime. The observed size distribution of the Jupiter Family Comets (JFCs), which were likely supplied from the scattering population (Duncan and Levison, 1997), in Solonoi et al. (2012) was found to have a break in the size distribution at  $H \approx 14.5$  from a steep  $\alpha = 0.73$  slope to a shallower  $\alpha = 0.19$  slope, in corroboration with the idea that the Kuiper belt’s size distribution is “wavy” like the main asteroid belt’s.

In Chapter 7, various values of  $\alpha$  and the shape of the Kuiper belt size distribution are used to explore their implications for Pluto’s cratering record in anticipation of the New Horizons fly-through of the Pluto system in July 2015. The difficulties and uncertainties inherent in the surveys and theoretical work of the size distribution as well as the origin of a knee or divot in the size distribution is not critical to this thesis. Size distributions from the literature are simply used to illustrate uncertainties inherent in crater production rates on Pluto.

### 5.3.1 Population Estimates of Kuiper Belt Objects

Petit et al. (2011) and Gladman et al. (2012) provide  $d > 100$  km ( $H_g = 9.16$  for g-band albedo  $p = 5\%$ ) population estimates for the classical and resonant population from the CFEPS (see Table 5.1). In Chapter 7, in order to pin the number of objects in each of the various Kuiper belt sub-populations to the  $H_g$ -magnitude corresponding to the break in the size distribution (at  $H_g = 9.0$ ), the CFEPS  $H_g < 9.16$  classical and resonant population estimates from Petit et al. (2011) and Gladman et al. (2012) were converted to  $H_g < 9.0$  (which corresponds to diameter  $d > 108$  km for  $p = 5\%$ ) population estimates using a minor multiplicative tuning of

$$\frac{N(< H_g = 9.0)}{N(< H_g = 9.16)} = 10^{(0.8(H_g - 9.16))} = 10^{(0.8(9.0 - 9.16))} = 0.745 \quad (5.2)$$

Population	$N(d \geq 100 \text{ km})$
Scattering Objects	$105,000 \pm 31,500$
Inner Classical	$3,000^{+3,500}_{-2,000}$
Hot Main Classical	$35,000^{+8,000}_{-7,000}$
Cold Main Classical	$95,000^{+22,000}_{-20,000}$
Outer Classical/Detached	$80,000^{+60,000}_{-40,000}$
3:2 Resonance	$13,000^{+6,000}_{-5,000}$
5:2 Resonance	$12,000^{+15,000}_{-8,000}$
4:3 Resonance	$800^{+1,100}_{-600}$
5:3 Resonance	$5,000^{+5,200}_{-3,000}$
7:3 Resonance	$4,000^{+8,000}_{-3,000}$
5:4 Resonance	$160^{+700}_{-140}$
7:4 Resonance	$3,000^{+4,000}_{-2,000}$
2:1 Resonance	$3,700^{+4,400}_{-2,400}$
3:1 Resonance	$4,000^{+9,000}_{-3,000}$
5:1 Resonance	$8,000^{+34,000}_{-7,000}$

**Table 5.1:** Kuiper belt classical and resonant sub-population estimates for  $d \geq 100$  km from the debiased Canada France Ecliptic Plane Survey (CFEPS) (Gladman et al., 2012; Petit et al., 2011) and scattering object estimate for  $d \geq 100$  km from Shankman et al. (2013).

In Table 5.1, the  $d > 100$  km ( $H_g = 9.16$ ) population estimates for the classical and resonant populations from the CFEPS provided by Petit et al. (2011) and Gladman et al. (2012) are given along with the scattering object population estimate from Shankman et al. (2013) using the Kaib et al. (2011) model of scattering objects, which has been converted from  $H_g = 9.0$  to  $H_g = 9.16$  using equation 5.2.

The scattering objects observed by the CFEPS only effectively sample the orbital distribution of the closest objects, which must then be extrapolated to larger distances. The Kaib et al. (2011) (KRQ11) model provides a much more accurate representation of the scattering population as it evolves from the Oort Cloud; it is thus the current model of choice for the orbital distribution of the scattering ob-

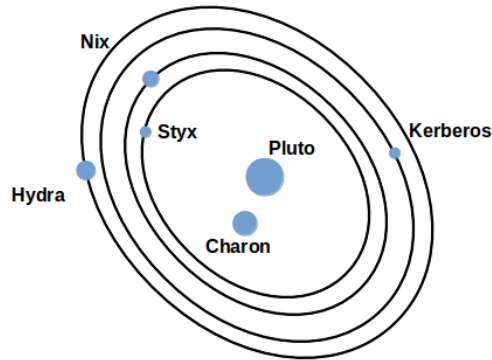


**Figure 5.5:** Schematic of the Pluto system. The tidally locked Pluto-Charon binary has four satellites: Styx, Nix, Kerberos, and Hydra.

jects and was coupled to the CFEPS to produce the absolutely-calibrated  $H_g < 9.0$  population estimates of the scattering population (of 80,000) by Shankman et al. (2013). Estimates from the Deep Ecliptic Survey (Adams et al., 2014) for some sub-populations were discrepant from the CFEPS estimates (Gladman et al., 2012; Petit et al., 2011) by factors of 1.5 to 1.7, but the surveys were acquired in different bandpasses; compiling the  $g$ -VR colors of objects seen in both surveys (K. Volk, private communication 2015) showed that colors of 0.4-0.6 (rather than 0.1) were appropriate and this eliminates virtually all discrepancy in the  $H$ -magnitude range common to both surveys when using the same dynamical-class definitions.

## 5.4 Cratering in the Outer Solar System

As mentioned above, the work presented in Chapter 7 uses the population estimates and orbital distributions of the various Kuiper belt sub-populations to compute impact and cratering rates onto Pluto and its moons in anticipation of the New Horizons fly-through in July 2015.

The Pluto system consists of the tidally locked Pluto-Charon binary as well as four smaller satellites: Styx, Nix, Kerberos, and Hydra, in order of increasing

Name	Discovery Year	Diameter (km)	$a$ ( $R_{Pluto}$ )	$P$ (days)	NH resolution (km)
Pluto	1930	$\approx 2400$	$\approx 1.7$	6.4	0.5
Charon	1978	$\approx 1200$	$\approx 17$	6.4	0.5
Styx	2012	$\approx 10$	$\approx 35$	20	3
Nix	2005	$\approx 45$	$\approx 40$	25	0.5
Kerberos	2011	$\approx 10$	$\approx 48$	32	3
Hydra	2005	$\approx 45$	$\approx 54$	38	1

**Table 5.2:** Pluto system characteristics. Radius estimates for the four smaller satellites are computed using mass, albedo = 0.4, and density estimates from Kenyon and Bromley (2014). Semimajor axis estimates relative to the Pluto-Charon barycenter are from Showalter and Hamilton (2015). The period for Pluto and Charon is their spin-orbit period and for the four satellites is their orbital period. All eccentricities are  $e < 0.01$  and all inclinations (relative to Pluto’s equator) are  $i < 1^\circ$ . Now that the final New Horizons fly-by geometry has been determined, the resolution of craters on the four smaller satellites has been calculated and is provided for the encounter hemispheres of each body.

distance from Pluto (a schematic of the system is shown in Figure 5.5). Table 5.2 provides physical and orbital characteristics for Pluto system. The image resolutions of the New Horizons spacecraft for the encounter hemispheres of each body, based on the final fly-by geometry, are listed in the final column of the table.

The first images of cratered surfaces in the outer Solar System came from the Voyager spacecraft in the late 1970s to the late 1980s. Of the four large moons of Jupiter, Ganymede and Callisto were observed to have heavily cratered surfaces. Io and Europa have little to no craters due to tidal heating that erases craters on their surfaces. Though Callisto is heavily cratered globally, Ganymede shows some areas of heavy cratering while other areas appear to be wiped clean due to past tidal heating effects.

Saturn’s large moons (Mimas, Enceladus, Tethys, Dione, Rhea, Titan, and Iapetus – in order of increasing distance from Saturn) show varying degrees of

cratering on their surfaces. Mimas and Tethys both exhibit a very large crater roughly one-third of their diameters as well as many smaller craters covering their surfaces. Enceladus, which sits between Mimas and Tethys, is currently geologically active, harboring a system of fractures in its southern region which emit jets of water vapor and dust. Tethys, Dione, and Rhea (each exhibiting cratered surfaces) show a difference in surface brightness between their leading and trailing hemispheres in images from the Cassini spacecraft, indicating that particles emitted from Enceladus' surface are coating the leading hemispheres of these satellites. Saturn's largest moon, Titan shows evidence of volcanic activity that erases craters on its surface. The farthest large moon from Saturn, Iapetus, exhibits an ancient surface of craters, and is thus of greatest interest.

Uranus has no major moons upon which to study craters, and Neptune has only one large moon, Triton, which clearly has had recent geologic activity due its sparsity of craters.

The outer Solar System satellites are all dominantly cratered by scattering objects that have perihelia in the giant planet region. The current location of Pluto in the Kuiper belt causes it to be cratered by a wider variety of sub-populations than all other cratered bodies studied in the outer Solar System to date. This makes the crater fields in the Pluto system of great interest, especially because at their smallest end one will be sampling Kuiper belt projectiles probed nowhere else yet in the Solar System and beyond the reach of direct observation by telescopes.

The crater scaling laws are traditionally written as equations (5.3), (5.4a), and (5.4b) from Zahnle et al. (2003) and convert an impactor diameter  $d$  into a crater diameter  $D$  given an impact velocity  $U$ , the gravitational acceleration  $g$  of the target, the densities  $\delta$  and  $\rho$  of the impactor and target (respectively), and a transition diameter  $D_{tr}$  (in km) from simple to complex craters (where we take  $\xi = 0.108$  from McKinnon and Schenk (1995) as estimated from the craters on the icy satellites of Jupiter).

$$D_s = 11.9 \left( \frac{U}{\text{km/s}} \right)^{0.434} \left( \frac{g}{\text{cm/s}^2} \right)^{-0.217} \left( \frac{\delta}{\rho} \right)^{0.333} \left( \frac{d}{\text{km}} \right)^{0.783} \text{ km} \quad (5.3)$$

and

$$D = \begin{cases} D_s & \text{for } D_s < D_{tr} \\ D_s (D_s/D_{tr})^\xi & \text{for } D_s > D_{tr} \end{cases} \quad (5.4a)$$

$$(5.4b)$$

It is clear from the crater scaling law that assumptions about the surface composition of Pluto will affect cratering calculations. Compared to a water-ice surface, craters formed entirely in solid  $N_2$  (similar density) or  $CH_4$  (lower density) will result in the simple crater diameter  $D_s$  corresponding to a given impactor diameter  $d$  increasing by up to 24% (for a  $CH_4$  density of  $\rho = 0.52 \text{ g/cm}^3$  (Lupo and Lewis, 1980)). In addition, the simple-to-complex transition in these weak materials may occur at a smaller diameter, increasing the size of a complex crater over that given in equation (5.4b). The unknown depth of regolith on the surface of Pluto, which could range from tens of m to several km thick, could plausibly also affect the transition diameter. Whether craters in volatile  $N_2$  and  $CH_4$  ice can survive intact on Pluto's surface for 4 Gyr or whether viscous relaxation would lead to poor crater retention on Pluto is an open question (Stern et al., 2015). The effect of atmospheric recondensation could also affect crater retention on Pluto (Stern et al., 2015).

The scaling law shown above is not the only one used in the literature. The slightly different crater scaling law from Housen and Holsapple (2011) (and used by Bierhaus and Dones (2015)) shown in equation (5.5) was developed from laboratory experiments studying the subsonic ejecta (and thus secondaries) produced during the crater formation process into sand-like material. This crater scaling law results in approximately 3% smaller simple crater diameters than those computed from the crater scaling laws (equations (5.3), (5.4a), and (5.4b)) in Zahnle et al. (2003), developed for solid, non-porous geological materials.

$$D_s = 9.3 \left( \frac{U}{\text{km/s}} \right)^{0.374} \left( \frac{g}{\text{cm/s}^2} \right)^{-0.187} \left( \frac{\delta}{\rho} \right)^{0.325} \left( \frac{d}{\text{km}} \right)^{0.813} \text{ km} \quad (5.5)$$

The lower limit on cratering efficiency is given by porous, “sand-like” scaling, which gives somewhat smaller craters overall. The scaling in Housen and Holsapple (2011) (and used by Bierhaus and Dones (2015)) could apply to the smallest craters likely to be seen on Pluto, those formed entirely within Pluto’s regolith, which will slightly affect the slope of the crater production function, all other things being equal, unless saturation occurs at the scales in question, in which case it will not matter. For the broad range of crater sizes discussed in Chapter 7, the crater scaling laws from Zahnle et al. (2003) that include the simple-to-complex transition (shown above) are applied in this thesis. In principle, however, one could use the observed transition diameter to learn something about the physical properties of Pluto’s surface.

A caveat to applying these equations to the Pluto system is that the physics of crater creation and the crater scaling laws have been studied mostly for the icy galilean and saturnian satellites. For these bodies, typical impact speeds range from 10–20 km/s (in the hypervelocity regime), because heliocentric orbital speeds are higher and impactors get more gravitational focussing from the giant planets than in the Kuiper belt, where impact speeds are typically 1–2 km/s (potentially sub-hypervelocity). Hypervelocity is reached when the impact speed exceeds the speed of sound in the target surface material; the sound speed in water-ice is approximately 3 km/s and up to roughly 40% higher for a solid CH<sub>4</sub> ice surface assuming a density of 0.52 g/cm<sup>3</sup>. Thus, applying crater scaling laws developed for the icy satellites of the giant planets to primary craters in the sub-km-diameter to a-few-hundred-km-diameter range on Pluto may incorrectly convert impact rates into cratering rates. However, given that the crater scaling laws have not been rigorously developed for the subsonic regime, the best way forward is to apply the above crater scaling laws. In addition, Singer et al. (2013) (their Appendix A) argue that existing scaling laws may be extrapolated to even lower speeds (those of secondary crater formation) as long as the Hugoniot elastic limit is exceeded, which is well satisfied for primary impacts on Pluto and Charon.

The uncertainties in the crater scaling law and their application to cratering in the Pluto system will affect the conclusions that can be drawn from estimating impact and cratering rates onto Pluto and its satellites. However, these uncertainties are dwarfed by the uncertainties in how the Kuiper belt size distribution extends to diameters below 100 km (outlined above in Section 5.3). This will be discussed in greater detail in Chapter 7.

# Chapter 6

## A Uranian Trojan and the Frequency of Temporary Giant-Planet Co-Orbitals

### 6.1 Discovery of the First Uranian Trojan

The first known Uranian Trojan, 2011 QF<sub>99</sub>, was discovered in the 32-square-degree survey of Alexandersen et al. (2014), designed to detect Trans-Neptunian Objects (TNOs) and objects between the giant planets ( $a_{Jupiter} < a < a_{Neptune}$ ) known as Centaurs with apparent r-band magnitude  $m_r < 24.6$ , using the Canada-France-Hawaii Telescope (Alexandersen et al., 2013). The low eccentricity along with a semimajor axis similar to that of Uranus ( $a_U \approx 19.2$  AU) indicated that 2011 QF<sub>99</sub> might be a Uranian co-orbital. Numerical integrations of the nominal orbit and all other orbits within the small orbital uncertainties indicated the object was most likely a Centaur temporarily trapped as a L4 Uranian Trojan (Alexandersen et al., 2013) (see Figure 6.1; left column).

---

This chapter is based on the following published work: M., Alexandersen, B. Gladman, S. Greenstreet, J. J. Kavelaars, J.-M. Petit, S. Gwyn, *A Uranian Trojan and the Frequency of Temporary Giant-Planet Co-Orbitals*, *Science* **341**,994 (2013).

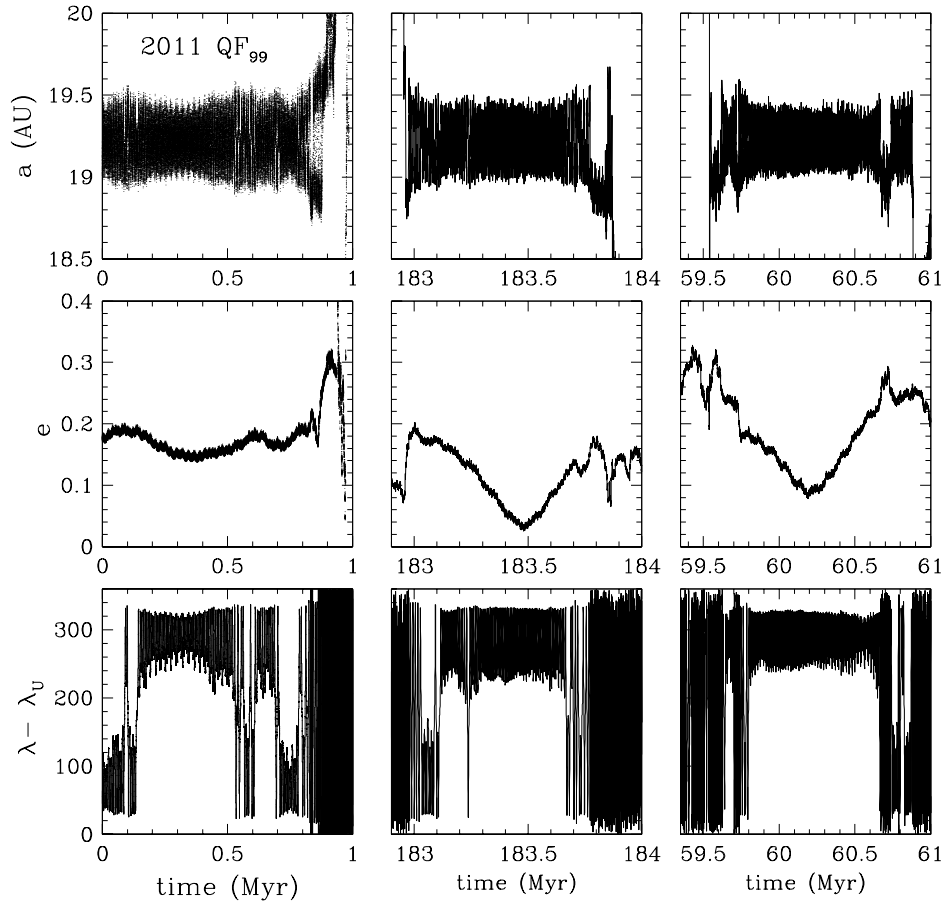


**Figure 6.1:** Left column: Evolution of the nominal semimajor axis  $a$ , eccentricity  $e$ , and resonant angle  $\phi_{11} = \lambda - \lambda_U$  of 2011 QF<sub>99</sub> for 1 Myr into the future. Center and right columns: Evolution for two temporary ( $\sim 1$  Myr duration) Uranian co-orbitals from our dynamical simulations for intervals in which their evolution is similar to that of 2011 QF<sub>99</sub>, showing that Centaurs can naturally become temporarily-trapped Uranian Trojans. Times are from the initial condition for the  $a_0 > 34$  AU scattering orbit.

In this survey, 2011 QF<sub>99</sub> was the only object with a semimajor axis within the planetary region (defined here as  $a < 34$  AU to include Neptune co-orbitals but exclude the exterior stable transneptunian populations). The Canada-France Ecliptic Plane Survey (CFEPS) detected three  $a < 34$  AU objects and the IAU Minor Planet Center (MPC) database contains 247 objects with  $6 \text{ AU} < a < 34 \text{ AU}$  as of 9 July 2013. We seek to estimate the steady-state fraction of Centaurs in temporary co-orbital states with Uranus and Neptune, similar to what has been done for the Earth (Morais and Morbidelli, 2002) and Venus (Morais and Morbidelli, 2006).

## 6.2 Numerical Integrations

Using a model of the orbital distribution (Kaib et al., 2011) (KRQ11) of today’s scattering TNOs, we simulated the interactions of scattering objects with the giant planets over 1 Gyr, building a relative orbital distribution for the  $a < 34$  AU region. The simulation outputs the state vector of planets and all  $a < 34$  AU particles at 300 yr intervals. This output interval was chosen so that the few-kyr variation of the resonant argument  $\phi_{11}$  would be well sampled (see Section 6.2.1), allowing detection of short-term co-orbitals of the giant planets. Such a meticulous search for co-orbitals trapped from an armada of incoming scattering objects is essential in order to accurately estimate the trapping fraction. An earlier analysis (Horner and Evans, 2006) started with a sample of currently known Centaurs, which was biased towards the lowest- $a$  Centaurs by observational selection, resulting in much lower trapping rates for Uranus and Neptune than we find (see Section 6.3).

The dynamical integrations computed to model the steady-state distribution of scattering objects in the  $a < 34$  AU region for this work were set up using a subset of particles from the Kaib et al. (2011) TNO population model. Here, “scattering objects” (Gladman et al., 2008; Petit et al., 2011) are those that experience  $\Delta a > 1.5$  AU in 10 Myr; scattering objects with  $a < 30$  AU are called “Centaurs”, whereas those with  $a > 30$  AU are the “scattering disk”. We use the term

“steady-state” only to refer to a constant relative distribution of objects (i.e., the distribution of Centaurs being constant, and thus the co-orbital fraction being constant), not to denote a constant absolute population, as the population of scattering disk objects is depleting on Gyr time scales (for more discussion of the different depletion rates for each Kuiper belt sub-population, see Section 7.2.5). This subset consisted of 17,800 particles with initial semimajor axes  $34 \text{ AU} < a < 200 \text{ AU}$  and that had their semimajor axes deviate by more than 1.5 AU during the last 10 Myr of the KRQ11 model integrations. This population of scattering TNOs was used as the initial conditions for the orbital integrations in this work. Two different KRQ11 models were used independently: one generated from a primordial inclination distribution that was dynamically cold when the particles left the giant planet region 4 Gyr earlier (the “cold” model) (Kaib et al., 2011), the other using an initially hot distribution (the “hot” model) integrated in the same way as the KRQ11 model (Shankman et al., 2013).

To perform this computation, we used the N-body code SWIFT-RMVS4 (provided by Hal Levison, based on the original SWIFT (Levison and Duncan, 1994)). A base time step of 73 days was used and the orbital elements were output every 300 years for any particle which at that moment had  $a < 34 \text{ AU}$ . The gravitational influences of the four giant planets were included. Particles were removed from the simulation when they hit a planet, went outside 2,000 AU or inside 6 AU from the Sun (resulting in rapid removal from the Solar System by Jupiter), or the final integration time of 1 Gyr was reached.

The goal of these orbital integrations was twofold: to search for temporary co-orbital trapping and to construct the steady-state orbital distribution of scattering TNOs that reach the giant planet region, chosen to be the  $a < 34 \text{ AU}$  region. The steady-state orbital distribution is expressed as a grid with  $a < 34 \text{ AU}$ ,  $e < 1.0$ ,  $i < 180^\circ$ , with cells of volume  $0.5 \text{ AU} \times 0.02 \times 2.0^\circ$ . The cumulative time spent by all particles in each cell is normalized to the total time spent by all particles in all cells in the  $a < 34 \text{ AU}$  region. This illustrates the steady-state distribution of objects in the  $a < 34 \text{ AU}$  region, shown in Figure 6.2, supplied by the scatter-

ing TNO population. This residence time probability distribution (Bottke et al., 2000a) can be interpreted as the steady-state fraction of scattering TNOs in each cell. Figure 6.2 shows two projections of the residence time probability distributions of the  $a < 34$  AU region for the two KRQ11 population models. From these plots it is clear the scattering TNO population enters the giant planet region ( $a < 34$  AU) at moderate eccentricities and inclinations. Although the hot model does produce higher inclinations, it is clear from Figure 6.2, that the choice of input model does not make a large difference for our results. We therefore only describe results from the simulations using the KRQ11 “hot” model here (unless otherwise noted).

### 6.2.1 Co-Orbital Detection in Numerical Integrations

To diagnose whether particles are co-orbital, the orbital history (at 300 year output intervals) was scanned using a running window 30 kyr long. This window-size was chosen to be several times longer than the typical Trojan libration period. While the formal definition of co-orbital is that the resonant angle  $\phi_{11} = \lambda - \lambda_{Planet}$  librates, detecting this is difficult to automate. As an automatic process is necessary to filter the large amounts of output from our dynamical simulations (110 GB), we used a simpler algorithm which we believe diagnoses co-orbitals well. A particle was classified as a co-orbital if, within the running window, both its average semimajor axis was less than 0.2 AU from the average semimajor axis of a given planet and no individual semimajor axis value deviated more than  $R_H$  (see equation 2.1) from that of the planet. Here  $R_H$  is the planet’s Hill-sphere radius (Murray and Dermott, 1999), where  $R_H = 0.47$  AU for Uranus and  $R_H = 0.77$  AU for Neptune. If these criteria were met, the orbital elements and current integration time for that particle (at the time-center of the window) were output to indicate co-orbital motion in that window. The window center then advances by a single 300-year output interval and performs the diagnosis determination again. In this manner, consecutive identifications of a particle in co-orbital motion with a planet can be recorded as a single “trap” until the object is scattered away. A minor

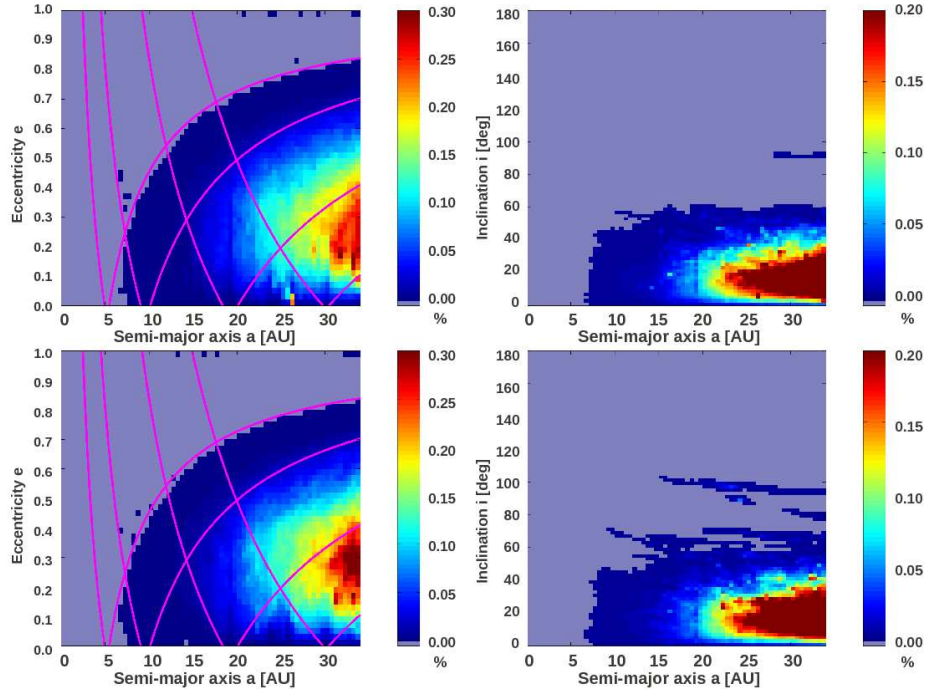


**Figure 6.2:** Residence time probability distributions. The top and bottom plots show the distribution resulting from the initially cold and hot KRQ11 models, respectively; the two different initial populations clearly produce very similar  $a < 34$  AU steady-states. To monitor the orbital evolution of each particle, a grid of  $a, e, i$  cells was placed throughout the giant planet region from  $a < 34$  AU,  $e < 1.0$ , and  $i < 180^\circ$  with volume  $0.5 \text{ AU} \times 0.02 \times 2.0^\circ$ . The  $a, e$  plot is summed over  $i$ , and the  $a, i$  plot is summed over  $e$ . The color scheme represents the percentage of the steady-state Centaur population contained in each bin; red colors represent cells where there is a high probability of particles spending their time. The curves indicate Jupiter, Saturn, Uranus, and Neptune crossing orbits.

shortcoming of this method of co-orbital identification is that the beginning and end of each trap is not diagnosed well due to the ends of the window not falling entirely within the trap at these times. This method provides us with estimates of the duration of traps, each of which must be greater than 30 kyr to be diagnosed by this analysis.

### 6.2.2 Resonant Island Classification

For each time step a particle has been deemed co-orbital, we wish to determine in which of the four resonant islands the particle is librating, i.e. whether it is a horseshoe, L4 Trojan, L5 Trojan, or quasi-satellite. As our co-orbital detection algorithm (described above) produces  $\sim 25,000$  trapping episodes, these cannot be inspected manually and require another automated process. As for the detection algorithm, this is also hard to automate, especially because complex variations and combinations can exist for high inclinations. For our classification algorithm, we examine the behavior of the resonant angle ( $\phi_{11} = \lambda - \lambda_p$ ) in each 30 kyr window. If  $\phi_{11}$  remained in the leading or trailing hemisphere during a window, we assigned the particle to the L4 or L5 state (respectively). If  $\phi_{11}$  crosses  $180^\circ$  at any time during the interval, then it was labelled a horseshoe orbit. The remaining objects are assumed to be quasi-satellites, as they must be co-orbitals that cross between leading and trailing at  $\phi_{11} = 0^\circ$  and not at  $180^\circ$ . The possibility of erroneous classification exists, however in a manually inspected subset we find these errors affect  $\ll 10\%$  of cases, thus not affecting our co-orbital fraction and resonant island distribution estimates greatly, sufficient for our goal of better than factor of two accuracy.

## 6.3 Frequency and Duration of Temporary Giant-Planet Co-Orbitals

Simulated scattering objects predominantly entered the giant planet region ( $a < 34$  AU) at intermediate inclinations and eccentricities, as has been previously

shown (Levison and Duncan, 1997; Tiscareno and Malhotra, 2003). After analyzing the particle histories to find co-orbital trapping, we find that 0.4% and 2.8% of the  $a < 34$  AU population is, at any time, in co-orbital motion with Uranus and Neptune, respectively (with less than a factor of 2 variation). This 3.2% fraction is much larger than the  $\approx 0.1\%$  of near-Earth asteroids temporarily trapped in Earth and Venus co-orbital motion (Morais and Morbidelli, 2002, 2006), presumably due to the fractionally larger co-orbital regions of the giant planets. We find that the simulated Uranian and Neptunian co-orbitals consisted of, respectively, 64% and 54% in horseshoe orbits, 10% and 10% quasi-satellites and 26% and 36% Trojans, roughly equally distributed between the L4 and L5 clouds. The duration of Uranian co-orbital captures in our simulations had mean, median, and maximum values of 108 kyr, 56 kyr, and 2.6 Myr, respectively, and 78 kyr, 46 kyr, and 18.2 Myr, respectively, for Neptune. The median co-orbital capture duration is roughly only twice the running window size (30 kyr), which means there are many captures that last between 30 and 60 kyr.

To confirm that our Centaur distribution is in fact in steady-state (fractionally, not absolutely), we divide our 1 Gyr integrations into  $< 100$  Myr and  $100 - 1,000$  Myr intervals. The  $< 100$  Myr interval contains about half (cold model) or one-third (hot model) of all entries into the  $a < 34$  AU regime. In all four cases the fraction of temporary co-orbitals is the same (0.31 – 0.62% for Uranus and 2.3 – 3.3% for Neptune) to well within a factor of 2 accuracy and the distribution of Centaurs are all similar to those seen in Figure 6.2. We thus believe this justifies treating the relative distribution of objects as being time independent, despite the absolute scattering/Centaur population slowly decreasing.

Numerical integrations of known Centaurs have previously been performed (Horner and Evans, 2006) in order to study the capture of Centaurs as temporary co-orbitals of the giant planets. That study found that captures are generally short (10 – 100 kyr, none greater than 500 kyr) with 0.29% of 23,328 Centaur clones experiencing a co-orbital capture during a 3 Myr simulation, of which 15%, 80%, 5% and 0% of these captures occur with Jupiter, Saturn, Uranus and Neptune,

respectively. The previous study used clones of the known Centaurs for initial conditions, a starting condition heavily biased towards smaller semimajor axes.

This is not the first work of its kind to perform numerical integrations in order to construct the steady-state population of Centaurs with  $a < 34$  AU from a scattering TNO population. Some works (Dones et al., 1999; Horner and Evans, 2006; Tiscareno and Malhotra, 2003) present numerical integrations of Centaurs (both known and test populations) initially within the giant planet region. Those that have modeled the evolution of scattering TNOs into the  $a < 34$  AU Centaur region (Levison and Duncan, 1997; Volk and Malhotra, 2008) did not search for temporary (often  $< 100$  kyr) co-orbital captures.

Work similar to that presented here has been performed simulating near-Earth asteroids captured as temporary co-orbitals of Earth (Morais and Morbidelli, 2002). Those authors found that the Earth’s temporary co-orbitals often experience several co-orbital phases, each of average duration 25 kyr (none longer than 1 Myr).

In the work presented here, where Centaurs are provided from a bias-free external scattering disk, we find that the average length of captures in co-orbital motion with Uranus is 108 kyr and with Neptune is 78 kyr. We were surprised to find that objects that experience at least one episode of co-orbital capture have a median of 2 captures with Uranus or 6 captures with Neptune. Objects typically escape with low relative velocities, so multiple temporary captures are not surprising. Some objects experience temporary co-orbital captures with both planets (see Figure 6.3, right column). Due to the  $r_{min} = 6$  AU distance cut in the integrations, which removes high-eccentricity Saturn-crossing Centaurs before they potentially could get trapped into co-orbital motion, we did not reliably measure the Saturnian trapping fraction, but estimate it at  $\ll 0.1\%$  of the incoming scattering population.

### 6.3.1 Quasi-Satellites

Quasi-satellites make up 10% of the steady-state Uranian and Neptunian co-orbitals in our numerical integrations. This is thus a rare

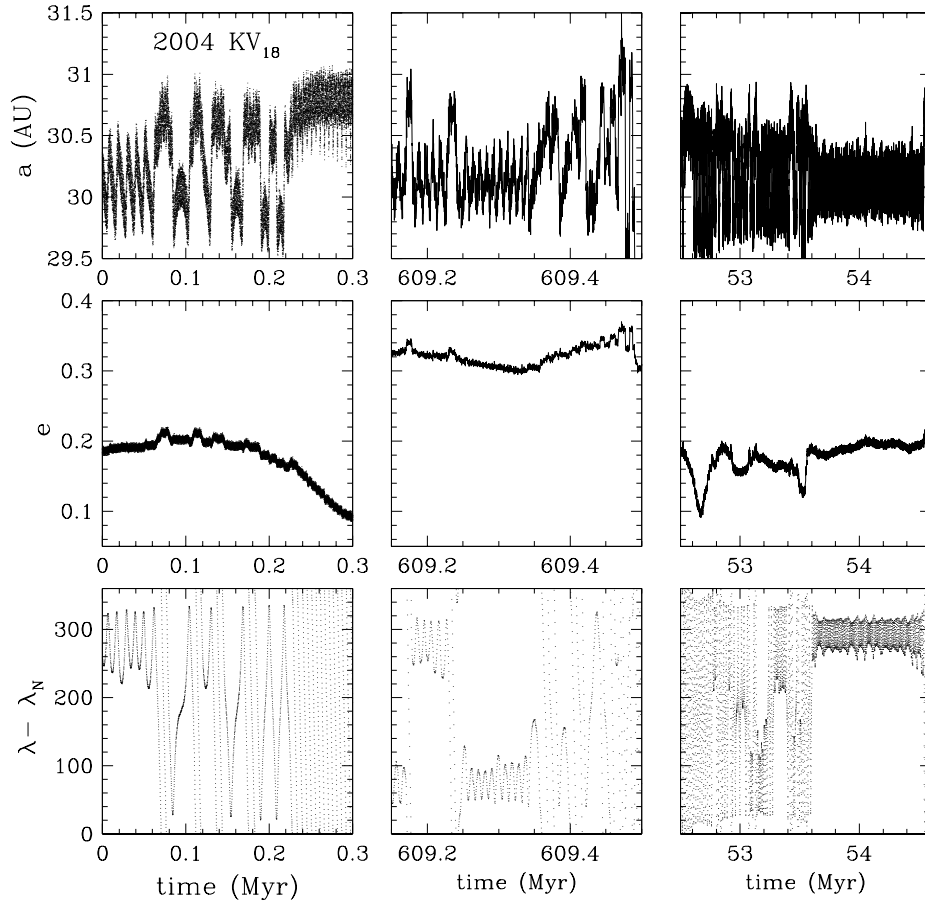


**Figure 6.3:** Left column: Evolution (for 0.3 Myr into the future) of the semimajor axis  $a$ , eccentricity  $e$ , and resonant angle  $\lambda - \lambda_N$  of 2004 KV<sub>18</sub> (the certainly-unstable Neptunian Trojan (Gladman et al., 2012; Horner and Lykawka, 2012)). Center and right columns: Evolution for two temporary Neptunian co-orbitals from our dynamical simulations for intervals in which their evolution is similar to that of 2004 KV<sub>18</sub>. Note: The object on the right is the same object as in right column of Figure 6.1. This object experiences co-orbital motion with both Uranus and Neptune, with  $\sim 5$  Myr between the two temporary captures.

state, but of great dynamical interest (Connors et al., 2002, 2004; de la Fuente Marcos and de la Fuente Marcos, 2012; Mikkola et al., 2004, 2006; Namouni, 1999; Namouni et al., 1999). There is currently one known temporary ( $\sim 100$  kyr duration) quasi-satellite of Neptune (de la Fuente Marcos and de la Fuente Marcos, 2012). The current existence of one known temporary quasi-satellite, out of a total of  $\sim 6$  known temporary Uranian and Neptunian co-orbitals, fits into our general picture of temporary traps in co-orbital states. Figure 6.4 depicts the semimajor axis, eccentricity, and resonant angle evolution of two temporary quasi-satellite captures found in our numerical integrations. The capture shown on the left is a quasi-satellite with Neptune for a duration of 694.5 kyr before it scatters away. The capture on the right in Figure 6.4 remains a quasi-satellite with Uranus for 1.45 Myr before leaving the co-orbital state.

## 6.4 Conclusions

The discovery of the first known temporarily-trapped Uranian Trojan led to the investigation of the fraction of the steady-state Centaur population in temporary co-orbital states with Uranus and Neptune (Alexandersen et al., 2013). By integrating the population of scattering objects as they enter the  $a < 34$  AU Centaur region, we found that at any time, 0.4% and 2.8% (with less than a factor of 2 variation) of the  $a < 34$  AU population is in temporary co-orbital motion with Uranus and Neptune, respectively. Alexandersen et al. (2013) show that when the  $a < 34$  AU steady-state Centaur distribution is put through a survey simulator, this is in agreement with the known fraction of Uranian and Neptunian co-orbitals.

Temporary co-orbital traps typically last for tens of thousands of years and up to several Myr. Objects can be trapped as horseshoes, Trojans, or quasi-satellites. A single object can be trapped in multiple resonant states, either switching between classifications in a single trap or in multiple traps (as shown in Figure 6.1 and Figure 6.3). A single object can also be temporarily trapped as a co-orbital with both Uranus and Neptune (Figure 6.1 and Figure 6.3, right columns). The

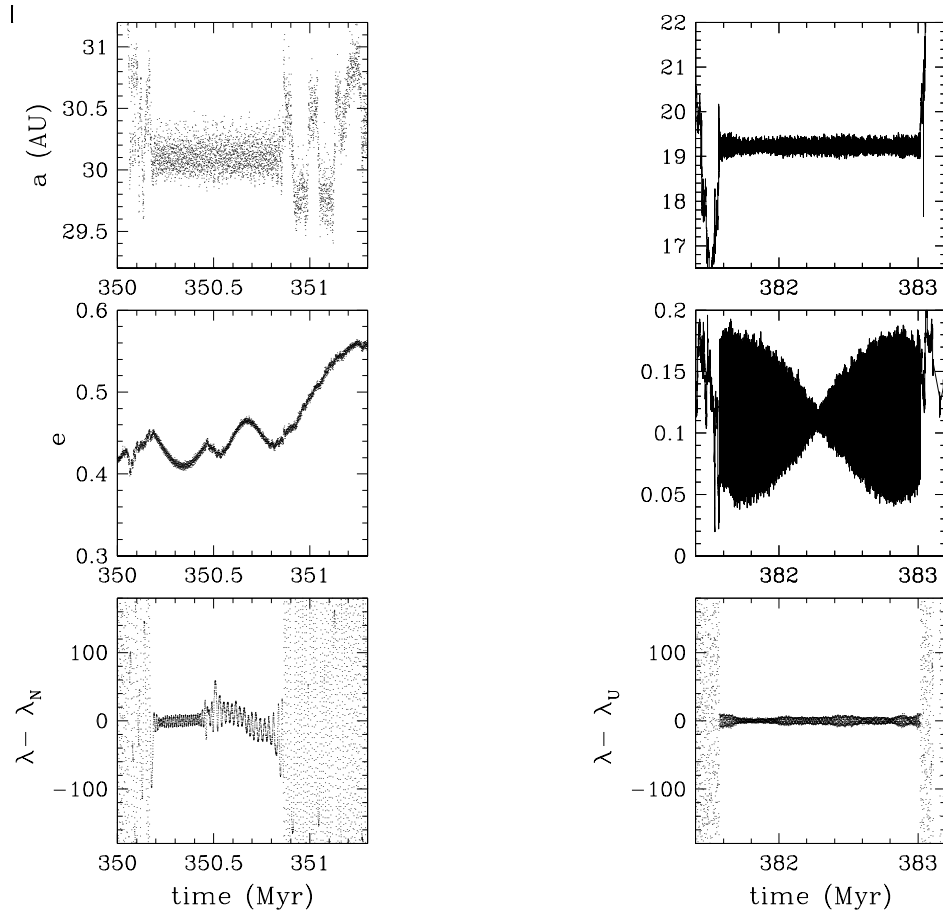


**Figure 6.4:** Evolution of the semimajor axis  $a$ , eccentricity  $e$ , and resonant angle  $\lambda - \lambda_{Planet}$  for two temporary quasi-satellite captures from our dynamical simulation, one Uranian (right) and one Neptunian (left). Note the different scales.

transient nature of temporarily-trapped co-orbitals make them an interesting dynamical population to study. In addition, the very short dynamical timescale of the unstable Uranian and Neptunian co-orbitals would require a very large reservoir of stable Uranian and Neptunian co-orbitals if the unstable co-orbital source are the stable co-orbitals that are becoming dislodged from the co-orbital state today. However, the roughly comparable number of stable and unstable Uranian and Neptunian co-orbitals requires an external source for the unstable co-orbitals with the scattering TNO population being consistent, as shown in this chapter and Alexandersen et al. (2014).

# Chapter 7

## Impact and Cratering Rates onto Pluto

### 7.1 Introduction

The New Horizons space probe will fly through the Pluto system in July 2015 and will be capable of taking high-resolution images of craters down to  $\simeq 0.5$  km in diameter on the encounter hemispheres of Pluto and Charon (Moore et al., 2015; Young et al., 2008) (for the image resolution for the four smaller satellites, see Table 5.2). Using the observed surface crater densities, one would like to compute crater retention ages for the various surfaces of Pluto, its binary companion Charon, and the small satellites. In order to do this, knowledge of the impact flux onto the surface is needed, both in terms of the number of projectiles and their impact speeds. To date, a study of the impact rates broken down into the various Kuiper belt sub-populations has never been done. Lacking any crater data, approximations of the number density of Kuiper belt objects that intersect the orbit of Pluto at an average impact velocity have sufficed (Durda and Stern, 2000; Weissman and Stern, 1994; Zahnle et al., 2003), but the observational opportunity

---

This chapter is based on the following published work: S. Greenstreet, B. Gladman, W. B. McKinnon, *Impact and Cratering Rates onto Pluto*, *Icarus* **258**, 267 (2015).

of the New Horizons Pluto-system fly-through requires a more accurate understanding of the impact rates, impact speed distributions, and thus the collisional history of the surface of Pluto and its satellites.

### 7.1.1 Motivation

Pluto likely formed in a different environment from the one in which it currently resides. Some recent dynamical models (discussed in Section 5.2) postulate a violent period of instability in the giant planet orbits roughly 3.9 Gyr ago; during this chaotic time period, an outward migration of Uranus and Neptune causes their orbits to approach each other, briefly pumping Neptune’s eccentricity which pushes the ancient population of Kuiper belt objects outward and rearranges the outer Solar System to roughly its current architecture ((Levison et al., 2008) and references therein). With or without a dramatic planetary re-arrangement 3.9 Gyr ago, in any scenario in which Neptune’s mean-motion resonances swept through a population of small bodies during outward migration, many objects, including Pluto, are swept up into resonance (Malhotra, 1993, 1995). Regardless of exactly how it arrived there, Pluto currently sits in the 3:2 mean-motion resonance with Neptune. A hypothetical turbulent time period during the first  $\approx 500$  Myr of Solar System history we refer to as the “pre-installation phase” of Pluto’s collisional history, and is not something we can model using estimates of today’s Kuiper belt orbital distribution. We assume the Pluto-Charon binary-forming event occurred during this “pre-installation phase”. The four smaller satellites in the Pluto system (Styx, Nix, Kerberos, and Hydra) are also hypothesized to have formed through post-collision reaccumulation, possibly during the Pluto-Charon binary-forming event (Stern et al., 2006). Because we do not know the orbital distribution of the Kuiper belt during this period of the Solar System’s history, we prefer to remain on relatively solid ground by performing an analysis of Pluto’s collisional history for the past  $\simeq 3.9$  Gyr, spanning the time period we think it reasonably certain Pluto has been on its current orbit,  $t \approx 0.6$  Gyr to 4.5 Gyr into the age of the Solar System. We refer to this period as the “post-installation phase” of Pluto’s

history. Pluto’s current location in the Kuiper belt causes it to be impacted by a wider variety of Kuiper belt sub-populations than the satellites of the giant planets, particularly by the cold classical objects, which do not reach into the giant planet region. We use current population estimates and orbital distributions of Kuiper belt sub-populations to determine the current impact flux and primary cratering rates onto the surface of Pluto in Sections 7.2.3 and 7.2.4. To extrapolate this back to the installation of Pluto onto its current orbit (not less than 3.9 Gyr ago), we assume each Kuiper belt sub-population has naturally eroded away with time and we use estimates of these decay rates from the literature to compute the number of primary craters formed on Pluto’s surface integrated over the past  $\simeq 4$  Gyr in Section 7.2.5 (secondary craters are considered separately in Section 7.3.5). We also compute the primary cratering rates and integrated number of craters for the surface of Charon in Section 7.3.7. In addition, we determine if the four smaller satellites of Pluto (Styx, Nix, Kerberos, and Hydra) have likely ever been catastrophically disrupted in the past  $\simeq 4$  Gyr in Section 7.3.8.

### **Kuiper Belt Sub-Populations**

The various Kuiper belt sub-populations are defined in Gladman et al. (2008) and discussed in Section 5.1.1. It was unclear at the outset of this project how the various Kuiper belt sub-populations would contribute to the impact flux onto the surface of Pluto. Each group populates different regions of phase space and thus interacts differently with Pluto, but how their respective impact fluxes compare with each other is not obvious. In previous work (e.g. Zahnle et al. (2003)), a Kuiper belt having objects with “typical” semimajor axes  $a \approx 40$  AU and “typical” impact speeds  $v_{impact} \approx 2$  km/s was used to roughly estimate the cratering rate onto Pluto. This, however, neglects the details of the differing orbital parameters of each Kuiper belt sub-population. It’s unclear whether Kuiper belt objects (KBOs) with these estimated orbital parameters contribute most of the impact flux onto Pluto or another type of Kuiper belt population dominates. Perhaps several populations contribute roughly equally. Campo Bagatin and Benavidez (2012) com-

puted the collision probability of the Pluto-Charon binary-forming event using a collisional evolution model of the transneptunian object (TNO) population taken from the Canada-France Ecliptic Plane Survey (CFEPS) L7 synthetic model of classical and resonant Kuiper belt populations (Gladman et al., 2012; Petit et al., 2011), but did not break this down into the individual Kuiper-belt sub-populations nor extend their analysis to the current epoch’s impact events.

Pluto shares the 3:2 Neptunian mean-motion resonance with  $\approx 13,000$  diameter  $d > 100$  km (Gladman et al., 2012) objects known as the plutinos. By performing numerical integrations of the collisional evolution of known plutinos, de Elía et al. (2010) computed the plutino impact flux onto Pluto assuming “typical” impact speeds ( $v_{\text{impact}} = 1.9$  km/s) to estimate the cratering rate onto Pluto from the plutinos alone. Dell’Oro et al. (2013) performed a statistical analysis of the collisional evolution of TNOs among themselves using the individual Kuiper belt sub-populations from the CFEPS L7 model, but did not extend their analysis to the cratering rate on Pluto. As we were writing up our work, we became aware of the recent paper by Bierhaus and Dones (2015) that addresses some of the issues we are concerned with. We discuss this latter paper in Section 7.2.3.

In addition to being affected by the 3:2 mean-motion resonance with Neptune, Pluto’s orbit experiences Kozai (Kozai, 1962) librations which cause its eccentricity  $e$  and inclination  $i$  to oscillate against each other (high- $e$  corresponds to low- $i$  and vice versa) on the timescale of several Myr. This libration causes Pluto’s orbit<sup>a</sup> to never intersect the Solar System plane outside  $\simeq 42$  AU or inside  $\simeq 33$  AU (see Figure 7.1). This results in complex changes in collision probability over time between Pluto and the inner, main, and outer classical Kuiper belt objects. For example, the classical inner KBOs have  $a$  between roughly 37 and 39 AU with perihelia  $35 \text{ AU} \lesssim q \lesssim 39 \text{ AU}$  (see Figure 5.2). This places the classical inner KBOs in the region where Kozai librations keep Pluto’s ecliptic nodal distances. As one may imagine, Pluto’s nodal distances constantly staying near the classical inner KBOs enhances their collision probability with Pluto compared with a

---

<sup>a</sup>For reference Pluto’s perihelion  $q = 29.7 \text{ AU}$  and aphelion  $Q = 48.9 \text{ AU}$ .

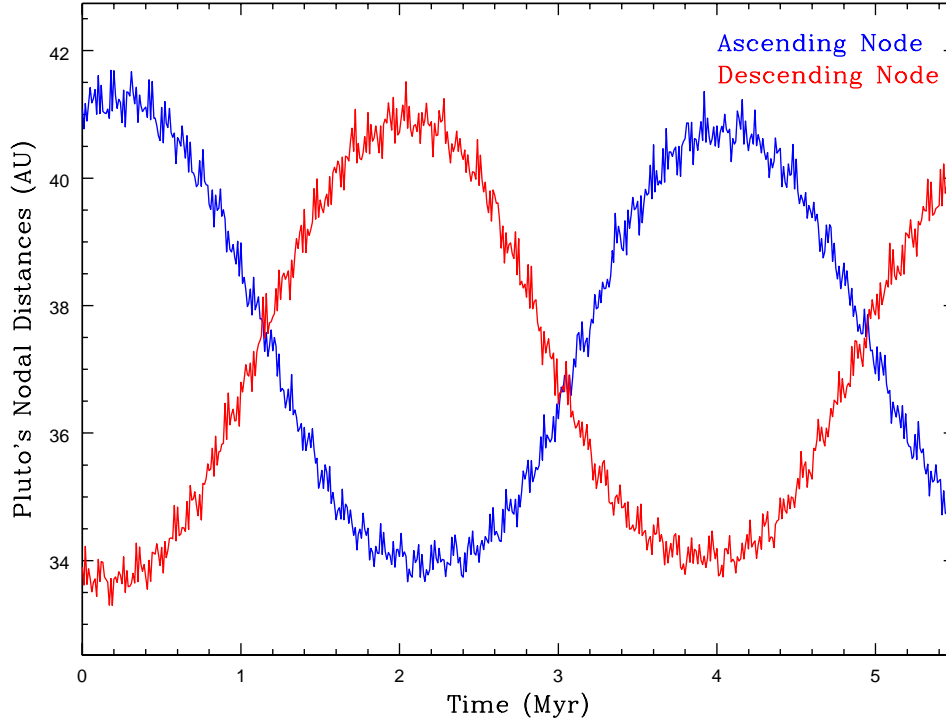


**Figure 7.1:** Numerical integration of Pluto’s ecliptic nodal distances.

situation where Pluto’s orbit uniformly precesses and nodal distance explores all values from perihelion  $q_{Pluto}$  to aphelion  $Q_{Pluto}$ . In contrast, most main classical KBOs lie between roughly 40 and 47 AU where the oscillation of Pluto’s ecliptic nodal distances cause its periodic intersection with the main classical KBOs. If all classical main KBOs had inclinations  $i \approx 0^\circ$ , the  $q > 42$  AU classical main objects should have zero collision probability with Pluto since Pluto’s orbit never intersects the plane of the Solar System outside  $\simeq 42$  AU. In reality, their non-zero inclinations cause some of them to have non-zero collision probability with Pluto. The two  $q < 42$  AU classical main populations (and their sub-components), however, are each affected by the repeated intersection of Pluto’s orbit with its

own. During the period when Pluto's nodal distance is between 40 and 42 AU, its collision probability with the main classical KBOs increases. This competes with the times when Pluto's orbit intersects the plane of the Solar System outside 42 AU, where its collision probability with the main classical Kuiper belt drops precipitously. As one may expect, this could cause the  $q < 42$  AU classical main KBOs to receive a smaller enhancement to their collisional probability with Pluto than the classical inner KBOs since the assumption of uniform orbital precession would also cause an orbital intersection oscillation. Lastly, the classical outer KBOs also experience complex changes in collision probability with Pluto over time. The classical outer KBOs, which in this study include the detached objects, have pericenters between  $\simeq 33$  AU and  $\simeq 42$  AU, the same region where Pluto's nodal distances remain. However, the classical outer KBOs have semimajor axes from roughly 47 AU out to  $\simeq 500$  AU causing them to only impact Pluto when they are near pericenter, dropping their collision probability. How do each of these competing phenomena affect the impact flux onto Pluto from the classical KBO sub-populations? Likewise, how do each of the complex interactions between Pluto and the Kuiper belt sub-populations stack up against each other when determining Pluto's cratering history? The answers are not obvious and provided some of the motivation for this study.

An additional complexity is that gravitational scattering has eroded each sub-population over the past 3.9 Gyr, but affecting each population differently (see discussion in Section 5.2.1). How this population decay affects the impact flux at Pluto when integrated over the age of the Solar System is also unclear. For example, the scattering objects spend a large fraction of their time at large distances from Pluto making their collisional cross-section with Pluto small. However, they are also thought to be one of the largest populations in the Kuiper belt 4 Gyr ago (Dones et al., 2004; Duncan and Levison, 1997; Levison and Duncan, 1997), which increases their contribution to Pluto's cratering history when integrated over the age of the Solar System. This large population decay competes with the low collisional cross-section of the scattering objects when determining

their contribution to the cratering history of Pluto, but is the large number of scattering objects in the past enough to dominate the cratering rate over other Kuiper belt sub-populations? To best understand the contribution of each Kuiper belt sub-population to the cratering history of Pluto, a study using the impact flux of debiased population models and their corresponding impact speed distributions is needed and presented here.

### Uncertainties in the Kuiper Belt Size Distribution

In addition to the dynamical complexities of the Pluto-crossing populations, there are major uncertainties about the Kuiper belt size distribution for objects with absolute g-band magnitude  $H_g > 9.16$  (corresponding to a diameter  $d < 100$  km for an assumed g-band albedo  $p$  of 5%) as discussed in Section 5.3. Because we wish to estimate crater production rates down to km scale, we must adopt a model of how the size distribution extrapolates from the break at  $d \simeq 100$  km down to sub-km impactor sizes. We adopt a break at  $H_g \approx 9$  (for typical TNO  $g - r$  colors of 0.5–1.0, the break at  $H_g \sim 9$  is shifted to  $H_r \sim 8 - 8.5$ , which is consistent with Fraser et al. (2014)’s results for the hot KBO and Jovian Trojan populations). Figure 7.2 shows a schematic of three size distribution extrapolation scenarios for  $H_g > 9$ . The (somewhat strawman) single power-law (SPL) extends the bright end of the size distribution ( $H_g < 9$ ) all the way down to the smallest objects. The model size distribution with a “knee” has a sharp break at  $H_g = 9$  (open circle) from a steep slope at the bright end of this  $H_g$ -magnitude to a shallower slope on the faint end. Lastly, the “divot” model has a discontinuous drop by a factor  $c$  in the differential number of objects at  $H_g = 9$  with a different power law for  $H_g > 9$ . All of these models are of course approximations to reality; we discuss the implications of changing  $\alpha_{faint}$  and using a “wavy” size distribution in Sections 7.3.4 and 7.3.6, respectively.)

To illustrate the consequences of not understanding how the relatively well-understood size distribution of large impactors connects to smaller sizes, we model five differential size distribution scenarios: a single power-law (SPL) with

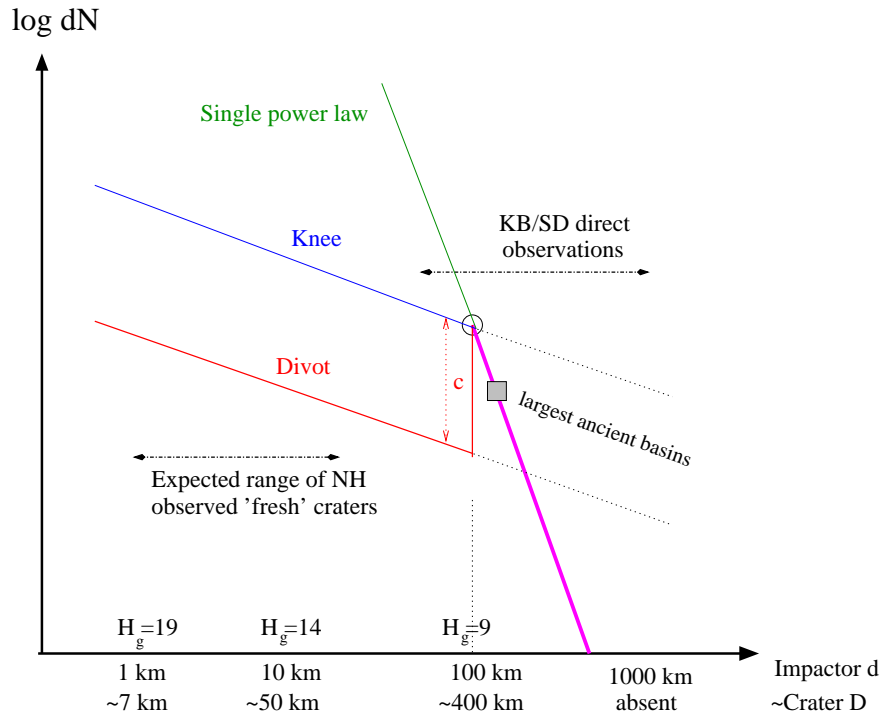


**Figure 7.2:** Schematic of three  $H_g$ -magnitude differential size distribution scenarios: a single power-law (SPL) (green), a knee (blue), and a “divot” (red). The Kuiper belt and scattering disk observations are calibrated down to  $H_g \approx 9$  (magenta), but beyond that (open circle) it is unclear how the size distribution extends to smaller sizes. The knee model is a simple transition to a shallower slope at the break diameter. The divot scenario has a rapid drop in the differential number of objects succeeded by a shallower recovery.  $H_g$ -magnitudes are converted to approximate impactor diameters  $d$  using equation (5.1) for an albedo  $p$  of 5%. Impactor diameters  $d$  are converted to rough crater diameters  $D$  using equations (5.3), (5.4a), and (5.4b), assuming an impact speed of 2 km/s and a transition from simple to complex craters at 4 km on Pluto (Moore et al., 2015). The expected range of “fresh” craters observed by New Horizons extends from  $D \approx 5$  km to  $D \approx 50$  km (created by impactors ranging from  $d = 1 - 10$  km), while the largest “ancient” basins ( $D \approx 200$  km) are not expected to have been created in the past 4 Gyr and therefore must date to Pluto’s *pre*-installation phase  $> 4$  Gyr ago.

logarithmic slope  $\alpha = 0.8$  ( $q = 5$ ); a power-law with a sharp knee at  $H_g = 9.0$ , slope  $\alpha_{bright} = 0.8$  on the bright side of the knee, and slope  $\alpha_{faint} = 0.4$  ( $q_{faint} = 3$ ) on the faint side of the knee; a power-law with a “divot” at  $H_g = 9.0$  with the same  $\alpha_{bright}$  and  $\alpha_{faint}$  as the knee scenario, but with a contrast (ratio of the differential number of objects in the population just bright of the divot to the number of objects just faint of the divot) value of  $c = 6$  (Shankman et al., 2013); and lastly the “wavy” size distributions of both Schlichting et al. (2013) and Minton et al. (2012) (as described by Schlichting et al. (2013)).

We adopt a value of  $\alpha_{faint} = 0.4$  (Bernstein et al., 2004; Fraser et al., 2014) for this work and discuss the implications of changing this value in Section 7.3.4. Although we assume a constant power law slope of the  $H_g$ -magnitude distribution from  $d = 100$  km down to smaller sizes ( $H_g = 9 - 25$ ), it is very unlikely that in reality the faint size distribution follows a single power-law all the way down to sub-km impactor sizes. We use a single extrapolation for simplicity’s sake and to illustrate many of the consequences of not understanding the impactor size distribution down to  $d < 100$  km to the cratering record on Pluto, but we understand that the size distribution in this regime likely has multiple slope changes which we refer to as being “wavy”. The main asteroid belt’s size distribution (O’Brien and Sykes, 2011), the analysis of Saturnian craters from Minton et al. (2012), and the model for the collision-generated population of KBOs today from Schlichting et al. (2013) all show that several slopes in the size distribution begin as one drops below roughly  $d < 60$  km and continue to the sub-km regime. We discuss the implications of such a shape in the size distribution on Pluto’s cratering record compared with a single-slope extrapolation in Section 7.3.6.

Because New Horizons should be able to observe craters down to 1-2 km in diameter on the encounter hemispheres<sup>b</sup> of Pluto and Charon, and down to 500 m in diameter in a high-resolution swath (Moore et al., 2015; Young et al., 2008), the uncertainties in the form of the Kuiper belt’s size distribution will be reflected in

---

<sup>b</sup>Pluto-Charon’s slow 6.39 day rotation combined with the speed of the New Horizons spacecraft mean that the non-encounter hemisphere will not be imaged at sufficient resolution and solar phase angle for meaningful crater counts.

the computation of surface ages in the Pluto system. This is well into the small end of the size distribution (a  $D = 500$  m crater corresponds to roughly a  $d = 40$  m impactor), but the uncertainties in the Kuiper belt size distribution will be apparent in larger craters as well. For example, the number of impactors in the differential size distribution with diameter  $d$  near 10 km varies by a factor of 6 (the value of the contrast  $c$ ) between the knee and divot scenarios and by a factor of 50 between the SPL and the knee distributions. Because the number of small impactors varies so widely between the three extrapolations, ages computed from observed crater densities based on these distributions naturally will rely heavily upon the intrinsic assumptions about the projectile size distribution. In addition, extrapolating the knee power-law size distribution from small diameters to projectiles just larger than the break (shown as dotted lines in Figure 7.2) overestimates the number of “largest ancient basins expected”, however, extrapolating the divot scenario underestimates the number of basins. Implications of these assumptions on both the computed crater retention ages and the determination of the impactor size distribution from Pluto’s cratering record are discussed in Section 7.3.

## **Triton**

Triton, Neptune’s major moon, is the closest body to Pluto for which we have crater counts (from the 1989 Voyager 2 flyby). Triton’s general characteristics (size, mass, and surface composition) are profoundly Pluto-like. Triton is also a geologically active body, and thus lightly cratered, and so should record only recent impacts from the scattering KBO population. Leaving aside the debate over whether Triton’s craters are predominantly due to heliocentric or planetocentric bodies (McKinnon and Singer, 2010; Schenk and Zahnle, 2007), the best global crater counts are from Schenk and Zahnle (2007). They find for *craters* between 5 and 25 km diameters (25 km being the size of the largest crater identified on the  $\approx 25\%$  of the surface imaged decently by Voyager) a differential power-law index of 3.25. Using simple crater scaling, they calculate a differential  $q_{slope}$  of 2.8 ( $\alpha = 0.36$ ) for the *projectile* population in the diameter range of  $d = 300$  m to  $d =$

2 km. Actually, because the craters span the simple-to-complex morphological transition, the actual  $q_{slope}$  and  $\alpha$  are likely slightly steeper. In either case, such  $\alpha$  values are close to the  $\alpha = 0.4$  adopted here for the faint branch of the KBO distribution down to this diameter. This value of  $\alpha$  is also consistent with the Minton et al. (2012) and Schlichting et al. (2013) size distribution models for this impactor diameter range (see Section 7.3.6). It will be of great interest to see, in 2015 New Horizons images, if the crater size-frequency distributions on Pluto and Charon are similar to Triton’s over comparable *projectile* diameter ranges.

## 7.2 Methods

In this section we present the methods used to compute current impact rates (Section 7.2.3), current cratering rates (Section 7.2.4), and the integrated number of craters on Pluto’s surface over the past  $\simeq 3.9$  Gyr (Section 7.2.5) from the various Kuiper belt sub-populations.

### 7.2.1 Kuiper Belt Population Models

In order to most accurately determine Pluto’s cratering history from the current Kuiper belt, we make use of the recent observational data encompassing each of the sub-populations. The Canada-France Ecliptic Plane Survey (CFEPS) L7 synthetic model (Gladman et al., 2012; Petit et al., 2011) was used to provide orbital distributions and  $H_g < 9.16$  (diameter  $d > 100$  km) population estimates for the resonant and classical Kuiper belt objects and the Kaib et al. (2011) (KRQ11) model provided the scattering population orbital distribution, which was absolutely-calibrated for  $H_g < 9.0$  by Shankman et al. (2013).

In order to pin the number of objects in each of the various Kuiper belt sub-populations to the  $H_g$ -magnitude corresponding to the break in the size distribution (at  $H_g = 9.0$ ), the CFEPS  $H_g < 9.16$  classical and resonant population estimates from Petit et al. (2011) and Gladman et al. (2012) were converted to  $H_g < 9.0$  (which corresponds to diameter  $d > 108$  km for a g-band albedo of 5%)

population estimates using equation 5.2. For example, the  $H_g = 9.16$  classical inner belt population estimate from Petit et al. (2011) of 3,000, implies  $\approx 2,200$  objects with  $H_g = 9.0$ .

### 7.2.2 Öpik Collision Probability Code

To compute the impact probability onto the surface of Pluto we modified a version of the Öpik collision probability code based on Dones et al. (1999), which implements the method described in Wetherill (1967). The code numerically integrates the collision probability of two bodies by assuming uniform precession of the nodal longitude and argument of pericenter of both the impactor and target over their precession cycles. The program adapts the integration step when the probability integrand becomes large. Our implementation of this code uses the relative fraction of each Kuiper belt sub-population (described in Section 7.1.1) divided into a grid of  $a$ ,  $e$ ,  $i$  cells of size 1 AU, 0.05, and  $2^\circ$ , respectively. The code uses each grid entry as the orbit of a potential Pluto impactor. The collision probability computed for the orbit is multiplied by the fraction of the population in that cell. The code gravitationally focuses the collision probability, providing the impact probability (/yr/object) as well as the impact velocity spectrum (in km/s) of the modeled population, with Pluto's escape speed (1.2 km/s) added in quadrature. The motion of Pluto about the Pluto-Charon system barycenter (25 m/s) is neglected.

The Öpik collision probability code used in this study was modified to bin the collision probability for each orbital precession orientation into individual impact velocity bins (as opposed to computing an average impact velocity from all possible impact orientations over a full orbital precession of the nodes). This produces detailed impact velocity distributions for each Kuiper belt sub-population onto Pluto (Figure 7.3).

As expected, each sub-population has a different impact velocity spectrum onto Pluto. Due to their large semimajor axes, unsurprisingly the scattering objects peak at the highest impact velocity of the Kuiper belt sub-populations.

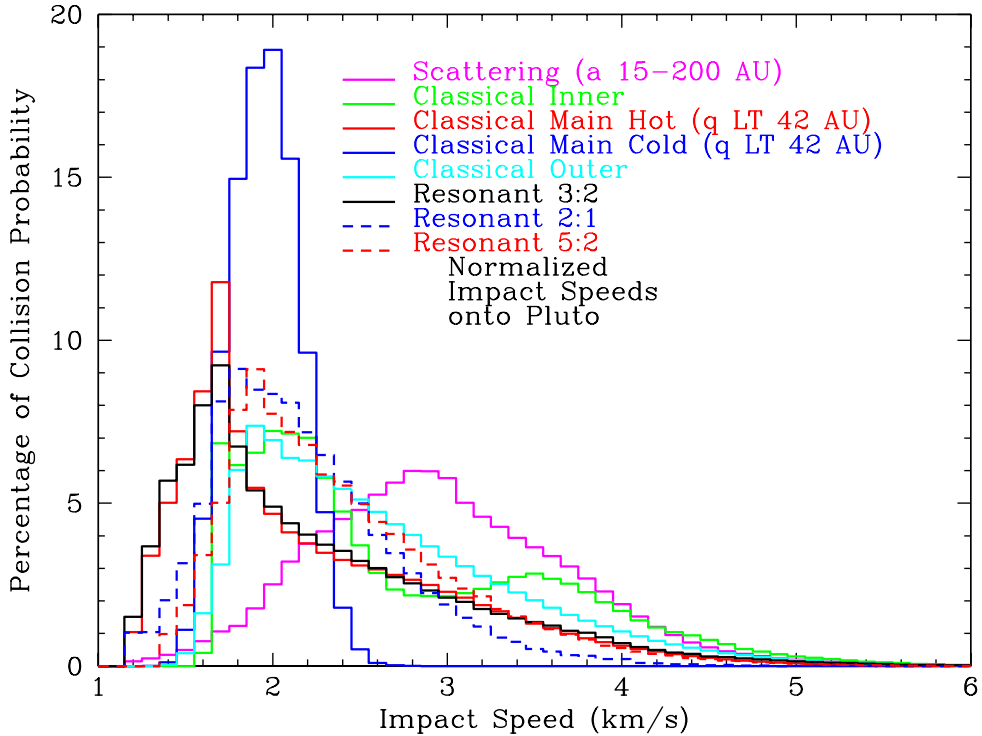


**Figure 7.3:** Impact velocity spectrum onto Pluto for KRQ11 and CFEPS L7 Kuiper belt sub-populations. Escape speed from Pluto is 1.2 km/s. Each sub-population’s distribution is separately normalized.

The classical inner objects have a bimodal impact velocity spectrum due to their bimodal inclination distribution which has a gap between roughly  $7^{\circ}$ – $20^{\circ}$  (Petit et al., 2011). The remaining populations have unimodal distributions peaking somewhere between 1.6 km/s and 2.0 km/s, with tails out to beyond 5 km/s. The impact speed spectrum produced by Dell’Oro et al. (2013) from a model of collisionally evolving TNOs (extracted from the CFEPS L7 synthetic model) impacting the plutinos independently reproduces these same main trends shown in Figure 7.3.

### 7.2.3 Impact Rates onto Pluto

The Öpik collision probability code produces impact probabilities with Pluto (/yr/projectile) that turn into impact rates (/yr) after multiplying by the estimated number of projectiles in each sub-population. Table 7.1 gives sub-population types (sometimes with orbital element cuts), impact probabilities (/yr/object in the group), telescopic population estimates for  $H_g < 9.0$ , and impact rates (/yr) from  $H_g < 9.0$  projectiles. The 42 AU pericenter cut for the classical main sub-populations corresponds to Pluto’s maximum nodal distance (see Section 7.1.1). There are very few hot classical main objects with  $q > 42$  AU. The scattering object (S.O.) 200 AU semimajor axis division is a useful boundary due to the fact that the  $a > 200$  AU S.O.s spend most of their time far from Pluto and so have a small impact probability, as can be seen by the factor of  $\approx 50$  in impact probability between the  $a < 200$  AU and  $a > 200$  AU S.O.s in Table 7.1. There are also essentially no S.O.s with  $a < 15$  AU, and, in any case,  $a < 15$  AU scattering objects require eccentricity  $e > 0.98$  to intersect Pluto.

The Öpik collision probability code assumes uniform precession of Pluto’s nodal longitude and argument of pericenter. There are methods that would help correct this assumption (Pokorný and Vokrouhlický, 2013; Vokrouhlický et al., 2012), but because Pluto experiences Kozai librations while also in the 3:2 mean-motion resonance with Neptune, its orbit neither uniformly precesses nor is it easily analytically modeled. In principle, the non-uniform precession could make important modifications to the impact rate. Our method to estimate the importance of this effect was to perform full N-body 100 Myr numerical integrations of the four outer planets and Pluto (resulting in Pluto performing its full dynamics) along with test-particle models of the CFEPS classical (inner, hot, stirred, kernel, and outer) and resonant 3:2 Kuiper belt sub-populations. We logged close encounters between Pluto and the KBOs and compared the number of close encounters logged in 100 Myr with the number expected from the Öpik code over this length of time. The Pluto dynamics correction factor in Table 7.1 accounts for this by providing the ratio of close encounters logged in these numerical integrations to

Kuiper belt Sub-Population Type	Öpik Impact Probability (/yr/KBO)	$H_g < 9.0$ Population Estimate	Öpik Impact Rate (/yr)	Pluto Dynamics Correction Factor	Corrected Impact Rate (/yr)	% of Total Impact Rate
S.O. ( $15 \text{ AU} \leq a \leq 200 \text{ AU}$ )	7.5e-17	8,000	6.0e-13		6.0e-13	1.3
S.O. ( $a > 200 \text{ AU}$ )	1.4e-18	72,000	1.0e-13		1.0e-13	0.2
Classical Inner	3.9e-16	2,200	8.6e-13	1.3	1.1e-12	2.3
Classical Main H ( $q < 42 \text{ AU}$ )	4.4e-16	2,000	1.1e-11	1.0	1.1e-11	<b>23.0</b>
Classical Main S ( $q < 42 \text{ AU}$ )	4.0e-16	30,000	1.2e-11	1.0	1.2e-11	<b>25.1</b>
Classical Main S ( $q > 42 \text{ AU}$ )	4.4e-16	18,000	7.9e-12	0.2	1.6e-12	3.4
Classical Main K ( $q < 42 \text{ AU}$ )	4.3e-16	8,300	3.6e-12	0.9	3.2e-12	6.7
Classical Main K ( $q > 42 \text{ AU}$ )	4.0e-16	4,700	1.9e-12	0.4	7.6e-13	1.6
Classical Outer	1.0e-16	60,000	6.0e-12	1.0	6.0e-12	<b>12.6</b>
Resonant 3:2	5.9e-16	10,000	5.9e-12	1.5	8.9e-12	<b>18.6</b>
Resonant 2:1	3.3e-16	2,700	8.9e-13	$\sim 1$	8.9e-13	1.9
Resonant 5:2	1.8e-16	9,000	1.6e-12	$\sim 1$	1.6e-12	3.3
<b>Total</b>					<b>4.8e-11</b>	<b>100.0</b>

**Table 7.1:** Öpik collision probability calculations. “Classical Main H” is the hot classical sub-population, “Classical Main S” is the stirred component of the cold classicals (Petit et al., 2011). Impact probabilities are (/yr/object). Population estimates are for  $H_g < 9.0$  (diameter  $d > 108 \text{ km}$ , for a g-band albedo  $p = 5\%$ ). Impact rates are (/yr) and determined using the number of  $H_g < 9.0$  objects in each sub-population. Pluto dynamics correction factors (see text) are accounted for in the corrected impact rates (/yr) as well as the % of total impact rate values (bold values show the four sub-populations that dominate the total impact rate onto Pluto).

that from the Öpik estimate. To provide enough logged close encounters in the integrations to reach  $\sqrt{n}/n = 10\%$  accuracy in the correction factors, both the numerical integrations and the Öpik estimate used for this purpose had a Pluto encounter radius of  $R = 0.005 \text{ AU} \sim 640 \text{ Pluto radii}$  (roughly 10% of Pluto's Hill radius). The corrected impact rates (/yr) shown in the second-to-last column of Table 7.1 account for the correction factors and should thus be used in future work.

As shown in Table 7.1, the effect of Pluto's Kozai dynamics, which causes its ecliptic nodal distances to always lie in the range  $\simeq 33 - 42 \text{ AU}$ , is most important for the  $q > 42 \text{ AU}$  stirred and kernel classical main objects, which have their impact rate drop by a factor of  $\approx 5$  and  $2.5$ , respectively, when corrected. As a result, the impact rates for the  $q > 42 \text{ AU}$  stirred and kernel classical main objects are each roughly an order of magnitude lower than the other populations that end up dominating the impact rate. The collision probability does not drop to zero due to the non-zero inclinations of some classical main KBOs. A curious phenomenon (as described in Section 7.1.1) regarding each of the  $q < 42 \text{ AU}$  classical main sub-populations is the oscillation of Pluto's ecliptic nodal distance between  $\simeq 33 \text{ AU}$  and  $\simeq 42 \text{ AU}$  which causes its intersection with the main classical KBOs to also oscillate. When Pluto's nodal distance is between  $\simeq 38 \text{ AU}$  and  $\simeq 42 \text{ AU}$ , roughly in the middle of the  $q < 42 \text{ AU}$  main belt population, its collision probability with the main classical KBOs increases. However, when Pluto's orbit intersects the ecliptic plane inside roughly  $38 \text{ AU}$ , the collision rate with the main classical KBOs drops due to the relative absence of such low- $q$  objects. Surprisingly, the intersection oscillation between Pluto's orbit and the  $q < 42 \text{ AU}$  classical main sub-populations due to Kozai results in the same impact rate onto Pluto as for the assumption that Pluto's orbit uniformly precesses (i.e., the correction factor = 1.0, to 10% accuracy). The  $q < 42 \text{ AU}$  hot and stirred classical main objects compete with two other populations (see below) for the dominant impact flux onto Pluto. The classical outer objects (which in this study include the detached objects) mostly have  $q < 42 \text{ AU}$  but, because their large

semimajor axes keep them mostly at large distances from Pluto, they experience a similar balancing phenomenon (correction factor = 1.0) and we find that Pluto’s Kozai oscillation contributes no appreciable correction to their impact rate onto Pluto. In contrast, the classical inner objects gain a non-negligible enhancement ( $\approx 30\%$ ) in their collision probability with Pluto, because they entirely lie in the region where Pluto’s ecliptic nodal distances always remain ( $\simeq 33 - 42$  AU) (see Section 7.1.1).

Our study shows that the basic Öpik collision probability algorithm (not including Pluto’s Kozai effect) also underestimates the impact rate of the plutinos (other 3:2 resonant KBOs) onto Pluto by  $\approx 50\%$ . In this case, our numerical integration had both the plutinos and Pluto in the 3:2 mean-motion resonance and some plutinos also undergoing Kozai. The net result is a mild (50%) increase of the impact rate due to the enhanced frequency of low-velocity encounters caused by a greater frequency of close orbital alignments. Even without the 50% correction factor, the plutinos are comparable to the impact flux of the other three dominant populations. The correction factors for the resonant 2:1 and 5:2 populations were not measured using numerical integrations, but we do not expect them to modify the Öpik approximation to  $> 10\%$  accuracy; in any case they are comparable to each other but down by roughly an order of magnitude from the dominant populations. We did not include other resonant populations in our analysis, because their contributions to Pluto’s impact flux will be small compared with the nearby and more numerous 2:1 and 5:2 populations (Gladman et al., 2012). The reader may be surprised that the scattering object impact flux onto Pluto is currently small, contributing only  $\approx 2\%$  of the total impact flux. Thus, Pluto is dominantly hit by a wider variety of Kuiper belt sub-populations than the satellites of Jupiter and Saturn, particularly by the cold classical objects, which do not reach into the giant planet region.

Examining all the Kuiper belt sub-populations, Table 7.1 shows that one is faced with the complication that no single population dominates the impact flux onto Pluto. In fact, the  $q < 42$  AU hot and stirred classical main, the classical outer

(which include the detached objects), and the plutino populations each provide roughly comparable (15 – 25%) contributions to the total impact flux, together outweighing the sum of all other sub-populations by roughly a factor of four. Computing impact rates and thus cratering rates onto the surface of Pluto using only a model of the cold classical Kuiper belt objects thus underestimates the age of Pluto’s surface, although this depends of course on the number of KBOs assumed in the classical belt.

In detail we find that our total impact rate of  $4.8 \times 10^{-11}/\text{yr}$  is a factor of  $\approx 2.5$  less than estimated by Durda and Stern (2000) for  $d > 100$  km impactors, who found an impact rate of  $\approx 1.2 \times 10^{-10}/\text{yr}$  assuming 70,000 KBOs greater than this size (see their fig. 6). Zahnle et al. (2003) found an estimated impact rate onto Pluto of  $2.3 \times 10^{-11}/\text{yr}$  (within a factor of 2) for  $d > 100$  km impactors scaled from the calculations of (Nesvorný et al., 2000) for plutino impacts on Pluto and from an Öpik-style estimate from W. Bottke (private communication) and using 38,000 KBOs of this size. Our total impact rate of  $4.8 \times 10^{-11}/\text{yr}$  for  $d > 100$  km impactors agrees within their uncertainty, even with our change in population estimates and our use of an impact velocity spectrum (which is used to gravitationally focus the Öpik impact probabilities computed for each target and projectile orbital precession orientation) rather than an average impact velocity. More important to the interpretation of the New Horizons crater density observations is that our production of an impact speed distribution allows us to examine its influence on Pluto’s cratering rates, which have velocity dependence in the crater scaling law.

The recent paper by Bierhaus and Dones (2015) found that the cold classical main objects (with stirred and kernel sub-components) contribute  $\approx 70\%$  and  $\approx 99\%$  of the projectile flux onto Pluto for  $d > 10$  km and  $d > 1$  km, respectively. This is primarily due to their use of a steeper slope ( $\alpha_{faint} = 0.38$ ) for the cold classical main objects compared with the hot classical main objects ( $\alpha_{faint} = 0.2$ ), citing Fraser et al. (2014). This steeper faint-end slope for the cold classicals compared with the hot classicals causes their contribution to increasingly dominate Pluto’s total impact flux for smaller and smaller impactor

sizes. In this paper, we assume all sub-populations have  $\alpha_{faint} = 0.4$  since the  $\alpha_{faint} = 0.38$  (+0.05, -0.09) slope for cold classicals is much better determined than the proposed  $\alpha_{faint} = 0.2$  (+0.1, -0.6) for hot classicals (uncertainties quoted from Fraser et al. (2014)). For the bright end of the size distribution, Bierhaus and Dones (2015) use the slopes for the hot and cold classicals from Fraser et al. (2014) ( $\alpha_{bright} = 0.87$  and  $\alpha_{bright} = 1.5$ , respectively). Our use of  $\alpha_{bright} = 0.8$  instead for all Kuiper belt sub-populations has little effect on conclusions about crater densities because we will show that  $D > 400$  km craters formed in the last 4 Gyr are absent, and thus only the total number of  $d > 100$  km projectiles is relevant in order to establish the absolute calibration linked to observed KBOs.

### Uncertainties in the Total Impact Rate

The uncertainty in our total impact rate comes from a variety of factors. The Öpik impact rate (/yr) depends on the accuracy of the population estimates used for each Kuiper belt sub-population. The absolute calibration for scattering objects (Kaib et al., 2011) is based on only 11 known objects (Shankman et al., 2013), contributing an uncertainty in the population estimate of  $1/\sqrt{N}=30\%$ ; however, the scattering objects contribute only a small fraction ( $\approx 2\%$ ) to Pluto’s impact flux. Uncertainties for the CFEPS classical and resonant population estimates are given in Petit et al. (2011) and Gladman et al. (2012), respectively, and shown in Table 5.1. As the four dominating sub-populations for the impact flux onto Pluto, the population estimates for the  $q < 42$  AU hot and stirred classical main objects have an uncertainty of roughly 25%, the classical outsiders roughly 75%, and the plutinos roughly 45%. Lastly, we aimed to have our Pluto dynamics correction factors good to 10% accuracy. Overall, we estimate a  $\pm 50\%$  uncertainty in our total impact rate shown in Table 7.1. To determine the uncertainty in how the impact rate translates to a cratering rate, one must understand the cratering physics and the caveats discussed in Chapter 5.

## 7.2.4 Cratering Rates onto Pluto

Because our analysis extends to include the impact speed distribution, there is not a simple one-to-one correspondence between impact rate and *crater formation rate larger than a given diameter threshold*. In order to convert impact rates (/yr) into primary cratering rates (/yr), we need to know the speed distribution and the differential size distribution for the individual populations (Gallant et al., 2009), which for the CFEPS model was expressed as  $dN/dH \propto 10^{\alpha H_g}$  for  $H_g < 9$ . There are several estimates for where a break in the  $H_g$ -magnitude size distribution occurs and how the distribution is extrapolated to small diameters (Adams et al., 2014; Bernstein et al., 2004; Fraser and Kavelaars, 2008; Fuentes and Holman, 2008; Gladman et al., 2001; Jewitt et al., 1998; Shankman et al., 2013). We simply adjust the CFEPS L7 population estimates from  $H_g = 9.16$  down to a break at  $H_g = 9.0$ , and then follow the analysis of Shankman et al. (2013) who placed a knee or divot at  $H_g = 9.0$ . We normalize the size distributions to the number of objects with  $H_g < 9.0$  as listed in Table 7.1.

For the first time in the literature, we compute primary cratering rates using the impact speed distribution for each given Kuiper belt sub-population (see Figure 7.3), looping over the velocity bins. Starting with the lowest velocity bin, the needed impactor diameter to create a crater of a desired size is computed using the simple-to-complex crater scaling laws from Zahnle et al. (2003) (equations (5.3), (5.4a), and (5.4b)), assuming Pluto's gravitational acceleration  $g = 64.0 \text{ cm/s}^2$ , impactor  $\delta$  and target  $\rho$  (at surface) densities  $\delta = \rho = 1.0 \text{ g/cm}^3$ , the transition diameter  $D_{tr} \simeq 4 \text{ km}$  (Moore et al., 2015), and  $\xi = 0.108$  (McKinnon and Schenk, 1995).

Once the needed impactor diameter  $d$  to create a crater of a desired threshold diameter  $D$  at the minimum impact speed (Pluto's escape speed) is computed, this  $d$  is converted to a  $H_g$ -magnitude using equation (5.1), assuming a g-band albedo  $p$  of 5%. By integrating down the size distribution which is pegged at  $H_g = 9.0$  for the population estimates shown in Table 7.1, the number of objects less than the impactor  $H_g$ -magnitude ( $N(< H_g)$ ) is computed. Because we have an im-

impact speed distribution rather than a single impact velocity, we must then repeat this process for each subsequently larger velocity bin. By progressing through the impact speed distribution, slightly higher impact speeds correspond to slightly smaller impactor diameters  $d$  for creating a fixed crater diameter  $D$ . This means that as we compute  $dN(H_g)$  for progressively smaller impactors we add the number of additional smaller objects to the total number of objects which can create the desired crater size. The number of additional objects added for each subsequent velocity bin is multiplied by the fraction of the velocity distribution with  $v$  greater than the current velocity bin before it is added to the cumulative number of objects for the desired crater size.

Once the above process is completed out to  $v_{impact} = 6$  km/s (the effective end of the tail of the distribution), the cumulative number of impactors which can make a crater larger than the desired crater threshold is multiplied by the impact probability (/yr/object) given in Table 7.1 and corrected by the “Pluto dynamics correction factor” also given in Table 7.1. The output is the current primary cratering rate (/yr) onto Pluto for the modeled Kuiper belt sub-population and a desired threshold crater diameter  $D$ . Note that this is more-or-less a direct calculation of the cumulative impact rate, and should be equivalent to the Monte Carlo approach used by Zahnle et al. (1998) to calculate the differential impact rates on planetary satellites from assumed cometary orbital distributions. We first repeated this process three times to study the variation in how the impactor differential  $H_g$ -magnitude size distribution might extend to  $d < 100$  km, using three extrapolation scenarios (Figure 7.2): a single power-law with logarithmic slope  $\alpha = 0.8$  ( $q_{slope} = 5$ ); a power-law with a sudden knee at  $H_g = 9.0$ , slope  $\alpha_{bright} = 0.8$  on the bright side of the knee, and slope  $\alpha_{faint} = 0.4$  ( $q_{faint} = 3$ ) on the faint side of the knee; and thirdly a power-law with a “divot” at  $H_g = 9.0$  with the same  $\alpha_{bright}$  and  $\alpha_{faint}$  as the knee scenario, but with a contrast (ratio of the number of objects in the population just bright of the divot to the number of objects just faint of the divot) value of  $c = 6$  (Shankman et al., 2013).

Kuiper belt Sub-Population Type	Current Cratering Rate $D \geq 400$ km (/yr)	Current Cratering Rate $D \geq 100$ km (/yr)	Current Cratering Rate $D \geq 30$ km (/yr)	Current Cratering Rate $D \geq 10$ km (/yr)	Current Cratering Rate $D \geq 3$ km (/yr)
	SPL/Knee/Divot	SPL/Knee/Divot	SPL/Knee/Divot	SPL/Knee/Divot	SPL/Knee/Divot
S.O. ( $15 \text{ AU} \leq a \leq 200 \text{ AU}$ )	2e-12	9e-10	2e-7	4e-5	1e-2
	1e-12	5e-11	7e-10	9e-9	2e-7
	7e-13	8e-12	1e-10	2e-9	3e-8
Classical Inner	2e-12	2e-9	4e-7	6e-5	2e-2
	2e-12	7e-11	1e-9	2e-8	3e-7
	1e-12	1e-11	2e-10	3e-9	4e-8
<b>Classical Main H</b> ( $q < 42 \text{ AU}$ )	2e-11	1e-8	3e-6	4e-4	1e-1
	1e-11	6e-10	1e-8	1e-7	2e-6
	1e-11	1e-10	2e-9	2e-8	4e-7
<b>Classical Main S</b> ( $q < 42 \text{ AU}$ )	1e-11	7e-9	2e-6	3e-4	8e-2
	1e-11	6e-10	9e-9	1e-7	2e-6
	1e-11	1e-10	2e-9	2e-8	3e-7
Classical Main S ( $q > 42 \text{ AU}$ )	1e-12	8e-10	2e-7	3e-5	1e-2
	1e-12	7e-11	1e-9	2e-8	3e-7
	1e-12	1e-11	2e-10	2e-9	4e-8
Classical Main K ( $q < 42 \text{ AU}$ )	3e-12	2e-9	5e-7	7e-5	2e-2
	3e-12	2e-10	2e-9	3e-8	5e-7
	3e-12	3e-11	4e-10	5e-9	9e-8
Classical Main K ( $q > 42 \text{ AU}$ )	7e-13	4e-10	1e-7	2e-5	5e-3
	7e-13	4e-11	6e-10	7e-9	1e-7
	7e-13	6e-12	1e-10	1e-9	2e-8
<b>Classical Outer</b>	1e-11	7e-9	2e-6	3e-4	9e-2
	1e-11	4e-10	7e-9	8e-8	1e-6
	7e-12	7e-11	1e-9	1e-8	2e-7
<b>Resonant 3:2</b>	1e-11	8e-9	2e-6	3e-4	1e-1
	1e-11	5e-10	8e-9	1e-7	2e-6
	8e-12	9e-11	1e-9	1.7e-8	3e-7
Resonant 2:1	1e-12	7e-10	2e-7	3e-5	8e-3
	1e-12	5e-11	8e-10	1e-8	2e-7
	8e-13	9e-12	1e-10	2e-9	3e-8
Resonant 5:2	3e-12	2e-9	4e-7	6e-5	2e-2
	2e-12	9e-11	2e-9	2e-8	3e-7
	2e-12	2e-11	3e-10	3e-9	6e-8
<b>Total</b>	<b>7e-11</b>	<b>4e-8</b>	<b>1e-5</b>	<b>2e-3</b>	<b>5e-1</b>
	<b>6e-11</b>	<b>3e-9</b>	<b>4e-8</b>	<b>5e-7</b>	<b>9e-6</b>
	<b>5e-11</b>	<b>5e-10</b>	<b>7e-9</b>	<b>9e-8</b>	<b>2e-6</b>

**Table 7.2:** *Current* primary cratering rates onto Pluto for a single power-law (SPL) (top), a knee (middle), and a “divot” (bottom) size distribution extrapolation for 5 sample crater-diameter-thresholds.

Table 7.2 shows the current cratering rate onto Pluto for 5 different sample threshold crater diameters and these three impactor size distribution scenarios (SPL/knee/divot), with the total cratering rates in the last row. The single power-law is somewhat of a strawman and is used for illustrative purposes of a very steep size distribution extending down to km-scale. The 400-km-diameter crater case corresponds roughly to a 100-km-diameter impactor travelling at 2 km/s, thus estimating the cratering rate at roughly the break in the impactor differential size distribution. For each population this crater diameter gives roughly the same current cratering rate for all three size distribution scenarios; they are not identical because some smaller “post-break” KBOs in the high-speed tail intrude into the  $D \geq 400$  km regime. The 100-km-diameter crater case is roughly at the limit for which we do not expect any craters of this size or larger to exist on Pluto over 4 Gyr (at *current* rates). Dropping down in scale to  $D \geq 30$  km craters, one begins probing the size distribution beyond the break where the SPL cratering rates are roughly a factor of 250 higher than for the size distribution with a knee. The factor of  $\approx 6$  between the knee and divot cratering rates reflects the value of 6 used for the contrast  $c$ . The deviation of the SPL from the knee size distribution of course increases for still-smaller crater diameters. Thirty-km-diameter and smaller craters should be observed by New Horizons, even if Pluto is as geologically active in degrading and erasing craters as Triton (Moore et al., 2015; Young et al., 2008).

### 7.2.5 Number of Craters on Pluto’s Surface

The cratering rates (/yr) given in Table 7.2 are for the *current* census of each sub-population of Kuiper belt objects. It is thought each of these sub-populations have naturally dynamically eroded with time at differing rates over the last  $\approx 4$  Gyr, so in order to convert the cratering rates into the cumulative number of craters on Pluto’s surface, we used theoretically estimated decay rates for each Kuiper belt population and integrated backwards in time to determine the enhancement. The time period we feel that can be reliably studied is Pluto’s post-installation phase

from 3.9 Gyr ago to the present day, where it is reasonable to assume only the number of projectiles in each population has changed, but the orbital distributions have remained the same because the Solar System architecture has not changed. We use the functional form:

$$\frac{N(t)}{N_0} = \left( \frac{4.5 \text{ Gyr}}{t} \right)^b, \quad 0.5 < t < 4.5 \text{ Gyr} \quad (7.1)$$

for the decay rate of each Kuiper belt sub-population, where  $N(t)$  is the number of objects in the population at some time  $t$  measured in Gyr forward from 4.0 Gyr ago,  $N_0$  is the number of objects in the population today at  $t \approx 4.5$  Gyr (see Table 7.1). The value of  $b$  is estimated from Kuchner et al. (2002), Hahn and Malhotra (2005), and Lykawka and Mukai (2005) for the classical Kuiper belt objects (where we take  $b = 0.1$ ), from Morbidelli (1997) and Tiscareno and Malhotra (2009) for the resonant 3:2 objects ( $b = 0.52$ ), from Tiscareno and Malhotra (2009) for the resonant 2:1 objects ( $b = 0.77$ ), and from Hahn and Malhotra (2005) for the resonant 5:2 objects ( $b = 0.05$ ). The scattering objects are estimated for the time period  $100 \text{ Myr} < t < 4 \text{ Gyr}$  using the data from Dones et al. (2004) directly (their figure 8), because a power-law does not represent the simulations well. A power-law of the form  $N(t) \propto t^{-b}$  with  $b \sim 0.7$  for the time period  $9 \text{ Myr} < t < 4 \text{ Gyr}$  approximately fits the decay (L. Dones, private communication, 2014), but only fits well at the end-points of the data so we chose to use the simulation results directly to compute the enhancement.

The enhanced bombardment factor (EBF) shown in Table 7.3 was computed by integrating the above functional form (equation (7.1)) over the past 4 Gyr ( $t \approx 0.5$  Gyr to 4.5 Gyr), comparing the integrated number of objects over the past 4 Gyr to that of a constant population. The EBF is thus a scaling factor needed to account for the decay of each Kuiper belt sub-population over the past 4 Gyr. It should be interpreted as the cumulative number of eroding objects in the past being equivalent to a constant population over the last 4 Gyr that is some multiplicative factor more than the current population. For example, the  $b$  value for the plutinos

Kuiper belt Sub-Population Type	EBF	Crater Number $D \geq 400$ km S/K/D	Crater Number $D \geq 100$ km S/K/D	Crater Number $D \geq 30$ km S/K/D	Crater Number $D \geq 10$ km S/K/D	Crater Number $D \geq 3$ km S/K/D
S.O. ( $15 \text{ AU} \leq a \leq 200 \text{ AU}$ )	4.9	3e-2 3e-2 1e-2	18 0.9 0.1	5000 10 2	7e+5 2e+2 3e+1	2e+8 3e+3 5e+2
Classical Inner	1.08	1e-2 9e-3 5e-3	6 0.3 0.06	2000 5 0.8	3e+5 7e+1 1e+1	8e+7 1e+3 2e+2
<b>Classical Main H</b> ( $q < 42 \text{ AU}$ )	1.08	7e-2 6e-2 4e-2	40 3 0.5	10000 40 7	2e+6 5e+2 9e+1	5e+8 9e+3 2e+3
<b>Classical Main S</b> ( $q < 42 \text{ AU}$ )	1.08	5e-2 5e-2 5e-2	30 2 0.5	8000 40 7	1e+6 5e+2 8e+1	4e+8 9e+3 1e+3
Classical Main S ( $q > 42 \text{ AU}$ )	1.08	6e-3 6e-3 6e-3	4 0.3 0.06	900 5 0.8	2e+5 6e+1 1e+1	4e+7 1e+3 2e+2
Classical Main K ( $q < 42 \text{ AU}$ )	1.08	1e-2 1e-2 1e-2	8 0.6 0.1	2000 10 2	3e+5 1e+2 2e+1	9e+7 2e+3 4e+2
Classical Main K ( $q > 42 \text{ AU}$ )	1.08	3e-3 3e-3 3e-3	2 0.2 0.03	500 3 0.4	8e+4 3e+1 5e+0	2e+7 5e+2 9e+1
<b>Classical Outer</b>	1.08	5e-2 5e-2 3e-2	30 2 0.3	8000 30 5	1e+6 4e+2 6e+1	4e+8 6e+3 1e+3
<b>Resonant 3:2</b>	1.53	8e-2 7e-2 5e-2	50 3 0.5	10000 50 8	2e+6 6e+2 1e+2	6e+8 1e+4 2e+3
Resonant 2:1	1.94	9e-3 8e-3 7e-3	5 0.4 0.07	1000 6 1	2e+5 8e+1 1e+1	6e+7 1e+3 2e+2
Resonant 5:2	1.04	1e-2 1e-2 7e-3	6 0.4 0.07	2000 6 1	3e+5 8e+1 1e+1	8e+7 1e+3 2e+2
<b>Total</b>		0.3 0.3 0.2	200 10 2	50000 200 40	8e+6 3e+3 4e+2	3e+9 5e+4 8e+3

**Table 7.3:** Cumulative number of craters over the past  $\approx 4$  Gyr on the surface of Pluto for 5 sample crater diameters for the three impactor size distribution scenarios (SPL/knee/divot) given in Table 7.2. EBF stands for the enhanced bombardment factor that is the scaling needed to account for the decay of each sub-population over the past 4 Gyr.

implies that this population was  $\approx 3.2$  times as populous 4 Gyr ago as it is today (from equation 7.1); its EBF of 1.53 means the integrated number of impacts from the decaying population over the age of the Solar System is equivalent to that from a constant population 1.53 times larger than today's.

Table 7.3 presents the number of craters larger than a given threshold crater diameter  $D$  obtained by multiplying Table 7.2's cratering rates by 4 Gyr and the EBF for each sub-population. For example, the number of craters with  $D \geq 30$  km generated by the plutinos for a divoted impactor size distribution was found the following way:  $(1 \times 10^{-9}) * (4 \times 10^9) * (1.53) = 8$  craters.

Perhaps unsurprisingly, we find that the 3:2 resonant population is the largest single contributor to the integrated collisional history onto Pluto, accounting for about a quarter of its impact craters over the last 4 Gyr. Compared with the other three competing populations that provide major contributions to Pluto's current impact flux (the  $q < 42$  AU hot and stirred classical main objects and the classical outer objects), the 3:2 objects have decayed the most over the past 4 Gyr, making them more dominant than these impactor population contributions when integrated over Pluto's post-installation phase. Even with an EBF of 4.9, the scattering objects contribute little to Pluto's collisional history over the last 4 Gyr, only contributing roughly half as much as each of the  $q < 42$  AU hot and stirred classical main objects and the classical outer objects. Thus, strictly speaking, the population of bodies that have cratered Pluto and Charon over the past 4 Gyr are not necessarily the same as the scattering population that impacted the giant-planet satellites. Although the scattering objects and the plutinos may have been drawn from the same parent population long ago and thus show the same size distribution, the cold classical belt might have a different break point, and is known to have a steeper  $H_g < 9$  slope (e.g., (Adams et al., 2014; Fraser et al., 2014; Petit et al., 2011)), which together with its ultra-red colors ((Doressoundiram et al., 2008; Sheppard, 2012)), have been interpreted as possibly indicating an in situ origin, and thus a separate population from the scattering, resonant, and hot classical Kuiper belt objects. It is also interesting to note that Table 7.3 indicates there is

only a  $\approx 20 - 30\%$  chance that Pluto has even one impact basin ( $D > 400$  km formed by  $d \gtrsim 100$  km impactors) formed in the current (i.e. post-installation) impacting environment.

## 7.3 Discussion

We anticipate that the interpretation of the cratering record will be fraught with complications, as we now describe.

### 7.3.1 Interpretation of Young Surfaces

If New Horizons finds a surface that appears “lightly-cratered” or “young” (especially if portions of Pluto or Charon appear like Triton), then one would first compute a crater retention age using the “current day” cratering rates given in Table 7.2. With very young regions there is always the difficulty of being sure one is selecting a region with a single coherent re-surfacing age, but let us assume this could be done. If the calculated age is small enough that the decay of the impactor populations is not a concern (roughly a few hundred million years), then the uncertainty on this derived age will depend essentially entirely on the assumption of which extrapolation one prefers for projectiles smaller than the break diameter in the impactor size distribution. Our calculations show that unless the single power-law impactor size distribution or some other steep size-frequency distribution (SFD) (e.g., cases A and B in Zahnle et al. (2003) and Schlichting et al. (2013)) actually were the correct model, all cratered surfaces will be unsaturated over the last 3.9 Gyr for  $D > 1$  km. As an example, Figure 7.4 shows the cumulative number of craters per square km that are larger than several threshold crater diameters  $D$  versus the crater retention age of a surface on Pluto. If the crater density of  $D \geq 3$  km craters on a young surface were to be  $10^{-4.5} \text{ km}^{-2}$ , then one would conclude a retention age of  $\approx 100$  Myr if the knee model is the best representation of the size distribution; in contrast, if the power-law break located up at impactor diameters of 100 km is a divot, this same surface would require

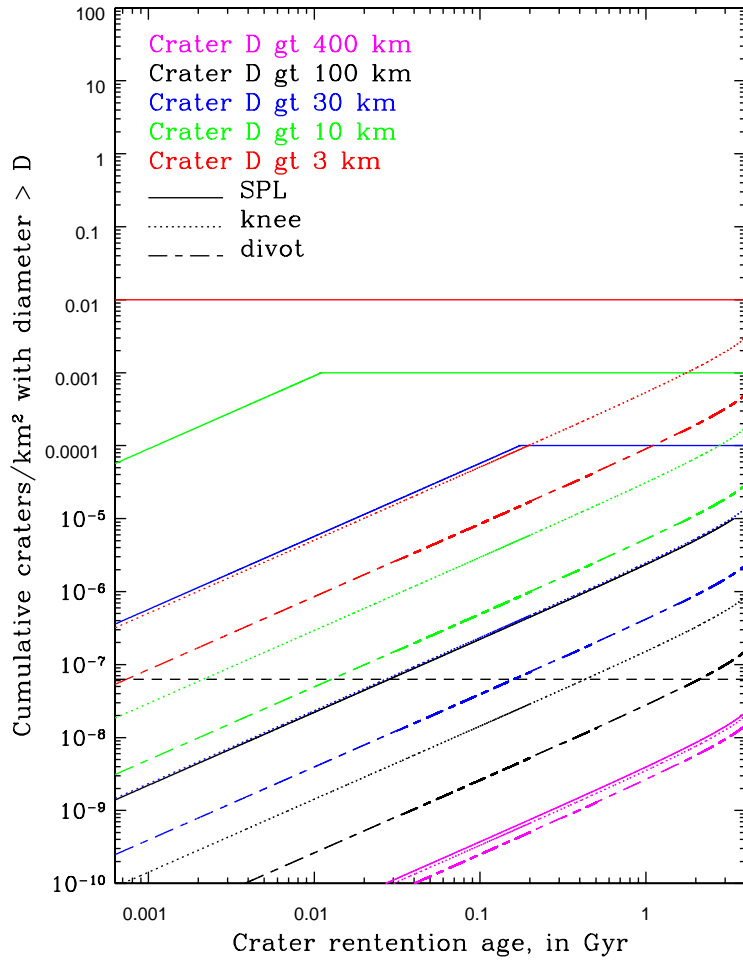


**Figure 7.4:** Logarithm of primary crater density (# craters/km<sup>2</sup>) on Pluto's surface versus age (Gyr) since last surface reset for 5 crater diameters and three impactor size distribution scenarios. For a given crater diameter, the inferred crater retention age can vary widely depending on assumptions of the size distribution. The horizontal line at -7.2 corresponds to 1 crater/Pluto surface. Note that the  $D \geq 100$  km crater curve for the SPL nearly overlaps the  $D \geq 30$  km crater curve for the knee scenario. Some SPL curves cease to rise above the empirically determined saturation level for the diameter in question (Melosh (1989); his fig. 10.2).

nearly  $\approx 600$  Myr of exposure to reach the same crater density. At small crater diameters the influence of the relatively tiny number of projectiles larger than the impactor power-law break diameter is irrelevant and this age ratio is essentially the contrast at the transition diameter. So, how can one know which (if any) assumption/distribution is valid?

### 7.3.2 The Issue of the Size Distribution Below the Break

At first glance, one might hope that Pluto's crater record will itself provide information that resolves the uncertainty in the behavior of the size distribution near the power-law break diameter, for without this resolution the factor-of-six is inherent and dwarfs all other uncertainties in the problem. Unfortunately, our calculations show that over the last  $\approx 4$  Gyr, Pluto is unlikely to have been struck by even a single impactor with a diameter larger than the break ( $d \approx 100$  km,  $D \approx 400$  km; see Table 7.3), so on *any* surface that post-dates Pluto's installation onto its current orbit (if any exist) we expect to see only craters caused by the projectiles smaller than 100 km in diameter.

However, if any young surfaces are visible upon arrival in the Pluto system, those young surfaces should record the slope or slopes of the size distribution over the range of visible craters. For example, if the entire surface of Pluto appears, like Triton, to be relatively young, then the existing craters will reflect the size-frequency distribution (SFD) of the production population (at least, down to the diameter where pollution by secondaries (Section 7.3.5) begins). In particular it should be trivial to differentiate between, e.g., the single power-law size distribution with  $\alpha \simeq 0.8$  ( $q \simeq 5$ ) and a shallower slope of  $\alpha_{faint} \sim 0.4$  ( $q_{faint} \sim 3$ ), most likely measured using craters in the 1–100 km diameter range. While finding the shallower of these two slopes would rule out the steep  $\alpha_{bright} = 0.8$  power-law continuing uninterrupted from the break diameter down to impactors in the sub-km-scale range, measuring an  $\alpha_{faint}=0.4$  does not resolve the question of how that connects to the well-measured and absolutely-calibrated projectile population with  $d > 100$  km. Our estimates (Table 7.3) show that we do not expect

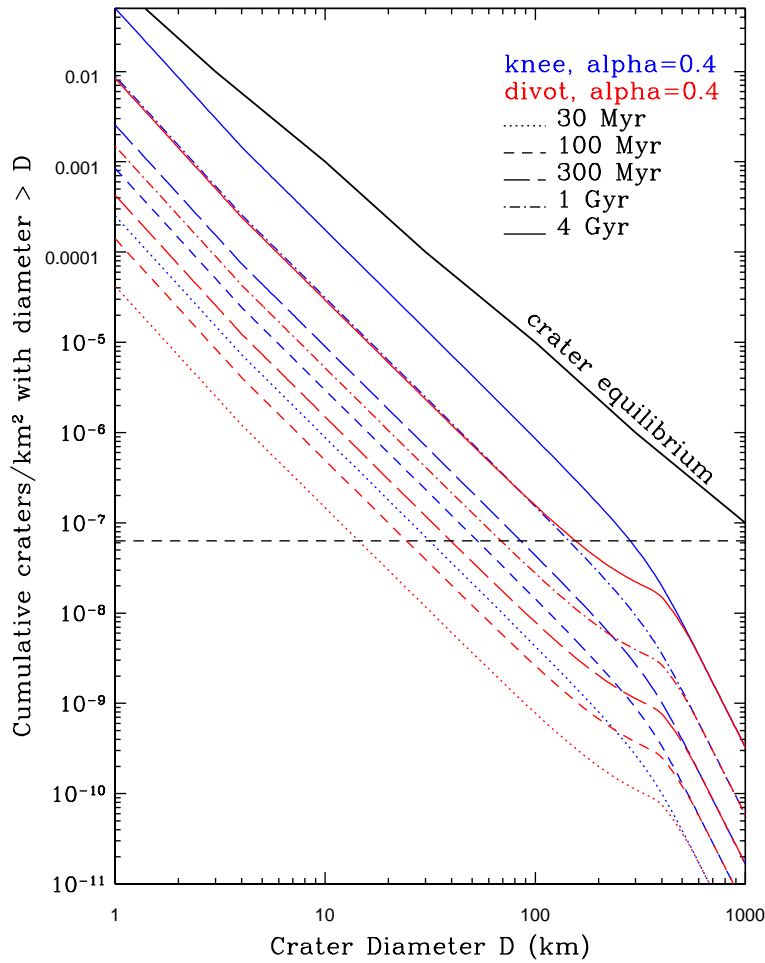


**Figure 7.5:** Logarithm of crater density (# craters/km<sup>2</sup>) larger than a given crater diameter  $D$  on Pluto's surface versus the logarithm of the crater diameter for an impactor size distribution with a knee and with a divot at various surface ages. The solid black line is the crater equilibrium curve from Melosh (1989). The horizontal line at  $-7.2$  corresponds to 1 crater/Pluto surface. The subtle change in slope at  $D = 4$  km corresponds to the transition from simple to complex craters.

the changing shape caused by the impactor distribution near the break (expected to be recorded only in the 200–500 km crater diameter range) to exist in post-installation terrains. This is illustrated in Figure 7.5, which shows the cumulative crater density for craters larger than a threshold diameter  $D$  for the knee and divot impactor size distribution extrapolation scenarios for different surface ages. The horizontal dashed line at  $-7.2$  corresponds to 1 crater/Pluto surface, meaning any finite crater density below this line will not be realized on Pluto in the last 4 Gyr. Thus, one cannot use the size distribution of craters present on “younger” terrains to differentiate between the knee and divot scenarios.

This being the case, obtaining better than “factor-of-six” crater retention ages in the Pluto system from our models will require one of two resolutions. First, future observations of the Kuiper belt that carefully probe the  $d = 10 - 100$  km impactor size range ( $H_g = 9 - 14$ ) should directly establish the number distribution of the current projectile population in an absolutely-calibrated way. This is most likely to be done first for populations whose members come to the smallest heliocentric distances (allowing detection of the smaller objects when they are at perihelion); meaningful improvements are most likely to be made in the near future by continuing to study the scattering objects (for which studies in the range  $H_g = 9 - 13$  are already possible (Adams et al., 2014; Shankman et al., 2013)) or even more likely in the more plentiful plutino population (for which deeper surveys can probe down to  $H_g \approx 11$  at the 28 AU perihelion of this population) (Alexandersen et al., 2014). While there currently are thus fragments of the observed size distributions across the outer Solar System small body populations, the entire diameter range is needed to make definitive statements about crater retention ages on the surfaces of Pluto and its moons.

Secondly, failing direct study of the current impactor population, it may be possible to at least detect the presence of the divot in Pluto’s or Charon’s cratering record itself. Because the current cratering rate is so low, we conclude the divot could only be visible on surfaces that *predate* the Pluto-Charon binary installation in the current Kuiper belt architecture. This could permit  $D \sim 200 - 400$  km

craters (which we shall term “basins”) that are caused by  $d = 50 - 100$  km impactors to be present on ancient surfaces.

What would be the signature on the crater distribution as the bombardment accumulates to the point where the power-law break diameter’s craters become present? The most obvious manifestation of this will be in the number of basins present relative to the number *expected* by extrapolation of the  $D < 100$  km craters to larger diameters; this produces very different behavior in the knee and divot scenarios as illustrated in Figure 7.2. This can also be seen in Figure 7.5 of the cumulative crater density. In Figure 7.5, the sharp power-law break present in Figure 7.2 has smoothed out to a broader slope change due to both the cumulative nature of this plot and the width of the impact velocity spectrum. The peak of the divot, for example, is still at  $D \approx 400$  km, but the slope change manifests itself over a broad range of crater diameters ( $D \approx 100$  km to  $D \approx 600$  km). Working from small projectiles up in Figure 7.2, the small craters follow the shallow slope of the  $\alpha_{faint} = 0.4$  ( $q_{faint} = 3$ ) impactor distribution, but upon reaching a knee, the slope changes to a much steeper  $\alpha_{bright} = 0.8$  ( $q_{faint} = 5$ ) large-impactor distribution which results in considerably *fewer* basins than the extrapolation of the shallower power-law would detect. In contrast, in a divot scenario there is a sudden *excess* of projectiles in the  $d = 100 - 200$  km range, and so there would be far more basins present than an extrapolation of the small craters would estimate. The horizontal line in Figure 7.5 at  $-7.2$  corresponds to 1 crater/Pluto surface. If the *pre*-installation bombardment is factors of many larger, and preserved, then this signal of a knee vs a divot will become accessible on Pluto’s surface. This sudden basin excess is represented by a positive slope on a relative crater frequency (R) plot normalized to a differential  $D^{-3}$  distribution as is shown in Figure 7.6 (Crater Analysis Techniques Working Group et al., 1979). The horizontal dashed line in Figure 7.6 refers to the approximate empirically observed level of crater saturation on various Solar System bodies (see Melosh (1989), chapter 10). The black squares correspond to 1 crater/Pluto surface on a cumulative plot, so unfortunately nothing to the right of those dots is expected to be visible on Pluto’s

post-installation terrains. Many times the current integrated bombardment rate would be needed from Pluto’s *pre*-installation period to move the basin signal to the visible diameter range on Pluto.

In fact, we postulate that such a basin-excess feature has already been observed on Saturn’s large moon Iapetus. Iapetus has been geologically inactive for its observable history; this and its distance from Saturn make Iapetus the best template to potentially record ancient Kuiper belt (scattering object) impacts. Dones et al. (2009) demonstrate that craters of this  $D > 400$  km scale are more than an order of magnitude more abundant than extrapolation of current impact rates (based on small impactors (their fig. 19.5 and table 19.4)) suggests. This is also illustrated in Figure 7.7 using relative crater densities from Kirchoff and Schenk (2010), where the  $R$ -values for basins of  $D \approx 400$  km are clearly substantially larger than those in the 100-to-400 km diameter range, and is statistically consistent with the Shankman et al. (2013) divot in the scattering object impactor population. Using the crater scaling law of equations (5.3), (5.4a), and (5.4b), assuming the following is true on Iapetus:  $g = 23 \text{ g/cm}^2$ ,  $\delta = \rho = 1 \text{ g/cm}^3$ ,  $U = 4.5 \text{ km/s}$ ,  $D_{tr}=15 \text{ km}$  (from Zahnle et al. (2003)), a divot (at impactor  $d = 100 \text{ km}$ ) corresponds to a crater diameter  $D = 600 \text{ km}$  on Iapetus (to be compared with  $D = 400 \text{ km}$  on Pluto). The peak in Figure 7.7 at roughly  $D = 400 \text{ km}$  could be the signature of the divot; note the factor of six (value of the contrast  $c$  in the “divoted” size distribution) between the average  $R$ -value of  $\approx 0.04$  for the  $100 \text{ km} < D < 300 \text{ km}$  basins and  $R = 0.25$  for the  $D \approx 400 \text{ km}$  basins in Figure 7.7.

The minor discrepancy between the 600 km predicted crater diameter  $D$  corresponding to the divot on Iapetus and what appears to be the divot in Figure 7.7 at  $D = 400 \text{ km}$  would be eliminated if one adjusted the assumed impactor albedo used to compute the impactor diameter corresponding to the  $H_g$ -magnitude (Equation 5.1) for which the divot is pegged. Creating a crater with  $D = 400 \text{ km}$  on Iapetus requires an impactor with diameter  $d \simeq 60 \text{ km}$ , while  $D = 600 \text{ km}$  corresponds to  $d \simeq 100 \text{ km}$ . Because constant flux  $\propto p * d^2$ , where  $p$  is the albedo, a decrease in the divot impactor diameter  $d$  by a factor of  $(100 \text{ km}/60 \text{ km}) = 1.7$

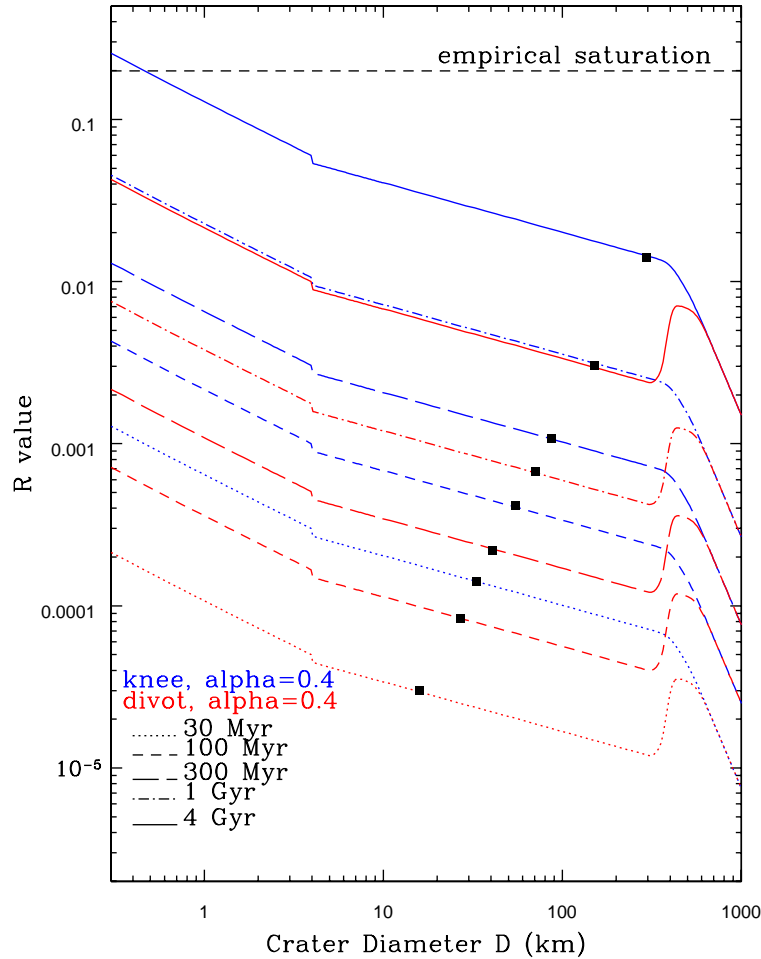


**Figure 7.6:** Relative crater frequency plot of the same information in Figure 7.5. The bump at  $D \approx 400$  km is due to the divot. The black squares correspond to 1 crater/Pluto surface on a cumulative plot, so unfortunately nothing to the right of those dots will likely be visible on Pluto's post-installation terrains, except by statistical fluctuation. It would require many times the current integrated bombardment rate to bring this portion of the relative crater frequency to the visible range on Pluto. The sudden slope change at  $D = 4$  km corresponds to the transition from simple to complex craters as shown in Figure 7.5.

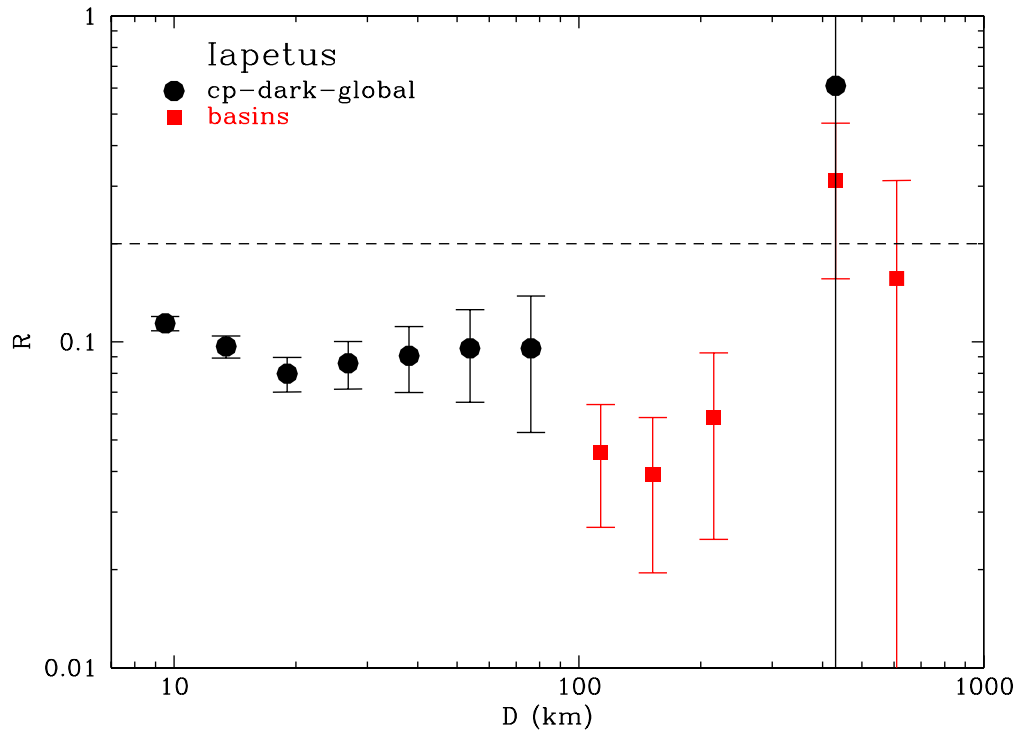


**Figure 7.7:** Relative crater densities as determined by Kirchoff and Schenk (2010) for Iapetus, the second largest mid-sized moon of Saturn. Compare with Figure 7.6. Cratered plains (cp) refer to broad counting regions. The horizontal line is empirical saturation. Note the factor of six (value of the contrast  $c$  in the “divoted” impactor size distribution) between the average  $R$ -value of  $\approx 0.04$  for the  $100 \text{ km} < D < 300 \text{ km}$  basins and  $R = 0.25$  for the  $D \approx 400 \text{ km}$  basins.

requires an albedo increase by a factor of 2.9 in order to move the crater diameter corresponding to the divot from  $D = 600$  km to  $D = 400$  km in Figure 7.7. This would require modifying our nominal  $p = 0.05$  albedo to  $\simeq 0.15$ . Observations estimate TNO albedos range from  $\simeq 2.5\%$  to  $\simeq 25\%$  (Fraser et al., 2014; Lacerda et al., 2014; Stansberry et al., 2008) so a mean visual albedo of  $p = 15\%$  may be reasonable. It is intriguing that one can use the basin excess on ancient cratered surfaces to find the physical impactor diameter corresponding to the divot, and therefore the albedo, given the uncertainty inherent in the crater scaling law. Because the uncertainties in the crater scaling law (equations (5.3), (5.4a), and (5.4b)) outweigh the uncertainty in TNO albedo measurements, we will not redo our analysis with the larger albedo.

However, given that the scattering objects are the primary impacting population onto Iapetus one wouldn't expect the "excess basin" feature to have arisen in the past 4 Gyr, but rather during the first 0.5 Gyr of Solar System evolution (sometimes referred to as the Late Heavy Bombardment (LHB), at least in regard to Saturn). Such a feature would be natural if the outer Solar System projectile population had a primordial divot at the break diameter of  $d \sim 100$  km. In a plausible "born big" accretional scenario (discussed in Shankman et al. (2013) and Johansen et al. (2014)), the "smaller"  $d < 100$  km projectiles could be extremely underabundant because they only exist as the collisional fragments of the  $d > 100$  km bodies that are the result of planetesimal formation; the small bodies slowly rise in number during the subsequent collisional evolution (see Campo Bagatin and Benavidez (2012) and Benavidez et al. (2012) for an illustration).

If Pluto, or possibly Charon, preserves its ancient surface, we expect a similar pattern of a large-basin excess to have been created when Pluto was in its pre-installation location, where the crater production rate was much higher but typical impact speeds may have been even lower than in the modern environment. How visible this basin excess signal will be on Pluto depends on whether crater saturation has been reached and whether even in a saturated state the signature can

persist (although the Iapetus case implies it can). Because the general form of the production population can be retained even in the saturated state when large impacts dominate, as Chapman and McKinnon (1986) and Richardson (2009) both conclude, this “basin excess” should still be present in terrains even after specific chronological utility has been lost. Such a terrain would still indicate a roughly 4 Gyr crater retention age. Note that the crater distribution superposed on the basin and its ejecta blanket could potentially provide an individual basin’s age.

### 7.3.3 Returning to Crater Retention Ages for Young Surfaces

Even if a basin excess is observed on Pluto or Charon, it may simply provide evidence for the presence of a divot in the impactor size distribution. This would not alleviate all uncertainties in the crater retention ages for young surfaces, because a precise measure of the contrast is needed to tell us how the well-characterized impactor size distribution connects to  $d < 100$  km impactors that produce the measurable crater densities on Pluto. If the observed  $D < 100$  km crater production function slope has a value of  $\alpha \simeq 0.4$  or greater, then one is in the regime in which the small craters will saturate first. Thus, we expect that it will be possible to assign model-dependent surface ages, either using the most-abundant (small) craters visible in unsaturated regions, or using the diameters above which the surface is not saturated if the smallest craters have reached saturation (this is standard for “steep” impactor populations). We remind the reader that what we refer to as a “shallow” Kuiper belt population (with  $\alpha_{faint} = 0.4$  and  $q_{faint} = 3$ ) is actually on the steep end insofar as inner Solar System crater populations are concerned (e.g., Chapman and McKinnon (1986)), thus populations with  $\alpha \sim 0.8$  ( $q \sim 5$ ) are much steeper than are ever discussed in inner Solar System cratering. To quantify this, Figure 7.6 shows that an R value of  $\approx 0.02$  at  $D = 1$  km corresponds to about 1 Gyr of bombardment for a knee scenario, but  $\approx 4$  Gyr for a divot. Because this is not saturated (R value  $< 0.2$ ), if these impactor distributions are valid, any surface region reset after Pluto’s installation onto its current orbit should not be saturated (except possibly at sub-km scales or by secondary craters;

Logarithmic Slope $\alpha_{faint}$	Current Cratering Rate	Current Cratering Rate	Current Cratering Rate	Current Cratering Rate	Current Cratering Rate
	$D \geq 400$ km (/yr) Knee/Divot	$D \geq 100$ km (/yr) Knee/Divot	$D \geq 30$ km (/yr) Knee/Divot	$D \geq 10$ km (/yr) Knee/Divot	$D \geq 3$ km (/yr) Knee/Divot
0.3	6e-11	1e-9	1e-8	8e-8	7e-7
	4e-11	3e-10	2e-9	1e-8	1e-7
0.4	6e-11	3e-9	4e-8	5e-7	9e-6
	5e-11	5e-10	7e-9	9e-8	2e-6
0.5	6e-11	5e-9	2e-7	4e-6	1e-4
	5e-11	8e-10	3e-8	6e-7	2e-5

**Table 7.4:** Total *current* primary cratering rates onto Pluto for two impactor size distribution scenarios: a knee (top) and a “divot” (bottom) for 5 sample crater threshold diameters with three different values of logarithmic slope  $\alpha_{faint}$ .

see Section 7.3.5) and a model-dependent age could be provided. Conversely, assuming the small impactor size distribution extrapolation follows a single slope of  $\alpha_{faint} = 0.4$ , any saturated surface in  $D \geq 1$  km craters necessarily dates to the pre-installation phase in which there is no absolute calibration of the bombardment rate; we would conclude that little can thus be said about such a region other than it must date to at least  $\gtrsim 4$  Gyr ago.

### 7.3.4 The Effect of Varying $\alpha_{faint}$

To cover a portion of the plausible range of values for the logarithmic slope at the small end ( $d < 100$  km) of the impactor size distribution, we computed cratering rates for two additional single-slope extrapolation  $\alpha_{faint}$  values:  $\alpha_{faint} = 0.3$  ( $q_{faint} = 2.5$ ) and  $\alpha_{faint} = 0.5$  ( $q_{faint} = 3.5$ ). Table 7.4 shows the total cratering rates for these two values of  $\alpha_{faint}$  as well as a repeat of the last line of Table 7.2 where  $\alpha_{faint} = 0.4$  ( $q_{faint} = 3$ ). The SPL is absent in Table 7.4 because the SPL cratering rates do not change when  $\alpha_{faint}$  is varied.  $D \geq 400$  km craters correspond to roughly the impactor diameter at the break in the power-law size

distribution, so the cratering rates at this threshold diameter are also unchanged as  $\alpha_{faint}$  varies. As one moves to smaller diameters, the cratering rates for different slopes diverge, while the factor-of-six difference between the knee and divot scenarios is maintained for crater diameters corresponding to  $d < 100$  km impactors.

Figure 7.8 shows the 4 Gyr curve from Figure 7.5 where  $\alpha_{faint} = 0.4$  along with the 4 Gyr curves for  $\alpha_{faint} = 0.3$  and  $\alpha_{faint} = 0.5$ . The crater equilibrium curve indicates saturation for  $D \lesssim 12$  km and  $D \lesssim 2$  km for the  $\alpha_{faint} = 0.5$  knee and divot scenarios, respectively, in  $\simeq 4$  Gyr of bombardment. Thus, a saturated surface in  $D \sim 1$  km craters does *not* necessarily date to the pre-installation phase.

Because New Horizons should be able to observe craters down to 1-2 km in diameter on the encounter hemisphere, and down to 500 m in diameter in a high-resolution swath (Moore et al., 2015; Young et al., 2008), saturation in either  $D \lesssim 12$  km craters or  $D \lesssim 2$  km craters could be visible on  $\leq 4$  Gyr terrains if  $\alpha_{faint} = 0.5$ . No saturation in  $D \lesssim 12$  km craters would put an upper limit on the value of  $\alpha_{faint}$  at  $\leq 0.5$ , for a heavily cratered terrain and if the impactor size distribution has a single-slope extrapolation in either the form of a knee or a divot at  $d = 100$  km down to sub-km sizes. For  $10 \leq D \leq 100$  km, the slope of the production function may be able to be measured. Again, the slope alone will not be sufficient to provide an absolute age.

Figure 7.9 compares the 4 Gyr relative crater frequency curves from Figure 7.6 with the  $\alpha_{faint} = 0.3$  and  $\alpha_{faint} = 0.5$  cases; clearly  $\alpha_{faint} \approx 0.35$  would produce a flat distribution on the R-plot (corresponding to  $q_{faint} = 2.75$ ). Varying  $\alpha_{faint}$  slightly changes the amount of basin excess visible in the divot scenario, but this will not be discernible. The  $\alpha_{faint} = 0.3$  ( $q_{faint} = 2.5$ ) curve shows a situation where a long-term bombardment would eventually saturate at the largest size craters before the smaller size craters, but in this case, even the smallest primary craters will be far below saturation in 4 Gyr of bombardment. For  $\alpha_{faint} = 0.5$ , craters with  $D \leq 3$  km or  $D \leq 20$  km would be saturated for the divot and knee scenarios, respectively. This would mean a more restricted visible crater diameter

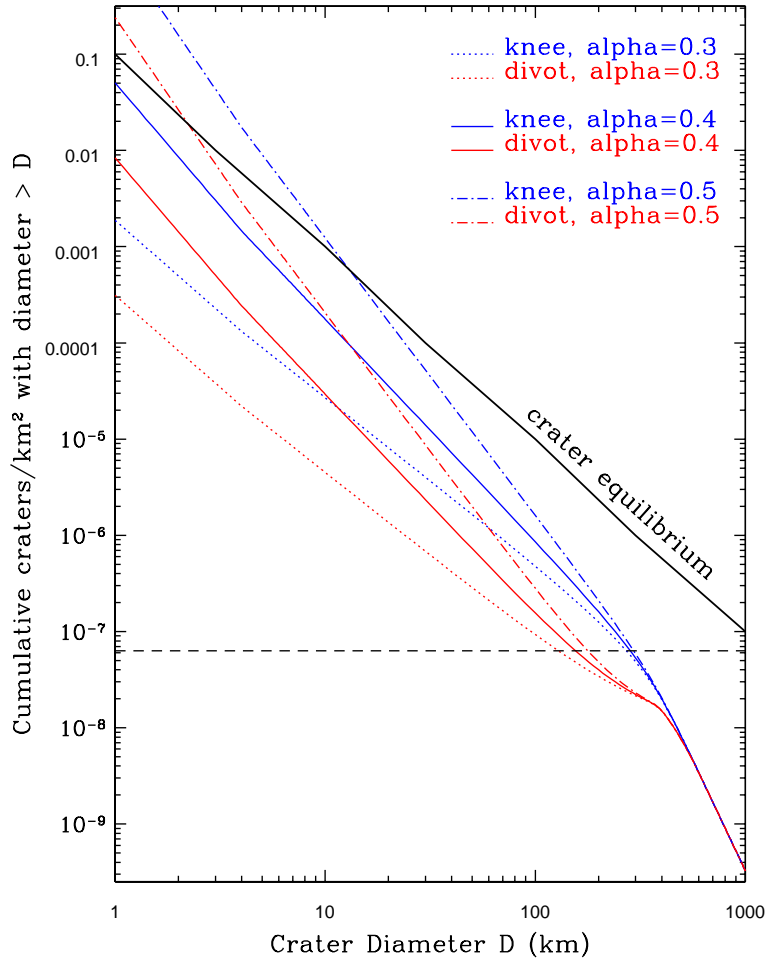


**Figure 7.8:** Logarithm of crater density ( $\#$  craters/ $\text{km}^2$ ) larger than a given crater diameter  $D$  on Pluto's surface in 4 Gyr versus the logarithm of the crater diameter for an impactor size distribution with a knee and with a divot for three values of  $\alpha_{faint}$ . The solid black line is the crater equilibrium curve from Melosh (1989). The horizontal line at  $-7.2$  corresponds to 1 crater/Pluto surface. The slight change in slope at  $D = 4$  km corresponds to the transition from simple to complex craters.

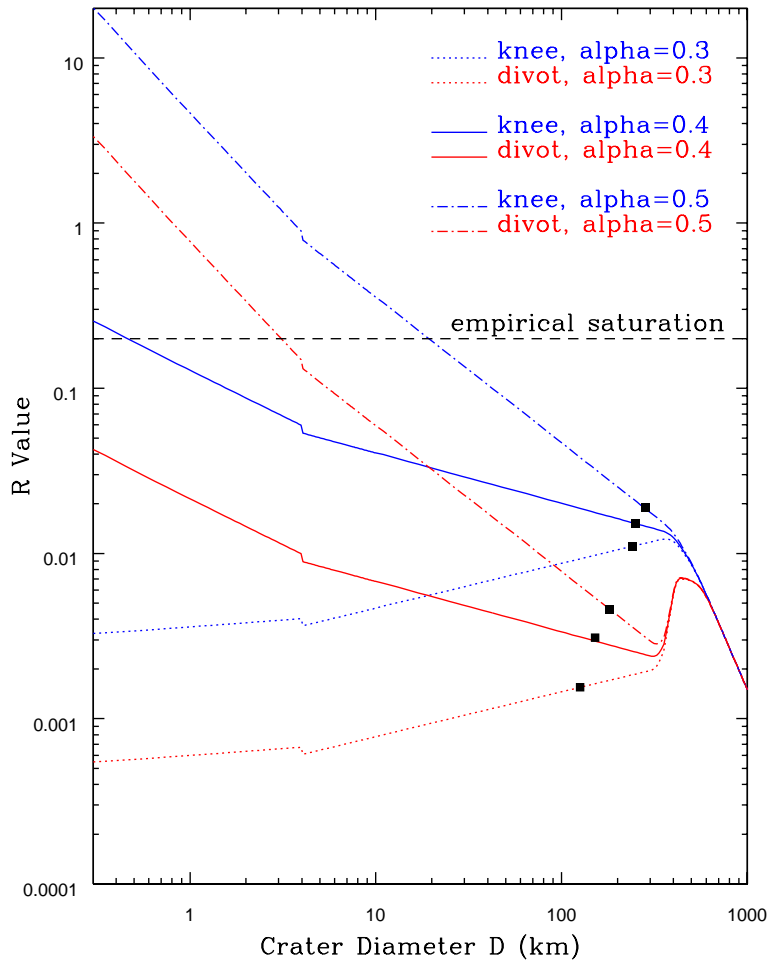


**Figure 7.9:** Relative crater frequency plot, similar to Figure 7.6, but for three values of  $\alpha_{faint}$  over 4 Gyr of flux. The black squares correspond to 1 crater/Pluto surface on a cumulative plot, so unfortunately nothing to the right of those dots will likely be visible on Pluto's post-installation terrains, except by statistical fluctuation. The sudden slope change at  $D = 4$  km corresponds to the transition from simple to complex craters as shown in Figure 7.8.

range (larger than saturation) would be usable for making inferences about the production population.

### 7.3.5 Secondary Craters

The discussion has so far concentrated on primary craters. Secondary craters are expected on Pluto and Charon as well (Bierhaus and Dones, 2015), although of course they are generally much smaller than the primary craters that cause them. A general rule of thumb is that the largest secondaries are 0.05 the size of a given primary (Melosh, 1989), which is in line with more recent studies of icy satellite secondaries (Bierhaus et al., 2012; Singer et al., 2013). Although the largest, proximal secondaries on icy satellites can reach 0.1 the size of their generative primary, the sizes of distant secondaries, which are the ones that can be confused with the primary population (McEwen and Bierhaus, 2006), are much smaller. Secondary populations are generally quite “steep”, with differential size-frequency indices (akin to  $q_{slope}$  for the impactor populations)  $> 3$ . Thus, steep crater SFDs on Pluto or Charon at sizes of a few km or less (Bierhaus and Dones, 2015) should be interpreted cautiously. This will depend on the characteristics of the global crater population, however; if there are relatively few large craters or basins, then their influence on the small crater population *that New Horizons can resolve* will be negligible. In addition, it is unclear if all characteristics of secondary crater production hold for the sub-hypervelocity impact regime. New Horizons should be able to find out, however. The exchange of ejecta between Pluto, Charon, and the four smaller satellites is possible (Stern, 2009). However, the resulting sesquinary craters produced by this exchange will be difficult to distinguish from secondary craters on Pluto.

### 7.3.6 Implications of a “Wavy” Size Distribution

The above analysis has been performed assuming a single-slope extrapolation from  $d > 100$  km impactors to smaller sizes. More likely, the break in the size distribution at  $d = 100$  km is instead the first of several slope changes between

the  $d > 100$  km impactors and the sub-km regime as the “wavy” size distributions of the asteroid belt show. Proposals for outer Solar System populations were made by Minton et al. (2012) (hereafter referred to as M12) and Schlichting et al. (2013) (hereafter referred to as S13). S13’s model for the collision-generated population of KBOs today (shown in their fig. 7) has  $\alpha_{bright} = 0.6$  ( $q_{bright} = 4$ ) for  $d > 60$  km,  $\alpha_{faint1} = 0.2$  ( $q_{faint1} = 2$ ) for  $20 \text{ km} < d < 60$  km,  $\alpha_{faint2} = 0.96$  ( $q_{faint2} = 5.8$ ) for  $2 \text{ km} < d < 20$  km,  $\alpha_{faint3} = 0.32$  ( $q_{faint3} = 2.6$ ) for  $0.2 \text{ km} < d < 2$  km, and  $\alpha_{faint4} = 0.54$  ( $q_{faint4} = 3.7$ ) for  $0.02 \text{ km} < d < 0.2$  km. S13 state the only difference between their small KBO size distribution and the results of the Saturnian crater analysis of M12 (their fig. 1) is that M12 find a shallower slope of  $\alpha_{faint2} = 0.64$  ( $q_{faint2} = 4.2$ ) for the  $2 \text{ km} < d < 20$  km range. D. Minton (private communication, 2014) states M12 was preliminary, so we use his model as stated in Schlichting et al. (2013) simply as another illustrative example of a “wavy” size distribution.

Portions of this “waviness” below  $d = 100$  km may already have been observed in the size distribution observations of the Jupiter family comets (JFCs) by Solonoi et al. (2012). Their fig. 10 shows the cumulative number of JFCs as a function of radius assuming an albedo of  $p = 0.04$ . They find a break in the size distribution at  $d \approx 6$  km from  $\alpha = 0.73$  for  $d \approx 6 - 12$  km to  $\alpha = 0.2$  for  $d \approx 2 - 6$  km. This break between the shallow and steep slopes does not match the location of the M12 and S13 models near  $d = 60$  km where they change from a steep slope ( $\alpha_{bright} = 0.6$ ) to a shallower slope ( $\alpha_{faint1} = 0.2$ ). This break between the steep and shallow slopes does not quite match the location of the M12 and S13 models near  $d = 2$  km where the latter models change from a steep slope ( $\alpha_{faint2} = 0.96$  or  $\alpha_{faint2} = 0.64$ ) to a shallower slope ( $\alpha_{faint1} = 0.32$ ). However, repeating the albedo exercise of Section 7.3.2, an albedo  $p = 0.24$  provides a factor of 3 decrease in break diameter (from  $d = 6$  km to  $d = 2$  km), which would shift the Solonoi et al. (2012) size distribution break to align with the similar diameter break in the M12 and S13 models at  $d = 2$  km.

To illustrate how multiple slope changes in the KBO size distribution affects the cratering history of Pluto, we modeled the described size distributions of M12 and S13 by pegging these two size distributions to the CFEPS KBO sub-population estimates at  $H_g = 9.0$  (corresponding to  $d = 108$  km assuming an albedo of  $p = 0.05$ ). Figure 7.10 shows the cumulative crater density on Pluto using the M12 and S13 impactor size distributions. Because this is a cumulative plot, the abrupt slope transitions smooth out over a range of crater diameters. The smoothing effect is enhanced by our use of the realistic impact velocity spectrum. The two models lie on top of each other for  $D \gtrsim 100$  km, then diverge due to their different slopes from  $10 \text{ km} \lesssim D \lesssim 100$  km before becoming parallel for  $D \lesssim 10$  km where their slopes once again match. The solid diagonal black line in Figure 7.10, representing crater equilibrium, indicates the S13 impactor size distribution saturates for any  $D \lesssim 20$  km in 4 Gyr, while the M12 model does not saturate for  $D \geq 1$  km. The S13 model in fact saturates for  $D \lesssim 12$  km craters in only  $\approx 1$  Gyr. To link this back to the discussion in Section 7.3.4, both the S13 and  $\alpha_{faint} = 0.5$  size distribution models saturate for  $D \lesssim 10$  km craters, so observing saturated craters at this diameter range in New Horizons images will not determine the preferred size distribution model alone. The *shape* of the production function may nonetheless be present in Pluto’s cratering record for craters with  $10 \text{ km} \lesssim D \lesssim 100$  km, however, as long as saturation of the entire surface in small craters does not corrupt (i.e., degrade recognition of) the  $D = 10 - 100$  km range.

Figure 7.11 compares the relative crater frequency for the M12 and S13 models with the single-slope knee and divot scenarios presented earlier, for three sample bombardment durations. The drop in relative crater frequency from  $D \approx 400$  km and  $D \approx 100$  km in Figure 7.11 for the M12 and S13 models is due to their shallow slope ( $\alpha_{faint1} = 0.2$ ) in this crater diameter range being less than  $\alpha \approx 0.35$ °. This drop is different from the sudden drop in the relative crater frequency from  $D \approx 500$  km to  $D \approx 350$  km due to a divot in the impactor size

---

°For the crater scaling law in use,  $\alpha \approx 0.35$  produces an R value that does not depend on  $D$ .

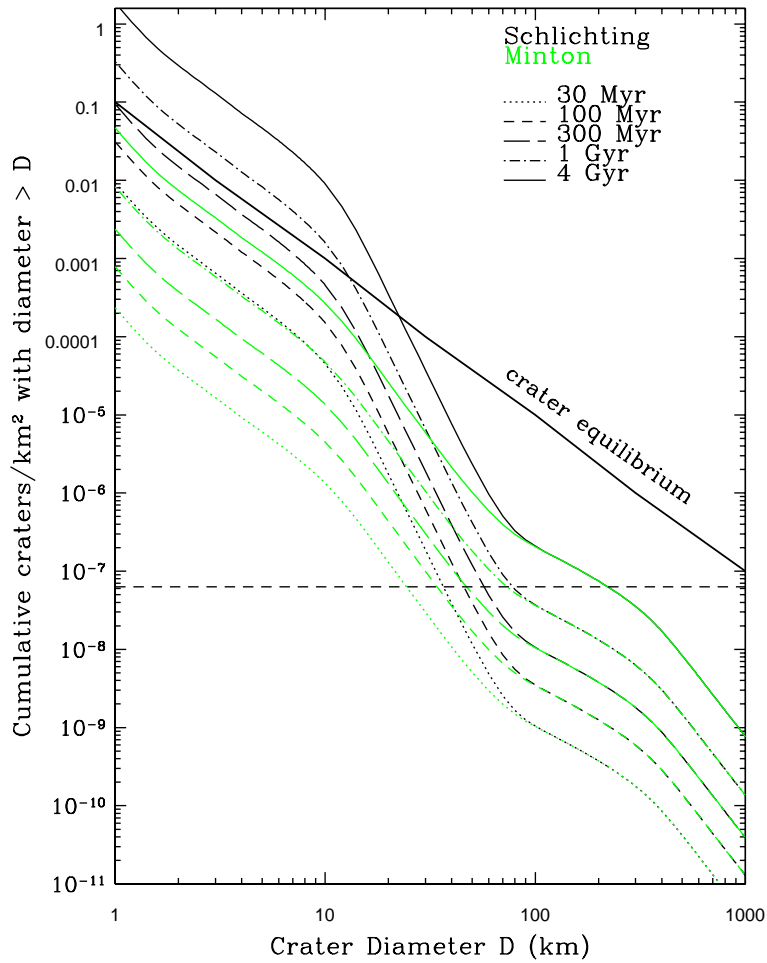


**Figure 7.10:** Logarithm of crater density (# craters/km<sup>2</sup>) larger than a given crater diameter  $D$  on Pluto's surface versus the logarithm of the crater diameter  $D$  for the impactor size distributions from Minton et al. (2012) and Schlichting et al. (2013), for various exposure durations. The solid black line is the crater equilibrium curve from Melosh (1989). The horizontal line at -7.2 corresponds to 1 crater/Pluto surface.

distribution. As shown in Figure 7.11, the basin excess due to the divot is more tightly confined to a small crater diameter range than the broad “dip” that would be present from  $D = 50$  km to  $D = 500$  km in the M12 and S13 models. Unfortunately, this size range will not be expressed in the Pluto cratering record in 4 Gyr of bombardment (solid squares in Figure 7.11, although it might be going further back in time). The very steep slope between  $D = 10$  km and  $D = 100$  km in the S13 model produces rapidly increasing crater densities as  $D$  drops and saturates at even  $D \approx 20$  km in 4 Gyr. We also note the upturn (steepening) of the crater SFD at small ( $D < 2$  km) sizes in Figure 7.11. Nominally, this could be interpreted as evidence of secondary contamination as discussed above, but given the overall steepness of the M12 and S13 distributions, this would be physically unlikely.

The crater diameter range most reliable for the interpretation of Pluto’s cratering record provided by the New Horizons spacecraft will likely be the  $D \approx 30 - 100$  km range where one might hope to have the slope of the production function measured. Because we expect models with multiple slope changes make a more realistic representation of the impactor size distribution than a single slope, the “waviness” should be present in the production function. Depending on the age of the surface, however, it is likely there will be difficulties in saying anything about the shape of the implied impactor size distribution for this crater diameter range. The range for which the production function would be measurable obviously increases as a function of surface age (left of the colored squares in Figure 7.11). While direct observation of the crater distribution in the  $30 \text{ km} \leq D \leq 100 \text{ km}$  range will thus establish relative numbers of impactors as well as the shape of the production function, it will *not* by itself provide a firm connection to the absolutely calibrated  $d > 100$  km impactors. As a result, only model-dependent ages can be found for the surfaces of Pluto and Charon. For example, if  $R \approx 0.003$  for  $D \approx 30$  km craters on Pluto, one would conclude a crater retention age of  $\approx 100$  Myr if the S13 model is the best representation of the impactor size distribution,  $\approx 1$  Gyr if the M12 or single-slope  $\alpha_{faint} = 0.4$

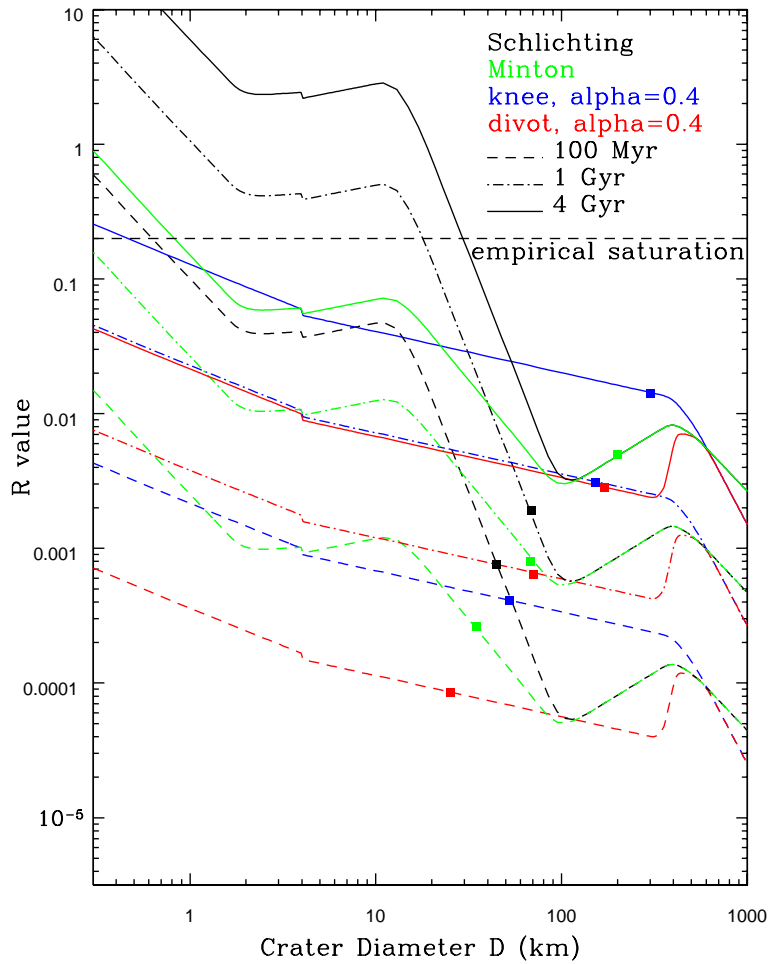


**Figure 7.11:** Relative crater frequency plot for the Minton et al. (2012) and Schlichting et al. (2013) impactor size distribution models and the  $\alpha_{faint} = 0.4$  knee and divot extrapolations. The colored squares correspond to 1 crater/Pluto surface on a cumulative plot, so nothing to the right of those dots will likely be visible on Pluto's post-installation terrains.

knee size distributions are most accurate, or  $\approx 4$  Gyr if one favors the  $\alpha_{faint} = 0.4$  divot size distribution.

Even if the surface of Pluto (and especially Charon) is completely saturated, one would still hope to be able to find the largest “fresh” crater to have formed on the surface and attempt to measure the production function superposed on this “fresh” crater and its ejecta blanket. Using any of the size distributions discussed (S13 model, M12 model, knee with  $\alpha_{faint} = 0.4$ , or divot with  $\alpha_{faint} = 0.4$ ), we compute that to 95% confidence there has been at least one  $D \gtrsim 50$  km crater formed within the past 1 Gyr and this thus sets the scale for the largest “fresh” feature one might hope to find on Pluto’s surface. Figure 7.12 is similar to Figure 7.10 for up to 1 Gyr of bombardment from the S13 and M12 models. The horizontal line corresponds to 1 crater/surface area of that largest “fresh”  $D \gtrsim 50$  km crater and its ejecta blanket (which we take to be roughly 100 km in diameter). The superposed production function can thus be measured above this horizontal line.

Because the S13 and M12 models have the same slope for the portion of the impactor size distribution corresponding to the above crater diameter range, only model dependent ages can be determined for such a surface. Such ages will differ by a factor of  $\approx 30$  between the S13 and M12 models, as indicated by the near overlap of the 1 Gyr M12 curve and the 30 Myr S13 curve in Figure 7.12. However, the two scenarios yield a rather different qualitative picture. The  $D \gtrsim 50$  km crater that formed to 95% confidence  $\approx 1$  Gyr ago will already have saturated if the S13 model is correct (and, dramatically, due to all craters at *all* diameter bins below  $\approx 15$  km). Even at the mean formation interval<sup>d</sup> for a  $D \gtrsim 50$  km crater of 300 Myr, the largest “fresh” crater present on Pluto should have nearly reached saturation in the S13 model scenario. Therefore, the S13 model would predict there are most likely *no* large unsaturated craters on Pluto; only such a steep size distribution can cause the surface to saturate so quickly. Observing such a sit-

---

<sup>d</sup>That is, the mean time between formation of  $D \gtrsim 50$  km craters on Pluto is 300 Myr, even if it takes a Gyr to be 95% confident that one will be formed on the surface.

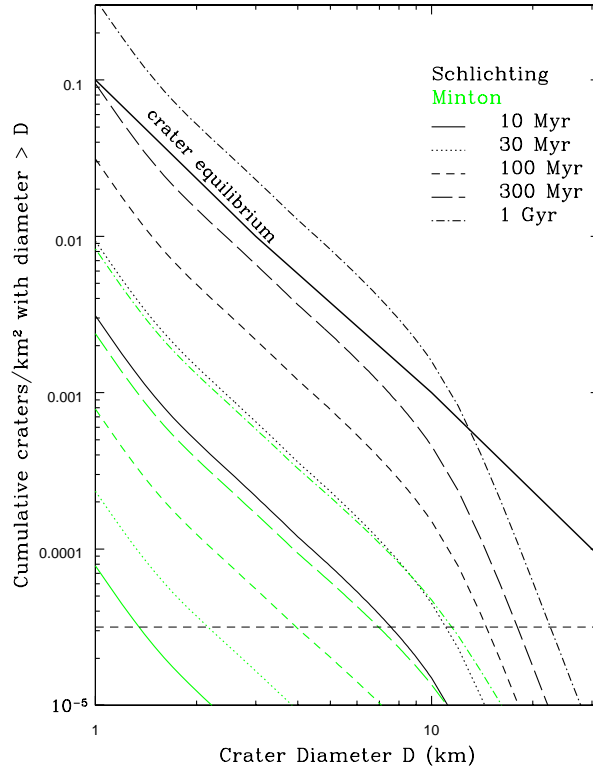


**Figure 7.12:** Logarithm of crater density ( $\# \text{ craters}/\text{km}^2$ ) larger than a given crater diameter  $D$  on Pluto’s surface versus the logarithm of  $D$ , for the impactor size distribution from Minton et al. (2012) and Schlichting et al. (2013), for various exposure durations. The dashed horizontal line corresponds to one crater superposed on a  $D \gtrsim 50$  km crater and its 100 km diameter ejecta blanket (to 95% confidence the largest “fresh” crater which will have formed in the past 1 Gyr). The solid diagonal line is the small-crater equilibrium curve. The S13 model indicates it is unlikely any  $D \gtrsim 50$  km “fresh” crater on Pluto’s surface will not appear heavily cratered and near saturation (e.g., see the crater Penelope on Tethys). In contrast, the M12 model suggests the “freshest”  $D \gtrsim 50$  km crater floor will not be near saturation and a production function should be measurable on the crater floor and surrounding ejecta blanket. A “freshest”  $D \gtrsim 50$  km crater which is lightly cratered would need to be tens of Myr old in the S13 model scenario.

uation on Pluto would support the occultation measurement (Schlichting et al., 2012) motivating the S13 model.

If, however, one or several un-saturated “fresh”  $D \gtrsim 50$  km craters are present on Pluto, a superposed crater production function should be measurable (depending on proximity to the terminator at encounter), and a model-dependent age (varying by a factor of  $\approx 30$ ) could be assigned to the region. For example, again examine the overlapping 30 Myr S13 and 1 Gyr M12 model curves in Figure 7.12. Nominally the production function might look like the 1 Gyr M12 model (with a largest superposed crater of  $D \approx 12$  km); but the S13 model would imply a 30 Myr crater retention age and that the 50 km crater formed extremely recently. However, the S13 model suggests a mean formation interval of 300 Myr for  $D \gtrsim 50$  km, with thus only a low  $30/300 = 10\%$  probability of the crater having formed recently enough to be so lightly cratered, making this proposed projectile size distribution less likely. In contrast, the M12 model would expect a mean formation interval of  $\approx 1$  Gyr for  $D \gtrsim 50$  km craters. There is thus likely a way to test the qualitative difference between these two models from the New Horizons data alone at least in terms of likelihood.

This “largest fresh crater in a Gyr” argument was chosen to illustrate how quickly the very steep size distribution of the S13 model would predict even the “freshest” craters saturate. The largest “fresh” crater expected to form (95% confidence) can, however, be computed for any time interval. For an event in the last Gyr, neither model would predict the “fresh” crater to be saturated, however the number of craters expected to be on the crater floor and its ejecta blanket will be different between the two models as the reasoning above describes. For example, the largest “fresh” crater expected to form (to 95% confidence) in 100 Myr ( $D \gtrsim 30$  km) is not much smaller than in 1 Gyr ( $D \gtrsim 50$  km) due to the steep impactor size distribution in this portion of the crater production function. The S13 model would predict there should be a measurable production function on this surface, especially if the crater is close to 100 Myr old. The M12 model, on the other hand, would predict very few craters should be present on the “fresh-

est”  $D \gtrsim 30$  km crater if it formed 100 Myr ago. Qualitatively, the S13 model’s very steep size distribution would predict that all “fresh” craters should be quickly re-cratered and the M12 model would predict re-cratering to occur less rapidly.

We note this line of argument will be complicated or obviated if Pluto’s surface is extremely young due to surface-atmospheric interactions (Stern et al., 2015). An analogous argument may work for Charon, however, and is discussed in Section 7.3.7.

### 7.3.7 Charon

Zahnle et al. (2003) state that the impact rate onto Charon is 16% that on Pluto accounting for gravitational focusing with an average system encounter velocity of 1.9 km/s. Using our modified Öpik collision probability code, we find the total impact rate onto Charon from the various Kuiper belt sub-populations is  $9.2 \times 10^{-12}$ /yr for  $H_g < 9$  impactors. This is  $(9.2 \times 10^{-12}/\text{yr}) / (4.8 \times 10^{-11}/\text{yr}) = 0.19$  that of the total impact rate on Pluto, in rough agreement with Zahnle et al. (2003). This multiplicative factor does not, however, convert total Pluto cratering rates into total Charon cratering rates. The crater scaling law (shown in equations (5.3), (5.4a), and (5.4b)) for Charon is influenced by the different value of gravitational acceleration  $g$  on Charon ( $g = 26 \text{ cm/s}^2$ ) from on Pluto ( $g = 64 \text{ cm/s}^2$ ) and a different impact velocity range because Charon’s escape speed ( $v_{esc} = 0.675 \text{ km/s}$ ) is smaller than Pluto’s ( $v_{esc} = 1.2 \text{ km/s}$ )<sup>e</sup>. The difference in the crater scaling law between Pluto and Charon means each crater diameter corresponds to a different impactor diameter for Charon than on Pluto, so each size distribution extrapolation (SPL/knee/divot) produces a different cratering rate *larger than some fixed crater D* on Charon compared with that on Pluto. The outcome is shown in Table 7.5.

The cratering rates for fixed threshold crater diameter on Charon are  $\approx 40\%$  that on Pluto for the SPL cases and  $\approx 25\%$  for the knee and divot scenarios. It is

---

<sup>e</sup>For a typical  $v_\infty$ , a fixed-diameter impactor is accelerated less by the smaller gravitational focusing of Charon compared with that of Pluto, but the  $\approx 2.5$  times smaller gravitational acceleration  $g$  for Charon outweighs this velocity effect, resulting in larger craters on Charon than on Pluto for a fixed impactor diameter.

Size Distribution Extrapolation	Current Total Cratering Rate $D \geq 400$ km (/yr)	Current Total Cratering Rate $D \geq 100$ km (/yr)	Current Total Cratering Rate $D \geq 30$ km (/yr)	Current Total Cratering Rate $D \geq 10$ km (/yr)	Current Total Cratering Rate $D \geq 3$ km (/yr)
SPL	2e-11	1e-8	4e-6	6e-4	2e-1
Knee	2e-11	7e-10	1e-8	1e-7	3e-6
Divot	1e-11	1e-10	2e-9	2e-8	4e-7

**Table 7.5:** Current total primary cratering rates onto Charon ( $\approx 25\%$  to  $\approx 40\%$  those on Pluto) using our derived impact velocity distribution for all Kuiper belt sub-populations and three impactor size distribution scenarios: single power-law (SPL) (top), knee (middle), and “divot” (bottom) for 5 threshold crater diameters.

unsurprising that the knee and divot scenarios give the same multiplicative factor for the cratering rate on Charon to that on Pluto, because they have the same slope for  $d < 100$  km impactors. The SPL slope diverges from the knee/divot slope at smaller diameters, so because Charon’s cratering rate accesses smaller impactors than Pluto for the same crater diameter threshold, the Charon SPL cratering rates should be a larger percentage of the Pluto SPL cratering rates than for the Charon-to-Pluto knee/divot cratering rates. The integrated number of craters estimated on Charon’s surface over the last 4 Gyr are shown in Table 7.6. Since there is not a simple conversion from cratering rates on Pluto to those on Charon, Figure 7.13 provides both the crater density plot and R-plot for Charon using the single-slope knee/divot size distribution extrapolations with  $\alpha_{faint} = 0.4$  as well as the M12 and S13 size distributions.

This allows model-dependent ages to be determined for a post-installation Charon just as is possible for a post-installation Pluto as discussed in Sections 7.3.1 and 7.3.3 above. As implied earlier, Pluto’s active surface-atmosphere exchange and volatile surface ices ( $\text{CH}_4$ ,  $\text{N}_2$ ) may work together to yield either a young surface, or obscure an older, heavily cratered one (Stern et al., 2015). Charon, however, has none of these ices on its surface to our knowledge, no de-

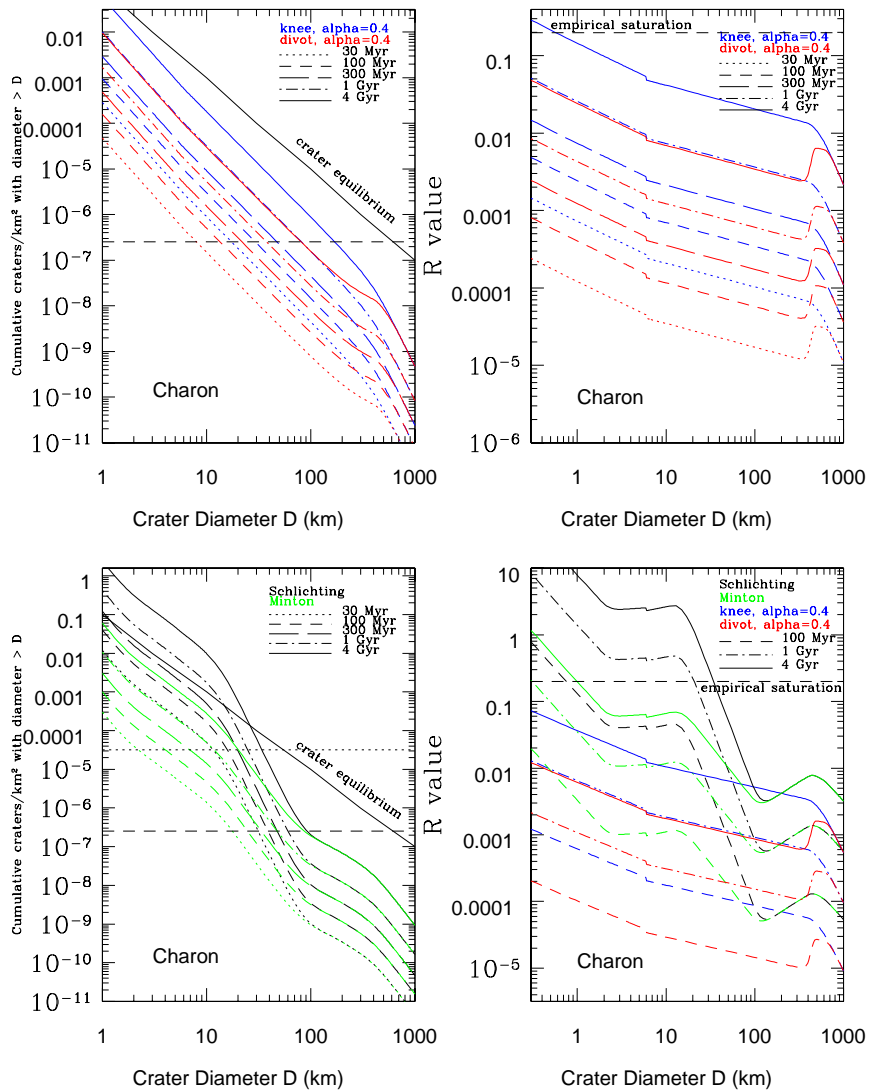


**Figure 7.13:** Top Left: Similar to Figure 7.5 except for Charon. The horizontal line at -6.6 corresponds to 1 crater/Charon surface. Top Right: Relative crater frequency plot for Charon. Similar to Figure 7.6 except for Charon. Bottom Left: Similar to Figure 7.10 except for Charon. Bottom Right: Similar to Figure 7.11 except for Charon.

Size Distribution Extrapolation	Total Crater Number $D \geq 400$ km	Total Crater Number $D \geq 100$ km	Total Crater Number $D \geq 30$ km	Total Crater Number $D \geq 10$ km	Total Crater Number $D \geq 3$ km
SPL	0.1	80	20000	3e+6	1e+9
Knee	0.09	3	50	7e+2	1e+4
Divot	0.05	0.6	9	1e+2	2e+3

**Table 7.6:** Cumulative number of craters over the past 4 Gyr on the surface of Charon for 5 sample threshold crater diameters for three impactor size distribution scenarios (SPL/knee/divot) given in Table 7.5.

tectable atmosphere (Sicardy et al., 2006), and as a smaller body should be internally cooler and less active (McKinnon et al., 2008). It should possess older if not ancient surfaces. In principle, a basin excess due to the presence of a divot in the impactor differential size distribution (discussed in Section 7.3.2) may possibly be visible on Charon’s most ancient surfaces. Note that the visible crater diameter range for which the production function (over 4 Gyr) can be measured is shifted to slightly smaller craters on Charon than on Pluto. The crater SFDs measured on both bodies for these overlapping crater diameter ranges ( $D = 20 - 60$  km on Charon and  $D = 30 - 100$  km on Pluto) should provide the most reliable insights into the cratering history of the Pluto system and thus the size distributions in the Kuiper belt. Note that because Charon is tidally locked, a leading/trailing crater asymmetry is possible; the ratio  $v_{orb}/v_{\infty} \sim 0.1$  is comparable to that of Earth’s Moon (Gallant et al., 2009) and so a  $\sim 10\%$  enhancement (deficit) of the of the crater density near Charon’s apex (antapex) of motion relative to the mean crater density may be visible if the global coverage is sufficient.

To parallel the discussion at the end of Section 7.3.6, the largest “fresh” crater to have formed on Charon in 3 Gyr (chosen to illustrate the timescale the S13 model predicts rapid resaturation for Charon, compared with 1 Gyr on Pluto) to 95% confidence according to the S13 impactor size distribution model is, coincidentally, also  $\approx 50$  km in diameter. As shown in Figure 7.12, the horizontal line at -4.5 in the bottom left panel of Figure 7.13 corresponds to 1 crater/surface

area of that largest “fresh”  $D \gtrsim 50$  km crater and its 100 km ejecta blanket. Just as on Pluto, the S13 model would predict this  $D \gtrsim 50$  km crater should saturate quickly, whereas the M12 model would not predict this crater to reach saturation in 3 Gyr. No matter the size of the “freshest” crater one looks for on Charon (as on Pluto), the distinguishing property of the two size distribution models is how likely the crater is to be re cratered after formation.

### 7.3.8 The Four Smaller Moons

We have not repeated our full analysis for the four smaller satellites of Pluto (Styx, Nix, Kerberos, and Hydra). Instead, we have estimated the time (to roughly a factor of three accuracy) it would take for each of these satellites to be catastrophically disrupted using the current Kuiper belt sub-populations. Our estimate is based on the timescale between collisions for catastrophic dispersal of the target body, calling this the “disruption timescale”. We compute one disruption timescale estimate for Nix and Hydra since they are of comparable size and another for Styx and Kerberos. Taking the diameter of Nix and Hydra to be  $\approx 45$  km (using mass, albedo = 0.4, and density estimates from Kenyon and Bromley (2014)), we use the catastrophic disruption threshold equation for the dispersal of half the target mass from Leinhardt and Stewart (2012),

$$Q^*_{RD} = 0.5\mu V^{*2}/M_{total} \quad (7.2)$$

where  $Q^*_{RD}$  is the specific energy required for dispersal of a catastrophically disrupted body,  $\mu$  is the reduced mass ( $M_{projectile}M_{target}/M_{total}$ ),  $V^*$  is the critical impact velocity for catastrophic disruption, and  $M_{total}$  is the total mass of the projectile and target. Assuming  $M_{target} \gg M_{projectile}$ , we solve the above equation for the mass of the projectile needed to disperse the target, assuming  $V^* \approx 1.5$  km/s (mostly from  $v_\infty$  since the orbital speed around the Pluto-Charon barycenter and escape velocity are small) and estimating  $Q^*_{RD}$  from figure 11 of Leinhardt and Stewart (2009) for an icy target 45 km in diameter ( $Q^*_{RD} = 7 \times 10^3$

J/kg, similar to that from figure 7 of Benz and Asphaug (1999)). We find that for catastrophic dispersal of either Nix or Hydra an impactor with diameter  $d \geq 8$  km is needed<sup>f</sup>. Scaling the impact probability onto Pluto by the ratio of surface areas corrected for gravitational focusing gives the impact probability (/yr/projectile) for each sub-population onto Nix and Hydra. Multiplying each impact probability by the number of objects with  $d \geq 8$  km for each sub-population gives the catastrophic disruption rate (/yr) for each sub-population. The resulting total current catastrophic disruption rate onto Nix and Hydra is  $3.5 \times 10^{-12}$ /yr for the  $\alpha_{faint} = 0.4$  knee size distribution scenario. The disruption time for Nix and Hydra is therefore  $\approx 300$  Gyr for the  $\alpha_{faint} = 0.4$  knee size distribution extrapolation for the *current* impactor population, and six times this,  $\approx 1800$  Gyr, for the divot. Integrating back to the larger impact rate  $\simeq 4$  Gyr ago, the disruption time decreases to  $\approx 200$  Gyr for the knee scenario and  $\approx 1200$  Gyr for the divot. Comparing these estimates to those from the two “wavy” impactor size distributions, at this impactor size, the number of objects in the projectile population is similar to the knee scenario, so these “wavy” size distributions also would not result in catastrophic disruption of Nix and Hydra. Even if the critical impact velocity is increased to the tail of Pluto’s impact velocity spectrum (6 km/s), where the speeds are higher but the impact probabilities are lower, the disruption timescale under the current bombardment is still longer than the age of the Solar System.

For comparison, the crater scaling law (equation (5.3)) requires an impactor of roughly  $d \geq 4$  km to produce a crater diameter that exceeds the moon’s. This translates to a “disruption timescale” a factor of a few smaller than the estimate given above, but this is because the dispersal of the target is not accounted for in the crater scaling law. In either case, Nix and Hydra have very likely never been catastrophically disrupted under the current bombardment of the past  $\approx 4$  Gyr.

---

<sup>f</sup>Strictly speaking, these estimates are for disassembly of the moon against its own gravitational binding. The dispersed fragments would mostly remain in orbit around Pluto-Charon and reassemble. Even larger impactors would be necessary to disperse a small moon permanently (eject fragments onto heliocentric orbits).

A similar argument was followed for Styx and Kerberos with diameters of roughly 10 km (mass and density estimates from Kenyon and Bromley (2014)), where we estimate  $Q^*_{RD}$  for an icy target 10 km in diameter ( $Q^*_{RD} = 8 \times 10^2$  J/kg). Using the same reasoning as before, the current disruption timescale for Styx and Kerberos is therefore  $\approx 70$  Gyr for the  $\alpha_{faint} = 0.4$  knee size distribution extrapolation under the current impactor population estimates, and six times this,  $\approx 420$  Gyr for the divot.

This begs the question of the smallest satellite that could survive against catastrophic disruption in the current bombardment environment. Figure 7.14 shows the catastrophic disruption timescale (in Gyr) as a function of target radius (in m) for the  $Q^*_{RD}$  curves from Leinhardt and Stewart (2009) and Benz and Asphaug (1999). The Benz and Asphaug (1999) curve for impacts at 3 km/s and an incidence angle of  $45^\circ$  is most typical for impacts in the Kuiper belt, so we will use it in the discussion to follow, while the Leinhardt and Stewart (2009) curve for low speed, head-on collisions is shown for comparison. As can be seen in Figure 7.14, for a knee size distribution with  $\alpha_{faint} < 0.5$  (down to sub-km sizes) all target sizes would survive catastrophic disruption over the past 4 Gyr. As the target size decreases, the  $\alpha_{faint} = 0.4$  knee size distribution corresponds to a situation where the cumulative number of impactors available to catastrophically disrupt the target increases at the same rate that the surface area of the target decreases (both as  $d^2$ ), causing the two effects to cancel. This results in the catastrophic disruption rate decreasing as large targets get smaller (down to  $d = 100$  m) and then increasing at smaller sizes as targets enter the strength-scaled regime for  $Q^*_{RD}$ . As  $\alpha_{faint}$  decreases, the catastrophic disruption timescale moves to higher values as the cumulative number of impactors rises less steeply at small sizes, resulting in longer timescales between catastrophic disruption events. Conversely, as  $\alpha_{faint}$  increases and more small impactors are available, the catastrophic disruption timescale drops. For  $\alpha_{faint} = 0.5$  and typical impacts in the Kuiper belt, the Benz and Asphaug (1999) curve shows that the smallest target expected to survive catastrophic disruption in the last 4 Gyr is  $\approx 4$  km in diameter. Thus, if New

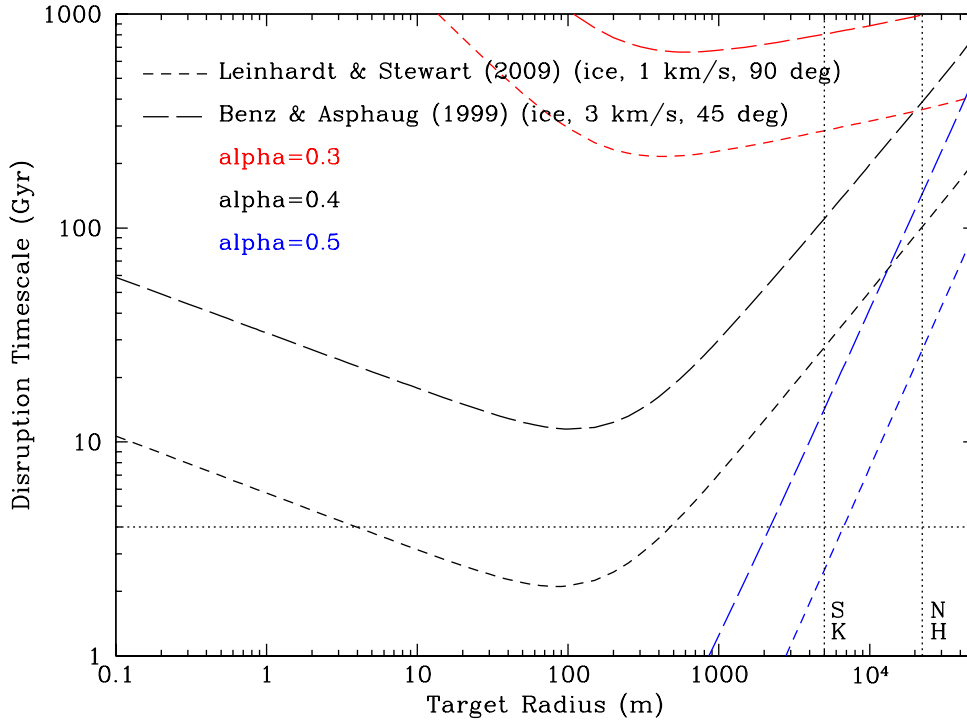


**Figure 7.14:** Catastrophic disruption timescale (Gyr) as a function of target radius (m) for the  $Q_{RD}^*$  curves from Leinhardt and Stewart (2009) and Benz and Asphaug (1999) and three values of  $\alpha_{faint}$  (size distribution with a knee). The vertical line at  $r = 5$  km is roughly the radius of Styx and Kerberos and the vertical line at  $r = 22.5$  km is roughly the radius of Nix and Hydra. For 3 km/s impacts at an incidence angle of  $45^\circ$  and  $\alpha_{faint} = 0.4$ , all size targets are able to survive against catastrophic disruption in the past 4 Gyr. For  $\alpha_{faint} = 0.4$ , the catastrophic disruption timescales for Styx and Kerberos is  $\approx 100$  Gyr and  $\approx 400$  Gyr for Nix and Hydra.

Horizons finds satellites in the Pluto system that are smaller than  $\approx 4$  km in diameter, it either means an impactor size distribution with  $\alpha_{faint} \geq 0.5$  (down to sub-km sizes) can be ruled out or that those satellites have catastrophically disrupted and reassembled in the past 4 Gyr. In principle, one could use the slope of the crater production function (for the sub-km diameter range) on Pluto or Charon to determine which of these two scenarios is more likely to be true.

Returning to the Pluto system four small satellites, Figure 7.14 shows that for typical impacts in the Kuiper belt (given by the Benz and Asphaug (1999) curve) it is unlikely that any of the four small satellites have catastrophically disrupted and reassembled in the past 4 Gyr.

## 7.4 Summary and Conclusions

By combining the contributions of each Kuiper belt sub-population from the well-calibrated CFEPS (Gladman et al., 2012; Petit et al., 2011) model and the Kaib et al. (2011) KRQ11 scattering object model calibrated by Shankman et al. (2013), the impact rates and especially impact velocity spectra onto Pluto as presented here are currently state of the art. Pluto’s environment before its installation onto its current orbit (which occurred roughly 4 Gyr ago) is unknown, so primary cratering rates have been presented for “current day” timescales (a few hundred million years) and the number of craters larger than a threshold diameter  $D$  have been provided for Pluto’s post-installation phase covering the past  $\simeq 4$  Gyr of the Solar System’s history accounting for the natural erosion of each Kuiper belt sub-population. We find it is unlikely Pluto has been hit by even a single impactor that would create a  $D > 400$  km crater, eliminating the chance that Pluto’s post-installation cratering record can be immediately linked to the absolutely-calibrated impactor size distribution for  $d > 100$  km. As a result, in order to date the surfaces of Pluto and Charon using observed crater densities, assumptions must be made about how the impactor size distribution extrapolates to small (sub-km) sizes. This is fraught with uncertainty, since we do not know how to connect the  $d > 100$  km impactors to the smaller impactors. In this study

we first adopt a single-slope  $\alpha_{faint} = 0.4$  ( $q_{faint} = 3$ ) power-law for the faint end ( $d < 100$  km) of the size distribution, which is motivated by direct observations of small Centaurs, and highlight the factor-of-six variation between the knee and “divot” size distribution scenarios for this size regime. In addition, we show the effect of varying  $\alpha_{faint}$  (to  $\alpha_{faint} = 0.3$  and  $\alpha_{faint} = 0.5$ ) on Pluto’s cratering record. We also study how the “wavy” size distributions of Schlichting et al. (2013) and Minton et al. (2012) (as presented in Schlichting et al. (2013)), which include several slope changes between the  $d = 100$  km impactors and the sub-km regime, would manifest in Pluto’s cratering record.

Complications and insights into computing and interpreting New Horizons observations of the cratering record on Pluto and its satellites include:

- No single Kuiper belt sub-population contributes the majority of the impact flux on the surface of Pluto (in fact, four sub-populations dominate the impact flux, the  $q < 42$  AU hot classical mains, the  $q < 42$  AU stirred classical mains, the classical outsiders, and the plutinos, each providing roughly equal contributions), so multiple Kuiper belt sub-populations must be used to accurately determine cratering rates.
- Impact velocities onto Pluto range from 1.2 km/s (Pluto’s escape speed) out to a tail at  $\approx 6$  km/s, so more smaller impactors can be accessed when computing the cratering rates on Pluto than a simple-impact-velocity assumption would give, resulting in slightly higher cratering rates than previously estimated, which translates into younger surface ages.
- The production function present in Pluto’s cratering record will not link the absolutely calibrated impactor size distribution for  $d > 100$  km objects to the size distribution of the  $d < 100$  km impactors, because we do not expect craters created by the  $d > 100$  km impactor size range to be present on Pluto’s post-installation terrains.
- The result is that for any surface region reset after Pluto’s installation onto its current orbit that has not reached saturation, absolute surface ages com-

puted for Pluto and Charon simply cannot be done to better than the uncertainties in the impactor size distribution extrapolation. Thus, the best that can currently be done is to compute model-dependent ages for young surfaces on Pluto and Charon.

- If a divot is present in the impactor size distribution, a narrow-diameter-range “basin excess”, similar to what has been observed on Iapetus, could possibly be visible on Pluto (or Charon) if a  $> 4$  Gyr Pluto (or Charon) surface can be identified, implying that any basins found on Pluto must date back to Pluto’s pre-installation phase.
- Because a size distribution model with multiple slope changes is likely a more accurate representation of the impactor population than an extrapolation of a single slope from impactors with  $d = 100$  km down to sub-km sizes, the “waviness” may be easily discernible in Pluto’s cratering record, both in the shape of the crater size distribution as well as in the crater saturation diameter, if non-saturated regions can be found.
- The “waviness” of the production function will most likely be discernible in the  $D \approx 30 - 100$  km craters on Pluto and the  $D \approx 20 - 60$  km craters on (smaller) Charon, making these the most reliable crater diameter ranges to the interpretation of the Pluto system cratering record provided by the New Horizons spacecraft. (These upper limits reflect likely maximum sized craters formed over 4 Gyr.)
- Even if the surface of Pluto appears saturated, one would like to measure the crater densities present on the largest “fresh” surfaces available. We estimate in Section 7.3.6 (at 95% confidence) that in 1 Gyr of bombardment at least one  $D \gtrsim 50$  km crater will be created on Pluto (using any of the impactor size distribution models discussed, except the SPL), providing a fresh surface upon which the production function should be measurable. The M12 and S13 “wavy” impactor size distribution models would make

different predictions about how likely that “fresh”  $D \gtrsim 50$  km crater would be at or near saturation. Thus, there is likely a way to test the qualitative difference between these two models from the New Horizons data alone.

- We find that Charon’s impact rate is 19% that on Pluto, roughly consistent with Zahnle et al. (2003)’s estimate. However, because the cratering rate depends on the size distribution extrapolation used, Charon’s cratering rate at fixed crater size is  $\approx 25 - 40\%$  that on Pluto for the knee/divot and SPL extrapolations, respectively.
- We estimate the timescale between collisions for catastrophic disruption for Pluto’s four smaller moons (Styx, Nix, Kerberos, and Hydra). We find it is likely that none of these satellites have been catastrophically disrupted in the past  $\approx 4$  Gyr.
- For a knee size distribution with  $\alpha_{faint} \leq 0.4$  (down to sub-km diameters), satellites of all sizes can survive catastrophic disruption in the past 4 Gyr. For  $\alpha_{faint} \geq 0.5$  and typical Kuiper belt impact speeds, the smallest satellite that should survive catastrophic disruption in the past 4 Gyr is  $\approx 4$  km in diameter.
- It will be difficult to accurately interpret Pluto’s cratering record until future observations of outer Solar System small bodies carefully probe the  $d = 10 - 100$  km ( $H_g = 9 - 14$ ) impactor size range (connecting the  $d \approx 1 - 10$  km JFC size distribution (Solonoi et al., 2012) to the  $d > 100$  km size distribution of the KBO/scattering/plutino populations from CFEPS (Gladman et al., 2012; Petit et al., 2011)) that could directly establish the linkage via the number distribution of the current projectile population. While there currently are thus fragments of the observed impactor size distributions across the outer Solar System small body populations, the entire diameter range is needed to make definitive statements about crater retention ages on the surfaces of Pluto and its moons.

## 7.5 Some Predictions for the 2015 New Horizons Observations of the Cratering Record in the Pluto System

- Craters large enough to connect Pluto’s visible cratering record ( $D < 100$  km) with the absolutely calibrated impactor size distribution for  $d > 100$  km impactors will not be present on Pluto’s post-installation terrains. The question will be how to separate Pluto’s post-installation terrains from its pre-installation surfaces.
- A basin excess on pre-installation terrains due to the presence of a divot in the impactor size distribution may possibly be visible on Pluto (or Charon), similar to what has been observed on Iapetus. The extensive presence of volatile ices on Pluto may very well cause Charon to have an older surface than Pluto, in which case a basin excess could possibly only be visible on Charon.
- The impactor size distribution should be easily discernible in Pluto’s cratering record via the shape of the production function in the  $D \approx 1 - 100$  km range for craters larger than the saturation diameter (if any).
- Only the very steepest size distribution of Schlichting et al. (2013) would predict the cumulative crater density measured on Pluto or Charon should rise  $\approx 4.5$  orders of magnitude from the  $D = 100$  km craters to the  $D = 10$  km craters, implying rapid saturation of the surface, unlike the M12, knee, and divot size distribution models. Thus, we expect at least one “fresh”  $D \approx 50$  km crater to exist on Charon that most likely has an unsaturated floor and ejecta blanket, which has been formed in the last 3 Gyr.
- If New Horizons finds satellites in the Pluto system smaller than  $\approx 4$  km in diameter, one could, in principle, use the slope of the crater production function (for the few-km diameter range) on Pluto or Charon to determine

whether an impactor size distribution with  $\alpha_{faint} \geq 0.5$  (down to sub-km sizes) can be ruled out or that those satellites have catastrophically disrupted and reassembled in the past 4 Gyr.

# Chapter 8

## Future Work

There are a number of logical extensions to the work presented in this thesis.

1. It would be valuable to recompute the NEOWISE biases using the Greenstreet et al. (2012a) NEO model rather than the biases computed from the Bottke et al. (2002) model and repeat the analysis presented in Chapter 3. It is unclear how the detailed pointing strategy of the NEOWISE spacecraft would affect the computation of the biases to determine whether a recomputation of the biases would improve the match between the Greenstreet et al. (2012a) NEO model and the detected orbital element distributions of the Aten-class NEOs from NEOWISE. However, to be rigorously consistent, the recomputation should be done. Such an effort is plausible (Mainzer, private communication 2013).
2. Further investigation into the mechanism which can cause asteroids in main belt mean-motion resonances to flip onto retrograde ( $i > 90^\circ$ ) orbits would help provide a more detailed understanding of the population of near-Earth asteroids on retrograde orbits. Currently, the extent of our understanding includes the importance of mean-motion resonances and the Kozai resonance located in those mean-motion resonances and the absence of planetary close encounters during the mechanism. Detailed investigation of the phase space

inside these resonances and more detailed analysis of particles in the numerical integrations which evolve onto retrograde orbits could help provide a more detailed picture of the flipping physics.

3. Estimating the intrinsic population of Earth co-orbitals using detections from the NEOWISE spacecraft is a future project that has been discussed with the NEOWISE team. This would utilize the method described in Chapter 6, based on Alexandersen et al. (2013), for determining the frequency and duration of temporary co-orbitals with Uranus and Neptune.
4. Subsequent to the New Horizons fly-through of the Pluto system in July 2015, a re-examination of Pluto's cratering record given images of the surface is anticipated using the conclusions presented in Chapter 7. This would include attempting to use the observed crater production function to infer, at least in part, the size distribution of the impacting sub-populations. Though the observed crater production function is not predicted to connect to the absolutely calibrated portion of the impactor size distribution, model-dependent ages could be inferred for Pluto's (and Charon's) surface. Furthermore, the observed crater production function on Pluto (or Charon) should imply whether or not the impactor size distribution has a very steep slope at intermediate diameters as the Schlichting et al. (2013) model would imply.

# Bibliography

- Abell, P. A., Korsmeyer, D. J., Landis, R. R., Jones, T. D., Adamo, D. R., Morrison, D. D., Lemke, L. G., Gonzales, A. A., Gershman, R., Sweetser, T. H., Johnson, L. L., and Lu, E.: 2009, *Meteoritics and Planetary Science* **44**, 1825 → pages 2
- Adams, E. R., Gulbis, A. A. S., Elliot, J. L., Benecchi, S. D., Buie, M. W., Trilling, D. E., and Wasserman, L. H.: 2014, *The Astronomical Journal* **148**, 55 → pages 77, 80, 118, 124, 129
- Alexandersen, M., Gladman, B., Greenstreet, S., Kavelaars, J. J., Petit, J. M., and Gwyn, S.: 2013, *Science* **341**, 994 → pages 4, 72, 86, 96, 164
- Alexandersen, M., Gladman, B., Kavelaars, J. J., Petit, J.-M., Gwyn, S., and Shankman, C.: 2014, *arXiv* → pages 73, 86, 98, 129
- Batygin, K., Brown, M. E., and Fraser, W. C.: 2011, *The Astrophysical Journal* **738**, 13 → pages 74, 75
- Benavidez, P. G., Durda, D. D., Enke, B. L., Bottke, W. F., Nesvorný, D., Richardson, D. C., Asphaug, E., and Merline, W. J.: 2012, *Icarus* **219**, 57 → pages 134
- Benz, W. and Asphaug, E.: 1999, *Icarus* **142**, 5 → pages 29, 30, 31, 154, 155, 156, 157
- Bernstein, G. M., Trilling, D. E., Allen, R. L., Brown, M. E., Holman, M., and Malhotra, R.: 2004, *The Astronomical Journal* **128**, 1364 → pages 77, 107, 118
- Bierhaus, E. B. and Dones, L.: 2015, *Icarus* **246**, 165 → pages 83, 84, 102, 116, 117, 140

- Bierhaus, E. B., Dones, L., Alvarelllos, J. L., and Zahnle, K.: 2012, *Icarus* **218**, 602 → pages 140
- Binzel, R. P., Perozzi, E., Rivkin, A. S., Rossi, A., Harris, A. W., Bus, S. J., Valsecchi, G. B., and Slivan, S. M.: 2004, *Meteoritics and Planetary Science* **39**, 351 → pages 2
- Borovička, J., Koten, P., Spurný, P., Boček, J., and Štork, R.: 2005, *Icarus* **174**, 15 → pages 61
- Bottke, W. F., Brož, M., O'Brien, D. P., Campo Bagatin, A., Morbidelli, A., and S., M.: 2015, in *Asteroids IV*, p. in prep, University of Arizona Press → pages 30, 31
- Bottke, W. F., Durda, D. D., Nesvorný, D., Jedicke, R., Morbidelli, A., Vokrouhlický, D., and Levison, H.: 2005, *Icarus* **175**, 111 → pages 31
- Bottke, W. F., Jedicke, R., Morbidelli, A., Duncan, M., Petit, J. M., and Gladman, B.: 2000a, *Science* **288**, 2190 → pages 90
- Bottke, W. F., Morbidelli, A., Jedicke, R., Petit, J. M., Levison, H. F., Michel, P., and Metcalfe, T. S.: 2002, *Icarus* **156**, 399 → pages iv, vii, xv, 5, 18, 19, 21, 22, 32, 33, 34, 35, 36, 37, 38, 39, 40, 41, 42, 45, 46, 50, 56, 163, 182, 186, 187
- Bottke, W. F., Rubincam, D. P., and Burns, J. A.: 2000b, *Icarus* **145**, 301 → pages 42
- Bottke, W. F., Vokrouhlický, D., Brož, M., Nesvorný, D., and Morbidelli, A.: 2001, *Science* **294**, 1693 → pages 23
- Campo Bagatin, A. and Benavidez, P. G.: 2012, *Monthly Notices of the Royal Astronomical Society* **423**, 1254 → pages 101, 134
- Carruba, V., Burns, J. A., Bottke, W., and Nesvorný, D.: 2003, *Icarus* **162**, 308 → pages 23
- Chapman, C. R. and McKinnon, W. B.: 1986, in J. A. Burns and M. S. Matthews (eds.), *Satellites*, pp 492–580, University of Arizona Press → pages 135
- Cohen, C. J. and Hubbard, E. C.: 1965, *The Astronomical Journal* **70**, 10 → pages 70

- Connors, M., Chodas, P., Mikkola, S., Wiegert, P., Veillet, C., and Innanen, K.: 2002, *Meteoritics & Planetary Science* **37**, 1435 → pages 96
- Connors, M., Veillet, C., Brasser, R., Wiegert, P., Chodas, P., Mikkola, S., and Innanen, K.: 2004, *Meteoritics & Planetary Science* **39**, 1251 → pages 96
- Crater Analysis Techniques Working Group, Arvidson, R. E., Boyce, J., Chapman, C., Cintala, M., Fulchignoni, M., Moore, H., Neukum, G., Schultz, P., Soderblom, L., Strom, R., Woronow, A., and Young, R.: 1979, *Icarus* **37**, 467 → pages 130
- Davies, J. K., McFarland, J., Bailey, M. E., Marsden, B. G., and Ip, W.-H.: 2008, in M. A. Barucci, H. Boehnhardt, D. P. Cruikshank, and A. Morbidelli (eds.), *The Solar System Beyond Neptune*, pp 11–23, University of Arizona Press → pages 63, 67
- Dawson, R. I. and Murray-Clay, R.: 2012, *The Astrophysical Journal* **750**, 43 → pages 74, 75
- de Elía, G. C., Di Sisto, R. P., and Brunini, A.: 2010, *Astronomy and Astrophysics* **521**, A23 → pages 102
- de la Fuente Marcos, C. and de la Fuente Marcos, R.: 2012, *Astronomy & Astrophysics* **545**, L9 → pages 96
- Dell’Oro, A., Campo Bagatin, A., Benavidez, P. G., and Alemañ, R. A.: 2013, *Astronomy and Astrophysics* **558**, A95 → pages 102, 111
- Dohnanyi, J. S.: 1969, *Journal of Geophysical Research* **74**, 2531 → pages 25, 27, 29
- Dones, L., Chapman, C., McKinnon, W., Melosh, H., Kirchoff, M., Neukum, G., and Zahnle, K.: 2009, in M. K. Dougherty, L. W. Esposito, and S. M. Krimigis (eds.), *Saturn from Cassini-Huygens*, pp 613–635, Springer Science Business Media B.V. → pages 131
- Dones, L., Gladman, B., Melosh, H. J., Tonks, W. B., Levison, H. F., and Duncan, M.: 1999, *Icarus* **142**, 509 → pages 34, 94, 110, 181
- Dones, L., Weissman, P. R., Levison, H. F., and Duncan, M. J.: 2004, in M. C. Festou, H. U. Keller, and H. A. Weaver (eds.), *Comets II*, pp 153–174, University of Arizona Press → pages 76, 104, 122

- Doressoundiram, A., Boehnhardt, H., Tegler, S. C., and Trujillo, C.: 2008, in M. A. Barucci, H. Boehnhardt, D. P. Cruikshank, and A. Morbidelli (eds.), *The Solar System Beyond Neptune*, pp 91–104, University of Arizona Press → pages 124
- Duncan, M. J. and Levison, H. F.: 1997, *Science* **276**, 1670 → pages 74, 78, 104
- Durda, D. D. and Stern, S. A.: 2000, *Icarus* **145**, 220 → pages 99, 116
- Dvorak, R., Bazsó, Á., and Zhou, L.-Y.: 2010, *Celestial Mechanics and Dynamical Astronomy* **107**, 51 → pages 73
- Edgeworth, K. E.: 1943, *Journal of the British Astronomical Association* **53**, 181 → pages 62
- Farinella, P., Froeschlé, C., Froeschlé, C., Gonczi, R., Hahn, G., Morbidelli, A., and Valsecchi, G. B.: 1994, *Nature* **371**, 315 → pages 14, 15, 20, 50
- Farinella, P., Gonczi, R., Froeschlé, C., and Froeschlé, C.: 1993, *Icarus* **101**, 174 → pages 23
- Farinella, P. and Vokrouhlický, D.: 1999, *Science* **283**, 1507 → pages 23, 42
- Fernandez, J. A. and Ip, W.-H.: 1984, *Icarus* **58**, 109 → pages 73
- Fraser, W. C., Brown, M. E., Morbidelli, A., Parker, A., and Batygin, K.: 2014, *The Astrophysical Journal* **782**, 100 → pages 77, 105, 107, 116, 117, 124, 134
- Fraser, W. C., Brown, M. E., and Schwamb, M. E.: 2010, *Icarus* **210**, 944 → pages 60
- Fraser, W. C. and Kavelaars, J. J.: 2008, *Icarus* **198**, 452 → pages 77, 118
- Fraser, W. C. and Kavelaars, J. J.: 2009, *The Astronomical Journal* **137**, 72 → pages 77
- Fuentes, C. I. and Holman, M. J.: 2008, *The Astronomical Journal* **136**, 83 → pages 77, 118
- Gallant, J., Gladman, B., and Čuk, M.: 2009, *Icarus* **202**, 371 → pages 118, 152
- Gladman, B., Kavelaars, J. J., Petit, J. M., Morbidelli, A., Holman, M. J., and Loredó, T.: 2001, *The Astronomical Journal* **122**, 1051 → pages 77, 118

- Gladman, B., Lawler, S. M., Petit, J. M., Kavelaars, J., Jones, R. L., Parker, J. W., Van Laerhoven, C., Nicholson, P., Rousselot, P., Bieryla, A., and Ashby, M. L. N.: 2012, *The Astronomical Journal* **144**, 23 → pages 63, 65, 66, 68, 70, 77, 78, 79, 80, 95, 102, 109, 115, 117, 157, 160
- Gladman, B., Marsden, B. G., and Vanlaerhoven, C.: 2008, in M. A. Barucci, H. Boehnhardt, D. P. Cruikshank, and A. Morbidelli (eds.), *The Solar System Beyond Neptune*, pp 43–57, University of Arizona Press → pages 63, 65, 88, 101
- Gladman, B., Michel, P., Cellino, A., and Froeschlé, C.: 2000, *Icarus* **146**, 176 → pages 16, 19
- Gladman, B. J., Davis, D. R., Neese, C., Jedicke, R., Williams, G., Kavelaars, J. J., Petit, J.-M., Scholl, H., Holman, M., Warrington, B., Esquerdo, G., and Tricarico, P.: 2009, *Icarus* **202**, 104 → pages 26, 27, 29
- Gladman, B. J., Migliorini, F., Morbidelli, A., Zappalà, V., Michel, P., Cellino, A., Froeschlé, C., Levison, H. F., Bailey, M., and Duncan, M.: 1997, *Science* **277**, 197 → pages 14, 20, 47, 50
- Gomes, R.: 2003, *Icarus* **161**, 404 → pages 73
- Gomes, R., Levison, H. F., Tsiganis, K., and Morbidelli, A.: 2005, *Nature* **435**, 466 → pages 74
- Gomes, R., Morbidelli, A., and Levison, H. F.: 2004, *Icarus* **170**, 492 → pages 74
- Gomes, R. S., Fernandez, J. A., Gallardo, T., and Brunini, A.: 2008, in M. A. Barucci, H. Boehnhardt, D. P. Cruikshank, and A. Morbidelli (eds.), *The Solar System Beyond Neptune*, pp 259–273, University of Arizona Press → pages 74, 75
- Granvik, M., Virtanen, J., Oszkiewicz, D., and Muinonen, K.: 2009, *Meteoritics and Planetary Science* **44**, 1853 → pages 59
- Greenberg, R. and Chapman, C. R.: 1983, *Icarus* **55**, 455 → pages 11, 14, 20, 23
- Greenberg, R. and Nolan, M. C.: 1993, in J. S. Lewis, M. S. Matthews, and M. L. Guerrieri (eds.), *Resources of near-Earth space*, pp 473–492, University of Arizona Press → pages 20

- Greenstreet, S., , Ngo, H., and Gladman, B.: 2012a, *Icarus* **217**, 355 → pages ii, iv, v, vii, xv, 3, 7, 8, 10, 21, 22, 23, 33, 34, 35, 36, 37, 38, 39, 40, 41, 42, 44, 45, 46, 48, 49, 57, 58, 163, 182, 186
- Greenstreet, S. and Gladman, B.: 2013, *The Astrophysical Journal Letters* **767**, L18 → pages 4
- Greenstreet, S., Gladman, B., and McKinnon, W. B.: 2015, *Icarus* **258**, 267 → pages 3, 4
- Greenstreet, S., Gladman, B., Ngo, H., Granvik, M., and Larson, S.: 2012b, *The Astrophysical Journal Letters* **749**, L39 → pages 4, 23
- Grun, E., Zook, H. A., Fechtig, H., and Giese, R. H.: 1985, *Icarus* **62**, 244 → pages 23, 42
- Hahn, J. and Malhotra, R.: 2005, *The Astronomical Journal* **130**, 2392 → pages 76, 122
- Hahn, J. M. and Malhotra, R.: 1999, *The Astronomical Journal* **117**, 3041 → pages 73
- Harris, A.: 2008, *Nature* **453**, 1178 → pages 29
- Harvey, G. A.: 1974, *Astronomical Journal* **79**, 333 → pages 61
- Hildebrand, A. R., Carroll, K. A., Tedesco, E. F., Faber, D. R., Cardinal, R. D., Matthews, J. M., Kuschnig, R., Walker, G. A. H., Gladman, B., Pazder, J., Brown, P. G., Larson, S. M., Worden, S. P., Wallace, B. J., Chodas, P. W., Muinonen, K., and Cheng, A.: 2004, *Earth, Moon, and Planets* **95**, 33 → pages 2, 22
- Holman, M. J. and Wisdom, J.: 1993, *Astronomical Journal* **105**, 1987 → pages 69
- Horner, J. and Evans, N.: 2006, *Monthly Notices of the Royal Astronomical Society* **367**, L20 → pages 88, 93, 94
- Horner, J. and Lykawka, P. S.: 2012, *Monthly Notices of the Royal Astronomical Society* **426**, 159 → pages 95
- Housen, K. R. and Holsapple, K. A.: 2011, *Icarus* **211**, 856 → pages 83, 84

- Ivezić, u., Tabachnik, S., Rafikov, R., Lupton, R. H., Quinn, T., Hammergren, M., Eyer, L., Chu, J., Armstrong, J. C., Fan, X., Finlator, K., Geballe, T. R., Gunn, J. E., Hennessy, G. S., Knapp, G. R., Leggett, S. K., Munn, J. A., Pier, J. R., Rockosi, C. M., Schneider, D. P., Strauss, M. A., Yanny, B., Brinkmann, J., Csabai, I., Hindsley, R. B., Kent, S., Lamb, D. Q., Margon, B., McKay, T. A., Smith, J. A., Waddel, P., York, D. G., and Collaboration, S.: 2001, *The Astronomical Journal* **122**, 2749 → pages 27, 29
- Jedicke, R. and Metcalfe, T. S.: 1998, *Icarus* **131**, 245 → pages 24, 26, 27, 29
- Jewitt, D. and Luu, J.: 1993, *Nature* **362**, 730 → pages 63
- Jewitt, D., Luu, J., and Trujillo, C.: 1998, *The Astronomical Journal* **115**, 2125 → pages 118
- Johansen, A., Blum, J., Tanaka, H., Ormel, C., Bizzarro, M., and Rickman, H.: 2014, in H. Beuther, R. Klesson, C. Dullemond, and T. Henning (eds.), *Protostars and Planets VI*, pp 547–570, University of Arizona Press → pages 134
- Kaib, N., Roškar, R., and Quinn, T.: 2011, *Icarus* **215**, 491 → pages xvi, 79, 88, 89, 109, 117, 157
- Kavelaars, J. J., Jones, R. L., Gladman, B. J., Petit, J.-M., Parker, J. W., Van Laerhoven, C., Nicholson, P., Rousselot, P., Scholl, H., Mousis, O., Marsden, B., Benavidez, P., Bieryla, A., Campo Bagatin, A., Doressoundiram, A., Margot, J. L., Murray, I., and Veillet, C.: 2009, *The Astronomical Journal* **137**, 4917 → pages 65, 66, 68
- Kenyon, S. J. and Bromley, B. C.: 2014, *The Astronomical Journal* **147**, 8 → pages 81, 153, 155
- Kirchoff, M. R. and Schenk, P.: 2010, *Icarus* **206**, 485 → pages 131, 133
- Kirkwood, D.: 1867, *Meteoric astronomy: a treatise on shooting-stars, fireballs, and aerolites*, Lippincott & co., Philadelphia → pages 17
- Kozai, Y.: 1962, *The Astronomical Journal* **67**, 591 → pages 14, 50, 102
- Kuchner, M. J., Brown, M. E., and Holman, M.: 2002, *The Astronomical Journal* **124**, 1221 → pages 76, 122

- Kuiper, G. P.: 1951, *Proceedings of the National Academy of Sciences, Canada* **37**, 1 → pages 62
- Kuiper, G. P., Fujita, Y., Gehrels, T., Groeneveld, I., Kent, J., van Biesbroeck, G., and van Houten, C. J.: 1958, *Astrophysical Journal Supplement* **3**, 289 → pages 26
- Lacerda, P., Fornasier, S., Lellouch, E., Kiss, C., Vilenius, E., Santos-Sanz, P., Rengel, M., Mueller, T., Stansberry, J., Duffard, R., Delsanti, A., and Guilbert-Lepoutre, A.: 2014, *The Astronomical Journal Letters* **793**, L2 → pages 134
- Larsen, J. A., Gleason, A. E., Danzl, N. M., Descour, A. S., McMillan, R. S., Gehrels, T., Jedicke, R., Montani, J. L., and Scotti, J. V.: 2001, *The Astronomical Journal* **121**, 562 → pages 77
- Larson, S., Beshore, E., Hill, R., Christensen, E., McLean, D., Kolar, S., McNaught, R., and Garradd, G.: 2003, *Larson, S.; Beshore, E.; Hill, R.; Christensen, E.; McLean, D.; Kolar, S.; McNaught, R.; Garradd, G.* **35**, 982 → pages 57
- Leinhardt, Z. M. and Stewart, S. T.: 2009, *Icarus* **199**, 542 → pages 153, 155, 156
- Leinhardt, Z. M. and Stewart, S. T.: 2012, *The Astrophysical Journal* **745**, 79 → pages 153
- Levison, H. F. and Duncan, M. J.: 1993, *The Astrophysical Journal Letters* **406**, L35 → pages 69
- Levison, H. F. and Duncan, M. J.: 1994, *Icarus* **108**, 18 → pages 20, 21, 33, 89
- Levison, H. F. and Duncan, M. J.: 1997, *Icarus* **127**, 13 → pages 19, 21, 60, 93, 94, 104
- Levison, H. F., Duncan, M. J., Dones, L., and Gladman, B. J.: 2006, *Icarus* **184**, 619 → pages 60
- Levison, H. F. and Morbidelli, A.: 2003, *Nature* **426**, 419 → pages 74
- Levison, H. F., Morbidelli, A., Van Laerhoven, C., Gomes, R., and Tsiganis, K.: 2008, *Icarus* **196**, 258 → pages 100

- Lupo, M. J. and Lewis, J. S.: 1980, *Icarus* **42**, 29 → pages 83
- Lykawka, P. S. and Mukai, T.: 2005, *Earth, Moon, and Planets* **97**, 107 → pages 76, 122
- Mainzer, A., Grav, T., Bauer, J., Masiero, J., McMillan, R. S., Cutri, R. M., Walker, R., Wright, E., Eisenhardt, P., Tholen, D. J., Spahr, T., Jedicke, R., Denneau, L., DeBaun, E., Elsbury, D., Gautier, T., Gomillion, S., Hand, E., Mo, W., Watkins, J., Wilkins, A., Bryngelson, G. L., Del Pino Molina, A., Desai, S., Gómez Camus, M., Hidalgo, S. L., Konstantopoulos, I., Larsen, J. A., Maleszewski, C., Malkan, M. A., Mauduit, J.-C., Mullan, B. L., Olszewski, E. W., Pforr, J., Saro, A., Scotti, J. V., and Wasserman, L. H.: 2011, *The Astrophysical Journal* **743**, 156 → pages 27, 29, 56, 57
- Mainzer, A., Grav, T., Masiero, J., Bauer, J., McMillan, R. S., Giorgini, J., Spahr, T., Cutri, R. M., Tholen, D., Jedicke, R., Walker, R., Wright, E., and Nugent, C. R.: 2012, *The Astrophysical Journal* **752**, 110 → pages ii, iv, 4, 23, 32, 33, 35, 37, 40, 41
- Malhotra, R.: 1993, *Nature* **365**, 819 → pages 74, 100
- Malhotra, R.: 1995, *The Astronomical Journal* **110**, 420 → pages 74, 100
- Masiero, J. R., Mainzer, A. K., Grav, T., Bauer, J. M., Cutri, R. M., Dailey, J., Eisenhardt, P. R. M., McMillan, R. S., Spahr, T. B., Skrutskie, M. F., Tholen, D., Walker, R. G., Wright, E. L., DeBaun, E., Elsbury, D., Gautier, T. I., Gomillion, S., and Wilkins, A.: 2011, *The Astrophysical Journal* **741**, 68 → pages 27
- McEwen, A. S. and Bierhaus, E. B.: 2006, *Annual Review of Earth and Planetary Sciences* **34**, 535 → pages 140
- McKinnon, W. B., Prialnik, D., Stern, S. A., and Coradini, A.: 2008, in M. A. Barucci, H. Boehnhardt, D. P. Cruikshank, and A. Morbidelli (eds.), *The Solar System Beyond Neptune*, pp 213–241, University of Arizona Press → pages 152
- McKinnon, W. B. and Schenk, P. M.: 1995, *Geophysical Research Letters* **22**, 1829 → pages 82, 118

- McKinnon, W. B. and Singer, K. N.: 2010, *Bulletin of the American Astronomical Society* **42**, 984 → pages 108
- Melosh, H. J.: 1989, *Impact cratering: A geologic process*, Oxford University Press, New York → pages 126, 128, 130, 138, 140, 143
- Michel, P. and Froeschlé, C.: 1997, *Icarus* **128**, 230 → pages 13
- Michel, P. and Thomas, F.: 1996, *Astronomy and Astrophysics* **307**, 310 → pages 14, 16
- Michel, P., Zappalà, V., Cellino, A., and Tanga, P.: 2000, *Icarus* **143**, 421 → pages 6
- Mikkola, S., Brassier, R., Wiegert, P., and Innanen, K.: 2004, *Monthly Notices of the Royal Astronomical Society* **351**, L63 → pages 96
- Mikkola, S., Innanen, K., Wiegert, P., Connors, M., and Brassier, R.: 2006, *Monthly Notices of the Royal Astronomical Society* **369**, 15 → pages 71, 96
- Minton, D. A., Richardson, J. E., Thomas, P., Kirchoff, M., and Schwamb, M. E.: 2012, *Asteroids, Comets, and Meteors Conference* **1667**, 6348 → pages 77, 107, 109, 141, 143, 145, 147, 158
- Moore, J. M., Howard, A. D., Schenk, P. M., McKinnon, W. B., Pappalardo, R. T., Ewing, R. C., Bierhaus, E. B., Bray, V. J., Spencer, J. R., Binzel, R. P., Buratti, B., Grundy, W. M., Olkin, C. B., Reitsema, H. J., Reuter, D. C., Stern, S. A., Weaver, H., Young, L. A., and Beyer, R. A.: 2015, *Icarus* **246**, 65 → pages 99, 106, 107, 118, 121, 137
- Morais, M. H. M. and Morbidelli, A.: 2002, *Icarus* **160**, 1 → pages 88, 93, 94
- Morais, M. H. M. and Morbidelli, A.: 2006, *Icarus* **185**, 29 → pages 88, 93
- Morbidelli, A.: 1997, *Icarus* **127**, 1 → pages 76, 122
- Morbidelli, A., Levison, H. F., Bottke, W. F., Dones, L., and Nesvorný, D.: 2005, *Nature* **435**, 462 → pages 74
- Morbidelli, A. and Nesvorný, D.: 1999, *Icarus* **139**, 295 → pages 20, 23
- Morbidelli, A., Thomas, F., and Moons, M.: 1995, *Icarus* **118**, 322 → pages 69

- Morrison, D., Chapman, C. R., and Slovic, P.: 1994, in T. Gehrels (ed.), *Hazards Due to Comets and Asteroids*, pp 59–92, University of Arizona Press → pages 2
- Murray, C. D. and Dermott, S. F.: 1999, *Solar System Dynamics*, Cambridge University Press, New York → pages 90
- Namouni, F.: 1999, *Icarus* **137**, 293 → pages 96
- Namouni, F., Christou, A. A., and Murray, C. D.: 1999, *Physical Review Letters* **83**, 2506 → pages 96
- Nesvorný, D. and Dones, L.: 2002, *Icarus* **160**, 271 → pages 73
- Nesvorný, D., Ferraz-Mello, S., Holman, M., and Morbidelli, A.: 2002, in W. F. Bottke, A. Cellino, P. Paolicchi, and R. P. Binzel (eds.), *Asteroids III*, pp 379–394, University of Arizona Press → pages 18
- Nesvorný, D. and Morbidelli, A.: 1998, *The Astronomical Journal* **116**, 3029 → pages 18, 19
- Nesvorný, D., Roig, F., and Ferraz-Mello, S.: 2000, *The Astronomical Journal* **119**, 953 → pages 116
- Noll, K. S., Grundy, W. M., Chiang, E. I., Margot, J.-L., and Kern, S. D.: 2008, in M. A. Barucci, H. Boehnhardt, D. P. Cruikshank, and A. Morbidelli (eds.), *The Solar System Beyond Neptune*, pp 345–363, University of Arizona Press → pages 75
- O’Brien, D. P. and Greenberg, R.: 2003, *Icarus* **164**, 334 → pages 25, 30, 31
- O’Brien, D. P. and Sykes, M. V.: 2011, *Space Science Reviews* **163**, 41 → pages 77, 107
- Peixinho, N., Lacerda, P., and Jewitt, D.: 2008, *The Astronomical Journal* **136**, 1837 → pages 75
- Petit, J. M., Kavelaars, J. J., Gladman, B. J., Jones, R. L., Parker, J. W., Van Laerhoven, C., Nicholson, P., Mars, G., Rousselot, P., Mousis, O., Marsden, B., Bieryla, A., Taylor, M., Ashby, M. L. N., Benavidez, P., Campo Bagatin, A., and Bernabeu, G.: 2011, *The Astronomical Journal* **142**, 131 → pages 63, 64, 65, 66, 68, 77, 78, 79, 80, 88, 102, 109, 110, 111, 113, 117, 124, 157, 160

- Pokorný, P. and Vokrouhlický, D.: 2013, *Icarus* **226**, 682 → pages 112
- Rabinowitz, D. L.: 1993, *Astrophysical Journal, Part 1* **407**, 412 → pages 29
- Reach, W. T., Vaubaillon, J., Kelley, M. S., Lisse, C. M., and Sykes, M. V.: 2009, *Icarus* **203**, 571 → pages 56, 60
- Richardson, D. C., Bottke, W. F., and Love, S. G.: 1998, *Icarus* **134**, 47 → pages 23, 42
- Richardson, J. E.: 2009, *Icarus* **204**, 697 → pages 135
- Schenk, P. M. and Zahnle, K.: 2007, *Icarus* **192**, 135 → pages 108
- Schlichting, H. E., Fuentes, C. I., and Trilling, D. E.: 2013, *The Astronomical Journal* **146**, 36 → pages 77, 78, 107, 109, 125, 141, 143, 145, 147, 158, 161, 164
- Schlichting, H. E., Ofek, E. O., Sari, R., Nelan, E. P., Gal-Yam, A., Wenz, M., Muirhead, P., Javanfar, N., and Livio, M.: 2012, *The Astrophysical Journal* **761**, 150 → pages 148
- Shankman, C., Gladman, B. J., Kaib, N., Kavelaars, J. J., and Petit, J. M.: 2013, *The Astrophysical Journal* **764**, L2 → pages 77, 79, 80, 89, 107, 109, 117, 118, 119, 129, 131, 134, 157
- Sheppard, S. S.: 2012, *The Astronomical Journal* **144**, 169 → pages 124
- Showalter, M. R. and Hamilton, D. P.: 2015, *Nature* **522**, 45 → pages 81
- Sicardy, B., Bellucci, A., Gendron, E., Lacombe, F., Lacour, S., Lecacheux, J., Lellouch, E., Renner, S., Pau, S., Roques, F., Widemann, T., Colas, F., Vachier, F., Martins, R. V., Ageorges, N., Hainaut, O., Marco, O., Beisker, W., Hummel, E., Feinstein, C., Levato, H., Maury, A., Frappa, E., Gaillard, B., Lavayssi re, M., di Sora, M., Mallia, F., Masi, G., Behrend, R., Carrier, F., Mousis, O., Rousselot, P., Alvarez-Candal, A., Lazzaro, D., Veiga, C., Andrei, A. H., Assafin, M., da Silva Neto, D. N., Jacques, C., Pimentel, E., Weaver, D., Lecampion, J.-F., Doncel, F., Momiyama, T., and Tancredi, G.: 2006, *Nature* **439**, 52 → pages 152
- Singer, K. N., McKinnon, W. B., and Nowicki, L. T.: 2013, *Icarus* **226**, 865 → pages 84, 140

- Solontoi, M., Ivezić, Ž., Jurić, M., Becker, A. C., Jones, L., West, A. A., Kent, S., Lupton, R. H., Claire, M., Knapp, G. R., Quinn, T., Gunn, J. E., and Schneider, D. P.: 2012, *Icarus* **218**, 571 → pages 77, 78, 141, 160
- Stansberry, J., Grundy, W., Brown, M., Cruikshank, D., Spencer, J., Trilling, D., and Margot, J. L.: 2008, in M. A. Barucci, H. Boehnhardt, D. P. Cruikshank, and A. Morbidelli (eds.), *The Solar System Beyond Neptune*, pp 161–179, University of Arizona Press → pages 134
- Stern, S. A.: 2009, *Icarus* **199**, 571 → pages 140
- Stern, S. A., Porter, S. A., and Zangari, A.: 2015, *Icarus* **250**, 287 → pages 83, 149, 150
- Stern, S. A., Weaver, H. A., Steffl, A. J., Mutchler, M. J., Merline, W. J., Buie, M. W., Young, E. F., Young, L. A., and Spencer, J. R.: 2006, *Nature* **439**, 946 → pages 100
- Stokes, G. H., Evans, J. B., Viggh, H. E. M., Shelly, F. C., and Pearce, E. C.: 2000, *Icarus* **148**, 21 → pages 57
- Strom, R. G., Malhotra, R., Ito, T., Yoshida, F., and Kring, D. A.: 2005, *Science* **309**, 1847 → pages 3
- Stuart, J. S.: 2001, *Science* **294**, 1691 → pages 56
- Szabó, G. M., Ivezić, Ž., Jurić, M., and Lupton, R.: 2007, *Monthly Notices of the Royal Astronomical Society* **377**, 1393 → pages 77
- Tera, F., Papanastassiou, D. A., and Wasserburg, G. J.: 1974, *Lunar and Planetary Science Conference* **5**, 792 → pages 3
- Tiscareno, M. and Malhotra, R.: 2009, *The Astronomical Journal* **138**, 827 → pages 76, 122
- Tiscareno, M. S. and Malhotra, R.: 2003, *The Astronomical Journal* **126**, 3122 → pages 93, 94
- Trujillo, C. A., Luu, J. X., Bosh, A. S., and Elliot, J. L.: 2001, *The Astronomical Journal* **122**, 2740 → pages 77

- Tsiganis, K., Gomes, R., Morbidelli, A., and Levison, H. F.: 2005, *Nature* **435**, 459 → pages 73, 74
- van Houten, C. J., van Houten-Groeneveld, I., Herget, P., and Gehrels, T.: 1970, *Astronomy & Astrophysics Supplement Series* **2**, 339 → pages 26, 27
- Veverka, J., Farquhar, B., Robinson, M., Thomas, P., Murchie, S., Harch, A., Antreasian, P. G., Chesley, S. R., Miller, J. K., Owen, W. M., Williams, B. G., Yeomans, D., Dunham, D., Heyler, G., Holdridge, M., Nelson, R. L., Whittenburg, K. E., Ray, J. C., Carcich, B., Cheng, A., Chapman, C., Bell, J. F., Bell, M., Bussey, B., Clark, B., Domingue, D., Gaffey, M. J., Hawkins, E., Izenberg, N., Joseph, J., Kirk, R., Lucey, P., Malin, M., McFadden, L., Merline, W. J., Peterson, C., Prockter, L., Warren, J., and Wellnitz, D.: 2001, *Nature* **413**, 390 → pages 2
- Vokrouhlický, D. and Milani, A.: 2000, *Astronomy and Astrophysics* **362**, 746 → pages 42
- Vokrouhlický, D., Pokorný, P., and Nesvorný, D.: 2012, *Icarus* **219**, 150 → pages 112
- Volk, K. and Malhotra, R.: 2008, *The Astrophysical Journal* **687**, 714 → pages 94
- Walker, G., Matthews, J., Kuschnig, R., Johnson, R., Rucinski, S., Pazder, J., Burley, G., Walker, A., Skaret, K., Zee, R., Grocott, S., Carroll, K., Sinclair, P., Sturgeon, D., and Harron, J.: 2003, *The Publications of the Astronomical Society of the Pacific* **115**, 1023 → pages 22
- Weissman, P. R. and Stern, S. A.: 1994, *Icarus* **111**, 378 → pages 99
- Wetherill, G. W.: 1967, *Journal of Geophysical Research* **72**, 2429 → pages 110
- Wetherill, G. W.: 1979, *Icarus* **37**, 96 → pages 11, 14, 19
- Wetherill, G. W.: 1985, *Meteoritics* **20**, 783 → pages 20, 23
- Wetherill, G. W. and Faulkner, J.: 1981, *Icarus* **46**, 390 → pages 13
- Wiegert, P., Balam, D., Moss, A., Veillet, C., Connors, M., and Shelton, I.: 2007, *The Astronomical Journal* **133**, 1609 → pages 27

- Wisdom, J.: 1985, *Nature* **315**, 731 → pages 18
- Yano, H., Kubota, T., Miyamoto, H., Okada, T., Scheeres, D., Takagi, Y., Yoshida, K., Abe, M., Abe, S., Barnouin-Jha, O., Fujiwara, A., Hasegawa, S., Hashimoto, T. and Ishiguro, M., Kato, M., Kawaguchi, J., Mukai, T., Saito, J., Sasaki, S., and Yoshikawa, M.: 2006, *Science* **312**, 1350 → pages 2
- Yoshida, F. and Nakamura, T.: 2007, *Planetary and Space Science* **55**, 1113 → pages 27, 29
- Yoshida, F., Nakamura, T., Watanabe, J.-I., Kinoshita, D., Yamamoto, N., and Fuse, T.: 2003, *Publications of the Astronomical Society of Japan* **55**, 701 → pages 27, 29
- Young, L. A., Stern, S. A., Weaver, H. A., Bagenal, F., Binzel, R. P., Buratti, B., Cheng, A. F., Cruikshank, D., Gladstone, G. R., Grundy, W. M., Hinson, D. P., Horanyi, M., Jennings, D. E., Linscott, I. R., McComas, D. J., McKinnon, W. B., McNutt, R., Moore, J. M., Murchie, S., Olkin, C. B., Porco, C. C., Reitsema, H., Reuter, D. C., Spencer, J. R., Slater, D. C., Strobel, D., Summers, M. E., and Tyler, G. L.: 2008, *Space Science Reviews* **140**, 93 → pages 99, 107, 121, 137
- Zahnle, K., Dones, L., and Levison, H.: 1998, *Icarus* **136**, 202 → pages 119
- Zahnle, K., Schenk, P., Levison, H., and Dones, L.: 2003, *Icarus* **163**, 263 → pages 82, 83, 84, 99, 101, 116, 118, 125, 131, 149, 160

# Appendix A

## Appendix

### A.1 Close Encounter Scheme of SWIFT-RMVS

As discussed in Section 3.2, the most challenging aspect of numerically integrating massless particles in the Solar System is accurately resolving close encounters with the planets. To ensure accurate resolution of close encounters, the SWIFT-RMVS integrator adaptively reduces the time step by up to a factor of 30 upon detecting an upcoming encounter. To anticipate a planetary close encounter, at each time step the integrator performs a linear extrapolation of an object's position forward by a single base time step. If the linear extrapolation shows the object will be within 3.5 Hill radii of a planet (where the gravitational influence of the planet becomes roughly comparable to that of the Sun), the integrator will reduce the time step by a factor of 10 in order to then accurately integrate the approach (and then recession) from the planet. On this and future time steps, if a linear extrapolation of the object's position shows it will be within a single Hill radii of a planet, the integrator will reduce the time step by an additional factor of three, using a patched-conic hyperbolic orbit in the planetocentric reference frame to continue the particle integration since at this distance at this distance the particle's motion is better described as a planetocentric Keplerian orbit than a heliocentric one.

The danger of using a base time step that is too large comes from the existence (especially in the perihelion  $q < 1.0$  AU regime) of NEAs on highly eccentric, highly inclined orbits that can encounter Venus and Mercury (in particular) at speeds of up to 50 or 60 km/s. At this speed, an NEA can travel  $> 15$  Venusian Hill spheres ( $> 80$  Mercurian Hill spheres) in a single 3.5 day time step (reduced to  $< 1$  Venusian Hill sphere ( $\approx 4$  Mercurian Hill spheres) in a 4 hour time step). The linear extrapolation computed using the larger time step is a worse approximation than the curvature of the actual motion of the object than the extrapolation using the smaller time step. This can result in the linear extrapolation performed by the integrator failing to predict an upcoming planetary close encounter (Dones et al., 1999) and thus drop the NEA into the planetary Hill sphere without correctly time-resolving the approach phase of the encounter. This can cause the NEA's post-encounter orbit to be incorrectly computed by the integrator as will be described below.

## A.2 Convergence Tests for SWIFT-RMVS4

To test the potential break-down of the numerical integrator during the highest speed planetary close encounters when too large a time step is used, I performed a set of numerical integrations designed to test the convergence of the integrator at various time steps. The very highest speed planetary close encounters for NEAs occur with Mercury, although Mercury's small size causes it to have a smaller affect on the post-encounter orbit of an NEA than Venus. Because the goal is test the scheme used by the integrator for detecting upcoming planetary close encounters for various base time steps, only Mercury was included in the numerical integration tests. A set of 1,000 test particles were uniformly distributed from  $0.95 \leq a \leq 1.0$  AU,  $0.2 \leq q \leq 0.25$  AU ( $0.75 \leq e \leq 0.8$ ), and  $40^\circ \leq i \leq 42^\circ$  with random argument of pericenters, longitude of ascending nodes, and mean anomalies. Another set of 1,000 test particles were uniformly distributed using the same  $a$  and  $q$  distributions as above and  $6^\circ \leq i \leq 8^\circ$  with random angles. The set of particles with high- $e$  and high- $i$  were chosen to have high speed close en-

counters with Mercury, while the set with lower  $i$  were chosen to have inclinations near that of Mercury ( $i \approx 7^\circ$ ) where close encounter probabilities are enhanced. Each set of test particles were numerically integrated for 1 Myr using five base integration time steps: 2 hours, 4 hours, 8 hours, 16 hours, and 84 hours (3.5 days). The Greenstreet et al. (2012a) NEO orbital distribution model integrations used a base time step of 4 hours, while the Bottke et al. (2002) NEO model used 3.5 days (84 hours). This thus allows us to test the convergence at the 4 hour time step used in the newer model. Particles were followed until they hit a planet, hit the Sun ( $r_{helio} < 0.005$  AU), migrated out past 19 AU, or the integration ended.

Figure A.1 shows the  $a, q$  distribution for the test particle set with  $6^\circ \leq i \leq 8^\circ$  at the end of the 1 Myr integrations for the five base integration time steps. The spread in pericenter distances is due to secular oscillations in  $e$  caused by Mercury. As can be seen in Figure A.1, some particles have close encounters with Mercury, which change their semimajor axes. The top four panels of Figure A.1 show similar  $a, q$  distributions for the 4 smaller time steps. As expected, a roughly comparable number of particles are scattered to lower  $a$  between each of these integrations as well as to higher  $a$ . Comparing the top 4 panels with the bottom panel, which used a base integration time step of 84 hours (3.5 days), however, shows a greater number of particles scattered to lower  $a$  in the larger time step integration. The same is true in Figure A.2, which shows the set of test particles with  $40^\circ \leq i \leq 42^\circ$ . Fewer particles are scattered to either lower or higher  $a$  in Figure A.2 due to the decreased close encounter probability with Mercury at high- $i$ , but the same trend is visible. Figure A.3 shows the semimajor axis distribution as a histogram for each of the test particle initial condition sets. For  $a < 0.95$  AU, the 84 hour (3.5 day) time step shows an enhancement of particles scattered to lower  $a$  compared to those for the four smaller time steps.

### A.3 Discussion

The similarity in the test particle orbital distributions at the end of the 1 Myr integrations for the 2, 4, 8, and 16 hour base time steps points to convergence at

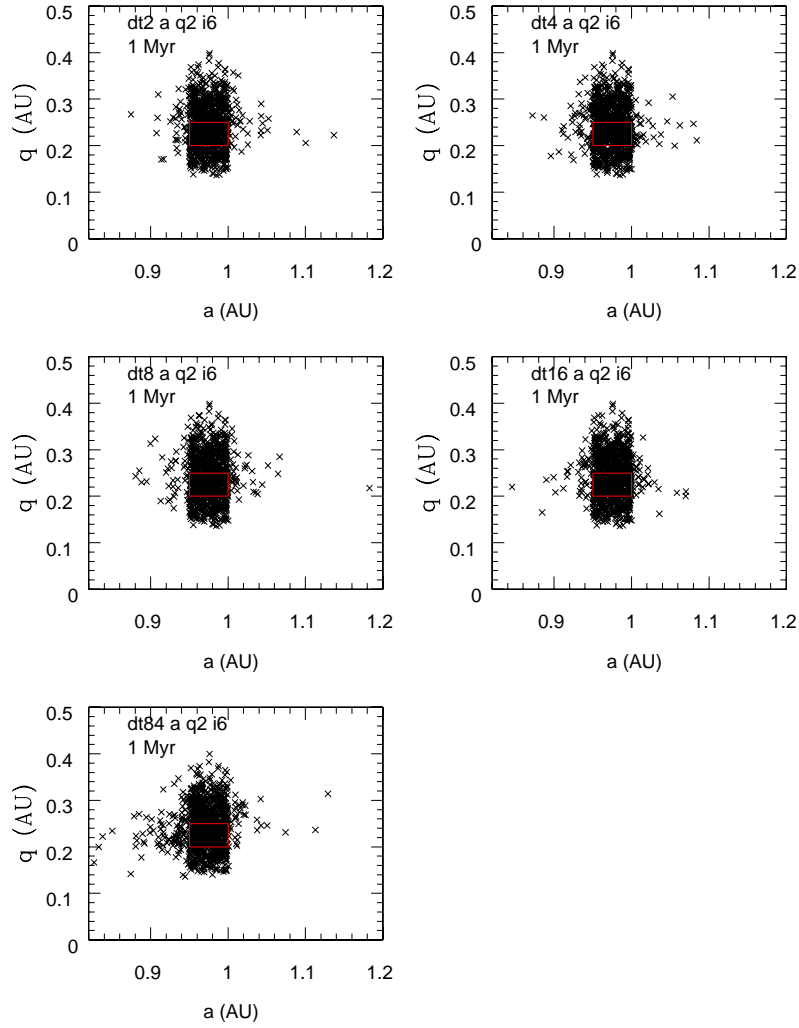


**Figure A.1:** The semimajor axis, pericenter distribution for the test particle set with  $6^\circ \leq i \leq 8^\circ$  for five base integration time steps: 2 hours (top left), 4 hours (top right), 8 hours (middle left), 16 hours (middle right), and 84 hours (3.5 days, bottom left) at the end of the 1 Myr integrations. The red box indicates the particle initial conditions.

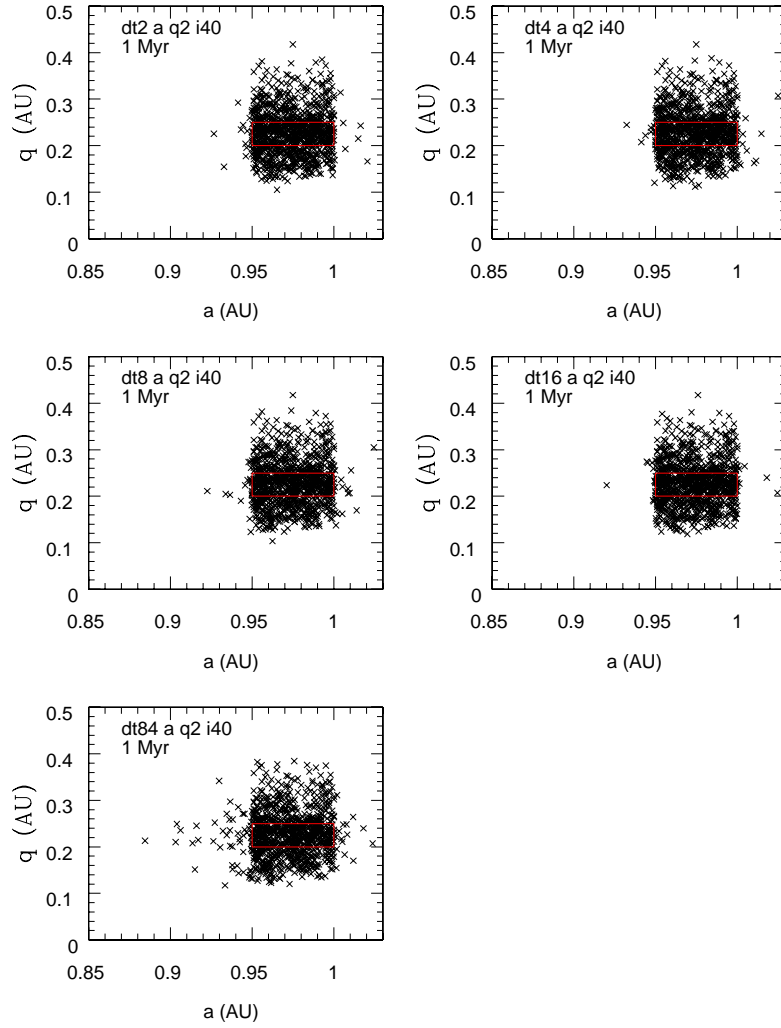


**Figure A.2:** The semimajor axis, pericenter distribution for the test particle set with  $40^\circ \leq i \leq 42^\circ$  for five base integration time steps: 2 hours (top left), 4 hours (top right), 8 hours (middle left), 16 hours (middle right), and 84 hours (3.5 days, bottom left) at the end of the 1 Myr integrations. The red box indicates the particle initial conditions.

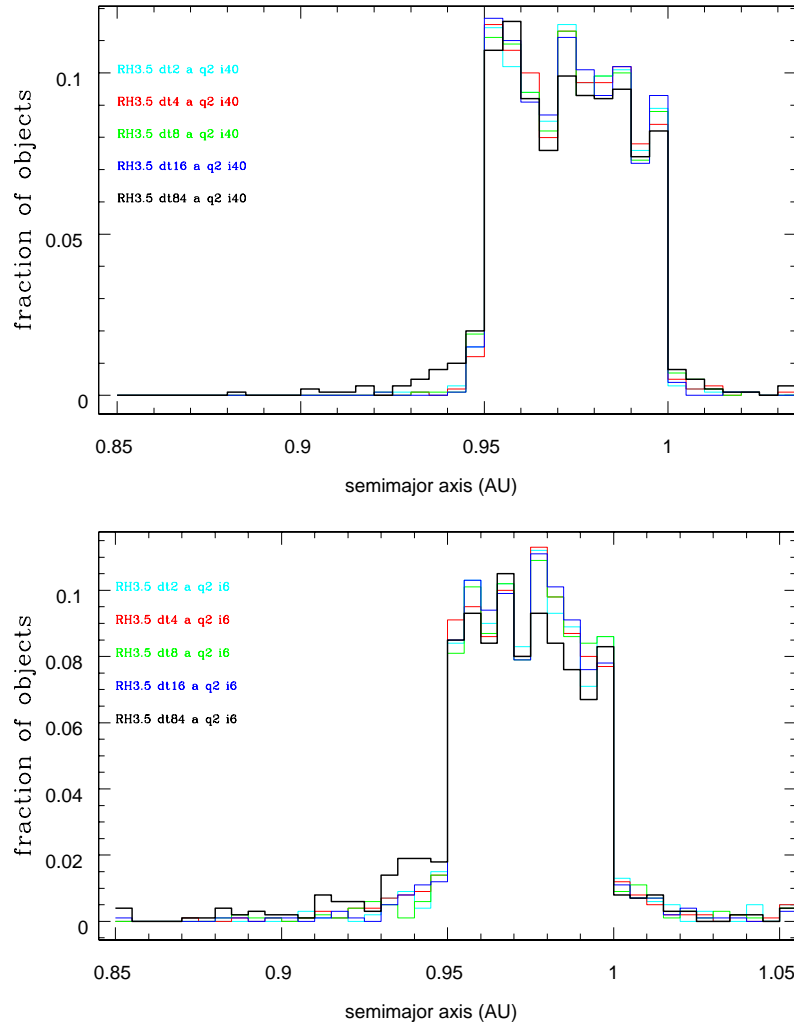


**Figure A.3:** Semimajor axis histograms for both test particle sets ( $40^\circ \leq i \leq 42^\circ$  shown on top and  $6^\circ \leq i \leq 8^\circ$  shown on bottom) for five base integration time steps: 2 hours (cyan), 4 hours (red), 8 hours (green), 16 hours (blue), and 84 hours (3.5 days, black) at the end of the 1 Myr integrations.

these small time step values. We thus believe the integrations used to create the Greenstreet et al. (2012a) NEO orbital distribution model, which used a base time step of 4 hours, have reached convergence and would not benefit from utilizing a smaller time step. The 84 hour (3.5 day) time step, however, does not produce the same particle evolution as the four smaller time steps. As discussed above, the failure of the predictive close encounter scheme in SWIFT-RMVS when too large a time step is used can artificially drop an NEA into a planetary Hill sphere without having correctly resolved the trajectory of the NEA as it fell into the planet's gravity well. In such a scenario, the integrator would suddenly find a NEA inside a planet's Hill sphere, and reduce the integration time step by up to a factor of 30 in order to accurately resolve the close encounter as the integration moves forward. However, computing the change in orbital speed for the NEA as it climbs out of the planet's gravity well after failing to monitor the increase in speed of the NEA as it fell into the planetary gravity well will cause the integrator to compute a post-encounter orbit for the NEA that has less heliocentric orbital speed, and thus less heliocentric orbital energy, than it should have. This results in the NEA having a smaller post-encounter semimajor axis than it should have, since orbital energy goes as  $-1/a$ . This provides an explanation for the increase in NEAs with smaller semimajor axes for the integrations using an 84 hour (3.5 day) base time step. In this case, the integrator is failing to predict and thus resolve upcoming high speed planetary close encounters during the approach phase, resulting in the inaccurate scattering of NEAs to small- $a$ .

As discussed in Chapter 3, the Aten-class ( $a < 1.0$  AU,  $Q > 0.983$  AU) NEA detections by the NEOWISE spacecraft have an orbital distribution that is more enriched in higher  $a$ , lower  $e$  and lower  $i$  objects than the Bottke et al. (2002) NEO model predicts. This can be explained by the break down of the integrator's close encounter prediction scheme for a too large time step as discussed above. The  $a$ ,  $q$  distributions shown in Figure A.1 and Figure A.2 show the enhancement of low- $a$  Atens for the 84 hour (3.5 day) time step at relatively low- $q$  or high- $e$ , but it is not clear whether the smaller  $a$  objects for the large time step have a higher

$e$  distribution than the four smaller time steps. Figures A.4 and A.5 show the  $a$ ,  $i$  distributions for the two initial condition sets, and it is clear the objects with smaller  $a$  for the 84 hour (3.5 day) time step have higher  $i$  than for the four smaller time steps. This is most obvious in Figure A.5.

In Chapter 3, we hypothesized that the too large time step used in the previous model was responsible for incorrectly scattering Atens to orbits with higher eccentricities and inclinations than they should have. However, the gravity well scenario described above does not easily lend itself to explaining artificial pumping of  $e$  and  $i$  of a NEA. More plausible is an interpretation that incorrect scattering to lower  $a$  would be *preferentially* occurring for objects with already high- $e$  and/or high- $i$ , at times causing high- $e$ , high- $i$  Apollos and Atens to be incorrectly scattered to lower  $a$ ; thus producing an enhancement of high- $e$ , high- $i$  Atens in the Bottke et al. (2002) model. This interpretation better matches Figure 3.1, in which the extra power at large  $i$  and large  $e$  in the Bottke et al. (2002) model is ‘intruding from the right’, rather than coming from scattering of low- $e$  and low- $i$  orbits with  $a < 1$  AU already.

## A.4 Recommendations

The above analysis makes it clear that the ‘missed encounters’ problem can be avoided by using a sufficiently small time step. However, an absolute requirement of ‘sufficiently small’ would require that the particle will move less than a Hill sphere radius when the relative velocities are those judged using the highest eccentricities, inclinations, and relative semimajor axis that are expected to arise in the integration. With no other information, then the ultimate bound would be the parabolic orbit that is retrograde with respect to the planet’s motion. Under a circular approximation, this encounter speed could be  $(\sqrt{2} + 1)v_p$ , where  $v_p$  is the circular orbital speed of the planet (about 48 km/s for Mercury, giving a maximal encounter speed of 116 km/s if a test particle were to somehow reach a retrograde near-parabolic orbit with heliocentric  $q$  at Mercury). Given that Mercury’s Hill sphere is 0.0015 AU ( $\sim 220,000$  km), during a 4 hour time step, the maximal en-

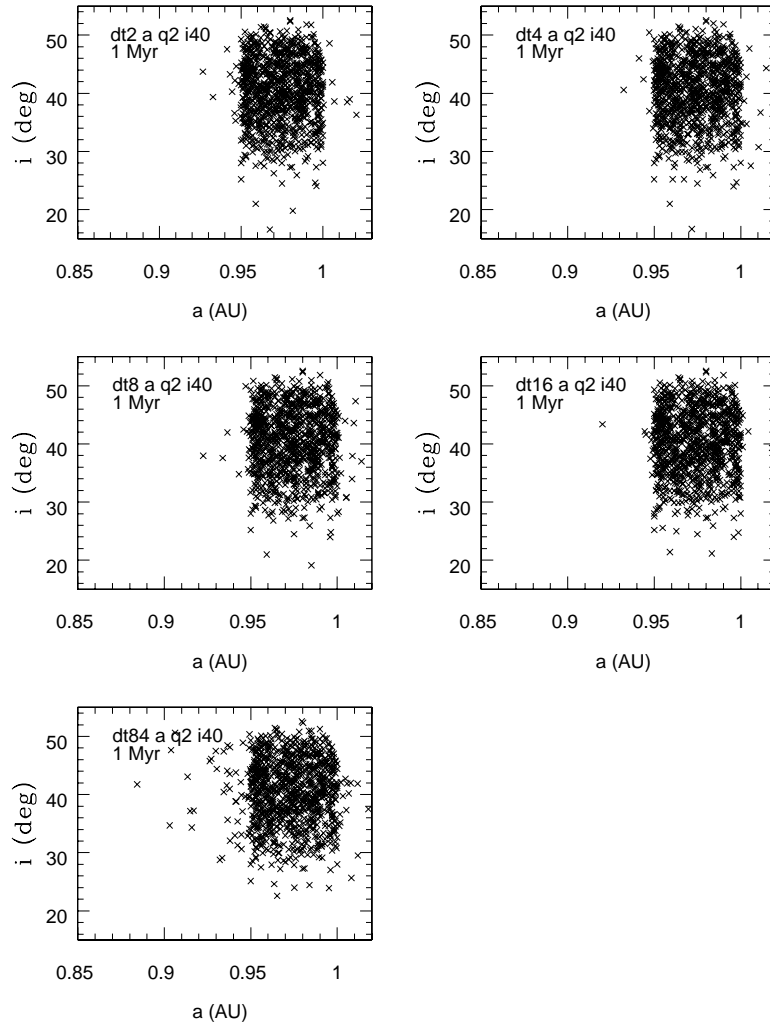


**Figure A.4:** The semimajor axis, inclination distribution for the test particle set with  $40^\circ \leq i \leq 42^\circ$  for five base integration time steps: 2 hours (top left), 4 hours (top right), 8 hours (middle left), 16 hours (middle right), and 84 hours (3.5 days, bottom left) at the end of the 1 Myr integrations.

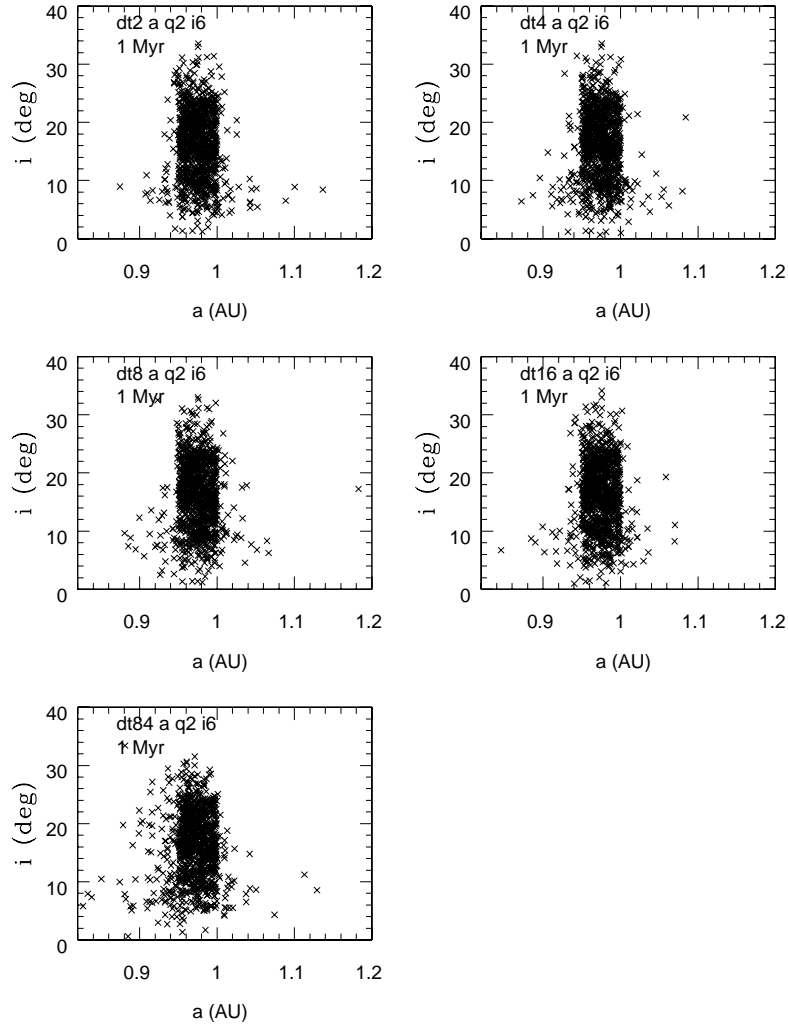


**Figure A.5:** The semimajor axis, inclination distribution for the test particle set with  $6^\circ \leq i \leq 8^\circ$  for five base integration time steps: 2 hours (top left), 4 hours (top right), 8 hours (middle left), 16 hours (middle right), and 84 hours (3.5 days, bottom left) at the end of the 1 Myr integrations.

counter speed would have a particle travelling 1.67 million km, or about 7.6 Hill sphere radii. In practice, relative speeds in bound orbits would seldom exceed half this, and so the 4 hour time step succeeds in travel by about 3.5 Hill sphere radii. Note that this analysis is somewhat over-cautious, as it is only the non-linear portion of the trajectory that matters for the encounter extrapolation for ‘missing’ an upcoming encounter. Thus, the 4 hour time step used is likely OK even for the most extreme cases. The analysis does show, however, that the 3.5 day time step used in previous studies would certainly not be sufficient for the highest-speed NEA encounters with the inner planets.